UNIVERSITÀ DI PARMA

UNIVERSITÀ DEGLI STUDI DI PARMA

DOTTORATO DI RICERCA IN

INGEGNERIA E ARCHITETTURA

CICLO XXXVII

Using Universal Thermal Climate Index Variations as a Multi-Scalar Metric for Assessing Built-Environment Resilience under Climate Change

Applications within the Italian Context

Coordinatore

Chiar.mo Prof. Andrea Spagnoli

Tutore:

Chiar.ma Prof.ssa Barbara Gherri

Co-tutore:

Chiar.mo Prof. Emanuele Naboni

Dottorando: Arch. Marcello Turrini

Anni Accademici 2021/2022 – 2023/2024

Table of contents

1 Introduction 11

1.1 Evidence from literature 16

1.2 Methodological gap 18

1.3 Outlining the scope of the research 19

2 Dynamics of Climate Change and its impact on human well-being 21

2.1 Causes and Global characteristics of climate change 21

2.2 Future climate scenarios 24

2.3 Mitigation and adaptation policies 28

2.4 Escalating overheating in Italy 31

2.5 Impacts on human well-being 32

3 Interactions between human physiology, microclimate and built environment 36

3.1 Human physiology and thermal comfort 37

3.1.1 Thermoregulation of the human body. 37

3.1.2 The heat balance equation for the human body. 38

3.2 Microclimatic Factors for human thermal comfort 43

3.3 The built environment as a microclimatic mediator of human exposure 46

3.3.1 From climate to microclimate 46

3.3.2 Spatial configuration and radiative exposure 47

3.3.3 Geometry and airflow: wind velocity, convection, and natural ventilation . 49

3.3.4 Surface properties, materiality and thermal inertia 51

3.3.5 Living systems and water under climate-change constraints 53

3.4 Outdoor energy balance mechanisms 55
3.4.1 Radiation and geometry 56
3.4.2 Turbulent and latent exchanges 58
3.4.3 Moisture-mediated partitioning and its coupling to sensible heat 59
3.4.4 Storage and delay 60
3.4.5 Residual terms and scale: anthropogenic heat and net advection 61
3.5 Indoor energy balance mechanisms in free-running buildings 64
3.5.1 Scope and operating regimes 65
3.5.2 Solar gains 67
3.5.3 Internal gains 69
3.5.4 Envelope heat transfer 71
3.5.5 Ventilation and air exchange 73
3.5.6 Heat storage 76
3.5.7 Radiant environment and surface temperatures 78
3.5.8 Air movement and humidity 79
3.5.9 Thermal Variability and Comfort 81
3.6 Psychological aspects 81
3.6.1 Microclimatic variables and thermal sensation 82
3.6.2 Psychological adaptation 83
3.7 Human thermal comfort indexes. A critical review 84
3.7.1 Wind Chill 85
3.7.2 Temperature Humidity Index (THI) 86
3.7.3 Comfort Formula (COMFA) 86

3.7.4 Outdoor Standard Effective Temperature (OUT-SET*) 87
3.7.5 Predicted Mean Vote (PMV) 87
3.7.6 Physiological Equivalent Temperature (PET) 88
3.7.7 Universal Thermal Climate Index (UTCI) 89
4 Assessing multi-scalar thermal resilience under climate change 90
4.1 Weather data and morphing to future scenarios 92
4.1.1 Weather data requirements for UTCI-based assessment 92
4.1.2 Choice of baseline year(s) and future horizon(s) 93
4.1.3 Scenario framework and climate-model reference 94
4.1.4 Morphing approach: tool selection and justification 95
4.1.5 Output: standardized EPW packages and traceability 95
4.2 Geometrical modeling of the built environment 96
4.2.1 Why geometry matters for microclimate and UTCI 96
4.2.2 Model types and data sources 97
4.2.3 Geometric resolution and material abstraction across scales 98
4.2.4 Pre-processing rules 100
4.3 Using UTCI for human-centered thermal assessment 102
4.3.1 Why UTCI: physiological model, applicability, comparability 102
4.3.2 UTCI calculation inputs and standard assumptions 104
4.3.3 Interpretation layer: categories vs continuous values 105
4.4 Multi-scalar assessment workflow 106
4.4.1 Inputs and model setup: climate, geometry and materials 108
4.4.2 Microclimate simulation: variables and engines 110

4.4.3 UTCI computation and spatial sampling 111

4.4.4 Post-processing and outputs: maps, statistics and comparability 112

4.4.5 Computational framework 113

4.5 UTCI variations as a metric for thermal resilience 115

4.5.1 Formal definition of ΔUTCI and resilience proxy 116

4.5.2 Aggregation rules across space and time 117

4.5.3 Ranking and decision logic 118

4.5.4 Visualization protocol and reporting standards 118

4.5.5 Limitations of ΔUTCI as resilience proxy 119

5 Multi-scalar case studies 122

5.1 Urban scale: the city of Sassuolo and its districts 123

5.1.1 Climate scenarios in Sassuolo. 123

5.1.2 Identification of Configurations 124

5.1.3 Processing of three-dimensional digital models 128

5.1.4 Preparation of the models for UTCI simulations 132

5.1.5 UTCI Variation for Each Configuration 141

5.1.6 Discussion 157

5.1.7 Conclusions for urban scale applications 161

5.2 Building Scale: the case of the cloister of San Sepolcro in Parma 163

5.2.1 Climate scenarios in Parma 164

5.2.2 Identification of Configurations 167

5.2.3 Processing of three-dimensional digital models 172

5.2.4 Preparation of the models for UTCI simulations 172

5.2.5 UTCI Variation for Each Configuration 178
5.2.6 Discussion 189
5.2.7 Conclusions for building scale 192
5.3 Component Scale: The case of the railway station of Xirbi 194
5.3.1 Climate scenarios in Xirbi 195
5.3.2 Identification of Configurations 197
5.3.3 Processing of three-dimensional digital models 198
5.3.4 Preparation of the models to UTCI simulations 198
5.3.5 UTCI variations for each configuration 199
5.3.6 Discussion 213
5.3.7 Conclusions for component scale. 216
6 Discussion 218
6.1 Synthesis of findings across scales 218
6.1.1 Urban scale: Sassuolo and district morphologies 218
6.1.2 Building scale: the cloister of San Sepolcro (Parma) 220
6.1.3 Component scale: the Xirbi railway station envelope 223
6.1.4 Cross-scale synthesis: recurring mechanisms and scale-specific effects ... 225
6.2 Contribution to knowledge 228
6.3 Limitations and uncertainties 230
6.3.1 Uncertainties shaping absolute UTCI values 230
6.3.2 Uncertainties that can influence comparative ranking 231
6.3.3 Limitations that condition transferability to other climates and contexts. 233
6.4 Implications for design and climate adaptation 234

6.5 Research and practical recommendations 237
6.6 Final remarks 240
7 Conclusions 242
7.1 Responses to the research questions 242
7.1.1 Addressing RQ1: multi-scalar assessment of thermal-comfort resilience . 243
7.1.2 Addressing RQ2: operational robustness and replicability 247
7.2 Concluding synthesis 250
7.3 Scope, transferability, and outlook 250
8 Future developments 252
8.1 Dynamic-exposure comfort 252
8.2 Accelerated exploration through surrogate modelling 253
8.3 Microclimate calibration and empirical credibility 255
8.4 Closing outlook 256
9 References 258
9.1 Climate System Fundamentals and Climate Change Scenarios 258
9.1.1 Physical basis of climate change 258
9.1.2 Emission pathways, SSPs and future climate scenarios 259
9.1.3 Observational evidence and large-scale climate trends 260
9.2 Heat, Human Health and Well-Being 261
9.2.1 Heat stress as a public-health risk 261
9.2.2 Epidemiological evidence and vulnerability patterns 262
9.2.3 Climate change, urbanization and health impacts 263
9.3 Human Thermophysiology and Thermal Comfort 264

9.3.1 Human heat balance and thermoregulation 264

9.3.2 Physiological limits, adaptation and acclimatization 264

9.3.3 Thermal stress and perception mechanisms 265

9.4 Thermal Comfort Indices and Assessment Metrics 265

9.4.1 Evolution of thermal comfort indices 265

9.4.2 Physiological and meteorological foundations of comfort metrics 267

9.4.3 UTCI: theoretical background, assumptions and domain of validity 269

9.4.4 Limitations and comparative use of thermal comfort indices 270

9.5 Microclimate, Built Environment and Heat-Exchange Mechanisms 271

9.5.1 Urban form, geometry and radiative environments 271

9.5.2 Surface properties, materials and thermal mass 274

9.5.3 Vegetation, water and coupled microclimatic processes 275

9.5.4 Indoor and semi-outdoor environments under free-running conditions 278

9.5.5 Indoor–outdoor microclimatic coupling 280

9.6 Microclimatic Modelling, Simulation Tools and Computational Methods 280

9.6.1 Microclimate and CFD-based modelling approaches 280

9.6.2 Human-centred simulation frameworks 282

9.6.3 Toolchains for multi-scalar thermal analysis 282

9.6.4 Modelling assumptions, uncertainties and scale effects 283

9.7 Thermal Resilience, Comparative Assessment and Design 285

9.7.1 Thermal resilience as a comparative construct 285

9.7.2 Baseline–future scenario comparison approaches 285

9.7.3 Multi-scalar assessment of thermal resilience 286

9.7.4 Design-oriented interpretation of thermal-comfort resilience 288

10 List of figures 289

11 Acknowledgements 300

1 Introduction

In the context of the current climate crisis, which is already responsible for a measurable increase in heat-related morbidity and mortality, architects and urban planners are increasingly required to reframe design as an act of climate adaptation. This thesis adopts a health-oriented perspective and argues that resilience and regeneration are not optional ambitions but design responsibilities, especially in climates where overheating is becoming a recurrent condition[1].

The relationship between climate, shelter and health is not a new concern. Vitruvius, in *De Architectura*, described how construction choices could protect inhabitants from rain and cold, and noted that excluding adverse winds could support bodily health and even recovery from severe illnesses[2]. This early intuition resonates with contemporary interpretations of climate-sensitive and regenerative design, where the built environment is considered an active determinant of health rather than a neutral backdrop.

Extending the protective function from the dwelling to the city, Ernesto Nathan Rogers famously argued that architects must provide design solutions “from the spoon to the city”[3]. Under climate change, this statement acquires a renewed operational meaning: decisions at the component, building and urban scales jointly shape exposure to heat and the possibility to live safely and comfortably in everyday outdoor and indoor spaces.

The scientific community gathered around the Intergovernmental Panel on Climate Change (IPCC) agrees that the climate is warming at an alarming rate and that the warming trend will intensify in the coming decades, with increasing frequency and intensity of extreme heat events under many plausible emission pathways[4] . Temperate climates, including Mediterranean ones, are progressively shifting towards hotter and more persistent summer conditions. In the Mediterranean basin, Italy is identified as a hotspot, recording particularly high warming trends and record summer temperatures in recent years[5].

[1] Naboni et al. 2019.
[2] Marcus Vitruvius Pollo, De Architectura.
[3] E. N. Rogers, 1946. *Domus: la casa dell’uomo*. Milano: Domus Editoriale.
[4] IPCC, 2023.
[5] Lazoglou et al. 2024.

Beyond local climate-related disasters such as floods and droughts[6], and beyond ecosystem disruption and economic losses[7], the most critical consequence of climate change for the built environment is the rapid growth of heat exposure and heat stress for the population. Large-scale evidence links recent European temperature patterns to substantial heat-related mortality burdens, with estimates in the order of ten thousand deaths per year over multi-decadal periods[8]. During summer 2022, Italy recorded one of the highest heat-related mortality rates in Europe[9]. In 2023, the implementation of emergency and surveillance plans contributed to reducing the observed mortality burden, although without eliminating the risk[10]. Public-health guidance stresses that heat impacts are largely preventable through coordinated preparedness and multi-sectoral risk management, which includes but is not limited to interventions on the built environment[11].

These trends imply a fundamental shift for architectural practice. Many buildings and urban fabrics that were conceived under past climatic normals and comfort expectations are increasingly misaligned with current and projected thermal exposures. In parallel, demographic ageing and urbanization intensify vulnerability and increase the share of people spending time in heat-prone environments. Designing only for current climate or relying on historical reference years therefore risks underestimating future heat stress. Designers need methods that allow them to anticipate climate-driven changes in comfort and risk, while decisions are still flexible and cost-effective, i.e., at early design stages[12]. At the same time, the outdoor microclimate cannot be treated as a separate specialist layer: it is directly influenced by designable parameters such as morphology, density, materials, shading systems and vegetation, and it feeds back into building performance and energy demand[13].

A design-oriented framing is therefore necessary. Climate-sensitive design has evolved from the mid-twentieth-century bioclimatic tradition to contemporary performance-based and regenerative approaches. The historical objective of optimizing form and envelope for a relatively stable climate is now complemented by the need to design under shifting baselines

[6] Spano et al. 2020.
[7] Alpino et al. 2022.
[8] García-León et al. 2024.
[9] Ballester et al. 2023.
[10] https://www.epicentro.iss.it/caldo/aggiornamenti.
[11] World Health Organization (WHO), 2024; WHO/Europe, 2008 (heat–health action plans guidance).
[12] Hendriks et al. 2025.
[13] Mauree et al. 2019.

and uncertainty, where robustness, adaptability and health protection become explicit criteria[14]. At the urban scale, a mature body of urban-climate research describes how local heat is modulated by surface characteristics, geometry, vegetation and anthropogenic heat; this knowledge is essential to translate climatic hazards into actionable design decisions across scales[15].

From a design standpoint, these epidemiological signals and policy responses converge on a practical question: how will the places people inhabit feel and perform as heat becomes more frequent and persistent? For architects and planners, the relevant risk is not only the occurrence of extreme events, but the day-to-day intensification of thermal exposure that shapes usability, behavior, and vulnerability. Translating climate forcing into design decisions therefore requires an outcome that is directly interpretable in terms of human experience and physiological strain, and that can be compared across contexts and scenarios. Accordingly, this thesis adopts thermal comfort as the operative bridge between climate and project and reads local changes in UTCI between present and future scenarios as a comparable construct for interpreting climate-driven shifts in exposure and design performance.

Modelling and simulation can support this translation, but only if they are embedded in workflows compatible with early-stage decision-making. At concept stages, designers require methods that are sufficiently rigorous to reflect key microclimatic drivers, computationally feasible, and capable of producing comparable outputs across scales and scenarios. Thermal comfort is treated here as a measurable outcome that can guide evidence-based design decisions. Thermal comfort assessment is understood as the combination of a metric and an assessment method that quantifies exposure and physiological strain. Standard approaches to comfort evaluation provide reference frameworks and thresholds, but their application must be adapted to outdoor microclimates and to future climate conditions[16].

To avoid terminological ambiguity, this work adopts the following conceptual distinctions and operational definitions, that here are concise and will be elaborated and justified (conceptually, physiologically, and methodologically) in the following chapters, where the metric choices and the workflow are discussed in detail:

[14] Olgyay, 1963.
[15] Oke et al., 2017 (Urban Climates).
[16] ISO 7730:2005; ASHRAE Standard 55.

- **Thermal comfort**: a state of psycho-physiological acceptability resulting from the interaction between a person and the surrounding thermal environment (air temperature, humidity, wind, mean radiant temperature), mediated by activity and clothing.
- **Thermal comfort assessment**: the procedure through which thermal comfort is quantified using a defined metric (index) and a defined assessment method (measurement and/or simulation).
- **Thermal resilience**: the capacity of a system (building, outdoor space, urban fabric) to maintain or recover acceptable thermal conditions under climatic stressors and across time, including heat extremes.
- **Thermal-comfort resilience** (operational construct): the ability of a built environment to limit the deterioration of thermal comfort under climate change, operationalized through local variations of the Universal Thermal Climate Index (UTCI) between present and future scenarios.

Because thermal exposure is shaped by multiple coupled processes (radiation, airflow, surface properties, and urban form), isolated indicators are rarely sufficient to support design choices that must hold across sites and futures. A comparative framework is therefore necessary to keep the chain from climate forcing to design decisions explicit, and to ensure that outputs remain interpretable when the scale of the intervention changes. In this sense, the diagram in the Figure 1 is a conceptual map of this logic. Its purpose is to clarify how comfort assessment becomes a bridge between scenarios, and why the analysis focuses on differences between present and future conditions (ΔUTCI) as a proxy for sensitivity, rather than on a single absolute comfort value.

Conceptually, the workflow links climate forcing and scenario data to local microclimate modelling, then to a human heat-balance index, and finally to design decisions. UTCI is adopted as the core index because it is grounded in advanced thermophysiological modelling and provides a physiologically consistent representation of thermal stress across outdoor and spatially complex exposure conditions, including transitional and semi-enclosed environments,

while supporting comparative analysis based on continuous values rather than categorical thresholds.[17].

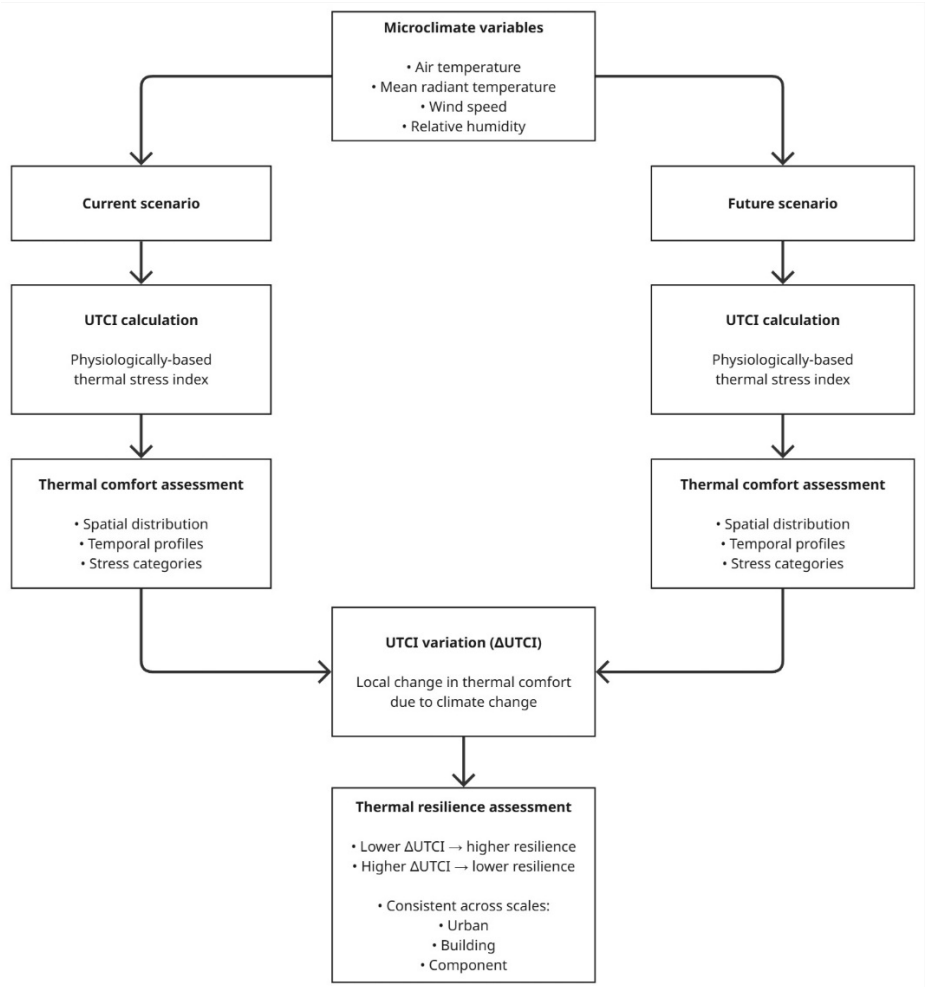

Figure 1. Conceptual framework for thermal-comfort resilience assessment.
The diagram illustrates the logical chain linking microclimatic variables to the assessment of thermal resilience through UTCI calculation, comfort evaluation, scenario comparison, and local UTCI variation (ΔUTCI). Thermal resilience is interpreted as the sensitivity of thermal comfort to climate change and is assessed consistently across urban, building, and component scales.

In literature and in practice, thermal comfort under climate change is commonly investigated at three interconnected scales[18]. At the urban scale, the focus is on neighborhood and city morphology, surface and vegetation strategies, and the spatial distribution of exposure in outdoor public space[19]. At the building scale, attention shifts to the interaction between outdoor microclimate, envelope behavior, ventilation, and energy demand[20]. At the

[17] Bröde et al., 2012; Jendritzky et al., 2012 (UTCI).
[18] Zou et al., 2023.
[19] Oke et al., 2017.
[20] Morales et al., 2025.

component scale, individual design elements (such as shading devices, facade systems, and microclimatic modifiers) are assessed as local levers of comfort[21]. Although these levels form a continuum for design, research often treats them separately, using different tools, inputs, and metrics; this fragmentation makes it difficult to compare findings and to carry evidence coherently from one design decision level to another[22].

1.1 Evidence from literature

The literature review that follows is framed around a single question: whether thermal comfort, read through local UTCI variations between present and future scenarios (ΔUTCI), is already assessed in a way that is comparable across the main design scales. It checks how studies define their scale of analysis, which comfort indices they adopt, and how they derive current and projected boundary conditions. This critical reading is therefore both descriptive and diagnostic: it identifies what is available, what is comparable, and where methodological discontinuities still prevent a unified, designer-oriented assessment.

To position the proposed approach, a critical reading of current literature was carried out to verify whether studies already exist that assess the thermal resilience of the built environment to climate change across three main scales—urban, building, and building component—using the same methodology and comparable metrics. The evidence indicates that explicit multi-scalar applications of a single thermal comfort assessment methodology are currently rare[23] [24] [25]. Most studies adopt a single-scale approach, often dictated by technology or design intervention under evaluation[26] [27]. A limited set of works combines different scales, but frequently in the sense of using urban microclimate simulations as boundary conditions for building energy models; while valuable, this does not necessarily constitute a consistent multi-scalar approach to thermal comfort assessment and resilience[28] [29].

[21] Santamouris et al., 2013.
[22] Zou et al., 2023.
[23] Ibid.
[24] Santamouris, 2020.
[25] Mauree et al., 2019.
[26] Santamouris, 2020.
[27] Zou et al. 2023.
[28] Ibid.
[29] Mauree et al., 2019.

When shifting the focus from individual case studies to review papers that systematically cover multi-scale issues, future climate data, and thermal comfort metrics computed with digital tools, the landscape becomes clearer. Some holistic multi-scale resilience frameworks exist (e.g., approaches such as iQRe[30]), which support diagnostic and strategic planning by quantifying climate-related risks at multiple scales. However, they typically do not compute thermal comfort indices such as UTCI or PET directly and therefore provide general resilience or risk scores rather than detailed comfort-based guidance for specific architectural and microclimatic design decisions[31].

Review contributions converge on recurring limitations that hinder comparability and operational uptake:

- **Scale heterogeneity**: dimensional inconsistencies across studies are often driven by contingent research objectives, resulting in partial insights that are difficult to translate across zone, neighborhood, and city, or across the urban–building–component continuum[32].
- **Procedural inconsistencies**: different approaches to climate model downscaling, reference years, and preparation of inputs lead to methodological discontinuities and to large variability in outcomes across studies[33].
- **Metric fragmentation**: the use of heterogeneous comfort indices (UTCI, PET, SET, PMV, and others) limits cross-study comparison and prevents the consolidation of shared assessment standards[34].
- **Toolchain inhomogeneity**: indoor and outdoor analyses are frequently carried out with separate tools and incompatible workflows; unified platforms or cross-validations remain limited, reducing transparency and replicability[35] [36].

[30] Khoja et al., 2022.
[31] Ibid.
[32] Santamouris, 2020.
[33] Zou et al., 2023.
[34] Morales et al., 2023.
[35] Santamouris, 2020.
[36] Mauree et al., 2019.

1.2 Methodological gap

Overall, the state of the art is extensive and technically mature: it offers robust microclimatic knowledge, a growing set of comfort metrics, and an expanding range of simulation-based applications under climate change. At the same time, the evidence is dispersed across scales and disciplines and is often operationalized through study-specific choices of tools, climate inputs, and indices. As a result, findings that are meaningful within one scale or workflow are not always transferable or comparable when the design question shifts from city form to buildings or to components. Against this background, a gap emerges as a consequence of fragmentation, rather than as a lack of research activity: there is currently no widely adopted standard for assessing thermal comfort and the thermal resilience of the built environment consistently across its main project scales[37] [38] [39] [40]. More specifically:

1. There is no methodology capable of consistently assessing thermal resilience to climate change across multiple built-environment scales (urban, building, and building component) while maintaining comparability[41] [42].
2. There is no shared, widely standardized procedure for generating future climate boundary conditions with the granularity required for microclimatic and built-environment applications[43] [44].
3. There is no universally used metric for quantifying thermal comfort and, crucially, its variation under future climate conditions in a way that supports transversal reading[45] [46].
4. There is no single digital tool or integrated toolchain that operates seamlessly across scales while returning compatible and cross-readable results[47] [48].

[37] Zou et al., 2023.
[38] Morales et al., 2023.
[39] Santamouris, 2020.
[40] Mauree et al., 2019.
[41] Santamouris, 2020.
[42] Zou et al., 2023.
[43] Ibid.
[44] Morales et al., 2023.
[45] Ibid.
[46] Santamouris, 2020.
[47] Mauree et al., 2019.
[48] Santamouris, 2020.

The methodology developed aims to address these procedural gaps in order to organize—and make operationally useful—the current, fruitful but fragmented landscape of approaches.

1.3 Outlining the scope of the research

In light of the identified problem and of the highlighted methodological gap, the overarching aim of this doctoral research is to develop and validate a quantitative–qualitative method that supports early-stage, evidence-based design decisions by assessing thermal-comfort resilience under climate change at multiple architectural scales. The method is based on the analysis of local UTCI variations across present and future climate scenarios and is validated through case studies at urban, building and component scales.

To pursue this aim, the research is structured around the following main questions:

RQ1: How can a quantitative–qualitative, designer-oriented methodology based on local UTCI variations be developed and validated to assess the thermal-comfort resilience of the built environment across urban, building and building component scales under current and future climate conditions?

In order to answer this question, the work is divided into specific operational objectives.

OB1: Develop and validate a single quantitative–qualitative methodology to measure thermal-comfort resilience to climate change across the three project scales: urban, building, and component.

OB1 is articulated into four sub-objectives:

OB1.1: Identify physiological and thermodynamic mechanisms that, indoors and outdoors, influence thermal comfort.

OB1.2: Validate through the literature the feasibility of UTCI variations as an indicator of thermal-comfort resilience and justify the selection of UTCI as the core thermal comfort index.

OB1.3: Apply the methodology to real case studies at three different scales (urban, building and component) to test and refine it under realistic design constraints.

OB1.4: Derive design-relevant interpretative criteria to translate ΔUTCI outputs into actionable guidance for climate-adaptive strategies.

The research question RQ1 and the operational sequence of objectives imply a second functional question:

RQ2: Which operational procedures, modelling tools and assessment mechanisms are needed to implement the methodology in a robust and replicable manner?

This question is addressed through a second objective:

OB2: Develop and validate a complete operational digital workflow so that the proposed method can be implemented in a robust, repeatable way with a consistent suite of available tools at the urban, building and component scales.

OB2 is divided into the following sub-objectives:

OB2.1: Identify appropriate software tools for three-dimensional geometric modelling, acquisition of current and future climate data, microclimatic and thermal simulation, and UTCI calculation.

OB2.2: Develop and document detailed and repeatable operating procedures for data collection, climate processing, microclimate simulation, and ΔUTCI calculation, ensuring methodological transparency and future replicability.

OB2.3: Verify the overall consistency and reliability of the workflow through its complete application to the selected case studies and produce operational guidelines to facilitate future use in other contexts.

2 Dynamics of Climate Change and its impact on human well-being

The climate crisis that threatens human health unequivocally stems from human economic activity. The developed part of the world has altered the composition of the Earth's atmosphere by relying on fossil fuels as the main source of energy, disrupting the balance of heat-trapping gases that regulate temperature. The future climate developments simulated by the scientific community span a range of severities because they are inseparably linked to the lifestyle that global society will adopt in the coming decades and to how far "business as usual" will diverge from current energy policies. Climate action is therefore not only ethical, but above all political. Against this backdrop, the climate crisis must be read not only as a global environmental challenge, but as a design problem: it is redefining the boundary conditions within which cities and buildings must perform, making thermal resilience a non-negotiable requirement of the built environment and, consequently, a constraint for contemporary design decisions. At the global and national levels, climate action is increasingly shaping the regulatory and economic frameworks within which the built environment is conceived and transformed. Italy has transposed the overarching directives and is implementing climate action primarily through environmental regulations and economic incentives.

2.1 Causes and Global characteristics of climate change

The main source of exogenous energy for the biological system of planet Earth is the sun, and the process of radiation and absorption between solar energy and the Earth's atmosphere is what drives the greenhouse effect. The visible part of solar radiation, in the form of short waves, passes almost unimpeded through the atmospheric gases, is absorbed by the soil and oceans, and re-emitted in the form of long-wave thermal radiation[49]. Gaseous molecules present in the atmosphere, mainly CO_2, CH_4, N_2O[50], and water vapor, intercept this thermal radiation and trap it in the lower layers of the atmosphere, pushing upwards the portion of the atmosphere through which the energy entering from the sun must be reflected back to maintain energy balance[51]. For the built environment, this mechanism matters because it

[49] Kiehl et al. 1997.
[50] Myhre et al. 1998.
[51] Etminan et al. 2016.

alters the thermal boundary conditions at the surface: urban materials absorb, store, and re-emit more heat, affecting both outdoor exposure and indoor overheating risk.

However, the upper layers of the atmosphere are colder than the lower ones, from which solar energy would normally be re-radiated into space. According to Boltzmann's law, colder bodies emit less energy, therefore the outgoing flow decreases, and a positive radiative forcing is established, which can only be canceled by an increase in surface temperature until equilibrium is restored[52]. Water vapor is the largest contributor to the greenhouse effect. However, CO_2, although accounting for about 20% of the greenhouse effect in clear skies, acts as a primary forcing agent by warming the air and allowing it to contain more water vapor, which is dominant in terms of absorption and therefore acts as an amplifier[53].

Satellite spectroscopy and data from surface radiometers confirm the theoretical picture, showing a reduction in outgoing longwave radiation in the CO_2 absorption bands and a concomitant increase in the longwave flux downward to the surface[54]. An increase in downward longwave radiation can raise surface temperatures and the radiant environment experienced by people, especially in dense urban settings where radiative exchange is partially "trapped" by geometry. This is one reason why air temperature alone may underestimate thermal stress at pedestrian level.

Currently, the concentration of CO_2 in the atmosphere has increased compared to two centuries ago: from 280 ppm in the pre-industrial era, it has risen to over 420 ppm in 2023[55]. Because CO_2 persists over long timescales, buildings and urban spaces designed today will operate under progressively warmer thermal conditions even under strong mitigation efforts. Three independent signals lead to the conclusion that there is a direct link between the increase in CO_2 and human activity. First, the global carbon budget shows that the amount of CO_2 released each year by fossil fuels and deforestation is almost equal to the sum of the increase measured in the atmosphere and that absorbed by the oceans and vegetation; therefore, no other significant sources are evident[56]. Second, the "isotopic signature" of atmospheric carbon is increasingly different from that of carbon produced by natural

[52] Trenberth et al. 2009.
[53] Schmidt et al. 2010.
[54] Feldman et al. 2015.
[55] Friedlingstein et al. 2023.
[56] Friedlingstein et al. 2023.

phenomena, which confirms the anthropogenic origin of the excess CO_2[57]. Third, the decline in oxygen relative to the increase in CO_2 is in a ratio typical of combustion, a signal that cannot be explained by other known natural processes[58]. Summarizing this evidence, the IPCC Sixth Assessment Report states that global warming "is unequivocally caused by human activities" and that the chemical and isotopic composition of the atmosphere cannot be reproduced by other causes[59].

The manifestations of these changes in the atmosphere are evident on the Earth's surface in a series of global climate anomalies, which have specific repercussions at the local level. Anthropogenic greenhouse gas emissions have caused the total average radiative forcing to rise to +2.72 W m^{-2} in 2019 compared to 1750. This energy imbalance has resulted in an average global surface warming of 1.09 °C in the decade 2011-2020 compared to the period 1850-1900, with land warming roughly double that of the oceans. The oceans absorbed more than 90% of the excess heat, contributing to a rise in the average sea level of 0.20 m since 1901, at an increasing rate, which rose from 1.3 mm $year^{-1}$ in the period from 1901 to 1971 to 3.7 mm $year^{-1}$ in the period from 2006 to 2018. AR6 also documents the intensification of the hydrological cycle with increasingly frequent extreme rainfall and intense and prolonged droughts in subtropical regions and the melting of polar ice and high-altitude glaciers[60].

In addition to contributing to sea level rise, ice melt also contributes to a decrease in the Earth's surface albedo, triggering positive feedback mechanisms[61]. For architecture and spatial design, the key implication of this planetary energy imbalance is not only a shift in mean temperature, but the intensification and persistence of heat extremes. These conditions increase heat storage in urban materials, reduce nocturnal cooling opportunities, and amplify both outdoor thermal exposure and the likelihood of cumulative indoor overheating.

At a global level, the distribution of warming is not uniform on the whole earth. Land areas are warmer than oceans, with an intensity approximately 1.4 times the global average. The poles, especially the Arctic, experience greater warming than other parts of the planet. During the warm season, the Arctic warms twice as much as the global average and in cold seasons it

[57] Keeling et al. 2017.
[58] Manning et al. 2006.
[59] IPCC, 2023
[60] Cooley et al. 2022
[61] IPCC, 2023

can reach up to three times as much, while Antarctica has the same characteristics, but more attenuated than the North Pole. Since most settlements are located on land, this land-amplified warming directly increases the thermal stress that the built environment must buffer through form, materials, and passive cooling strategies.

Overall, the picture is that rising greenhouse gas concentrations are changing the thermal conditions at the surface. In cities, this translates into a combination of hotter air, persistent warmth at night, and increased radiant heat from built surfaces—precisely the mix that drives heat stress at pedestrian level and overheating indoors. This is the starting point for the next steps of the thesis: moving from large-scale climate signals to the microclimatic and thermo-physiological processes that matter for design.

2.2 Future climate scenarios

The IPCC's Sixth Assessment Report (Working Group I, 2021) explores possible future climates based on five scenarios. These are outlined against the backdrop of specific socioeconomic backgrounds ranging from a sustainable future (SSP1) to a future that continues with business as usual (SSP5). For each of these societal settings, the approximate level of radiative forcing is projected for 2100. SSP1-1.9, SSP1-2.6, SSP2-4.5, SSP3-7.0, and SSP5-8.5 are the scenarios, where SSP1 - SSP5 indicate community behaviors and the numbers from 1.9 to 8.5 are the resulting radiative forcings in W/m^2 by 2100 relative to 1750[62]. Although these pathways differ in their socioeconomic assumptions, they converge in indicating a sustained intensification of heat-related conditions at the surface. This common signal underpins the relevance of climate change for the built environment, where increased heat exposure is already emerging as a dominant constraint.

Climate scenarios are treated here as conceptual frameworks that describe possible future climatic conditions. Their role is to define a coherent climatic context within which the relationship between climate change and the thermal performance of the built environment can be examined. Accordingly, the analysis focuses on how changes in climate are translated

[62] Meinshausen et al. 2020

into changes in human thermal exposure, by considering future conditions in relation to the present.

The low-emission pathways SSP1-1.9 and SSP1-2.6 assume global action towards sustainability trends, with CO_2 emissions peaking early and falling to net zero around mid-century, becoming negative thereafter. In contrast, scenarios SSP3-7.0 and SSP5-8.5 describe a future with insufficient mitigation measures: in SSP3, a world characterized by regional rivalries leading to an increase in emissions until 2100 is assumed, and in SSP5, a resource-intensive, fossil fuel-based development path is outlined, with CO_2 emissions roughly doubling by 2050. SSP2-4.5 represents an intermediate case, with modest mitigation, keeping global emissions close to current levels by mid-century. Importantly, near-term warming differs relatively little across scenarios, meaning that heat adaptation for buildings and public space is necessary even under ambitious mitigation.

These SSP pathways provide the narrative backbone for the temperature projections assessed in IPCC AR6. As shown in Figure 2, all scenarios show steady warming up to +1.5°C above pre-industrial levels until almost mid-century, while by 2050 the five scenarios are clearly separated. After this date, temperatures diverge significantly, and this divergence is determined by cumulative greenhouse gas emissions: in a low SSP future, decisive mitigation reduces additional radiative forcing and consequently temperatures, while in a high SSP future, emissions push temperatures ever higher. By 2100, the divergence between scenarios is considerable, including higher overheating risk, reduced outdoor thermal comfort, and increased cooling demand, especially during prolonged heat events.

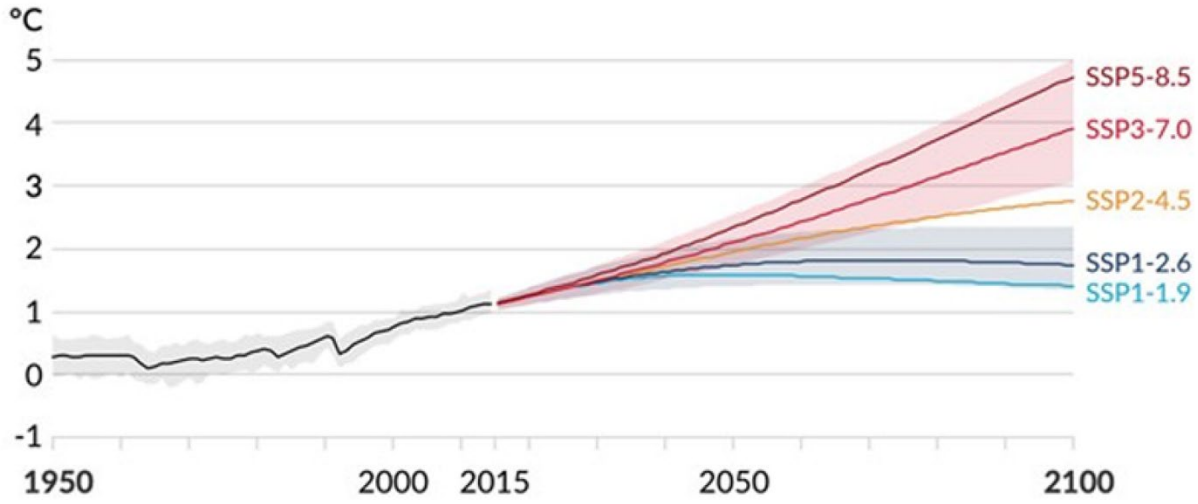

Figure 2. Projections of the average global surface temperature change relative to the period 1850-1900 (°C). The black line shows the trend observed from 1950 to 2020. From 2015 onwards, the average projections of the CMIP6 models are shown for the five illustrative scenarios of the IPCC-AR6. The colored bands represent the range of each distribution, while the central curves indicate the median. The divergence between scenarios becomes evident after the middle of the century: in 2100, median warming ranges from about 1.4 °C in the rapid decarbonization scenario (SSP1-1.9) to about 4.4 °C in the high emissions scenario (SSP5-8.5). (Source: IPCC, AR6 WG I, Figure SPM 8a).

Figure 3 shows that the warming associated with a given global temperature increase is distributed very unevenly. Large positive anomalies are concentrated over land, and particularly at high latitudes, while oceanic regions warm much less. Even at lower warming levels, Arctic temperatures depart strongly from the global mean[63]. In the Mediterranean area, the signal is different. Absolute temperature increases are smaller, typically on the order of 1.5–2 °C, but they occur in combination with more frequent and persistent heat waves[64]. In urban contexts, this background warming does not act in isolation, but combines with local effects related to urban form and surface characteristics, contributing to higher heat stress conditions.

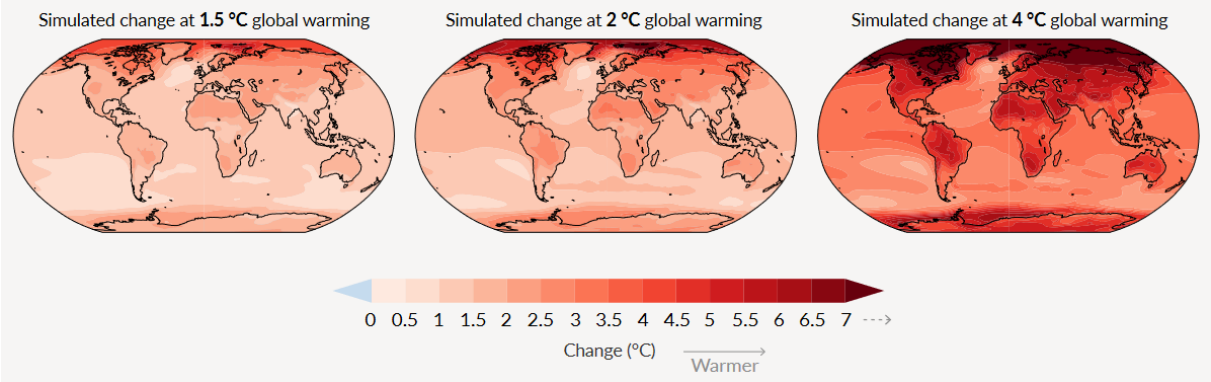

Figure 3. Predicted global warming for three temperature increase scenarios. Source: IPCC

[63] IPCC, 2021.
[64] IPCC, 2022.

At the local scale, the predicted temperature rise due to climate change also varies depending on the geographical location of the site. The temperature increases between current conditions and 2050, considering the high-emission scenario, will take the form of intense heat waves in colder climates such as Copenhagen and Vienna, where the temperature difference will reach peaks of 19°C, occurring as short-term extremes during heat events rather than as a uniform shift in seasonal averages, while the intensity of the heat will diminish throughout the year in temperate and warm climates. In Rome, less pronounced peaks of around 4-5°C are likely to occur during the hottest hours of summer or in autumn, and in Riyadh, where the climate is hot and dry, there will be a fairly uniform increase of around 4°C throughout the year (Figure 4).

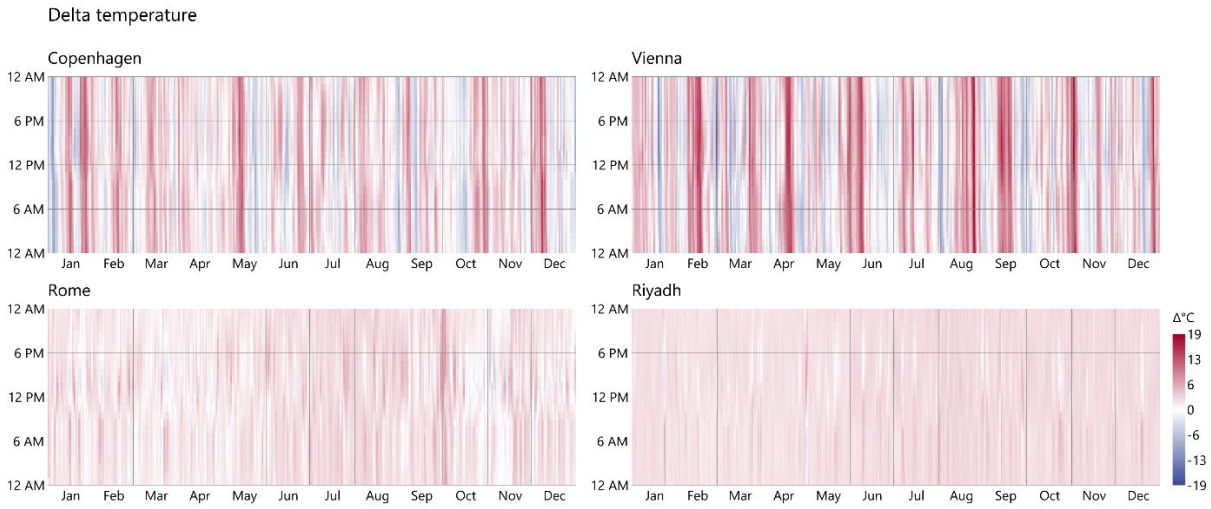

Figure 4. Delta air temperature between the current scenario and 2050 under a high-end emission pathway. in four capitals located in different climate zones. The difference in the nature of the warming can be seen, concentrated in heat waves in colder climates and more uniform in warmer climates. Graphs produced by the author of this thesis based on weather data generated using Meteonorm 8.0. Copyright: Marcello Turrini, Emanuele Naboni, 2023

On a hyperlocal scale, increasing average temperatures and heat peaks will affect European cities both outdoors—through urban heat island effects and deteriorating outdoor thermal comfort—and indoors, where insufficient ventilation and limited shading increase vulnerability. Under the SSP3-7.0 scenario, when global mean warming reaches about +2 °C, around half of Europe's urban population will be exposed to a very high risk of heat stress in summer, with heat waves becoming a threat at all European latitudes. In indoor spaces, the number of hours of summer thermal comfort could be reduced by up to 74% in the SSP3-7.0

scenario, when global mean warming reaches about +3 °C, and even highly insulated buildings designed to fit the current climate will be vulnerable if not adequately adapted. Under warmer summers, insulation alone may reduce winter losses but can also slow down heat release if solar gains and internal loads are not controlled. Shading, ventilative cooling, and envelope strategies therefore become primary heat control measures. At the same time, energy demand for cooling is expected to increase by 81–104% in the Mediterranean area by 2035 and by 91–244% after 2065, while in Northern Europe the estimated increases are 31–73% by 2050 and 165–323% by 2100.

2.3 Mitigation and adaptation policies

Climate action is commonly articulated through two complementary strategies. Mitigation addresses the causes of climate change by reducing greenhouse-gas emissions and enhancing sinks, while adaptation addresses its consequences by reducing exposure and vulnerability to climate hazards. In the built environment, mitigation relates to lowering operational and embodied emissions, whereas adaptation focuses on limiting indoor and outdoor heat stress through passive cooling, shading, ventilation, and urban form. The following overview summarizes how these two strands have been translated into policy frameworks that directly shape thermal resilience.

Globally, various institutions have been actively working to combat climate change for around thirty years. In 1992, the United Nations Framework Convention on Climate Change (UNFCCC) laid the legal foundations for subsequent sectoral decarbonization strategies, including those relating to buildings, establishing the principle of “Common but Differentiated Responsibilities” (CBDR). This principle is based on the relationship between industrial development and climate change and recognizes that all states have a common obligation to address the problem of environmental destruction but denies that all states have the same responsibility for environmental protection due to their unequal economic and developmental conditions. In 1997, the Kyoto Protocol introduced the first quantified emission reduction commitments for industrialized countries to implement this principle, indirectly stimulating the first demand-side efficiency standards and voluntary green building programs that linked comfort to carbon intensity. The 2015 Paris Agreement marked a paradigm shift: for the first

time, all countries were asked to contribute to reducing CO2 emissions, highlighting passive design and renovation as effective mitigation tools. The 2021 “Glasgow Climate Pact” called on countries to make deep, rapid, and sustained emissions cuts and to limit temperature rise to 2.0 °C and preferably to 1.5 °C by the end of this century, a mandate that is redefining green mortgage markets and climate-aligned building codes.

In order to keep the increase in temperature to 1.5 °C, the European Union has taken on the role of regulatory forerunner in this global framework for action. The European Green Deal (2019) and the subsequent Climate Law enshrine the goal of achieving net-zero greenhouse gas emissions by 2050 in a legally binding manner, with interim targets of at least 55% by 2030[65]. The extreme deadline for net zero greenhouse gas to remain in the 2 °C of maximum temperature rise is 2080-2085. As regards policies on the built environment, the EU is finalizing the emissions trading system, including buildings and transport in carbon pricing, and strengthening the Effort Sharing Regulation and the Land Use, Land-Use Change and Forestry (LULUCF) rules to regulate emissions embedded in construction products.

Other initiatives, such as incentives for renovation and the updating of building energy performance legislation, aim to double the annual renovation rates and require nearly zero-energy standards using passive cooling technologies, adaptive facades, and vegetation-based shading, thereby reducing peak heat loads and carbon emissions. From a financial perspective, a series of public incentives are being promoted by the Investment Plan for a Sustainable Europe, also ensuring that low-income households have access to healthier indoor climates at affordable costs. The overall effect is a set of standards that combine climate change mitigation with distributive equity, as called for by the IPCC, which identifies this approach as essential for the social acceptability and behavioral adoption of efficiency measures.

Pathways broadly consistent with limiting global warming to around 2 °C typically reach net-zero CO_2 emissions in the early 2070s, with some scenarios extending towards the 2080–2085 range. This time window delineates an outer temporal boundary within which climate adaptation of the built environment becomes unavoidable, irrespective of the ultimate success of mitigation strategies.

[65] European Commission (2019). *The European Green Deal* (COM(2019) 640 final).

The IPCC assessments outline a decisive 30-year window for achieving the Paris-Glasgow temperature thresholds. Pathways compatible with 1.5°C converge towards net global CO_2 emissions of zero in the early 2050s; those limiting warming to 2°C are concentrated in the early 2070s, with the slowest 10-15% slipping to 2080-2085. Table 3.1 of the AR6 Summary Report explicitly lists this 2080-2085 range for the tail of the 2°C scenarios. Therefore, the 2050-2080 range marks the outer boundary within which decarbonization must be achieved to honor the Paris ambitions.

Italy is working within this European framework, adapting the supranational targets to its Mediterranean climate. Through the Integrated National Energy and Climate Plan (PNIEC), there is a commitment to achieve a 43% share of renewable energy in final energy consumption and a 55% reduction in emissions from the building sector by 2030[66]. These targets can be achieved through nearly zero-energy buildings (NZEBs). In the long term, a strategy for 2050 sets the goal of complete decarbonization of the building stock through the use of heat pumps, district-scale geothermal systems, and natural thermal insulation, viewing mitigation as resilience to summer overheating, which is now a key public health concern due to the intensification of current and projected heat waves[67].

Fiscal instruments such as the Ecobonus[68] offer transferable tax credits that fully cover renovation costs, incentivizing the thermal renovation of buildings and the use of solar energy; initial assessments indicate an average reduction of 70% in energy consumption for heating and appreciable reductions in indoor temperature variations during heat waves[69]. Additional municipal regulations, such as Milan's Climate Adaptation Plan, promote indoor and outdoor environmental actions such as cool roofs, urban greening, and high-albedo paving, thus offering collateral benefits for outdoor comfort and urban heat island mitigation[70].

A converging narrative emerges from the actions promoted at these three levels of governance: mitigation policies are increasingly evaluated not only on their potential to reduce carbon emissions, but also on their ability to safeguard or improve thermal comfort under

[66] Italy, Ministry of Economic Development 2019

[67] Romanello et al. 2021

[68] Italian national tax-incentive scheme for building energy retrofits, introduced in 2007 and implemented through successive national budget laws under the Ministry of Economy and Finance.

[69] ENEA 2023

[70] Municipality of Milan, 2022

climate stress conditions[71]. The promoted policies prioritize the renovation of existing buildings, supporting passive and nature-based solutions and integrating social justice mechanisms, considering the built environment as both a mitigation vector and an adaptation refuge. This policy convergence clearly suggests a clear design methodology: building envelope technologies, spatial morphologies, and material choices must simultaneously minimize emissions during the life cycle and protect occupants from the increasingly intense extremes predicted by IPCC AR6. In practical terms, this translates into the implementation of passive indoor[72] and outdoor strategies to achieve thermal resilience, minimizing carbon emissions through the use of renewable energy to meet residual energy needs.

2.4 Escalating overheating in Italy

Almost two generations have passed since the great heatwave that struck Central Europe and Italy with exceptional intensity in July 1983[73]. The widespread media coverage it received in Italy testifies to the extraordinary scale of the event. Its uniqueness, apart from the extreme temperatures reached, which did not exceed the previous record highs of July 1962, was its duration: a full two weeks, something never seen before. Since then, heatwaves have become increasingly frequent, with a decreasing time interval between two consecutive events.

Year	Period	Maximum temperature recorded	Area	Difference from typical summer temperatures	Duration
1983	July	43.6 °C	Cagliari Elmas	+12.6 °C	About 2 weeks
1994	July	About 40 °C	Varie località		About 1 week
1998	July	About 40 °C	Varie località		About 1 week
2003	July -August	41.1 °C	Firenze	+9.1 °C	About 3 weeks
2012	July -August	42.7 °C	Pescara	+12.7 °C	About 2 weeks

[71] Orsetti et al. 2022
[72] Hong et al. 2023
[73] CDC / MMWR: *Heat-related mortality—Latium Region, Italy, summer 1983* (1984; 33(37):518–521).

2015	July	40.3 °C	Roma Ciampino	+ 10.3 °C	About 3 weeks
2017	August	42.0 °C	Ferrara, Roma	+9.0 °C - +12.0 °C	About 2 weeks
2019	June - July	41.0 °C	Northern Italy (Torino, Milano)	+12.0 °C - +11.0 °C	About 2 weeks
2021	August	48.8 °C	Siracusa (Sicilia)	+17.8 °C	About 2 weeks
2022	July	42.0 °C	Many		About 3 weeks
2023	July	44.6 °C	Cagliari Elmas (Sardegna)	+13.6 °C	About 2 weeks
2024	July	40 °C	Palermo	+10.0 °C	About 4 weeks

Table 1. Successive heat waves from 1983 to 2024. Sources: elaboration based on long-term observational records and official communications from the World Meteorological Organization (WMO), the Italian Air Force Meteorological Service (MISTRAL), and the Italian National Institute of Statistics (ISTAT).

Table 1 lists the latest heatwaves in Italy. Three trend data stand out here. The deviation from typical seasonal temperatures of record highs, which tended to be more than 10 °C higher. The intensification of the frequency with which abnormal seasons occur, which have occurred every year for the past five years, and the increasing duration of the events, from around one week to four weeks in 2024. Unfortunately, the record high temperatures, with the resulting thermal discomfort, are only one aspect of the ongoing change. News of the rising temperature is also accompanied by gloomy reports of environmental disasters because the disruption of the climatic balance triggers chain mechanisms that generate catastrophic events. Multi-seasonal drought events, flash floods, widespread fires and the progressive receding of the coastline paint a picture of greater instability and vulnerability of the land. These events are very different from each other, but all can be associated with global warming: warmer air retains more moisture and energy, which in colliding with colder air masses in the upper layers of the atmosphere gives rise to torrential rainfall events and extreme heatwaves; rising sea levels and anomalies in ecosystems such as drier forests and weaker coastlines are direct or indirect consequences of rising temperatures.

2.5 Impacts on human well-being

As shown, climate change is significantly intensifying heat stress in Mediterranean European population, with Italy being identified as a hot spot for overheating. The impact on health and human well-being of increasing temperatures is already severe. Over the last century, the average temperature in Italy has risen by around 1.2–1.5 °C, contributing to more frequent and intense heat waves. The catastrophic heatwave of 2003, which caused around 70,000 excess deaths across Europe[74], represented a turning point in the recognition of heat as a major public health hazard. In Italy alone, summer mortality increased by 11.6% compared with the average of the 1998–2002 period[75].

Subsequently, in 2015, the surveillance service recorded a summer increase of around 10% in overheating-related mortality among the adult population[76]. In contrast, during summer 2017, the second hottest since 1800, overheating had a comparatively modest impact on health: the combination of dry temperatures, post-winter flu harvesting, and effective heat-health alert plans limited excess mortality, which emerged only among people over 85 years old in August, particularly in cities lacking a dedicated health alert system[77].

More recently, during the record-breaking summer of 2022, Europe experienced one of the most severe heat-related mortality events ever documented. A comprehensive epidemiological assessment estimated 61,672 heat-related deaths across Europe between 30 May and 4 September 2022. Mediterranean countries accounted for the largest shares, with Italy among the most affected: with a temperature anomaly of +2.28 °C, approximately 18,010 heat-related deaths were estimated, corresponding to 295 deaths per million inhabitants, the highest rate in Europe[78]. Most of the victims were mainly in the over-80s range and, to a lesser extent, those aged 65-79, with a general majority of women over men. These extreme rates underscore how excessive heat is now recognized as a serious public health risk[79], with a significant increase in heat-related morbidity and mortality, especially among vulnerable

[74] Robine et al. 2008.
[75] Michelozzi et al. 2003.
[76] Michelozzi et al. 2016.
[77] Italian Minstry of Health et al. 2018.

[78] Ballester et al., 2023
[79] Kovats et al. 2008.

groups such as the elderly. In Italy and other southern European countries with a higher average age, older people have proven to be the most susceptible to heat[80].

The threat to human health posed by overheating is amplified by the urban environment. Recent studies found that heat-related mortality increases more rapidly in urban centers due to the synergy between overheating and urban heat island (UHI) effect[81]. A multi-city analysis showed that a 1°C increase in apparent temperature above a certain threshold resulted in a greater increase in mortality in Mediterranean cities than in colder cities in Northern Europe[82]. Analogously, in the most important urban centers of the Emilia-Romagna region, intense heat, measured by apparent temperature, is strongly associated with a significant increase in ambulance calls for non-traumatic illnesses[83].

These findings highlight how urban environment under overheating threatens human health and Italian urbanized environments are at the forefront of this problem. It is also noted that the impacts of urban heat are unevenly distributed, disbalanced on social inequalities. Some populations are shown to be much more vulnerable to heat. Epidemiological studies identify the older generations, infants, and people with chronic illnesses as most at risk, especially if they live alone or without social support[84]. Moreover, low-income and socially marginalized communities often live in hotter neighborhoods with lack of green space and higher sealed surfaces, resulting in greater exposure to extreme heat[85].

The awareness that improving the resilience of the built environment to thermal comfort is essential for reducing heat-related health risks in cities is increasing. Urban planners and health experts are now collaborating on strategies that mitigate heat stress, such as expanding green infrastructure to cool down the urban microclimate, implementing cool roofs and sidewalks, and, most innovative, creating cooling centers for vulnerable citizens, like the climate refugees of Barcelona[86]. These measures aim to improve urban thermal comfort and prevent the worst health consequences during extreme heat.

[80] Stafoggia et al. 2006.
[81] Santamouris, 2020.
[82] Baccini et al. 2008.
[83] Alessandrini et al. 2011.
[84] Stafoggia et al, 2006.
[85] Santamouris 2020.
[86] https://ajuntament.barcelona.cat/serveissocials/es/noticia/crece-la-red-de-refugios-climaticos-para-protegerse-del-calor_1523924

Projections for the future decades depict a strong increase in heat-related health impacts in Mediterranean cities. By 2050, annual heat-related deaths in southern Europe are expected to more than double without adaptation measures, under the worst-case scenario [87]. Mediterranean countries such as Italy and Spain show the highest projected increases in heat-attributable mortality anomalies, and in the worst-case scenario (RCP8.5) and in the latter part of the 21st century (2070-2099), they could reach a percentage increase in heat-attributable death anomalies of 9.09% and 7.37%, respectively[88].

The World Health Organization (WHO) has also weighed in on the debate, dedicating an entire module of its 2008 *Heat-Health Action Plans: guidance* to the issue, identifying indoor heat reduction and long-term urban planning as essential measures for managing weather-related health alerts[89]. Subsequently, in 2018, it introduced a comfort threshold for indoor temperatures of 24 °C, recommending mitigation strategies such as thermal insulation, reflective materials, passive shading, night ventilation, and even a moderate use of air conditioning to avoid exacerbating the heat island effect[90]. Finally, in 2021, it reiterated that measures such as cool roofs, green corridors, and compact but well-ventilated cities are among the most effective preventive measures[91].

From these tendencies for the future, it is more and more clear that improving the resilience of the built environment to extreme heat is a public health imperative. Urban heat and its health impacts are not only a climate issue but also intimately linked to urban design, architecture, and social policies[92].

In many European cities, especially in Mediterranean ones, higher average temperatures and repeated heat episodes are already evident in everyday outdoor conditions. The effects are uneven, since local climate, urban form, and surface materials strongly influence how heat is perceived at pedestrian level. As a result, the same regional warming signal can translate into very different levels of thermal stress depending on microclimatic conditions.

[87] Gasparrini et al. 2017.
[88] Martinez-Solanas et al. 2021
[89] World Health Organization, 2008
[90] World Health Organization, 2018
[91] World Health Organization, 2021
[92] Mavrogianni et al. 2022

3 Interactions between human physiology, microclimate and built environment

In order to interpret how climatic conditions translate into human thermal comfort, it is necessary to bring order to the intricate and varied realm of thermal comfort assessment, retracing the steps that led to the development of the most widely used metrics today.

Thermal comfort assessment is here understood as the procedure through which the interaction between the human body and the thermal environment is translated into measurable descriptors, by adopting a defined comfort index and an explicit assessment method. This assessment logic is intentionally framed to remain valid across multiple architectural scales, because thermal exposure is shaped by coupled processes that act continuously from the urban environment down to individual technological components.

Accordingly, the chapter adopts a multi-scalar perspective: from the urban scale, where morphology and land-cover configurations shape outdoor exposure; to the building scale, where envelope behavior and ventilation mediate indoor and semi-indoor conditions; to the component scale, where localized design solutions act as microclimatic modifiers.

The analysis begins with an examination of human physiology and the mechanisms of thermoregulation. Attention then shifts to the microclimatic factors that trigger the human body's responses to thermal stress. Subsequently, the characteristics of the built environment that influence these microclimatic conditions are investigated. Through this sequence, microclimatic variables provide the link between the physical and technological characteristics of the built environment (morphology, materials, typologies and design solutions) and the physiological response of the human body to thermal discomfort.

Once these built environment aspects have been clarified, the focus turns to evaluation metrics. The most widely used thermal comfort indices are reviewed, drawing on established considerations in scientific literature, in order to identify the index that, in the current state of the art, is most suitable for an objective assessment.

3.1 Human physiology and thermal comfort

3.1.1 Thermoregulation of the human body.

Two different kinds of temperature for the human body are observed. The *core temperature*, that must be mostly constant at 37 °C to let the main organs and brain work, and the *shell temperature*, that is the peripheral temperature of the skin and of the extremities and depends on the amount of blood contained in them according to the environmental and metabolic heat gains. Usually, the shell temperature is about 4 °C lower than the core temperature[93], and the thermoregulatory system, through the hypothalamus, keeps the gradient between core and shell temperature constant. Under the effect of climate change, higher temperatures stimulate vasodilation, which brings the surface temperature closer to the external temperature. This mechanism obstructs heat dissipation from the core of the human body, leading to hyperthermia[94] and heat strokes.

Internal heat is produced by metabolism and extra work (i.e. running or climbing) and when it is exceeding the balance level it is released by the human body by convection (sensible heat flux) by about 15%, evaporation (latent heat flux) by about 22%, radiation (long and short wave) by about 60%, respiration (latent and sensible) and conduction (contact with surfaces) by about 3%, to reach the so-called *homeostatic* state. Through respiration, if the external air is colder than the core temperature, it takes heat from the body during inspiration and releases it to the environment during the expiration. Through convection, the colder external air takes heat from our body. Through radiative exchange, colder surface temperatures take radiative heat from our body. Under the effect of climate change, with extreme temperature conditions, the heat exchange from the body to the external environment reverts and the human body gains heat. The only mechanism for dissipation is evaporation with higher levels of sweat, which becomes excessive during extra work activities[95].

There are two different thermoregulatory systems. The first one, active, is the controlling one. It is the complex action of shivering, sweat moisture excretion and peripheral blood flow regulation. The second one is the passive, controlled one. It is the effect of the interaction of

[93] Ahima, 2020
[94] Tansey et al. 2015.
[95] Ibid.

the environment and the human body, that is the heat loss (or gain when it occurs) by convection, long-wave radiation exchange with surrounding surfaces, solar irradiation, evaporation of moisture from the skin, heat and mass transfer through non-uniform clothing. In extreme conditions of overheating due to climate change, maximum vasodilation and sweating are quickly reached but may not be sufficient to compensate for the enormous environmental heat load. In such cases, active thermoregulation fails and, in addition to the possibility of heat-related illnesses, the burden of heat balance shifts from passive to active thermoregulation, requiring the body to resort to external strategies such as shade, hydration, or ventilation to avoid overheating[96].

Physiologically, the thermoregulatory system and the capability of the human body to adapt to the thermal misbalance and to tolerate discomfort depends on personal characteristics like age, gender, weight, fat thickness, acclimatization, fitness. The most important among them are age and fitness, and they are strictly correlated. High age and low fitness cause low tolerance. In particular, advanced age is one of the most critical vulnerability factors, and epidemiological studies show that older people are the most susceptible to mortality during heat waves[97].

3.1.2 The heat balance equation for the human body.

Many and different are the forms to express the human body thermal balance in outdoor and indoor environments, but all of them are generally based on three main principles, which are heat generation in the body, heat transfer between the body and the environment, heat storage in the body[98]. Heat generation is affected by the metabolic activity, which provides the "fuel" for the body to operate mechanical work. The exceeding energy is released as heat (sensible and latent) to the environment by radiation, convection, evaporation and conduction.

In outdoor conditions, solar radiation and wind speed play an important role, which in a normal indoor environment is not relevant. These factors cause rapid heating or cooling to the human body, which normally adapts slowly to the external conditions, therefore they are the

[96] Ahima, 2020.
[97] Kenney et al. 1987
[98] Parsons, 2002.

main causes of thermal discomfort. As seen above, there is a strict correlation between solar radiation and wind speed with the form of the city. To understand how the urban landscape may influence human comfort, it is necessary to analyze the energy balance of the human body and the way it exchanges with its surroundings.

The most recent equation of the human body thermal balance is the following[99]:

$$M + W + R + C + K + E_D + E_{Re} + E_{Sw} + S = 0$$

Where *M* is the metabolic rate, *W* is the physical work output, *R* is the net radiation of the body, *C* the convective heat flux, K is the heat flux through clothing by conduction (mainly negligible), E_D the latent heat flux, E_{Re} the heat flux by respiration, that is needed to warm up and humidify the inspired air, E_{Sw} the heat flux by evaporation of sweat, *S* the storage of the body mass.

The elements of this equation that are affected by the characteristics of the built environment and by climate change are radiation, convection and evaporation.

Radiation *R*

The exchange by *radiation* between the human body and the surrounding depends on the number of short waves and long waves coming from the sun and from the sky dome absorbed by the body in outdoor environments only, and by the amount of radiative heat that the body itself emits toward the surrounding[100].

In unshaded environments, short waves can hit the human body coming straight from the sun as direct radiation, from the sky dome as diffuse short-wave radiation, and reflected by horizontal and vertical surfaces.

[99] Blazejczyk et al. 2010.

[100] $R_n = \left(K_{dir} + K_{dif} + K_h + K_v\right)(1 - \alpha_s) + L_d + L_h + L_v - L_s$ where R_n is the net exchange radiation between the body and the environment, K_{dir} is the direct short wave radiation, K_{dif} is the diffuse short wave radiation, K_h is the short radiation reflected by a horizontal surface, K_v is the short radiation reflected by a vertical surface, α_s is the albedo of the body or of the clothes, L_d is the is the diffuse long wave radiation, L_h is the long wave radiation reflected by a horizontal surface, L_v is the long wave radiation reflected by a vertical surface, L_s is the long wave radiation emitted by the body.

In addition to the intensity of the solar beam, the magnitude of direct radiation coming from the sun depends on the 3-dimensional geometry of the space, which is relevant for the shadows that can be cast by the objects, like canopies, buildings or trees. On the other hand, it depends on the solar geometry, which is the altitude angle of the sun in the different hours of the day. That means that the position of the city on the Globe, i.e. the latitude, is an important factor[101].

Diffuse short wave radiation is approximated as isotropic. Its source is the sky and its magnitude is about 20, 30 per cent of the global radiation with a clear sky and increases with the level of cloudiness. Therefore, its magnitude depends on the exposition of the body to the sky, i.e. on the sky view factor *SVF* as seen by the pedestrian[102]. It is measured at a symbolic point at the middle of the head, and it is a geometric parameter, whose magnitude assumes a value of maximum 0.5, because the human body is exposed to it only in the upper hemisphere of its surroundings.

Short wave radiation can hit the body also after its reflection on the surfaces that surround the body. When it comes from a horizontal surface (K_h), it depends on the fraction of the surface that is exposed to the direct radiation, the reflectivity of the surface and the floor view factor *FVF*, which is the angle of exposure between the pedestrian and the horizontal surface[103]. If the floor is made of different materials, the total radiation is given by the sum of the contributions coming from each surface.

Vertical surfaces reflect direct radiation as well, but their contribution to the overall diffuse short-wave radiation that hits the body is less intense, due to the lower angle of incidence of the solar rays. In fact, it depends on the zenith angle of the sun and on the angle between the

[101] The formula to calculate the direct radiation is: $K_{dir} = I_{dir}\left(\frac{tan\text{Ⓜ}}{\pi} SC_{sv} + SC_{sh}\right)$, where I_{dir} is the intensity of the direct radiation on a horizontal plan, Ⓜ is the zenith angle of the sun, which depends on latitude and time, SC_{sv} and SC_{sh} are respectively the shading coefficients for the vertical and horizontal-top side of the body and depend on the geometry of the urban environment.

[102] The magnitude of the diffuse short-wave radiation is given by: $K_{dif} = I_{dif}\overline{SVF}$, where I_{dif} is the intensity of diffuse radiation and $\overline{SVF}$ is the average sky view factor or the pedestrian.

[103] $K_h = I_{dir} SC_h \alpha_h \overline{FVF}$, where I_{dir} is the intensity of the direct radiation, SC_h is the shading coefficient, α_h is the albedo or reflectivity of the surface and $\overline{FVF}$ is the average floor view factor.

sun and the surface, besides the amount of direct radiation that hits the surface, its reflectivity and the wall view factor *WVF*[104].

The human body that is exposed to the short-wave radiation, so as explained above, absorbs only a part of it, according to the albedo of its skin, which is more important in summer, and to the clothing it wears.

Long wave radiation, as seen in the previous section, is emitted by the surfaces that are exposed to direct radiation, including the ground. The number of emissions received by the human body depends on the temperature and the emissivity of the surfaces and on the view factor. Another important source of long wave radiation is the atmosphere. It radiates heat from above, downwards, and the intensity of the emission is directly depending on the intensity of the sky emission and from the sky view factor[105]. This value increases with the increase of temperature and of humidity, and with cloudy skies it is still more intense.

Long wave radiation coming from horizontal and vertical surfaces, which hits the body, depends on the emissivity of the surfaces, their temperature and their view factors[106]. The temperatures are influenced by the contact with the air and by their solar absorption, which of course increases with the exposure of the surfaces to direct solar rays.

In indoor environments, there is no contribution from direct or diffuse solar radiation from the sky, except for the portion that penetrates through openings in the building envelope. This can be filtered by glass or other types of screens. Therefore, from the point of view of short-wave radiation, the term R in the equation includes mainly filtered solar radiation and radiation reflected by internal surfaces. Consequently, the dominant part of R is long-wave radiation emitted by surrounding surfaces, which depends on their surface temperature, emissivity, and view factor.

[104] $K_v = I_{dir}\left(\frac{\tan\theta_z \cos\varphi}{2}\right) SC_v \alpha_v \overline{VWF}$, where I_{dir} is the direct radiation, θ_z is the zenith angle, φ is the angle relative to the wall, SC_v is the wall's shading coefficient, α_v is the albedo of the wall and $\overline{VWF}$ is the wall view factor.

[105] $L_d = L\downarrow \overline{SVF}$, where $L\downarrow$ is the intensity of the long way radiation from the sky and $\overline{SVF}$ is the sky view factor.

[106] $L_h = \varepsilon_h \sigma {T_h}^4 \overline{FVF}$ and $L_v = \varepsilon_v \sigma {T_v}^4 \overline{WVF}$ are respectively the intensity of the long wave radiation that hits a human body emitted by horizontal and vertical surfaces, where ε is the emissivity of the material composing the surface, σ is the Stefan-Boltzmann constant, T is the surface temperature, $\overline{FVF}$ and $\overline{WVF}$ are the floor view factor and the wall view factor.

As a result of climate change, the R factor of the equation changes. In the outdoor environment, the change is mainly due to an increase in longwave radiation from the sky. The increase in greenhouse gases causes an increase in the amount of longwave radiation that the atmosphere re-emits towards the ground[107]. Physiologically, in a climate change context, the radiative exchange of longwave radiation between the human body and the surrounding surfaces is only affected by the increasing surface temperature, while the shell temperature of the body remains almost unchanged. Classical studies show that with changing in air temperature, the infrared emissivity of the skin remains constant[108] and any other slight variations in emissivity caused for example by sweat are minimal and due to behavior, not to climate[109].

Convective heat flux *C*

A human body exchanges heat with the surroundings through convection. The quantity of energy exchanged with the environment depends on the air velocity and on the temperature difference between the body and the air around it[110]. If the air temperature is lower than the body's shell temperature (about 34°C), the effect of convection is cooling, because the cooler air absorbs heat. Recent studies[111] show as the turbulence intensity affects the convective heat flux at elevated wind speed.

With global warming, days when the air temperature approaches or exceeds skin temperature will become more common, especially during heat waves. This implies that natural convection will become less effective or even harmful. Furthermore, heat waves are often associated with anticyclonic conditions of atmospheric stability with still air: the combination of very hot air and lack of wind is particularly dangerous because it eliminates the effect of convection in extreme overheat[112]. In dense urban environments, cities have reduced airflow in alleys compared to the countryside, which amplifies heat stress because

[107] Forster et al. 2021

[108] Togawa, 1989

[109] Mazdeyasna et al. 2023

[110] The rate of convective heat transfer from the body may be given as: $C = h_c \Delta T$, where h_c is a heat transfer coefficient depending on wind speed and ΔT is the difference of temperature between the body and the air.

[111] Ono et al. 2008

[112] Kautz et al. 2022

body heat stagnates around the person instead of being dispersed[113]. Therefore, outdoors, wind can be an ally against the heat, but in climate change scenarios, we may face both more frequent periods of scorching calm and, paradoxically, episodes of intense hot winds that keep the perceived temperature high.

In indoors, in a climate change scenario, temperatures are predicted to rise as well and the magnitude of the delta depends on urban fabric compactness and envelope typology[114].

Evaporation E_{Sw}

In warm conditions, the human body loses heat by evaporation of sweat. In fact, the human body produces heat by metabolism, and to keep the thermal balance in equilibrium it must cede the surplus energy to the environment. The amount of heat loss is expressed by the ITS, Index of Thermal Stress. The mechanism is the evaporative cooling, the body gives up moisture to the environment through sweat and the evaporation of this liquid subtracts energy. Of course, wind speed, i.e. convection, is an important factor for evaporation, as well as radiation, the moisture content of the surrounding air and the clothing factor. Therefore, the outdoor factors that affect evaporation are wind velocity and humidity.

3.2 Microclimatic Factors for human thermal comfort

Thermal comfort conditions are dependent on microclimatic factors, which regulate the energy balance of the environment and the interaction between the individual and its surroundings[115] [116]. The main factors considered are:

- Mean Radiant Temperature (MRT): This represents the combined effect of the surrounding surface temperatures and solar radiation, when it occurs.[117] MRT significantly influences the heat balance of the human body, as it determines the intensity of radiative exchange between the body and the environment. The

[113] Liu et al. 2017
[114] Maiullari et al. 2021
[115] Campbell et al., 1998.
[116] Chatzidimitriou et al., 2016.
[117] Guo et al., 2020.

distance between the human body and radiating surfaces plays a crucial role: closer surfaces increase the perceived radiative effect, while more distant surfaces reduce the impact. In addition, factors such as trees, architectural structures, or other obstacles can provide shade from thermal radiation, altering the overall heat balance[118].

In warm and hot environments, variations in the radiative conditions of the surroundings can produce substantial changes in the thermal load experienced by the human body, even when variations in air temperature remain limited[119] [120]. Accordingly, outdoor situations characterized by comparable air temperature and humidity may nevertheless be associated with distinct levels of thermal stress when radiative exposure differs, for instance due to the presence or absence of direct solar radiation or heated surrounding surfaces[121] [122].

- Air Temperature (DBT): This indicates the heat perceived in the environment and is a key parameter in defining thermal comfort. The mechanism by which air changes temperature is related to the change in thermal energy contained in air molecules. When air absorbs heat, its molecules increase their speed of movement, raising the temperature. Conversely, when it gives up heat to cooler surfaces or its surroundings, the molecular speed decreases, causing the temperature to fall. This energy exchange takes place mainly through conduction, convection, and radiation, influencing local climatic conditions and the perception of comfort.
- Relative Humidity (RH): Relative humidity affects the atmospheric energy balance mainly through latent energy. When water in the air is in the gaseous phase, it stores energy in the form of latent heat, which is released or absorbed during condensation and evaporation processes. This phenomenon alters the distribution of heat in the atmospheric system. Under high humidity conditions, the air contains more water vapor, increasing the system's capacity to retain energy but reducing the effectiveness of heat dissipation processes. Conversely, low humidity conditions

[118] Nasrollahi et al., 2021.
[119] Guo et al., 2020.
[120] Ji et al., 2022.
[121] Nasrollahi et al., 2021.
[122] Ji et al., 2022.

favor a more rapid redistribution of latent energy, directly affecting the perception of thermal comfort and the climatic response of surfaces.

- Air velocity (av): Air velocity is a crucial factor in the energy balance, as it influences the dissipation of body heat through convection. When moving air comes into contact with the skin surface, it promotes heat transfer from the body to the environment, accelerating cooling. This process becomes particularly effective when accompanied by low relative humidity (RH) conditions, which increase the evaporation of sweat. Conversely, under high humidity conditions, the effectiveness of air flow in improving thermal comfort is reduced, as the air is already saturated with water vapor, limiting evaporative cooling[123].

  When ambient air temperature approaches or exceeds skin temperature, increased air movement does not necessarily result in net cooling and can contribute to additional heat gain through convective exchange[124] [125]. Under such conditions, convective heat transfer may shift from a cooling contribution to a warming one, as moving air transfers heat to the body rather than removing it[126].

The interaction between air velocity and relative humidity is crucial for thermal comfort. Under moderate air velocity and low humidity, evaporative heat loss through sweat effectively removes thermal energy from the body, improving thermal sensation. As thermal conditions intensify, however, the effectiveness of convective and evaporative mechanisms becomes increasingly dependent on the surrounding thermal gradients and moisture conditions.

As a consequence, the relative influence of individual microclimatic factors cannot be assumed to be constant, but varies with the overall thermal regime under which heat exchange occurs[127]. For instance, a factor that plays a relevant role under moderate conditions may become less influential when overall thermal loads increase and other heat-exchange pathways become more constraining.

Accordingly, thermal comfort should be understood as the outcome of interacting microclimatic variables acting within a spatial context defined by surface properties, material

[123] Vellei et al., 2017.
[124] Fanger 1970.
[125] Parsons, 2014.
[126] Ibid.
[127] Parsons, 2014.

characteristics, and geometric configuration [128]. The analysis and management of these parameters are therefore central to understanding and addressing overheating phenomena[129].

3.3 The built environment as a microclimatic mediator of human exposure

After introducing the human heat-balance framework and the microclimatic variables relevant to thermal comfort (air temperature, MRT, wind velocity and humidity) in the previous section, this paragraph clarifies how the built environment shapes those variables at the human scale. The scope is intentionally broad: the built environment is considered here as that continuum of domains, from outdoor to indoor, where thermal exposure is highly coupled to external boundary conditions. In this way, the paragraph provides the conceptual bridge toward the urban-scale energy perspective developed in the next section and toward the choice of assessment metrics later in the chapter.

3.3.1 From climate to microclimate

Rapid climatic change is progressively shifting the boundary conditions under which the built environment is expected to secure habitability. For the Mediterranean basin, and Italy in particular, increasing temperatures, more frequent heat extremes and the persistence of warm nights amplify the burden of heat stress on human well-being, making thermal exposure a central issue for public health and for the future performance of urban and architectural environments[130] [131] [132]. From a physiological perspective, the relevance of this shift is not only incremental: there are limits to human thermoregulation under combined high temperature and humidity conditions, which implies that spatial and technological adaptation needs to be treated as a necessary component of climate resilience[133] [134]. Within this context, the built environment should be framed as a physical system that mediates climatic forcing and reorganizes it into localized microclimatic conditions that people actually experience, outdoors,

[128] Oke et al., 2017.
[129] Santamouris, 2020.
[130] IPCC, 2023.
[131] Santamouris, 2020.
[132] Mavrogianni et al., 2022.
[133] Sherwood et al., 2010.
[134] Ahima, 2020.

in transitional spaces, and indoors when spaces are operated in free-running or mixed-mode regimes.

In urban climatology, this mediating role is commonly described through the distinction between macroclimate and microclimate: the same regional weather can translate into substantially different near-ground thermal environments depending on urban morphology, land cover, and surface properties[135] [136]. For design-oriented disciplines, this translates into a key principle already established in bioclimatic and microclimatic design traditions: environmental comfort emerges from the interaction between climate and form, and therefore can be influenced, within limits, by the way space is structured, oriented, enclosed, and materialized[137] [138] [139]. The implications of this principle are explored here through the lens of the microclimatic variables introduced in the previous section, air temperature, mean radiant temperature, wind velocity, and humidity, because, as shown in previous sections, these are the parameters through which the built environment connects to the human heat-balance pathways and, crucially, because they are also the boundary conditions that shape thermal trajectories under climate change[140] [141] [142].

Building on this premise, the following subsections discuss the main mechanisms through which built form, materials, and living systems shape those variables across outdoor, transitional and indoor non-conditioned contexts.

3.3.2 Spatial configuration and radiative exposure

A first, primary mechanism is spatial configuration, which organizes radiative exposure and controls the degree of coupling between pedestrians and the sky, surrounding surfaces, and solar geometry. Street canyons and courtyard-like morphologies are particularly instructive because they combine enclosure, shading, and constrained ventilation. Classic urban climate

[135] Oke, 1987.
[136] Oke et al., 2017.
[137] Olgyay, 1963.
[138] Givoni, 1998.
[139] Brown, 2010.
[140] Hong et al., 2023.
[141] Morales et al., 2025.
[142] Hendriks et al., 2025.

research emphasizes how street design parameters (e.g., height-to-width ratios and street orientation) structure the urban canopy layer climate and create systematic differences between locations that may be only tens of meters apart[143] [144].

In comfort-relevant terms, this is often expressed as a strong sensitivity of MRT to geometry: the proportion of visible sky and the configuration of surrounding surfaces govern both short-wave gains (solar access and shading) and long-wave exchange with warmer or cooler surfaces[145]. Empirical and simulation-based studies have repeatedly shown that the same air temperature can correspond to very different perceived heat loads depending on canyon depth, aspect ratio, and exposure, because radiative conditions can dominate the energy balance of the human body in summer[146] [147] [148]. The design implications are not univocal: deeper canyons may reduce direct solar exposure during daytime, but reduced sky view can also limit nocturnal radiative cooling and affect the persistence of warmth, which is particularly relevant under heat-wave conditions [149] [150]. This duality is central for Mediterranean environments, where traditional compact fabrics have historically combined shading and moderated solar access with specific ventilation practices, but where future conditions may challenge the reliability of passive moderation alone[151] [152].

Typically, in Mediterranean architectural typologies, this geometric control of radiative exchange relies on semi-enclosed and in-between spaces (e.g., courtyards, porticoes, loggias), which restructure solar access and long-wave radiative coupling in ways that generate spatial gradients of thermal exposure. Recent courtyard-focused studies underline that geometry and surface reflectance can significantly shape microclimate and thermal comfort in hot

[143] Oke, 1988.
[144] Oke et al., 2017.
[145] Herrmann et al., 2011.
[146] Johansson, 2006.
[147] Holst et al., 2011.
[148] Mayer et al., 2008.
[149] Oke, 1987.
[150] Oke et al., 2017.
[151] Givoni, 1998.
[152] Santamouris, 2020.

Mediterranean summers, and that courtyard microclimate can be meaningfully integrated into building performance simulation when extreme heat impacts are considered[153] [154] [155] [156].

This geometric control of radiative exchange is not confined to outdoor or semi-outdoor environments, but also applies to indoor spaces operated without continuous mechanical conditioning, where the absence of a fixed thermal setpoint allows external climatic forcing to penetrate through the envelope. In free-running buildings, indoor thermal conditions emerge from the interaction between spatial configuration, façade orientation, solar access, and the thermal response of enclosing surfaces. Under these conditions, mean radiant temperature remains a key driver of perceived heat stress, as solar gains and warmed envelope elements govern long-wave exchange within the space and can lead to markedly different indoor exposure levels under similar outdoor air temperatures[157] [158] [159]. This continuity of geometric and radiative control across outdoor, transitional, and indoor non-conditioned domains reinforces the need for a unified microclimatic interpretation of thermal exposure.

Geometry, however, does not only structure radiative exchange. The same spatial configurations that shape MRT also condition the local wind field and, by extension, the convective and evaporative pathways through which the body can dissipate heat.

3.3.3 Geometry and airflow: wind velocity, convection, and natural ventilation

Connected to geometry is the modulation of wind velocity and, consequently, of convective and evaporative heat exchange: at the human scale, buildings create roughness, channeling, sheltering, recirculation zones, and local accelerations. In outdoors, the street-canyon literature, including numerical and experimental investigations, shows how aspect ratio and configuration can shift flow regimes and turbulence structures, with direct consequences for ventilation potential and for the removal (or trapping) of heat and moisture within the canyon

[153] Diz-Mellado et al., 2021.
[154] Diz-Mellado et al., 2023.
[155] López-Cabeza et al., 2022.
[156] Lizana et al., 2022.
[157] Givoni, 1998.
[158] Santamouris et al., 1996.
[159] Balaras, 1996.

volume[160] [161] [162]. From a design standpoint, this implies that ventilation is a morphological outcome: the same city can simultaneously contain windy corridors and stagnant pockets, and these differences matter for thermal comfort because air movement amplifies convective cooling and supports sweat evaporation, especially under hot conditions[163] [164].

Architectural and urban design approaches that treat wind as an “instrument” emphasize the need to read airflow as a spatial resource shaped by form, permeability, and orientation, rather than as a uniform ambient parameter[165] [166]. Importantly, ventilation and shading can interact in non-trivial ways: adding elements that provide solar protection may also reduce airflow, weakening evaporative cooling exactly when it is most needed. This interaction is particularly relevant for semi-outdoor environments and dense morphologies, where small geometric decisions can decisively shift the balance between radiative load reduction and convective heat removal[167] [168].

The same logic extends indoors in naturally ventilated and free-running buildings, where airflow is the primary dissipative mechanism available when mechanical cooling is absent or intermittent. In such cases, the porosity of the building envelope, defined by the size, distribution, operability, and orientation of openings, plays a role analogous to urban permeability: openings, airflow paths, and ventilation strategies govern the magnitude and spatial distribution of air exchange, and therefore the extent to which indoor temperatures can track or decouple from outdoor conditions[169] [170] [171]. Mediterranean studies on natural cross-ventilation and vernacular cooling strategies emphasize how ventilation effectiveness is strongly context-dependent and can be constrained by site exposure, wind regimes, urban density, and the resulting pressure fields acting on the envelope[172] [173].

[160] Cui et al., 2004.
[161] Vardoulakis et al., 2003.
[162] Assimakopoulos et al., 2003.
[163] Allard, 1998.
[164] Awbi, 2003.
[165] Aynsley et al., 1977.
[166] Krautheim et al., 2014.
[167] Oke, 1988.
[168] Chatzidimitriou et al., 2016.
[169] Allard, 1998.
[170] Etheridge et al., 1996.
[171] Awbi, 2003.
[172] Faggianelli et al., 2014.
[173] Michael et al., 2017.

Under climate change, this dependency becomes more critical because the persistence of hot nights and multi-day heat sequences can reduce the potential for nocturnal purge ventilation, limiting passive recovery even in buildings with high envelope porosity[174] [175] [176] .Alongside radiative and aerodynamic effects shaped by configuration, the thermal behaviour of surfaces and envelopes provides a second layer of control, affecting both the magnitude and the timing of heat exchange in outdoor and setpoint-free indoor environments.

3.3.4 Surface properties, materiality and thermal inertia

Beyond geometry, surface properties and materiality act as secondary but critical regulators of both air temperature and MRT by influencing surface temperatures, reflection patterns, and the timing of heat release. Research on urban overheating and heat islands highlights the role of construction materials and pavements in controlling near-surface thermal conditions, especially through their radiative properties and their ability to store and re-emit heat[177] [178]. From the perspective of outdoor comfort, material interventions are often discussed in terms of albedo and thermophysical behavior: cool materials can reduce surface temperatures and sensible heating of adjacent air layers, yet the pedestrian-level benefit depends on how reflected short-wave radiation contributes to the radiative load experienced by people[179] [180]. This is why the evaluation of high-albedo strategies in street canyons has increasingly relied on comfort indices and not only on surface temperature metrics, showing that the net effect on perceived heat stress can depend on urban geometry and on the balance between reduced surface heating and increased reflected radiation[181] [182]. Materiality also includes the thermal behavior of vertical “skins” and façade finishes, which can be decisive in climates where solar exposure of walls contributes to elevated surface temperatures and radiant exchange with pedestrians[183]. Finally, surface permeability and water availability interact with humidity and

[174] Santamouris, 2020.
[175] Hong et al., 2023.
[176] Morales et al., 2025.
[177] Gartland, 2012.
[178] Santamouris, 2020.
[179] Doulos et al., 2004.
[180] Errel et al., 2004.
[181] Ibid.
[182] Schrijvers et al., 2016.
[183] Bougiatioti et al., 2009.

latent heat processes: permeable pavements and evaporative surfaces can alter near-ground thermal conditions by enabling moisture exchange and evaporative cooling, yet their performance depends on climatic conditions and resource constraints[184] [185].

In parallel, materiality and thermal inertia are central for indoor environments operated without continuous mechanical conditioning, where envelope properties determine whether indoor air and internal surfaces follow the outdoor diurnal cycle closely or instead exhibit damped and delayed responses. The envelope should be understood as a dynamic filter, in a way that thermal resistance limits the amplitude of heat fluxes, while thermal capacity distributes heat exchange over time, producing phase lag and attenuation in indoor temperatures[186] [187] [188]. In Mediterranean contexts, this time-domain behaviour is often exploited through heavy masonry, solar control and night ventilation; however, under persistent heat waves—especially when night-time temperatures remain high—thermal inertia can become a liability as stored heat accumulates across consecutive days, raising baseline indoor temperatures and increasing overheating risk[189] [190] [191]. Recent analyses of overheating vulnerability in Mediterranean dwellings and reviews of modelling approaches under future climate conditions highlight the need to represent these transient processes explicitly[192].

The same surface-driven mechanisms are central in indoor environments operated without continuous mechanical conditioning, where envelope materials and internal surfaces govern the magnitude and temporal distribution of radiative exchange and heat storage. In free-running buildings, thermal inertia and surface temperatures directly shape indoor mean radiant temperature and multi-day heat accumulation, making materiality a key determinant of overheating risk under climate change[193].

[184] Asaeda et al., 2000.
[185] Hendel et al., 2015.
[186] Balaras, 1996.
[187] Santamouris et al., 1996.
[188] Tribuiani et al., 2020.
[189] Santamouris et al., 1996.
[190] Santamouris et al., 2013.
[191] Hong et al., 2023.
[192] Morales et al., 2025.
[193] Tribuiani et al., 2020

If geometry, materials and ventilation define the “passive structure” of microclimate, living systems and water-based elements provide an additional layer of modulation. Their cooling potential can be substantial, but it is also more sensitive to boundary conditions, an aspect that becomes increasingly consequential under climate change.

3.3.5 Living systems and water under climate-change constraints

Within the built environment, vegetation and water function as spatial and microclimatic elements components across scales: from parks and street trees to courtyards, green roofs and green walls. Their microclimatic effects are supported by a substantial body of research, but they should be framed with the appropriate status: as conditional modulators that can strongly improve local exposure under suitable boundary conditions. Vegetation affects thermal comfort through two dominant mechanisms: shading (directly reducing short-wave gains and MRT) and evapotranspiration (supporting evaporative cooling and modifying humidity fields). Studies focusing on green roofs and green walls have explored these effects in both building-scale and canyon-scale settings, documenting reductions in surface temperatures and local air temperatures and highlighting the dependence on climate, geometry, and implementation details[194] [195] [196] [197] [198]. At the urban scale, parks and greenspaces can create cool island effects, influencing local thermal environments and sometimes contributing to nocturnal mitigation, although magnitude and spatial reach depend on size, morphology, and background climate[199] [200] [201] [202]. These findings are particularly relevant for Mediterranean and coastal contexts where outdoor space use is culturally significant, and where microclimatic differences can influence perception, attendance, and behavioral patterns[203] [204].

[194] Alexandri et al., 2008.
[195] Djedjig et al., 2015.
[196] Djedjig et al., 2016.
[197] Berardi, 2016.
[198] Mazzali et al., 2013.
[199] Cao et al., 2010.
[200] Doick et al., 2014.
[201] Chang et al., 2014.
[202] Eyisa et al., 2014.
[203] Cohen et al., 2013.
[204] Nikolopoulou et al., 2007.

However, under climate change, the performance of living systems must be interpreted together with the changing constraints that affect their operation. Warming trends and the increased persistence of heat extremes increase the demand for cooling and shading, but they can also amplify water stress and limit the availability of moisture-driven cooling. For roof- and façade-integrated greenery in particular, the cooling contribution is tightly linked to plant health, substrate conditions and water management, and performance in warm or semiarid contexts highlights the sensitivity to climatic and operational conditions[205] [206] [207]. This introduces an explicit water–energy–comfort chain: maintaining evapotranspiration-based cooling may require irrigation or water supply strategies, which in turn interact with resource availability and operational constraints[208] [209] [210]. In this sense, green roofs and green walls are living components whose microclimatic function is increasingly shaped by climate-change-driven boundary conditions.

Similarly, blue infrastructures—rivers, lakes, canals, fountains, and irrigated surfaces—modify microclimate through high heat capacity, evaporative cooling, and interactions with urban form and wind. Empirical studies have examined the influence of rivers and water bodies on urban thermal environments, showing that cooling effects can be detectable locally and can interact with street orientation and airflow in shaping the spatial footprint of mitigation[211] [212] [213]. Reviews and modelling studies further indicate that the effectiveness of water-based cooling is strongly conditional: it depends on synoptic conditions, humidity levels, wind, and the design and operational strategy of the water system[214] [215]. At the scale of specific devices, the literature on water facilities and fountains demonstrates that microclimatic benefits exist but require careful integration with spatial configuration to avoid negligible effects or unintended increases in humidity under already humid conditions [216] [217]. Green and blue

[205] Victorero et al., 2015.
[206] Semaan et al., 2016.
[207] Berardi, 2016.
[208] Yang et al., 2015.
[209] IPCC, 2023.
[210] Santamouris, 2020.
[211] Murakawa et al., 1991.
[212] Saaroni et al., 2003.
[213] Hathway et al., 2012.
[214] Manteghi et al., 2015.
[215] Tominaga et al., 2015.
[216] Nishimura et al., 1998.
[217] Xue et al., 2015.

infrastructures are part of the built environment and can be powerful, but their performance must be interpreted within the coupled system of climate boundary conditions, spatial morphology and resource constraints, an aspect that becomes increasingly critical under climate-change-driven extremes[218].

3.4 Outdoor energy balance mechanisms

To understand the outdoor fluxes of energy it is useful to analyse the energy balance of an urban area, in line with the First Law of Thermodynamics and the conservation of energy: over a given time window, all the energy entering the urban system from external sources must be matched by the energy leaving the system plus the energy stored within it (Figure 5).

Commonly the Surface Energy Balance (SEB) in an outdoor context is expressed by the following expression:

$$Q^* + Q_F = Q_H + Q_E + \Delta Q_S + \Delta Q_A$$

This formulation matters because it clarifies the structure of the physical problem: it makes explicit that the urban microclimate is governed by multiple concurrent pathways: radiative forcing (Q*), anthropogenic releases (Q_F), turbulent sensible and latent exchanges (Q_H and Q_E), storage and delayed release (ΔQ_S), and horizontal transport through heterogeneity (ΔQ_A). The relevance of the complete balance lies in the fact that it forces every “simplified” descriptor to declare, implicitly or explicitly, what it is leaving out: whenever a formulation collapses the problem to a single variable, the SEB makes explicit which channels are being treated as dominant and which are being neglected.

What follows uses the terms of the SEB as a set of constraints: each block shows why a mono-variable reading of thermal exposure is structurally fragile.

[218] Santamouris, 2020.

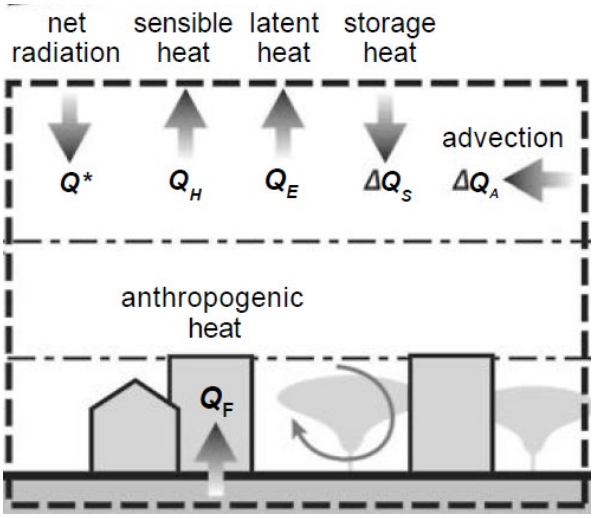

Figure 5. Scheme showing urban energy balance. From Erell et al., 2012.

3.4.1 Radiation and geometry

Within the SEB, *Q** gathers the all-waves net radiative forcing, i.e., a short-wave component shaped by absorption/reflection and a long-wave component shaped by emission and sky conditions[219]. In terms of thermal comfort, this is the point where the balance makes explicit that the radiative environment (and thus MRT) is not a simple function of air temperature DBT. Even when DBT is known, the net radiative load depends on how surfaces see each other and the sky, and on how they absorb, reflect, transmit, and emit radiation.

Several urban features illustrate why this radiative channel is intrinsically geometric and material:

- Short-wave interactions are shaped by material + form. Solar energy can be reflected or absorbed by the surfaces it hits, and the portion absorbed depends on the materials composing roofs and ground[220] and on the geometrical arrangement of the urban fabric. Latitude matters because the angle of incidence changes the effective interception and reflection patterns within canyons.

[219] The balance equation to calculate *Q** is: $Q^*=(K_{dir}+K_{dif})(1-\alpha)+(L\downarrow-L\uparrow)$, where $(K_{dir}+K_{dif})$ is the short wave component, respectively direct and diffuse, α is the albedo and $(L\downarrow-L\uparrow)$ is the long wave component, as a difference between the incoming long wave radiation and the outgoing one.

[220] Of course the characteristics of the materials composing the roofs or the ground influence the reflectivity as well.

- Density does not act monotonically. High densities and very low densities can both increase albedo and produce high reflections (e.g., by roofs in one case, or by exposed ground in the other). Conversely, medium densities can facilitate absorption because solar rays penetrate into the canyon and bounce on vertical facets more times, increasing the portion of radiation dissipated in the system.
- Height uniformity and canyon orientation alter the "radiative itinerary." Uniform building heights increase albedo because reflected rays do not intercept other vertical facades. Canyon axis orientation changes solar penetration through the day, affecting the energy weighted albedo (EWA)[221] because it is sensitive to the time-varying solar position and intensity[222].
- Envelope transparency redirects short-wave energy. With a higher Window-To-Wall Ratio (WTWR), a significant portion of short-wave radiation can be transmitted into buildings and thus subtracted from the outdoor balance unless it is reintroduced by mechanical systems; in that sense, increasing WTWR tends to lower the canyon albedo.
- Long-wave exchanges are driven by sky state, not by Ta alone. The long-wave component depends on altitude, cloudiness, and cloud type. Beyond that, atmospheric pollutants can have a compound effect on Q*: they reflect short waves (reducing daytime solar gains), obstruct the outgoing long-wave radiation from the terrestrial surface, and increase long-wave radiation from the sky; overall, the combined result can reduce the effects of solar radiation up to about 10%[223].

Taken together, these elements are the reason the SEB is useful here: it makes explicit that radiative forcing is mediated by geometry and surface properties, and therefore any comfort assessment that attempts to proxy radiative exposure through DBT alone is, by construction, discarding an entire channel that the balance shows to be structurally independent from DBT.

[221] Sailor et al.,, 2002.
[222] Assimakopoulos et al., 2003.
[223] Oke, 1979.

3.4.2 Turbulent and latent exchanges

The SEB also makes explicit that the urban thermal environment is not "temperature + humidity" as two separable knobs. The partition of energy into Q_H (sensible, turbulence-mediated exchange) and Q_E (latent, moisture-mediated exchange) is coupled: the same net input can be routed into warming the air, evaporating water, or some mix of both. This is exactly what breaks a naive separation between "temperature effects" and "humidity effects" in comfort descriptions.

Turbulent sensible exchange as a geometry-dependent pathway

Rather than treating Q_H as a term to define, the balance clarifies that a major share of energy is exported from surfaces to the atmosphere through turbulent exchange—whose effectiveness depends on both *gradients* and *mixing*.

At the scale close to building facets, Q_H depends on the temperature difference between an emitting surface and the adjacent air, and on the effectiveness of exchange between surface and atmosphere, often represented through a convective transfer coefficient [224]. That coefficient is affected by wind speed, turbulence, and surface characteristics, and it varies with position and shading: lower parts of facades can be more shaded than higher ones, altering the local temperature contrast with the air [225]. Canyon depth matters here as well; deep canyons can facilitate pockets of stagnant air, changing exchange conditions.

At the urban scale, Q_H is also referred to as turbulent sensible heat flux and represents the heat exchange between the atmosphere and the larger urban surface composed of buildings, streets, trees and other city elements [226]. It is measured within the portion of the urban atmosphere where the flow "sees" the city as a rough surface rather than as individual

[224] The formula to calculate Q_H at a low scale of measurement is the following: $Q_H=h_c(T_s-T_a)$, where h_c is the convective heat transfer coefficient and T_s and T_a are the temperatures of the surface and of the ambient respectively.

[225] Alexandri et al., 2008.

[226] Cui et al., 2004

obstacles, i.e., within the surface layer/inertial sublayer of the urban boundary layer[227] [228]. In this regime, turbulent exchange is governed by the global geometry of the city and by broader climatic conditions more than by individual buildings. One representation of this large-scale turbulent exchange links Q_H to friction velocity and scaling temperature[229], making explicit that Q_H is not simply "a function of *DBT*", but a function of how effectively the atmosphere can remove (or supply) heat through turbulence.

3.4.3 Moisture-mediated partitioning and its coupling to sensible heat

The latent channel Q_E is tied to evaporation/transpiration at the surface and subsequent condensation in the troposphere; its magnitude is strongly controlled by moisture availability. In urban terms, this means that the water budget (precipitation, piped water supply, and water vapor released by anthropogenic activities) interacts with evapotranspiration, run-off, moisture export by advection, and changes in water storage.

A practical way to see the coupling is through surface permeability and irrigation regimes:

- Impervious surfaces (buildings, roads, waterproof pavements) have limited capacity to supply moisture.
- Pervious non-irrigated surfaces (parks, dirt plots) can supply moisture conditionally.
- Pervious irrigated surfaces (lawns, gardens) act as persistent moisture sources.

This immediately clarifies why "temperature" and "humidity" are not independent: when surface water is available, surplus energy can be routed into evaporation; when water is absent, surplus energy is converted into sensible heating, increasing air temperature. Even the same wind regime can shift this partitioning, because evaporation can be limited when the air

[227] The atmosphere above the city that is influenced by the solid surface is thick about ten times the average height of the objects composing the city shape. It is called urban boundary layer and is usually divided into 4 sub-layers: the urban canopy layer, from the surface level up to the maximum buildings height; the roughness sub-layer from the top of the canopy layer up to a height of the double of the buildings height, where the air flux is very influenced by the single objects and is characterized by the presence of plumes and trays; the surface layer, from a height of the double of the buildings up to 4 times it; the mixed layer, from 4 to 10 times the height of the buildings, characterized by minimum or no influence from the city shape.

[228] Oke et al., 2017.

[229] $Q_H=\rho c_p k u_* T_*$, where ρ is the density of air, c_p is the specific heat of air, k is von Karman constant (0.4), u_* is the friction velocity and T_* is the scaling temperature.

immediately above a wet surface becomes saturated; wind (even at low velocity) removes the saturated air and replaces it with drier air that can receive moisture[230].

The link between Q_H and Q_E is often expressed through the *Bowen ratio*, $\beta = Q_H/Q_E$, which indicates the relative importance of sensible versus latent pathways; its typical range can be around 0.4–0.8 in temperate areas and can exceed 10 in desert conditions[231]. This is a compact way to state the point: the same net input does not translate into "more *DBT*" unless the latent pathway is constrained.

Urban vegetation reinforces this coupling by increasing evapotranspiration and, in many cases, increasing latent heat while decreasing sensible heat. Conversely, contexts with high atmospheric humidity can limit evaporation; for instance, near large water bodies, the combination of low radiant temperature of water and high humidity can lead to low sensible heat and reduced latent production.

So the SEB does not indicate what Q_H and Q_E are"; it makes explicit that any comfort metric must treat heat and moisture exchanges as coupled, because the physical system routes energy through these pathways simultaneously.

3.4.4 Storage and delay

The storage term (ΔQ_S) is where the SEB makes explicit that the problem is dynamic, not instantaneous. A portion of the radiative input is absorbed by the urban fabric (buildings and pavements) according to material properties and geometry, and then released back to the atmosphere later. This is not a secondary correction: the net storage heat flux can be a major component of the urban energy balance and can account for up to about half of daytime net radiation[232].

Two consequences follow directly:

Materials matter because they control the lag. Storage is driven by the ability of materials to absorb and release energy, governed by thermal conductivity and heat capacity. This is the

[230] Davarzani et al., 2014.
[231] Oke et al., 2017.
[232] Roberts et al., 2006.

reason similar meteorological conditions can produce different thermal trajectories in different urban fabrics.

Peaks do not align in time. Even when net storage is primarily driven by net radiation, the peak of Q^* does not generally correspond in time to the peak of ΔQ_S; the storage peak typically occurs one or two hours later, depending on the materials composing the surface. In comfort terms, this is the mechanism that makes afternoon heat and evening heat physically connected: the thermal state at a given moment contains a memory of earlier radiative forcing.

At street-canyon scale, the geometry of the canyon changes not only the magnitude of storage but also its timing:

- Canyon orientation has a minor effect on overall energy stored.
- Deeper canyons can produce larger net radiation and larger storage because solar rays bounce more times on canyon facets.
- Deep canyons can display a larger time gap between peak radiation and maximum storage rate.

This is precisely why the SEB is used as an argument: it makes explicit that time, especially the delayed release that structures evening and night-time conditions, is part of the thermal exposure problem, and any metric that is insensitive to this delay is implicitly assuming storage to be negligible.

3.4.5 Residual terms and scale: anthropogenic heat and net advection

Finally, the SEB makes explicit two terms that are often treated as residual in simplified reasoning but are structurally important for comparability across contexts: anthropogenic heat (Q_F) and net advection (ΔQ_A). Their key role is that they show how the same physical channels persist across scales and climates, while their relative weights shift.

Anthropogenic heat as a context-dependent forcing

Q_F condenses the direct heat additions associated with human activity: vehicular traffic, buildings (including industrial activity), and metabolism. The methodological difficulty of estimating Q_F is itself informative: it reflects that anthropogenic heat is spatially

heterogeneous (concentrated where activities and density are high) and temporally structured (diurnal, weekly, seasonal).

Some order-of-magnitude statements clarify why Q_F cannot be assumed away universally:

- The metabolism fraction is generally small, at most around 2–3% of the entire anthropogenic heat[233], but it can become relevant locally where bodies concentrate.
- Globally averaged anthropogenic heat may be around 0.03 W/m², associated with an increase in mean surface temperature of about 0.06 K[234], yet it is concentrated and non-negligible in developed areas, reported up to about 20 W/m² and around 0.5 K in the Ruhr Basin[235]; it can be low or absent in developing or undeveloped areas.

Two commonly used calculation approaches further highlight why Q_F is scale- and context-sensitive. A top-down approach divides total energy consumption by city area and time, but it can fail to represent source types, vertical structure (relevant in high-rise contexts), and the fact that not all consumed energy becomes a heat flux in the same way. A more detailed approach estimates building contributions through boundary conditions (e.g., internal–external temperature differences or envelope characteristics) and then adds traffic and other sources, but it is sensitive to user behaviour, solar impacts on envelopes, and varying outdoor temperatures and thermal inertia.

The SEB makes explicit what this means for comfort assessment: even if Q_F is modest on average, it can become comparable to other terms locally and temporally, and therefore a method that aims to be comparable across climates and urbanization levels must accommodate the possibility of Q_F being either negligible or dominant.

Net advection as the signature of heterogeneity

ΔQ_A expresses that urban landscapes are not uniform: within short distances, dense built neighborhoods and large green areas can coexist, generating heat and moisture flows from one location to another. Many models neglect advection for simplification, yet evidence shows that even in supposedly homogeneous suburban residential areas, energy fluxes can vary up

[233] Sailor et al., 2015.
[234] Chen et al., 2014.
[235] Block et al., 2004.

to about 40% over distances from roughly 100 to 1000 metres, comparable in magnitude to urban–rural differences[236]. The most important contrast associated with advection is often between paved and vegetated surfaces, especially when soil moisture is present. Moreover, net advection is inherently time dependent because wind direction and magnitude change.

Here the point is to state what the balance makes explicit: a local comfort condition can be shaped by non-local processes, so any reduction that assumes the point behaves like its immediate surface must be understood as a deliberate neglect of a physically present pathway.

Scale-dependent mechanisms

Across the whole section, a consistent pattern emerges: changing scale, from facet to canyon to neighborhood to city, does not remove terms from the balance; it changes which terms dominate and how they are parameterized. This is why the SEB is methodologically important for your thesis.

A few examples, already implicit in the discussion, show this clearly:

- Geographical position: latitude changes solar angles and thus affects Q^*, and indirectly influences Q_H and ΔQ_S through shading and storage patterns.
- Climate: beyond *DBT*, wind, radiation, humidity and precipitation all modulate the partitioning among Q_H, Q_E and ΔQ_S; climate also feeds back on Q_F through heating/cooling demand.
- Socio-economic aspects: population density, energy consumption, industrialization and public transportation structure Q_F; pollution alters radiative conditions (Q^*).
- Large-scale morphology: overall city geometry shapes friction velocity and thus turbulent exchange (Q_H) and evapotranspiration patterns (Q_E); large water and green bodies shift the sensible/latent partition and can generate “cool island” effects; building density modifies albedo and thus Q^*.
- Small-scale morphology: ground permeability and vegetation primarily shape Q_E (and thus indirectly Q_H); materials change absorption/storage and therefore Q^* and ΔQ_S; canyon H/W and L/W ratios alter both radiative trapping and wind/turbulence

[236] Schmid et al., 1991.

pathways; permanently wet surfaces locally increase Q_E because energy is routed into evaporation.

This is the epistemic output of the SEB for the chapter: the urban thermal environment is intrinsically multi-channel, and any attempt to simplify it must be read as an explicit choice of neglected pathways. A coherent comfort assessment, especially one that aims to remain valid across scales and climates, therefore cannot rest on a single-variable proxy without stating what parts of the physical problem it is excluding.

3.5 Indoor energy balance mechanisms in free-running buildings

Most daily thermal exposure occurs within built environments [237]; in contemporary societies, the majority of time is spent indoors, and a substantial share of that exposure takes place in buildings that are not maintained at a strict, continuous HVAC setpoint (e.g., free-running dwellings, schools, workplaces, or buildings operated opportunistically by opening windows and modulating shading). In parallel, many urban and architectural typologies, especially in climates with strong seasonal and diurnal variability, include transitional or semi-indoor spaces (loggias, arcades, courtyards, stairwells, atria, entrance halls, porticoes), where enclosure is partial and the thermal environment is explicitly designed to "dialogue" with outdoors[238] [239] [240]. These spaces are neither fully outdoor nor conventionally indoor; they function as buffers and gradients of exposure, and their comfort cannot be reduced to the logic of a fixed mechanical setpoint[241] [242].

In the context of climate change, this "setpoint-free" domain becomes central for at least two reasons. First, global and regional warming is increasing the frequency, duration, and intensity of heat events[243], pushing indoor conditions, especially in free-running buildings, toward overheating risk [244] with critical implications for health, productivity, and

[237] Klepeis et al., 2001.
[238] Olgyay, 1963.
[239] Givoni, 1998.
[240] Diz-Mellado et al., 2023
[241] Heschong, 1979.
[242] Avantaggiato et al., 2021.
[243] IPCC, 2023.
[244] Morales et al., 2025.

vulnerability[245]. Second, decarbonization trajectories require not only mitigation (reducing operational emissions) but also adaptation (maintaining acceptable indoor conditions under hotter climates), often under constraints of limited energy and infrastructure capacity[246]. In this framework, climate-responsive indoor environments, operated primarily through passive or low-energy means such as shading, natural ventilation, thermal mass, and behavioral adaptation, are a key part of climate resilience in the built environment[247] [248].

This section therefore frames indoor thermal comfort as an emergent property of a coupled system: external climate and microclimate, building envelope and spatial configuration, internal gains, ventilation and moisture dynamics, and occupant behavior[249] [250]. The emphasis is deliberately placed on naturally ventilated or predominantly free-running conditions (including transitional spaces), where indoor environmental variables are not stabilized by continuous mechanical conditioning, and where indoor comfort must be interpreted as a dynamic range rather than a static target[251] [252].

3.5.1 Scope and operating regimes

Indoor environments can be described along a continuum of operating regimes, from tightly controlled spaces (nearly constant setpoints and narrowly bounded variability), through mixed or intermittent regimes (partial conditioning, time-limited operation, or hybrid strategies), to fully climate-responsive or “free-running” spaces in which indoor conditions primarily track outdoor climate and are moderated through envelope performance, passive strategies, and occupant actions[253] [254]. Importantly, the continuum is not only technological; it is also social and cultural. Expectations, perceived entitlement to thermal constancy, and the availability of environmental controls shape what is judged acceptable, even under comparable physical

[245] Mavrogianni et al., 2022.
[246] Hong et al., 2023.
[247] Givoni, 1998.
[248] Hong et al., 2023.
[249] Givoni, 1998.
[250] Morales et al., 2025.
[251] Nicol et al., 2002.
[252] Brager et al., 1998.
[253] Nicol et al., 2012.
[254] Deuble et al., 2012

conditions[255] [256]. Within this continuum, the naturally ventilated/free-running regime is characterized by high coupling to external boundary conditions and high sensitivity to time-dependent processes.

The most influential control "levers" are often architectural rather than mechanical. Openings and airflow paths (windows, vents, cross-ventilation routes) govern the magnitude and distribution of natural air exchange[257] [258], while solar control (orientation, shading devices, glazing properties) and envelope properties (thermal resistance and inertia) determine the timing and persistence of heat gains[259] [260]. Spatial organization then mediates how effectively these levers support or constrain air exchange and heat dissipation[261] [262].

In Mediterranean contexts, where cooling needs can be intense, but diurnal cycles may allow nocturnal recovery, vernacular and climate-responsive architectures frequently exploit these levers through thick masonry, controlled apertures, shutters, courtyards, and shaded in-between spaces[263] [264]. Climate change modifies how this operating regime should be interpreted and assessed. In free-running and naturally ventilated buildings, thermal acceptability is not solely a function of instantaneous temperature but depends on multi-day sequences and the capacity for night-time recovery: heat stored in building mass and surfaces can accumulate during persistent heat waves and become a dominant driver of indoor discomfort[265] [266]. Recent monitoring-based studies in Mediterranean dwellings underline that night ventilation combined with envelope strategies can extend comfort hours during extreme events yet also show that ventilation rates may become insufficient under hot nights and prolonged heat waves, highlighting the limits of purely passive recovery[267].

[255] Brager et al., 1998.
[256] Deuble et al., 2012.
[257] Allard, 1998.
[258] Awbi, 2003.
[259] Givoni, 1998.
[260] Santamouris, 1996.
[261] Allard, 1998.
[262] Givoni, 1998.
[263] Olgyay, 1963.
[264] Givoni, 1998.
[265] Santamouris, 1996.
[266] Hong et al., 2023.
[267] Calama-González et al., 2023.

From a building-physics standpoint, this climate-driven regime can be framed through a time-dependent energy balance: indoor air, internal surfaces, furnishings and structural mass exchange sensible and latent heat with each other and with the exterior, while receiving solar and internal gains[268] [269]. When a system is mechanically controlled, the balance is closed by active heating/cooling at a target setpoint; under setpoint-free operation, closure relies on passive dissipation and storage, natural ventilation and infiltration[270] [271], and occupant-driven controls such as window opening and shading adjustment[272] [273]. For the purposes of the present thesis, it is helpful to disaggregate the indoor heat balance into five interacting contributors, solar gains, internal gains, envelope heat transfer, ventilation and air exchange, and heat storage, because each responds differently to Mediterranean diurnal cycles and to the non-stationary boundary conditions associated with heat waves[274] [275].

3.5.2 Solar gains

At first order, the absorbed short-wave gain at an indoor surface can be expressed as:

$$Q_{sol} = \alpha \cdot G$$

where Q_{sol} is the absorbed short-wave heat flux, α the surface short-wave absorptivity, and G the incident global solar irradiance (direct and diffuse components).

In setpoint-free indoor and transient environments, solar radiation is often the most variable and spatially heterogeneous driver of overheating. Whenever short-wave radiation is admitted through glazing, open façades, or partial enclosure, a direct radiative load is introduced into the indoor control volume and can create strong gradients: sunlit patches on floors, walls, or furniture can reach high surface temperatures quickly, while shaded zones remain cooler. These localized gains matter for comfort because absorbed short-wave energy is rapidly converted into sensible heat, raising surface temperatures that subsequently reemit

[268] Bergman et al., 2011.
[269] Çengel et al., 2014.
[270] Allard, 1998.
[271] Awbi, 2003.
[272] Brager et al., 1998.
[273] Deuble et al., 2012.
[274] Santamouris et al., 1996.
[275] Morales et al., 2025.

long-wave radiation and warm adjacent air layers by convection[276] [277]. As a consequence, identical air temperatures can correspond to substantially different operative temperatures and perceived comfort depending on solar access, view factors to heated surfaces, and radiant asymmetry, a point particularly relevant for semi-indoor typologies where sunlight is intentionally filtered rather than eliminated[278] [279].

The magnitude and timing of solar gains depend on a chain of design decisions, orientation, window-to-wall ratio, glazing transmittance, and shading geometry, as well as on context-related boundary conditions such as surrounding reflectance, sky view, and obstructions from adjacent buildings or vegetation[280] [281]. In Mediterranean cities, this chain is shaped by both climate and culture: high summer solar altitude and intense direct radiation have historically been countered by deep reveals, arcades, loggias and adjustable external shutters, which reduce short-wave penetration while allowing ventilation and daylight when desired[282] [283]. Contemporary retrofits can alter this balance (e.g., via changes in insulation, airtightness, and glazing configurations), making solar control a critical complement to energy-efficiency interventions when overheating risk is considered alongside winter performance[284] [285].

From a physical perspective, limiting solar gains at the exterior plane is typically more effective than attempting to mitigate them once they have entered the space, because any transmitted short-wave radiation ultimately becomes heat within the indoor environment[286] [287]. External shading devices, movable screens, vegetation, and high-reflectance finishes can therefore be interpreted as first-order control levers in climate-responsive indoor design[288] [289]. Their performance, however, is inherently dynamic: it depends on seasonal solar geometry, occupant operation, and competing requirements such as daylight, view and security. This

[276] Bergman et al., 2011.
[277] Çengel et l., 2014.
[278] Parsons et al., 2014.
[279] Diz-Mellado et al., 2021.
[280] Givoni, 1998.
[281] Oke, 2017.
[282] Olgyay, 1963.
[283] Heschong, 1979.
[284] Calama-González et al., 2023.
[285] Morales et al., 2025.
[286] Bergman et al., 2011.
[287] Çengel, 2014.
[288] Givoni, 1998.
[289] Santamouris, 2013.

dynamism is one reason why solar gains remain a major source of uncertainty in models of free-running buildings and of urban building stocks under future climates[290] [291].

For transitional spaces, solar gains also shape the role of the space as a buffer in a sequence of thermal exposures. A shaded arcade or loggia can provide a perceptible step-change in radiant load and operative temperature relative to an exposed street, even if air temperature differences are modest; conversely, courtyards and atria with high solar access can become radiative “hot spots” in summer, compromising their buffering role and potentially transferring heat to adjacent rooms[292] [293]. In the Mediterranean basin, where these typologies are widely used as climatic mediators, solar design cannot be treated as a purely architectural “form” issue: it directly conditions the feasibility of naturally ventilated comfort and the ability of the building to avoid overheating during heat events[294] [295].

3.5.3 Internal gains

In line with the physiological heat-balance formulation introduced earlier in this chapter, the net metabolic heat released by an occupant can be expressed as:

$$Q_{int} = M - W$$

where M is metabolic rate and W is external mechanical work on the environment (typically negligible in indoor and transitional contexts).

Internal gains comprise the sensible and latent heat released within a space by occupants, lighting, appliances, cooking and other equipment. In mechanically cooled buildings these gains are treated primarily as cooling loads to be removed; in free-running operation they act as persistent inputs that must be dissipated or stored within the building’s thermal mass and air volume [296] [297]. Their importance increases in compact spaces, in high-occupancy environments such as classrooms and offices, and in airtight buildings where air exchange is

[290] Morales et al., 2025.
[291] Hendriks et al., 2025.
[292] Diz-Mellado et al., 2021.
[293] Martinelli et al., 2015.
[294] Diz-Mellado et al., 2023.
[295] Morales et al., 2025.
[296] Bergman et al., 2011.
[297] Çengel et al., 2014.

limited, conditions that can occur in both contemporary low-energy design and in retrofitted building stock[298]. Crucially, internal gains are not only a matter of energy: they co-determine humidity levels (via occupant and cooking moisture), perceived freshness, and the capacity for evaporative cooling from the human body, linking internal heat and moisture generation to thermal comfort and heat stress[299]. Occupants are simultaneously the recipients of thermal exposure and a variable source of heat.

Metabolic heat release depends on activity and is not constant across individuals, cultures, or tasks; recent work has highlighted that the metabolic rate, a parameter sometimes treated as fixed in comfort studies, is in practice variable and can influence predicted comfort and heat balance [300]. Together with clothing and behavioral adaptation [301] [302], this implies that occupant-related internal gains have both a physiological dimension (human heat production) and an operational dimension (how people choose to use windows, shading, fans, and internal heat sources). Time-activity surveys further indicate that the bulk of exposure occurs indoors[303], meaning that internal gains and indoor microclimate are central drivers of heat exposure during heat events, particularly at night when occupancy concentrates in bedrooms and recovery becomes critical[304] [305].

Non-metabolic internal gains are governed by usage patterns and by technology. Even when design values are available, their real-world magnitude is shaped by behavioral schedules and by the functional program of the space[306]. In setpoint-free buildings, the timing of these gains can be as important as their total amount: gains occurring during late afternoon and evening may coincide with reduced ventilation potential and with rising surface temperatures due to solar absorption, thereby intensifying discomfort in periods relevant for sleep and domestic activities[307] [308]. In semi-indoor circulation zones or atria, internal gains may be intermittent

[298] Morales et al., 2025.
[299] Parsons, 2014.
[300] Luo et al., 2016.
[301] Nicol et al., 2012.
[302] Brager et al., 1998.
[303] Klepeis et al., 2001.
[304] Hong et al., 2023.
[305] Mavrogianni et al., 2022.
[306] Morales et al., 2025.
[307] Santamouris et al., 1996.
[308] Calama-González et al., 2023.

but can become locally significant under crowding, especially when air movement is limited and radiant temperatures are elevated[309].

For climate-change adaptation, internal gains also represent a challenge for modelling and for resilience assessments. In urban building stock studies, assumptions about occupancy, appliance use, and internal heat schedules can significantly alter overheating predictions—particularly in future scenarios where the margin between acceptable and critical temperatures narrows[310] [311]. From a resilience perspective, the interaction is two-way: higher internal gains increase the likelihood of overheating during heat waves[312], while behavioral responses to discomfort (e.g., turning on devices, opening windows) can either mitigate or exacerbate indoor conditions depending on outdoor enthalpy and air quality[313] [314]. This reinforces the need to treat internal gains as part of a coupled socio-technical system rather than as a fixed input[315] [316].

3.5.4 Envelope heat transfer

In steady-state form, conductive heat flow through an envelope element is commonly written as:

$$Q_{cond} = U \cdot A \cdot (T_i - T_e)$$

where U is the overall thermal transmittance, A the element area, and T_i and T_e the indoor and outdoor air temperatures; the product U·A expresses the strength of envelope coupling to the exterior.

Envelope heat transfer governs how strongly and how quickly indoor environments couple to the outdoor climate. Heat moves through walls, roofs and glazing by conduction; it is exchanged at surfaces by convection; and it is redistributed by long-wave radiation between

[309] Diz-Mellado et al., 2021.
[310] Morales et al., 2025.
[311] Hendriks et al., 2025.
[312] Morales et al., 2025.
[313] Deuble et al., 2012.
[314] Awbi, 2003.
[315] Brager et al., 1998.
[316] Morales et al., 2025.

surfaces and to the exterior environment (including the sky and surrounding urban surfaces)[317] [318]. In free-running buildings, these processes are not simply background phenomena: they define whether the indoor air and surfaces follow the outdoor diurnal cycle closely or instead exhibit damped and delayed responses. For this reason, the envelope should be understood as a dynamic filter rather than a static barrier: thermal resistance limits the amplitude of heat fluxes, while thermal capacity distributes heat exchange over time, producing phase lag and attenuation (decrement) in indoor temperatures[319] [320].

Mediterranean architecture has historically exploited this time-domain behavior by combining mass and controlled openings: heavy masonry and shaded external surfaces can reduce daytime peak fluxes[321] [322], while night ventilation purges stored heat when outdoor temperatures drop [323] [324]. Contemporary research on passive cooling and thermal inertia confirms that thermal mass can be beneficial for summer comfort, yet its performance is conditional on the availability of nocturnal recovery and on operational patterns that effectively discharge the mass[325] [326]. Under persistent heat waves—especially when night-time temperatures remain high—thermal inertia can become a liability because the envelope's "memory" increases, elevating baseline indoor temperatures across consecutive days[327] [328].

Monitoring-based evidence from Mediterranean dwellings illustrates this mechanism during warm nights and prolonged events[329]. The envelope's effectiveness also depends on microclimatic boundary conditions that are often altered in urban settings. Urban overheating and heat-island effects can raise nighttime ambient temperatures and reduce wind speeds, diminishing both conductive and convective heat rejection from external surfaces and limiting natural ventilation potential[330] [331]. At the scale of dense historic fabrics, indoor temperatures

[317] Bergman et al., 2011.
[318] Çengel et al., 2014.
[319] Balaras, 1996.
[320] Tribuiani et al., 2020.
[321] Santamouris et al., 1996.
[322] Santamouris et al., 2013.
[323] Allard, 1998.
[324] Etheridge et al., 1996.
[325] Santamouris et al., 2013.
[326] Tribuiani et al., 2020.
[327] Santamouris et al., 1996.
[328] Hong et al., 2023.
[329] Calama-González et al., 2023.
[330] Santamouris, 2020.
[331] Oke et al., 2017.

can therefore be influenced by urban form and density through modifications of radiative exchange, shading, and ventilation paths, an interaction documented for Venetian buildings in relation to climate change and urban morphology[332]. For Mediterranean cities, envelope heat transfer cannot be decoupled from the surrounding microclimate[333] [334]. In dense urban fabrics, microclimatic boundary conditions are modified by urban form and overheating, so the same wall or roof assembly can perform differently depending on street geometry, exposure, and nocturnal cooling potential[335] [336].

These interactions have methodological consequences. Predicting overheating and comfort in free-running spaces requires transient models that capture thermal inertia, solar radiation, and boundary-condition variability, rather than relying only on steady-state U-values and design-day assumptions[337] [338]. Recent reviews of urban building-stock modelling highlight that envelope characterization (including thermal bridges, glazing properties, shading, and thermal mass) is a major determinant of uncertainty in overheating projections under future climates[339]. Accordingly, the adaptation of housing design tools increasingly calls for metrics and workflows that explicitly address overheating risk and thermal resilience, not only annual energy demand[340]. For this thesis, envelope heat transfer is therefore treated as a key component of climate-responsive comfort, particularly in Mediterranean contexts where traditional “passive” principles must be reassessed under warming climates[341] [342].

3.5.5 Ventilation and air exchange

The sensible heat exchange associated with air exchange can be approximated as:

$$Q_{vent} = \rho \cdot c_p \cdot \dot{V} \cdot (T_{out} - T_{in})$$

[332] Maiullari et al., 2021.
[333] Olgyay, 1963.
[334] Givoni, 1998.
[335] Santamouris, 2020.
[336] Maiullari et al., 2021.
[337] Balaras, 1996.
[338] Morales et al., 2025.
[339] Ibid.
[340] Hendriks et al., 2025.
[341] IPCC, 2023.
[342] Santamouris et al., 1996.

where ρ is air density, c_p the specific heat capacity of air, $\dot{V}$ the volumetric airflow rate, and T_{out} and T_{in} the outdoor and indoor air temperatures; the sign depends on the temperature gradient.

In naturally ventilated buildings, ventilation and air exchange provide the most direct and rapidly adjustable coupling between indoor and outdoor environments. Air exchange, driven by wind pressure, buoyancy (stack effect), and occupant operation of openings, transports both sensible and latent heat, linking indoor comfort to outdoor temperature and humidity as well as to airflow pathways within the building[343] [344]. From a thermodynamic standpoint, the effect of ventilation provides cooling only when the incoming outdoor air has lower enthalpy than the indoor air and surfaces, while it becomes a heat and moisture source when outdoor conditions are warmer or more humid[345]. This sign change is fundamental in setpoint-free operation, because “more ventilation” is not intrinsically beneficial; its value depends on timing, flow rates, and the degree to which air movement reaches occupied zones[346] [347].

In Mediterranean climates, the diurnal temperature cycle often provides opportunities for ventilative cooling, particularly through night-time ventilation (night flushing) that aims to reset the building’s thermal mass and lower indoor temperatures before the next day’s solar load[348] [349]. The integration of ventilation with solar control and envelope inertia is a recurring theme in climate-responsive design, including vernacular typologies[350] [351]. Empirical and simulation-based studies in Mediterranean coastal zones demonstrate the potential of natural cross-ventilation as a passive cooling strategy, while also showing that performance is sensitive to wind availability, opening configuration, and building layout[352]. Vernacular strategies—such as controlled apertures, courtyards and shaded circulation spaces—can be interpreted as architectural devices that moderate solar gains while enabling airflow paths and stack-driven

[343] Allard, 1998.
[344] Awbi, 2003.
[345] Çengel et al., 2014.
[346] Allard, 1998.
[347] Awbi, 2003.
[348] Allard, 1998.
[349] Etheridge et al., 1996.
[350] Olgyay, 1963.
[351] Givoni, 1998.
[352] Faggianelli et al., 2014.

exchange[353] [354]. A Mediterranean case study illustrates how these principles can be re-read in vernacular architecture of Cyprus[355].

The limits of ventilation as a cooling strategy become evident during extreme events. When outdoor air temperatures remain high at night, ventilation may provide insufficient recovery; when humidity is high, perceived relief may be reduced because evaporative cooling potential is constrained, even if air temperature drops[356] [357]. Under such conditions, ventilation can still be valuable for indoor air quality and perceived freshness, yet its contribution to cooling may diminish or even reverse, particularly in dense urban environments where nocturnal cooling is weakened by urban overheating[358] [359]. These limitations are not merely technical; they also intersect with safety, noise, pollution exposure, and security concerns that can reduce the willingness or feasibility of window opening, thereby influencing real-world airflow rates[360] [361]. For modelling and assessment, ventilation thus represents both an opportunity and a major source of uncertainty.

Reviews of indoor overheating methods emphasize that window-opening schedules, infiltration assumptions, and occupant control strategies can dominate predicted indoor temperatures in free-running buildings, especially under future scenarios[362] [363]. This is particularly relevant for transitional spaces, where partial enclosure and complex airflow fields blur the boundary between “indoor” and “outdoor” ventilation regimes[364]. In the broader framework of this thesis, ventilation is treated as a microclimatic mechanism that couples building physics and human adaptation: its performance must be evaluated in relation to outdoor microclimate, radiant load, and multi-day sequences rather than as a static ventilation rate[365] [366].

[353] Olgyay, 1963.
[354] Givoni, 1998.
[355] Michael et al., 2017.
[356] Parsons, 2014.
[357] Calama-González et al., 2023.
[358] Awbi, 2003.
[359] Santamouris, 2020.
[360] Deuble et al., 2012.
[361] Morales et al., 2025.
[362] Ibid.
[363] Hendriks et al., 2025.
[364] Diz-Mellado et al., 2021.
[365] Allard, 1998.
[366] Hong et al., 2023.

3.5.6 Heat storage

A compact representation of sensible heat storage (or release) in a material mass is:

$$Q_{store} = m \cdot c \cdot (dT/dt)$$

where m is mass, c specific heat capacity, and dT/dt the temporal rate of temperature change. This term formalizes the role of thermal inertia in buffering short-term gains and shaping multi-hour responses.

Heat storage in building mass and internal contents is a defining feature of free-running indoor environments, because it provides the primary "buffer" that substitutes, at least partially, for the active control of mechanical systems. Thermal mass—walls, floors, ceilings, and furnishings—absorbs and releases heat as indoor surface temperatures change, shaping both the amplitude of indoor peaks and the rate of temperature drift over time[367] [368]. In energy-balance terms, storage introduces a memory: the indoor environment responds not only to current outdoor conditions and instantaneous gains, but also to the cumulative history of previous days and nights[369] [370]. This time dependence is central for interpreting comfort during heat waves[371], when consecutive hot days can load the mass faster than it can be discharged[372].

Under typical Mediterranean diurnal cycles, thermal inertia can reduce daytime peaks and improve comfort by delaying the penetration of outdoor heat and by stabilizing surface temperatures[373] [374]. The benefit is strongest when night-time ventilation can effectively discharge the mass[375] [376] and when solar gains are controlled[377]. In this sense, thermal mass supports a strategy of time-shifting: heat is absorbed when outdoor conditions are most severe and released when the outdoor environment is cooler and ventilation can reject it. Computational overviews and recent case studies underline, however, that the benefit is

[367] Balaras, 1996.
[368] Tribuiani et al., 2020.
[369] Bergman et al., 2011.
[370] Çengel et al., 2014.
[371] Hong et al., 2023.
[372] Santamouris et al., 1996.
[373] Balaras, 1996.
[374] Tribuiani et al., 2020.
[375] Allard, 1998.
[376] Etheridge et al., 1996.
[377] Santamouris et al., 2013.

contingent on how the building is operated; without adequate purge or night ventilation, the same mass can remain warm and maintain elevated radiant temperatures into the evening and night, deteriorating comfort during periods critical for sleep[378] [379].

Heat storage becomes particularly salient in the context of climate resilience and passive survivability. When heat events are prolonged and nocturnal recovery is limited, storage can turn from a protective buffer into a driver of sustained exposure: indoor temperatures drift upward across days, and discomfort is shaped by cumulative load rather than by instantaneous extremes[380] [381]. This mechanism helps explain why overheating risk in housing is often discussed in relation to vulnerability and health outcomes, not only to short-term discomfort[382]. Reviews focusing on urban building stock further note that capturing storage dynamics is essential to evaluating overheating under future climates, because the interaction between thermal mass, ventilation behavior, and elevated nighttime temperatures determines whether a building can "reset" or instead accumulates heat over successive days[383] [384].

For Mediterranean architecture, the practical implication is that thermal mass should be considered together with the feasibility of discharge[385] [386]. In dense urban contexts, radiative cooling potential and night-time boundary conditions can be constrained by urban overheating and reduced wind, diminishing passive recovery[387] [388]. In transitional spaces, mass can also create favorable thermal gradients (cooler surfaces in shaded arcades) but may conversely store solar heat in courtyards and later reradiate it, altering comfort in adjacent interiors[389] [390]. The following sections therefore move from the components of the indoor heat balance to

[378] Balaras, 1996.
[379] Tribuiani et al., 2020.
[380] Hong et al., 2023.
[381] Mavrogianni et al., 2022.
[382] Ibid.
[383] Morales et al., 2025.
[384] Hong et al., 2023.
[385] Olgyay, 1963.
[386] Givoni, 1998.
[387] Santamouris, 2020.
[388] Oke et al., 2017.
[389] Heschong, 1979.
[390] Diz-Mellado et al., 2021.

comfort-relevant descriptors—radiant environment and air movement/humidity—highlighting why overheating assessment must remain microclimatic in nature[391] [392].

3.5.7 Radiant environment and surface temperatures

In indoor (and semi-indoor) environments without continuous conditioning, the radiant field frequently becomes as important as the air temperature for comfort evaluation. Thermal sensation and physiological heat exchange depend on the combined action of convective and radiative pathways; when interior surfaces warm up—due to solar gains, conductive heat flow, or stored heat in mass—mean radiant temperature can rise significantly even if air temperature changes modestly[393]. This effect is amplified in spaces with large view factors to warm surfaces (e.g., top-floor rooms under heated roofs, sunlit floors, or masonry walls that have absorbed solar heat), and in transitional spaces where direct solar exposure and radiative asymmetry are integral to the spatial experience[394]. The physics linking solar access to indoor comfort follows a clear chain: short-wave radiation enters (or strikes) the space; a portion is absorbed by interior materials; absorbed energy increases surface temperature; surfaces emit long-wave radiation and drive convective warming of adjacent air layers[395] [396]. Material properties (solar absorptance, thermal conductivity, heat capacity, and emissivity) and geometric factors (surface orientation and view factors) govern how quickly and how strongly this chain affects human exposure[397].

For Mediterranean architecture, the interplay of high solar intensity and design strategies such as shutters, deep reveals, and shaded semi-open spaces can be interpreted as a longstanding “radiant control culture” aimed at reducing radiant load during daytime while maintaining ventilation potential[398] [399]. Thermal mass is central in this context, not simply as an energy concept but as a radiant comfort concept. By damping and delaying temperature

[391] Parsons, 2014.
[392] Morales et al., 2025.
[393] Parsons, 2014.
[394] Heschong, 1979.
[395] Bergman et al., 2011.
[396] Çengel et al., 2014.
[397] Parsons, 2014.
[398] Olgyay, 1963.
[399] Heschong, 1979.

swings, massive envelopes can reduce peak surface temperatures and stabilize mean radiant temperature during the hottest hours[400] [401]. However, if night-time cooling is reduced (e.g., during heat waves), the same mass may store heat and re-radiate it indoors during the evening and night, worsening sleep conditions and prolonging exposure[402] [403].

Studies on Mediterranean buildings highlight that high thermal inertia can be beneficial for summer comfort under typical diurnal cycles, but that performance depends critically on ventilation and operational patterns that allow heat release when outdoor conditions permit it[404] [405]. For thermal comfort research and modelling, these mechanisms imply that climate-responsive indoor analysis must go beyond air temperature as a single descriptor. Capturing surface temperatures and radiant exchange (especially in sun-exposed rooms, top floors, and transitional spaces) is essential to represent the thermal environment experienced by occupants and to anticipate when passive strategies may fail under extreme conditions[406] [407].

3.5.8 Air movement and humidity

Unlike outdoor wind, indoor air movement is shaped by architectural pathways, openings configuration, pressure differences, and obstructions. Cross-ventilation, single-sided ventilation, and stack-driven flows generate uneven velocity fields: jets near openings, recirculation zones, and stratification can coexist within the same space[408] [409]. In transitional spaces (e.g., courtyards and atria), air movement is further influenced by geometry and partial enclosure, producing complex local microclimates that can differ substantially from both outdoor street conditions and adjacent indoor rooms[410] [411]. When air temperature is below (or moderately close to) skin temperature, increased air speed enhances convective heat transfer and—crucially—supports evaporative cooling by removing saturated boundary layers

[400] Allard, 1998.
[401] Etheridge et al., 1996.
[402] Santamouris et al., 1996.
[403] Calama-González et al., 2023.
[404] Allard, 1998.
[405] Calama-González et al., 2023.
[406] Parsons, 2014.
[407] Allard, 1998.
[408] Allard, 1998.
[409] Awbi, 2003.
[410] Heschong, 1979.
[411] Diz-Mellado et al., 2021.

from the skin and clothing surface[412] [413]. Experimental and modelling work on convective heat transfer shows how convective coefficients increase with air speed, clarifying why even modest indoor air movement can improve comfort in warm conditions[414].

In naturally ventilated Mediterranean buildings, this principle underpins strategies such as cross-ventilation corridors, night flushing, and the use of in-between spaces that act as ventilated buffers[415] [416]. However, the benefits of air movement have well-defined limits. When air temperature exceeds skin temperature, convection can reverse from heat loss to heat gain; in such cases, airflow may worsen physiological strain unless evaporation remains effective[417] [418]. Moreover, at high humidity, evaporative capacity decreases, so perceived relief from ventilation may be weaker even when air speed increases. Under extreme heat and humidity, the combined constraints of thermoregulation can approach human adaptability limits, making “more ventilation” an insufficient or even counterproductive response[419] [420].

These limits are particularly relevant for Mediterranean coastal cities and for heat-wave periods associated with high night-time temperatures, when natural ventilation may not provide adequate nocturnal recovery [421] [422]. Therefore, in climate-responsive indoor environments, airflow must be interpreted as one component of a coupled thermal system: its effectiveness depends on simultaneous conditions of air temperature, humidity, and radiant load, as well as on the temporal profile of exposure (daytime peaks vs nocturnal recovery)[423] [424]. This reinforces the need for an integrated microclimatic assessment rather than a single-variable approach.

[412] Fanger, 1970.
[413] Parsons, 2014.
[414] de Dear et al., 1997.
[415] Olgyay, 1963.
[416] Allard, 1998.
[417] Fanger, 1970.
[418] Parsons, 2014.
[419] Parsons, 2014.
[420] Sherwood et al., 2010.
[421] Calama-González et al., 2023.
[422] Sherwood et al., 2010.
[423] Parsons, 2014.
[424] Allard, 1998.

3.5.9 Thermal Variability and Comfort

Naturally ventilated and semi-indoor environments behave as microclimatic volumes whose thermal conditions emerge from interacting drivers: solar and internal gains, envelope heat transfer, thermal storage, ventilation and moisture exchange, and occupant operation[425] [426]. In these regimes, spatial non-uniformity and temporal variability are defining features. Comfort becomes a question of ranges, gradients, and sequences: how quickly surfaces warm and cool, how long heat is retained, where airflow is effective, and whether night-time conditions allow the system to reset[427] [428].

This microclimatic framing is especially pertinent in the Mediterranean basin, where architectural traditions have long exploited transitional spaces and passive moderation to create habitable gradients between outdoor summer heat and interior refuge[429] [430]. At the same time, observed and projected warming challenges the reliability of those gradients during heat waves and warm nights, highlighting the need to connect indoor comfort theory with climate resilience and operational realism[431] [432].

3.6 Psychological aspects

Human thermal experience cannot be treated as a "closed system": energy and matter are continuously exchanged between the body and the surrounding environment [433]. This exchange is governed by physiological thermoregulation, but it is also shaped by behavior and cognition, which influence how people respond to and interpret outdoor conditions. A robust account of outdoor thermal comfort therefore requires subjective parameters to be considered alongside microclimatic measurements.

[425] Givoni, 1998.
[426] Allard, 1998.
[427] Santamouris et al., 1996.
[428] Calama-González et al., 2023.
[429] Olgyay, 1963.
[430] Givoni, 1998.
[431] IPCC, 2023.
[432] Calama-González et al., 2023.
[433] Cabanac, 2011.

3.6.1 Microclimatic variables and thermal sensation

Field surveys conducted in Cambridge across different seasons combined microclimatic monitoring with interviews of 1,453 users in four outdoor sites about their momentary thermal comfort state. The results highlighted a clear gap between theoretically predicted dissatisfaction and the levels reported in situ, indicating that a purely physiological description is not sufficient, on its own, to characterize outdoor thermal comfort[434].

Subsequent field campaigns across diverse climates have reinforced this broader framing. The RUROS (Rediscovering the Urban Realm and Open Spaces) project, for example, evaluated climatic, social and cultural parameters across seven European cities, pairing nearly 10,000 questionnaires with simultaneous microclimatic measurements in two sites per city[435].

Across the surveyed cities, despite wide differences in air temperature and solar exposure, reported comfort levels were relatively homogeneous: on a scale from -2 (very cold) to +2 (very hot), only a small share of respondents selected the extreme discomfort categories, while around 90% reported sensations between -1 and +1, and about 48% reported neutrality (0)[436]. Thermal neutrality corresponded to different annual air temperatures across locations (neutral temperatures), ranging from about 25.3°C in Thessaloniki to 12.9°C in Fribourg. Neutral temperatures also tended to track the seasonal course of local climate, with smaller gaps between neutral and climatic temperature in warmer cities. This pattern aligns with physiological evidence that humans can acclimate effectively to heat stress and, in many contexts, tolerate heat more readily than cold[437].

A related psychological mechanism is captured by the concept of alliesthesia: the same external thermal stimulus can be perceived as pleasant or unpleasant depending on the individual's internal state and context. In other words, a condition that appears physiologically suboptimal in abstract can still be experienced as acceptable, or even enjoyable, in a specific situation[438].

[434] Nikolopoulou et al., 2001.
[435] Nikolopoulou et al., 2006.
[436] Ibid.
[437] Sawka et al., 2011.
[438] Cabanac, 1971.

3.6.2 Psychological adaptation

In relation to indoor environments, it has been argued that "psychological adaptation might actually play the most significant role in explaining the differences in observed and predicted thermal sensations and acceptability, particularly in light of different environmental contexts"[439].

More generally, adaptation can be described as a gradual reduction in response when a stimulus is repeatedly experienced, supported by behavioral adjustments and changes in expectation that help individuals cope with a modified environment. In the present context, this translates into thermal adaptation.

In outdoor settings, thermal adaptation is often discussed through three complementary mechanisms: physical adaptation, such as adjusting clothing, posture, or using hot or cold beverages; physiological adaptation, referring to automatic responses such as shivering or sweating; and psychological adaptation, which captures how perception, appraisal and expectations modulate thermal sensation and comfort[440].

Several psychological factors can influence how outdoor thermal conditions are perceived and evaluated. The main ones considered here are described below.

Naturalness. Outdoor conditions are often interpreted as inherently variable; sudden changes in temperature or wind speed may therefore be tolerated when they are perceived as normal features of the natural environment, rather than as failures of control.

Experience and expectations. Long-term memory and habituation influence what is judged extreme or acceptable in outdoor settings, shaping thermal evaluation through expectation[441]. Large field datasets also indicate that many users report only moderate discomfort despite substantial variation in microclimatic conditions across countries, and that difficulty can be asymmetric: people in warmer climates may report greater discomfort during cold conditions, while the reverse tends to occur in colder climates[442].

[439] Brager et al., 1998.
[440] Nikolopoulou et al., 2003.
[441] Knez et al., 2009.
[442] Nikolopoulou et al., 2006.

Short-term thermal history can also bias evaluation: people often judge current conditions relative to the previous days or season. In the RUROS interviews, for instance, the reported comfort zone tended to shift toward warmer temperatures in autumn and toward cooler temperatures in spring, consistent with seasonal acclimatization and expectation[443].

Time of exposure. Brief exposure to uncomfortable outdoor conditions may be tolerated when it is perceived as temporary and non-threatening, for example when moving from a warm car to the entrance of a building on a cold winter evening.

Personal choice and perceived control. Willingly choosing to be outdoors, and perceiving control over when exposure will end, can increase tolerance of discomfort (for example, meeting friends or taking a walk). Conversely, enforced exposure - such as waiting or working outdoors - reduces perceived control and is more likely to be associated with dissatisfaction.

Environmental stimulation. The decision to use an outdoor space is not driven by thermal neutrality alone: environmental quality, activity and social motivation can make people willing to tolerate, or even seek, mild thermal stimulation. Questionnaire studies have reported that many users enjoy being outdoors even when they describe feeling warm or cold rather than neutral, and that warmth is often perceived positively in open-air contexts. Patterns of sun-seeking shortly after leaving indoor environments, followed by a tendency to move toward shade after prolonged exposure, have also been observed, suggesting that preferences evolve with exposure time and internal state[444] [445].

3.7 Human thermal comfort indexes. A critical review

To work properly, the human body must maintain a constant core temperature of 37 °C. This condition is preserved through continuous heat exchange with the surrounding environment via the skin: heat gains from metabolism and from the environment must be balanced by heat losses, as expressed by the human heat-balance equation discussed in the previous section. Behavioral actions—such as clothing adjustment, activity level, and posture—further modify this balance and shape thermal experience in real settings.

[443] Nikolopoulou et al., 2006.
[444] Nikolopoulou et al., 2001.
[445] Nikolopoulou et al., 2006.

Over time, thermal comfort and thermal stress have been operationalized through a large number of indices, developed either empirically or from increasingly sophisticated energy-balance models[446]. Here, thermal comfort indices are treated as the operational interface between microclimatic conditions and human thermal experience: they translate combinations of air temperature, humidity, wind, and radiation into a human-centered descriptor that can be interpreted and compared across spatial configurations.

Because the built environments investigated in this work include outdoor spaces, transitional/semi-outdoor conditions, and naturally ventilated free-running indoor environments, the focus is placed on indices that can be applied under variable, non-uniform, and non-controlled exposures. Within this scope, the indices reviewed below are framed as different “lenses” on thermal stress: each of them prioritizes specific heat-exchange pathways or simplifying conventions, thereby highlighting particular aspects of human–environment interaction that become relevant when thermal conditions are shaped by climate forcing and built form.

3.7.1 Wind Chill

Wind Chill is among the earliest and most widely known cold-stress indicators. It combines air temperature and wind speed to express the increased cooling power of moving air and its implications for human tolerance to cold[447]. The original formulation was rooted in an analogy with the time required for wind to freeze water and was not derived from a full physiological heat-balance representation of the human body[448]. Subsequent revisions progressively moved toward an equivalent-temperature interpretation, including the Wind Chill Temperature formulation introduced in 1997[449] and the Wind Chill Equivalent Temperature adopted in 2001, defined through an equivalent calm-air condition producing the same skin heat loss as the actual windy exposure[450] [451]. Conceptually, Wind Chill provides a focused reading of cold stress dominated by convective cooling: it is effective where wind-driven heat loss is the primary

[446] Havenith et al., 2016
[447] Siple et al., 1945.
[448] Brauner et al., 1995.
[449] ASHRAE, 1997.
[450] OFCM, 2003.
[451] Osczevski et al., 2005.

driver, while it is not designed as a general descriptor of combined thermal stress mechanisms across contrasting climatic regimes.

3.7.2 Temperature Humidity Index (THI)

The Temperature Humidity Index (THI), also referred to as the Discomfort Index, addresses heat stress by combining air temperature and humidity [452]. It builds on the effective temperature concept [453] and was formulated as an empirical transformation intended to remain in close agreement with effective temperature across recorded dry-bulb and wet-bulb conditions[454]. THI therefore provides a thermo-hygrometric lens on warm discomfort in which moisture availability—through its control on evaporative heat loss—plays a central role. By construction, THI reduces the thermal environment to temperature–humidity forcing; consequently, radiative exposure and wind-driven convective effects are not represented explicitly. This makes THI informative in contexts where humidity is a dominant stress component, while it becomes less discriminating when geometry-driven radiation fields and localized airflow patterns are central to thermal experience.

3.7.3 Comfort Formula (COMFA)

COMFA is an outdoor comfort formulation developed in 1986 that explicitly frames thermal comfort through an energy-balance perspective[455]. It accounts for metabolic heat production, radiative exchanges, sensible heat gains or losses, long-wave emission from the body, and the resulting heat storage term, which approaches zero under thermal equilibrium. In conceptual terms, COMFA sees comfort as a balance between gains and losses rather than as a single climatic proxy, making it sensitive to the combined influence of radiation, wind, and personal parameters. At the same time, its practical application depends on the consistent estimation of multiple environmental and human-related inputs, which affects how easily the index can

[452] Thom, 1959.

[453] The ET index was the temperature of a standard environment, at 50% relative humidity, in which a subject would experience the same heat loss as in the actual environment. Houghten et al., 1923.

[454] Thom, 1959.

[455] Brown et al., 1986.

be adopted as a stable comparative layer across different modelling scales and across matched baseline–future scenario pairs.

3.7.4 Outdoor Standard Effective Temperature (OUT-SET*)

OUT-SET* extends the Standard Effective Temperature (SET*) concept to outdoor conditions through an equivalent-temperature framing [456]. SET* is defined as the air temperature of a standardized reference environment in which an occupant would experience the same total heat loss from the skin as in the actual environment, under specified reference assumptions for humidity, air movement, radiation, clothing, and activity[457]. The outdoor formulation introduces an explicit treatment of outdoor mean radiant temperature (OUT_MRT) to represent the radiative load that distinguishes outdoor from indoor reference conditions. In its original form, the model was developed for open-field situations and not for complex urban settings, where long-wave radiation from surrounding surfaces can become dominant relative to direct solar exposure[458]. Within the scope of this thesis, OUT-SET* is therefore read as an important step in translating indoor-based equivalent temperature concepts to outdoor exposure, while highlighting the sensitivity of such approaches to how radiative exchange is represented in geometry-dependent environments.

3.7.5 Predicted Mean Vote (PMV)

The Predicted Mean Vote (PMV) is the most widely used thermal sensation index in building-related studies, developed in 1970 to predict thermal sensation on a standardized vote scale [459]. PMV was formulated for steady-state indoor environments—typically mechanically controlled—where assumptions of near-uniform conditions and relatively stable clothing and activity are plausible. Its relevance within an outdoor-oriented review reflects the fact that various attempts have been made to adapt PMV to outdoor contexts by introducing additional terms for radiation or by extending wind ranges beyond typical indoor limits. A

[456] Pickup et al., 2000.
[457] ASHRAE, 2010.
[458] Erell et al., 2011.
[459] Fanger, 1970.

widely used approach is the Klima-Michel model, which extends PMV by adding a short-wave radiation component to better represent outdoor exposure[460]. Nevertheless, even under these extensions, PMV remains fundamentally static and relies on simplified links between environmental forcing and physiological response; in particular, key thermoregulatory variables remain constrained by internal assumptions tied to metabolic activity, which limits responsiveness under rapidly varying outdoor conditions[461]. In the logic of this thesis, PMV therefore functions as a paradigmatic example of how an indoor-centric framework can be stretched toward outdoor use—and where this stretching becomes conceptually and operationally problematic when the objective is comparative interpretation across scales and under shifting climatic boundary conditions.

3.7.6 Physiological Equivalent Temperature (PET)

PET is grounded in the Munich Energy Balance Model for Individuals (MEMI)[462] and expresses thermal conditions as a physiological equivalent temperature. It is defined as the air temperature of a typical indoor reference setting in which the human heat balance would be maintained with core and skin temperatures equal to those observed under the actual conditions being evaluated, under standardized activity and clothing assumptions[463]. Operationally, PET is obtained by solving the human energy balance within MEMI and translating the resulting physiological state into an equivalent air temperature under the defined reference environment[464]. This equivalent-temperature framing makes PET relatively intuitive to communicate, and PET values are often interpreted through qualitative stress or comfort classes rather than through raw numbers alone[465]. Conceptually, PET "sees" thermal stress through an indoor-reference equivalence: this supports interpretability but introduces a dependence on the chosen reference conventions when comparisons span different environmental regimes. Moreover, PET is a steady-state index and does not directly represent transient exposure along movement paths or rapid microclimatic shifts; for this reason,

[460] Jendritzky et al., 1981.
[461] Erell et al., 2011.
[462] Höppe, 1999.
[463] Ibid.
[464] Matzarakis et al., 2008.
[465] Matzarakis et al., 1996.

dynamic extensions such as dPET have been proposed to simulate physiological response during walking in outdoor environments[466].

3.7.7 Universal Thermal Climate Index (UTCI)

UTCI was developed in 2009 through a COST Action involving an international consortium of researchers, with the explicit goal of defining an index applicable across a wide range of climates and capable of assessing both heat and cold stress[467] [468]. Like several of the indices above, UTCI is formulated as an equivalent temperature: it maps the combined effects of air temperature, humidity, wind, and radiation into the reference air temperature that would elicit the same physiological response as the actual condition. A key distinctive feature is the underlying thermophysiological model: while several earlier indices rely on simplified representations of the human body, UTCI is based on the UTCI–Fiala multi-node model[469], which resolves heat exchange and thermoregulation across differentiated body segments and layers. In addition, UTCI incorporates a clothing model dynamically coupled with activity and accounting for non-uniform insulation and the effect of motion on effective air movement[470]. UTCI has been validated and tested across a broad spectrum of outdoor climatic conditions, supporting its use as a standardized descriptor of thermal stress in diverse contexts[471].

On the basis of this critical review, UTCI is adopted in this work as the reference metric for thermal comfort assessment. The rationale for this choice, together with the assumptions, inputs, and the way UTCI is operationally used for comparative analysis across scales and scenarios, is discussed in the following chapters, where the methodological workflow is presented and applied.

[466] Bruse, 2000.
[467] Błażejczyk et al., 2010.
[468] Jendritzky et al., 2012.
[469] Fiala et al., 2012.
[470] Havenith et al., 2012.
[471] Psikuta et al., 2012.

4 Assessing multi-scalar thermal resilience under climate change

This methodological chapter formalizes a comparative, multi-scalar methodology to assess the thermal resilience of the built environment under climate change. Thermal resilience is operationalized as the stability of outdoor thermal comfort when the boundary climate shifts from a present-day baseline to a future scenario.

It specifies inputs, assumptions, and processing steps so that the workflow can be replicated: from weather data and a three-dimensional model to UTCI computation, ΔUTCI-based resilience assessment, and cross-variant comparison within an explicit evaluation domain.

The methodological workflow is applied to a set of predefined spatial configurations. These configurations may correspond to existing territorial morphologies or to alternative geometric arrangements derived from a common case study, but they are always defined prior to simulation and are held constant when comparing baseline and future climate scenarios.

The method is operationally developed across these steps:

1. Select site and analysis scale (urban / building / component).
2. Prepare baseline and future-scenario weather files and identify a comparable heat-stress analysis period to minimize cloud-cover artefacts between scenarios.
3. Build a simulation-ready 3D model with materials and vegetation attributes.
4. Define the evaluation domain and the sampling strategy (grid/sensors).
5. Simulate microclimate variables needed for UTCI (DBT, RH, wind speed, MRT).
6. Compute UTCI for baseline and future scenarios on the same domain.
7. Compute ΔUTCI and derive comparative indicators (maps and statistics).
8. Compare and rank variants using explicit decision rules.

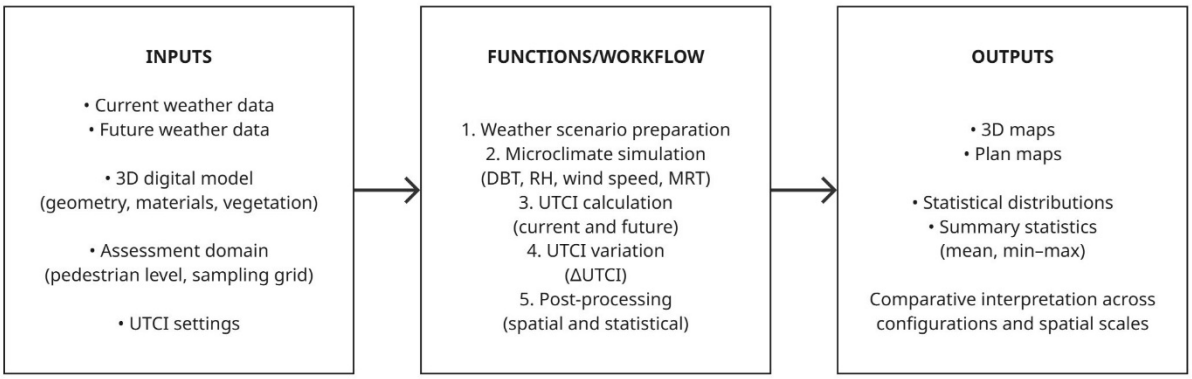

Figure 6. The diagram illustrates the Inputs–Functions–Outputs structure of the proposed methodology. Current and future EPW weather files, together with a three-dimensional digital model of the built environment and a defined assessment domain at human exposure level, constitute the inputs of the workflow. These inputs are processed through a sequence of steps including weather scenario preparation, microclimate simulation, UTCI calculation for current and future conditions, and the computation of local UTCI variations (ΔUTCI). Post-processing operations generate spatial and statistical representations of the results. The outputs support a comparative interpretation of thermal resilience across different configurations and spatial scales.

Table 2 shown here below reports the definitions of the main methodological terms employed in this chapter, establishing a common reference for the interpretation of the workflow and the comparative analyses that follow.

Term	Definition
Scale	Spatial level of analysis (urban, building, or component scale), defining the extent and resolution of the built environment while preserving the same methodological workflow.
Configuration	Design alternative defined by changes in geometry, materials, openings, shading devices, or vegetation, characterized exclusively by input parameters and not by resulting microclimatic or comfort outcomes.
Evaluation domain (space of influence)	Human-exposure-relevant spatial subset of the model used for sampling and comparison of microclimatic variables and UTCI, typically defined through a grid of points at a specified height above ground and excluding boundary regions affected by numerical artefacts (e.g. edge effects).
Workflow	Ordered sequence of computational steps transforming climate and geometric inputs into microclimatic variables, UTCI values, and comparative outputs. While software implementations may vary, the workflow structure remains invariant across scales and case studies.
Microclimatic variables	Environmental variables governing human heat exchange and required for UTCI calculation: air temperature (DBT), relative humidity (RH), wind speed, and mean radiant temperature (MRT), evaluated within the defined evaluation domain.
Baseline and future scenario	Climatic conditions representing current and projected states, respectively, applied to the same geometric model, evaluation domain, and workflow settings in order to isolate the effect of climate change on thermal comfort.
ΔUTCI (UTCI variation)	Difference between UTCI values computed under future and baseline scenarios at the same spatial location and time, representing the local change in thermal comfort induced by climate change and used to assess relative thermal resilience across configurations and spatial scales.

Table 2– Methodological glossary of key terms.

4.1 Weather data and morphing to future scenarios

4.1.1 Weather data requirements for UTCI-based assessment

Multiple sources of climate data are available, characterized by different structures, spatial resolutions, temporal coverage, and intended applications [472]. In the context of built-environment and microclimatic analyses, however, climate data cannot be treated as a generic input. In order to support thermal comfort assessment at the human scale, climate information must provide a coherent and complete set of atmospheric boundary conditions that can be consistently coupled with three-dimensional geometric models and comfort-assessment tools.

Within the methodology developed, climate data are therefore introduced as operational boundary conditions for the simulation of microclimatic variables and the subsequent calculation of the Universal Thermal Climate Index. This implies that climate inputs are not analyzed per se, but are required to be structurally compatible with microclimatic simulation engines and thermophysiological models, ensuring that the same data structure can be applied uniformly across different spatial scales and design configurations.

To ensure consistency, interoperability, and replicability across case studies, climate information is handled through the EnergyPlus Weather (EPW) format[473]. EPW files provide a compact and standardized representation of hourly atmospheric conditions and are widely supported by simulation environments used in urban microclimate and building-performance analyses. The adoption of a single climate data format allows the assessment workflow to remain invariant while only the geometric model, spatial resolution, and scenario-specific climate signal are varied.

EPW files collect, within a single hourly dataset, the atmospheric variables required for UTCI calculation, including air temperature (DBT), relative humidity (RH), wind speed, and radiation components required for MRT calculation. The availability of these variables in a consistent temporal structure allows their direct use within the simulation environments adopted in the

[472] Zou et al., 2023.
[473] Crawley et al., 2001

workflow. As a result, current and future climate conditions can be compared under identical modelling settings.

4.1.2 Choice of baseline year(s) and future horizon(s)

Baseline and future reference years are selected with the explicit aim of enabling direct comparison within each case study across configurations and spatial scales. The baseline year refers to current climatic conditions and is taken directly from the weather file used for the simulations. Future conditions are represented by reference years corresponding to projected climate horizons (e.g., mid-century or end-of-century), selected according to the specific scope of each case study. Importantly, comparative analyses are always performed between baseline and future conditions within the same case study, while no direct comparison is made across different future horizons, as the methodological framework is insensitive to the absolute calendar year and depends only on internally consistent baseline–future pairs

In all simulations the geometric model, the evaluation domain, the spatial sampling grid and the simulation workflow are kept exactly the same. No changes are introduced between baseline and future runs, apart from the climate input. This allows differences in UTCI and ΔUTCI to be traced back to the modified climatic forcing, rather than to changes in the model setup or in the simulation procedure.

In addition to selecting baseline and future years, a specific analysis period is defined to ensure comparability between scenarios. The assessment is anchored to a representative extreme summer period identified from the EPW statistics, typically corresponding to the hottest week of the year. Within this period, candidate days are screened by jointly analyzing dry-bulb temperature and global horizontal radiation profiles in both baseline and future EPW files. This screening is used to exclude days characterized by abrupt variations in radiation associated with cloud-cover differences, which could otherwise dominate the microclimatic signal and bias the comparison.

Once a representative day is selected, results are extracted at the peak afternoon hour, corresponding to the maximum daily heat load in the EPW files (typically between 15:00 and 16:00 local time, depending on location and scenario). To ensure physically meaningful

boundary conditions at the reporting time, a pre-run or spin-up period is introduced by starting the simulation on the previous day. This approach allows the thermal mass of surfaces and the near-ground air field to undergo at least one full charging and discharging cycle before the analyzed time slice, reducing the influence of initial conditions on the computed microclimatic variables and UTCI values.

4.1.3 Scenario framework and climate-model reference

Future weather files are obtained by modifying a baseline EPW file according to emission scenarios implemented in climate-data morphing tools. In this work, the scenario framework follows the Representative Concentration Pathways (RCPs) associated with CMIP5 climate projections, which are used to describe changes between present and future climatic conditions.

In the case studies presented, a single scenario (RCP 8.5) is adopted and applied consistently to all simulations. This choice reflects a pragmatic assumption on future climatic trends and provides a coherent reference condition for the assessment. The methodological procedure itself does not depend on the specific scenario label: the same workflow can be applied to alternative pathways, provided that baseline and future weather files are generated in a consistent manner and that all modelling assumptions remain unchanged.

Within this framework, RCP-based projections are used to describe relative changes between baseline and future conditions, driving the transformation of baseline weather data into plausible future-year EPW representations for comparative microclimatic and thermal-comfort analysis. During the preparation of this dissertation, CMIP6-based approaches for future weather-file generation were introduced in the literature, including methods based on Shared Socioeconomic Pathways (SSPs) [474]. These developments post-date the simulation campaign presented here; the adoption of an RCP-based framework therefore ensures full internal consistency between the applied case studies and the methodological assumptions adopted throughout the work.

[474] Rodrigues et al., 2023.

4.1.4 Morphing approach: tool selection and justification

The generation of future EPW files is performed through climate-data morphing tools that apply scenario-driven change factors to an existing baseline weather file. Among the available approaches, CCWorldWeatherGen[475] offers an accessible implementation of the Belcher–Hacker–Powell "shift and stretch" algorithm, operating through a spreadsheet-based workflow. While effective for temperature-related variables, this approach may involve simplified treatments of some radiative components, depending on the implementation.

A more comprehensive alternative is provided by Meteonorm v8[476], which regenerates complete EPW years by combining observational data with climate-model projections consistent with the RCP framework. Meteonorm allows the simultaneous modification of temperature, humidity, wind, and radiation variables, producing internally consistent future weather files. For this reason, Meteonorm v8 is adopted as the primary tool for future weather generation in this workflow.

4.1.5 Output: standardized EPW packages and traceability

The climate-data processing stage results in a standardized set of EPW files, including one baseline file and one or more future-scenario files. These EPW files constitute the sole climatic input to all subsequent simulations. Baseline EPW sources are obtained from established global repositories, while future EPW files are generated through the selected morphing procedure.

For traceability and reproducibility, each EPW file is archived using a consistent naming convention and is associated with minimal metadata, including geographic coordinates, data source or tool, scenario label, and reference horizon. This organization ensures that simulations can be repeated under identical climatic assumptions and supports systematic comparison across different case studies and spatial scales.

[475] Jentsch et al. 2013.
[476] Meteotest AG, 2020

4.2 Geometrical modeling of the built environment

Beyond climatic boundary conditions, the assessment of outdoor thermal resilience requires an explicit representation of the built environment through geometry and material attributes. While climate inputs define the external forcing, it is the three-dimensional configuration of space that mediates radiative exposure, airflow patterns, and surface–atmosphere exchanges at human exposure level, ultimately shaping the microclimatic variables entering UTCI computation. In this methodology, geometrical modelling is therefore treated as a second core input of the workflow, complementary to weather data and invariant across baseline and future scenarios. The objective is not geometric fidelity per se, but the construction of a simulation-ready representation capable of isolating design-driven effects under identical climatic forcing, ensuring that variations in thermal comfort can be attributed to spatial configuration rather than to modelling artefacts.

4.2.1 Why geometry matters for microclimate and UTCI

Thermal comfort in complex built environments is strongly mediated by geometry. This applies not only to fully outdoor conditions, but also to transitional and naturally ventilated indoor spaces, where external climatic forcing penetrates the envelope and interacts with spatial configuration. Urban-canyon proportions, building heights and setbacks, sky view factor, and the degree of enclosure of human occupancy spaces govern the local balance between shortwave and longwave radiation, modulate shading patterns throughout the day, and influence wind permeability and turbulence at the scale of human exposure. In hybrid conditions—such as courtyards, semi-enclosed passages, or permeable envelopes of indoor spaces—geometry also regulates how external heat and airflow enter, persist, or dissipate, shaping the microclimatic conditions experienced by occupants.

From a methodological perspective, this implies that a purely climatic or statistical description of boundary conditions is insufficient for resilience assessment. While weather data define the external forcing, it is the three-dimensional form of the built environment that translates this forcing into spatially differentiated microclimates. Mean radiant temperature, in particular, is geometry-sensitive because it depends on surface temperatures, view factors, and the spatial distribution of shaded and sunlit areas. Since MRT is a dominant input in UTCI

computation under warm and hot conditions, neglecting geometric mediation risks misrepresenting both absolute stress levels and their spatial variability across open, semi-open, and indoor-adjacent domains.

Geometry also shapes airflow in a very concrete way. At pedestrian level and in semi-enclosed spaces, the orientation of streets, the proportions of canyons, and the porosity of building façades largely determine how wind enters a space, how it propagates through it, or whether it dissipates altogether. Openings, passages, and changes in section further modify these patterns, often producing localized accelerations or zones of reduced air movement. Under high temperature conditions, such differences become particularly relevant, as air movement may contribute to heat dissipation but can also increase thermal stress when incoming air is already warm. These interactions are highly site-specific and do not scale linearly with boundary climate data. As a consequence, the same meteorological forcing can result in markedly different UTCI values when applied to different geometric configurations, even within the same location and at the same moment in time.

For these reasons, explicit geometric representation is not a matter of visual realism, but a methodological necessity. In the framework developed, geometry functions as the mediator between climate boundary conditions and the microclimatic variables required for UTCI calculation across scales—urban, building, and component. Only by controlling and declaring the geometric configuration can thermal comfort variations be consistently attributed to design choices rather than to external climatic differences or modelling artefacts, ensuring coherent and reproducible comparative assessments of thermal resilience.

4.2.2 Model types and data sources

Three-dimensional geometry is not obtained in a uniform way across the different scales addressed in this work. In urban studies, usable models are often already available through public GIS datasets or open mapping platforms, while in other cases geometry has to be assembled from drawings, technical material, or direct surveys. This is particularly common at the building and component scale. As a consequence, models rarely enter the workflow with the same level of completeness or consistency, and their initial quality largely depends on the context in which they were produced.

For the purposes of this methodology, however, the origin of the model is not a discriminating factor. What matters is whether the geometry can be effectively handled within a common modelling and simulation workflow. Models developed in GIS, CAD, or BIM environments are therefore treated as equivalent, as long as they can be converted into formats that allow geometric manipulation, attribution of physical properties, and subsequent use within the selected simulation tools. The methodological focus is thus placed on interoperability rather than on the modelling paradigm itself.

This choice is intentional. By avoiding a dependency on a specific data source or modelling culture, the proposed framework remains applicable across different contexts, levels of detail, and research conditions. In a comparative assessment, differences in model provenance should not influence the results: a geometry reconstructed from open data, a simplified survey-based model, or a detailed design model should all support the same analytical steps, provided that they are processed in a consistent manner.

This does not imply that all models are expected to contain the same amount of geometric or semantic information. On the contrary, different scales and case studies naturally require different representations. What is preserved across all applications is the methodological backbone: a geometry that can be prepared, simplified when necessary, and integrated into a unified workflow. In this way, observed differences in thermal comfort and resilience can be traced back to spatial configuration and design choices, rather than to inconsistencies introduced by incompatible data sources or modelling environments.

4.2.3 Geometric resolution and material abstraction across scales

The proposed methodology relies on a three-dimensional digital model whose geometric resolution is adequate to represent the microclimatic phenomena relevant to the scale of analysis. Resolution is therefore not defined in absolute terms, but in relation to the physical processes that need to be captured. At the urban scale, a metric resolution is generally sufficient to describe building volumes, street canyons, and large shading patterns. At the building and component scale, finer resolutions are required to correctly represent façade articulation, openings, overhangs, and local airflow paths. The objective is not geometric

completeness, but the faithful representation of those spatial features that directly affect radiative exposure and air movement at the level of human experience.

This scale-dependent approach implies that geometric simplification is not only allowed, but methodologically necessary. Elements whose size or detail falls below the effective resolution of the simulation domain or the sampling grid do not contribute meaningfully to the assessment and may introduce unnecessary computational cost or numerical noise. Conversely, features that control shading, sky exposure, or ventilation must be preserved even when operating with otherwise simplified geometry. In this sense, the level of detail is defined by relevance rather than by formal accuracy.

In parallel with geometric resolution, a minimal attribution of material properties is required. Surfaces must be classified or parameterized in a way that allows the simulation tools to distinguish between different radiative and thermal behaviors. At a minimum, this includes the differentiation of ground surfaces, façades, and roofs, as well as the assignment of properties affecting albedo and thermal response. The aim is not to reproduce construction stratigraphies in detail, but to ensure that differences in surface behavior are consistently represented across variants and scenarios.

Vegetation is encoded when it plays a role in the microclimatic processes under investigation. Depending on the scale and on the selected toolchain, this may range from a simplified representation of shading elements to a more detailed modelling of evapotranspiration and canopy effects. When vegetation is not expected to influence the specific comfort mechanisms being assessed, it can be omitted without compromising the comparative logic of the methodology. This selective inclusion ensures coherence between model complexity and research objectives.

Geometric data and associated attributes can be managed through a variety of digital environments, including parametric modelling platforms, BIM systems, and 3D GIS workflows. These environments differ in the level of control they offer and in the effort required to modify geometry and attributes, particularly during early-stage exploration. Within the framework of this thesis, they are treated as interchangeable means to an end, as long as they support the attachment of data to geometry and the export of models into simulation-ready formats. This flexibility allows the methodology to be applied consistently across different case studies,

scales, and levels of design maturity, without binding the assessment to a specific modelling paradigm.

4.2.4 Pre-processing rules

In order for microclimatic simulations to produce comparable results, three-dimensional models require a preliminary phase of preparation. This phase addresses issues of consistency and numerical stability that are not always apparent at the modelling stage. If such aspects are left implicit, variations in thermal comfort outcomes may reflect geometric irregularities, misaligned reference systems, or scale-related problems, rather than the spatial configurations that the analysis is intended to evaluate. In a comparative framework, such effects would compromise the interpretability of results and undermine the attribution of UTCI variations to design choices.

Pre-processing operates as a bridge between geometric modelling and simulation. Its purpose is to translate heterogeneous source models—originating from GIS datasets, CAD/BIM environments, or reconstructed geometries—into a form that is coherent with the assumptions and limitations of the selected simulation tools. This includes the alignment of orientation and coordinate systems, the verification of scale, and the simplification of geometry in accordance with the effective resolution defined in the previous section. At this stage, simplification is not a loss of information, but a controlled reduction of detail that preserves those features influencing shading, radiative exchange, and airflow.

Equally important is the removal of geometric conditions that may introduce numerical instability. Non-manifold edges, duplicated surfaces, unintended overlaps, or discontinuities between adjacent elements can significantly affect simulation outputs, particularly in CFD-based workflows. Similarly, the explicit separation of ground, façade, roof, and vegetation elements is required to ensure that material and surface attributes are correctly interpreted by the simulation engines. These operations are common to all case studies presented and remain invariant across baseline and future scenarios, as well as across design variants.

To support rapid iteration and consistent handling of multiple configurations, parametric modelling is adopted as a practical backbone for pre-processing. A parametric environment allows geometry and associated data to be adjusted, replicated, and re-exported without

redefining the workflow at each iteration. Within this framework, simulation tools are treated as downstream components: climate data are coupled with enriched geometries for microclimate analyses, airflow is evaluated through CFD interfaces when required, and dedicated microclimate solvers are integrated where vegetation and surface–atmosphere exchanges must be resolved. The methodological focus, however, remains on the consistency of inputs rather than on the specific software employed.

Aspect	Requirement	Methodological rationale
Spatial reference and orientation	Model orientation and North direction explicitly defined and consistent across all variants and scenarios	Ensures that solar exposure, shading patterns, and wind direction are comparable and not affected by implicit rotations or reference mismatches
Coordinate system and scale	Coordinate system and model scale verified and consistent with climate data and simulation domain	Prevents distortions in distances, heights, and airflow paths that could bias microclimatic results
Geometric simplification	Geometry simplified in accordance with the effective resolution of the analysis scale and sampling domain	Avoids unnecessary computational complexity while preserving features that influence radiation and airflow
Topological consistency	Removal of non-manifold edges, duplicated surfaces, unintended overlaps, and open volumes where not required	Reduces numerical instability and artefacts in radiative and CFD-based simulations
Watertight volumes	Closed and watertight volumetric geometry for built elements, with no unintended openings or leaks	Ensures correct resolution of radiative exchange, airflow, and surface–atmosphere interactions, preventing numerical artefacts in MRT and CFD-based simulations
Surface normal orientation	Consistent orientation of surface normals, directed outward for enclosed volumes and toward the sky for exposed surfaces	Guarantees correct interpretation of radiative exposure, view factors, and sky–ground relationships in radiation and comfort calculations
Surface differentiation	Explicit separation of ground, façades, roofs, and other relevant surface types	Allows correct assignment and interpretation of material and boundary conditions by simulation engines
Vegetation handling	Vegetation included, abstracted, or omitted consistently with the research objective and selected toolchain	Ensures coherence between model complexity and the microclimatic processes under investigation
Material attribution	Minimal and consistent assignment of surface properties affecting radiative and thermal behavior	Guarantees that differences in results reflect spatial configuration rather than untracked material assumptions
Invariance across comparisons	Pre-processing rules applied identically across baseline, future scenarios, and design variants	Preserves the validity of comparative indicators such as ΔUTCI

Table 3. Pre-processing requirements defining the minimum conditions under which three-dimensional geometric models are considered simulation-ready within the proposed methodology. The listed aspects ensure internal consistency, numerical robustness, and comparability across baseline and future scenarios, as well as across design variants.

For clarity and replicability, the pre-processing requirements adopted in this study are summarized in Table 3. The checklist does not prescribe a specific modelling environment but

defines the minimum conditions that a three-dimensional model must satisfy in order to be considered simulation-ready within the proposed methodology.

4.3 Using UTCI for human-centered thermal assessment

The methodological framework developed in the previous sections defines the climatic forcing and the spatial conditions under which thermal phenomena occur. The present section introduces the layer through which these conditions are translated into human thermal experience, allowing microclimatic variations to be interpreted in terms of comfort and stress. By adopting a human-centered assessment perspective, the methodology establishes a direct link between environmental conditions and their effects at the scale of occupants and users. The thermal comfort metric is therefore treated as an integral component of the workflow, enabling consistent evaluation and comparison of thermal resilience across scenarios, configurations, and spatial scales.

4.3.1 Why UTCI: physiological model, applicability, comparability

The assessment of thermal comfort can rely on different indices, whose theoretical foundations, assumptions, and domains of applicability have been discussed in the previous chapters. Within this established framework, the present methodology requires an index that can be applied consistently across outdoor, transitional, and naturally ventilated indoor environments, and that remains robust when used for comparative analyses under changing climatic conditions. The adoption of UTCI is therefore driven by methodological requirements that are specific to the structure and objectives of this work, rather than by a general evaluation of available comfort indices.

A primary motivation for this choice lies in the underlying physiological model. UTCI is based on the multi-node thermophysiological model developed by Fiala, which represents heat exchange through differentiated body parts and layered mechanisms. This structure allows UTCI to respond in a detailed manner to combined variations in air temperature, radiation, wind, and humidity—variables that are strongly shaped by spatial configuration in the built environment. Indices such as PET, while also grounded in human energy balance models, rely

on more aggregated representations[477] and tend to be less responsive to localized variations in radiative and convective conditions[478]. Within a geometry-driven workflow, this difference becomes relevant, as the capacity to resolve spatial contrasts is central to the assessment.

The way behavioral adaptation is handled is another reason why UTCI is well suited to the contexts considered in this work. Instead of relying on fixed values of thermal insulation of clothing, UTCI incorporates a clothing model that adapts to environmental conditions. This becomes particularly relevant in outdoor and semi-outdoor situations, where thermal exposure may vary over short distances and where occupants respond continuously through small behavioral adjustments. Under these conditions, UTCI is better able to reflect spatial and temporal variations in thermal stress that arise from design-related changes in the built environment.

Beyond its role as a comfort metric, UTCI has also been widely employed in studies linking thermal stress to heat-related health outcomes. While the present work does not aim to establish direct epidemiological relationships, the adoption of an index that is compatible with health-oriented interpretations ensures conceptual coherence between the assessment of thermal comfort and its broader implications for human well-being. In this sense, UTCI supports a reading of thermal comfort that remains connected to human well-being without extending beyond the scope of environmental assessment.

Finally, comparability represents a key requirement for a multi-scalar and climate-change-oriented methodology. UTCI has been formulated and applied within a standardized framework that spans a wide range of climatic contexts, allowing results obtained under different conditions to be interpreted on a common basis. This consistency is essential for comparative assessments based on relative variations in thermal comfort, such as those developed here. The index is therefore employed within its established domain of applicability and under explicitly stated assumptions, which are discussed in the following sections and revisited when addressing the limitations of the proposed approach.

[477] Blazejczyk et al. 2012

[478] Blazejczyk et al. 2012

On this basis, UTCI is adopted throughout the thesis as the reference metric for thermal comfort assessment. The choice reflects its alignment with the physiological, spatial, and comparative requirements of the proposed methodology, rather than an implicit claim of universal superiority over alternative indices.

4.3.2 UTCI calculation inputs and standard assumptions

The computation of UTCI requires a limited but specific set of environmental variables, namely air temperature, humidity, wind speed, and a radiative term commonly expressed through mean radiant temperature (MRT). These variables jointly describe the thermal environment as experienced by the human body and form the input space within which the physiological model operates. In the context of this methodology, they are not treated as abstract descriptors, but as spatially and temporally resolved quantities derived from the interaction between climate forcing and the built environment.

To ensure internal consistency and comparability, UTCI inputs are evaluated over a clearly defined human-exposure-level domain and within a declared temporal window. The same sampling geometry and time reference are maintained across baseline and future scenarios, as well as across design variants. In addition, all input variables are produced through a single, explicitly stated toolchain. This constraint is methodological rather than technical: it ensures that differences in UTCI values can be attributed to changes in climate or spatial configuration, rather than to inconsistencies in data sources or modelling approaches.

Wind speed requires particular attention, as its definition follows meteorological conventions that do not coincide with the scale of human exposure. In UTCI formulation, wind speed is conventionally referenced at 10 m height, reflecting standard practice in weather observations. When wind conditions at human level are required for interpretation or post-processing, they are derived from the 10 m reference value using standard logarithmic profiles. This transformation is performed consistently across all simulations, and the associated assumptions on surface roughness are stated explicitly.

Radiative conditions are represented through mean radiant temperature, which integrates shortwave and longwave exchanges between the human body and its surroundings. MRT is computed from the spatial configuration, surface properties, and solar conditions resolved by

the simulation workflow, and it is evaluated at the same locations and time steps as the other UTCI inputs. Given its strong sensitivity to geometry, MRT plays a central role in linking the built environment to thermal comfort outcomes within the proposed framework.

By fixing the definition, spatial reference, and derivation of all UTCI inputs, the methodology establishes a stable basis for comparative assessment. In this context, standard assumptions are introduced to constrain modelling choices that are not the object of the analysis, so that relative differences in thermal comfort can be attributed to climate forcing and spatial configuration rather than to variations in input definition or processing. Standard assumptions are therefore intended to make explicit and replicable the conditions under which UTCI values are computed and compared.

4.3.3 Interpretation layer: categories vs continuous values

UTCI values can be interpreted either as continuous numerical quantities or through discrete stress categories. These two representations serve different purposes and operate at different levels of the assessment. In the context of this methodology, their roles are clearly separated in order to avoid ambiguity between analytical evaluation and interpretative communication.

For the purposes of thermal resilience assessment, the continuous representation of UTCI is essential. Continuous values preserve the full magnitude of thermal conditions and allow pointwise differences to be computed between baseline and future scenarios. This is a prerequisite for the definition of ΔUTCI, which constitutes the core metric adopted in this methodology. Any categorical discretization applied prior to comparison would introduce threshold effects and information loss, reducing the sensitivity of the analysis to gradual but spatially significant changes in thermal stress. For this reason, all calculations, spatial aggregations, and comparative indicators are based exclusively on continuous UTCI values.

UTCI categories are instead employed as an interpretative layer, applied only after the analytical phase. Stress classes provide a qualitative frame that supports the reading of results, particularly when discussing the practical implications of observed changes. Transitions across categories—for instance from moderate to strong heat stress—can help convey the significance of ΔUTCI patterns in terms that are meaningful beyond numerical values. In the

case studies presented in the following chapter, categories are therefore used to annotate and contextualize results, not to generate them.

This distinction is particularly important in a design-oriented and multi-scalar framework. At local scale, small numerical variations in UTCI may not immediately correspond to a category change, yet they can still be relevant when distributed over space or when accumulated under future climatic conditions. Conversely, categorical representations alone may overemphasize boundary effects and obscure spatial gradients that are central to the assessment of resilience. In this way, retaining continuous UTCI values for computation and reserving categories for interpretation, the methodology maintains both analytical precision and communicative clarity.

Accordingly, categorical UTCI classes are not used for ranking, threshold-based decision rules, or performance scoring. Their function is limited to supporting the discussion of results and facilitating dialogue with non-specialist audiences. This controlled use ensures consistency between the methodological framework and the analytical treatment adopted in the case studies, while avoiding the conflation of numerical assessment and interpretative representation.

4.4 Multi-scalar assessment workflow

Building on the definition of climate data and future scenarios, on the representation of the built environment through geometry and material attributes, and on the adoption of UTCI as a human-centered metric for outdoor thermal comfort, this section formalizes the assessment workflow adopted in the thesis. The workflow translates these elements into a coherent and replicable procedure for the comparative evaluation of thermal conditions across scenarios, physical configurations, and spatial scales. It structures the sequence of modelling, simulation, and post-processing operations through which UTCI is computed under current and future climatic conditions, and its variation is used to characterize thermal resilience. The workflow provides the methodological backbone that ensures continuity between the conceptual framework developed so far and its application in the multi-scalar case studies presented in the following chapter, explicitly defining inputs, microclimatic variable generation, and sampling and comparison procedures.

Within the methodological framework adopted, a limited set of terms plays a central role in structuring the comparative analysis across physical configurations, climate scenarios, and spatial scales. These terms define the objects being compared, the procedural structure through which simulations are carried out, and the spatial frame within which thermal comfort indicators are evaluated. Their meaning is fixed here to ensure internal consistency across the methodology and to support a clear and unambiguous interpretation of the results presented in the case studies.

In this context, the term *configuration* denotes a specific spatial arrangement of the built environment, defined prior to simulation and represented through a three-dimensional model with associated material and vegetation attributes. Configurations may correspond to existing territorial morphologies or to alternative geometric layouts, but they are always treated as fixed inputs within the assessment workflow. All configurations are evaluated under identical modelling assumptions, sampling procedures, and climate scenarios, so that differences in thermal performance can be attributed to differences in spatial and material characteristics rather than to changes in the simulation setup.

The term *workflow* refers to the structured methodological sequence through which input data are transformed into microclimatic variables and, subsequently, into UTCI values. It defines the coordinated operation of multiple software components acting together within a single procedural logic, including aligned data handoffs, solver settings, and temporal assumptions. The workflow, by abstracting from individual tools and focusing on their combined operation, provides a stable methodological structure that supports consistent implementation across different climate scenarios and spatial scales while preserving variable definitions, boundary conditions, and sampling conventions.

A further key concept is the *evaluation domain*. The evaluation domain defines the spatial or functional region within which UTCI and its variation are computed and interpreted. While the criteria used to define the evaluation domain remain invariant, its geometric instantiation may vary across configurations, provided that the same functional relevance and sampling logic are preserved. It is constructed to represent the portion of space relevant for human occupancy and exposure, typically at a height corresponding to human presence, and it includes a predefined sampling set that is reused consistently across simulations. In extended or large-domain models, the evaluation domain is identified as an inner subdomain embedded

within the larger computational grid. This inner region captures both direct and secondary microclimatic effects generated by the built environment and provides a stable spatial reference for comparative analysis across variants and scenarios.

Together, these definitions establish a shared reference framework for the assessment workflow. Configurations define what is compared, climate scenarios define the temporal dimension along which the comparison is performed, the workflow defines how simulations are carried out, and the evaluation domain defines where thermal comfort is measured. Their combined use ensures that the analysis remains internally coherent across urban, building, and component scales, and that the results presented in the following chapter can be interpreted within a single, consistent methodological structure.

4.4.1 Inputs and model setup: climate, geometry and materials

The first phase of the assessment workflow is articulated through three closely related setup operations, which together establish the complete set of inputs for the comparative analysis. This phase brings together climate data, the three-dimensional representation of the built environment, and the definition of the evaluation domain into a single, coherent setup. At this stage, the objective is to construct a simulation-ready configuration in which all elements that are not the subject of comparison are explicitly fixed, so that subsequent differences in thermal comfort can be interpreted within a stable and controlled analytical framework.

Climate inputs are introduced through the selection of baseline and future EPW files representing the climate scenarios adopted in the analysis. These files constitute the sole source of atmospheric boundary conditions for all subsequent simulations. Their role within the workflow is not descriptive but operational: EPW data provide the external forcing through which current and projected climatic conditions are applied to the same spatial configuration. Baseline and future files are therefore selected, verified, and paired consistently, ensuring that they can be used interchangeably within the same modelling environment and under the same temporal and spatial assumptions.

In parallel with the definition of climate inputs, the three-dimensional model of the built environment is prepared at the intended scale of analysis. Geometry, material attributes, and

vegetation elements are assembled and abstracted in accordance with the resolution required to capture the microclimatic processes relevant at that scale. The modelling effort focuses on representing those spatial features that directly mediate radiative exchange, airflow patterns, and surface–atmosphere interactions at human exposure level. Material and vegetation properties are assigned in a consistent manner across all design configurations, so that the model functions as a stable spatial mediator between climatic forcing and local microclimatic response.

A further component of the setup phase is the definition of the evaluation domain. The evaluation domain identifies the spatial region within which microclimatic variables and UTCI values will be sampled and compared. It is defined in conjunction with the geometry and scale of the model, and it is constructed to include both direct effects generated by local spatial features and secondary effects arising from their interaction with the surrounding environment. Where large computational domains are required, the evaluation domain is delineated as an inner region within the overall model extent, providing a consistent spatial reference for analysis across scenarios and configurations.

At the end of this setup phase, all elements required for the subsequent simulations are fixed and carried forward without further modification. Climate forcing is defined through the selected pair of scenario-specific EPW files, the built environment is represented by a three-dimensional model prepared at the appropriate scale with its associated material and vegetation attributes, and the spatial frame of analysis is established through the declared evaluation domain and its sampling geometry. Taken together, these components constitute the reference configuration upon which microclimatic simulations are performed and against which comparative assessments are developed.

The composition of this initial configuration is documented in a compact and explicit manner, recording the input files, the essential metadata associated with them, and the state of the model at the conclusion of the setup process. This documentation supports consistent reconstruction of the workflow across case studies and maintains continuity between the definition of inputs and the simulation stages that follow.

4.4.2 Microclimate simulation: variables and engines

The second phase of the workflow addresses the simulation of local microclimatic conditions required for UTCI computation. At this stage, the climatic forcing associated with each scenario is applied to the previously defined spatial configuration, and the interaction between atmospheric conditions and the built environment is resolved through microclimate simulation. The purpose of this phase is to translate scenario-specific climate inputs into spatially differentiated environmental variables that reflect the influence of geometry, materials, vegetation, and airflow at human exposure level.

Across the workflow, climatic boundary conditions are introduced consistently for each scenario and applied to each spatial configuration under identical modelling assumptions. In this way, microclimatic differences observed across scenarios capture the effect of changing climatic forcing under constant spatial conditions, whereas differences observed across configurations reflect differences in spatial and material inputs under the same climatic scenario.

The set of environmental variables produced in this phase includes air temperature, relative humidity, wind speed, and a radiative term suitable for UTCI calculation. Radiative conditions may be obtained either directly as mean radiant temperature or through the resolution of its contributing shortwave and longwave components, depending on the modelling approach adopted. In all cases, the workflow requires that radiative conditions be defined and evaluated in a consistent manner across scenarios and configurations within a given application, so that resulting UTCI values remain directly comparable.

Once the microclimatic fields have been resolved, a subsequent step of the workflow concerns the extraction and organization of the variables required for UTCI computation. All microclimatic variables are evaluated at the predefined sampling locations within the evaluation domain and at the temporal resolution selected for the analysis. The workflow ensures that the microclimatic conditions used for UTCI computation are representative of the applied climatic forcing and of the modelled environment, so that evaluated variables reflect physically meaningful states suitable for comparative assessment.

Throughout this phase, a clear separation is maintained between climatic forcing, which varies across scenarios, and spatial configuration, which varies across morphological

differences. Simulation settings, variable definitions, and sampling conventions are fixed within each application of the workflow, providing a stable basis for the generation of microclimatic fields. This phase produces the physical inputs required for UTCI computation resolving air, humidity, wind, and radiative conditions in an internally consistent and scale-appropriate manner, and is addressed in the subsequent step.

4.4.3 UTCI computation and spatial sampling

This step of the workflow concerns the computation of UTCI and the spatial framework through which thermal comfort is evaluated. At this stage, the microclimatic variables produced by the simulation phase are combined to derive UTCI values at a defined set of locations within the evaluation domain. This step establishes the explicit correspondence between the simulated physical environment and the human-centered metric adopted for the assessment.

Spatial sampling is treated as a methodological decision rather than as a purely technical setting. Sampling strategies may take different forms—such as regular grids, path-based sensor arrays, or surface-oriented sampling—depending on the scale of analysis and on the spatial characteristics of the environment under investigation. Sampling height is fixed at a human-relevant level, while sampling resolution is selected to reflect the expected spatial variability of thermal conditions. Sampling resolution is selected in relation to the expected spatial variability of the microclimatic fields that influence UTCI. Contexts in which radiative exposure and airflow patterns vary gradually over space can be represented using coarser sampling, whereas environments characterized by frequent transitions between sun and shade, strong geometric control of air movement, or highly localized thermal conditions require finer spatial resolution in order to capture meaningful differences in UTCI.

Once the sampling geometry has been defined, it is kept invariant throughout the assessment. The same spatial locations are used to compute UTCI values across all physical configurations and across all climate scenarios, ensuring that comparisons are performed point by point within a common spatial reference. This invariance is central to the interpretation of local differences and provides the basis for the subsequent computation of ΔUTCI, which relies on paired comparisons at identical locations within the evaluation domain.

UTCI values are computed using a consistent set of input variables and assumptions across the workflow. Air temperature, humidity, wind speed, and radiative conditions are combined according to the standard UTCI formulation, and each computed value is unambiguously associated with its corresponding sampling coordinate. In each application of the workflow, the spatial sampling framework adopted for UTCI computation is described explicitly within the methodological narrative, so that sampling choices are transparent and can be replicated under the same assumptions.

4.4.4 Post-processing and outputs: maps, statistics and comparability

Following the computation of UTCI over the selected evaluation domains, the workflow produces a set of outputs explicitly structured to support comparative analysis. Post-processing organizes the computed data into representations that preserve spatial meaning, allow aggregation across time, and maintain a stable interpretative framework across all evaluated configurations.

The core outputs of the workflow are spatially explicit UTCI fields. These fields retain the geometric correspondence between the evaluation domain and the thermal conditions defined over it, allowing thermal stress to be interpreted as a spatial phenomenon. By expressing UTCI as a continuous field rather than as a collection of discrete values, the workflow captures gradients, clusters, and spatial contrasts that are essential for understanding how thermal conditions are distributed within the evaluated space.

From these fields, spatial representations are derived in the form of maps that share a common spatial reference and scale. The use of consistent spatial resolution and value ranges ensures that each map conveys the same type of information, regardless of the specific configuration being evaluated. Maps thus function as directly comparable representations, in which differences reflect changes in thermal conditions rather than differences in representation or processing.

In parallel, the workflow derives statistical descriptors that summarize the UTCI fields while preserving their link to the underlying spatial data. These descriptors characterize thermal conditions through distributional properties and class-based frequencies computed over predefined UTCI categories. Temporal aggregation follows a fixed logic, applied uniformly

across all variants, so that statistical summaries remain aligned in both temporal scope and semantic meaning.

Comparability across configurations is established through the joint use of spatial fields and statistical descriptors generated under invariant rules. Each output is defined using the same spatial framework, temporal reference, and classification structure, creating a stable analytical space in which results can be juxtaposed without additional transformation. In this way, post-processing functions as the stage at which heterogeneous simulation outputs are consolidated into a coherent and comparable set of evidence, forming the basis for subsequent interpretation and synthesis.

4.4.5 Computational framework

The workflow formalized in this chapter is implemented within a single computational framework that constitutes the operational core of the methodology. This framework is provided by Grasshopper [479], embedded within Rhinoceros [480], and functions as the environment in which the entire assessment process is defined, executed, and controlled. All stages of the workflow—geometric construction, configurations setup, mathematical and logical operations, simulation orchestration, data exchange, post-processing, and output synthesis—are carried out within this shared computational space.

Within this context, Grasshopper does not serve as a connector between external tools, but as the place where the methodological logic is explicitly encoded. Simulation engines, comfort models, and data-processing environments are invoked as specialized executors whose inputs are prepared parametrically and whose outputs are reabsorbed into the same computational context. This organization enables simulation results to be treated as intermediate data objects that can be transformed, aggregated, and recombined within the workflow, rather than as terminal products of isolated analyses.

The generation of microclimatic variables required for UTCI computation is supported through alternative modelling pathways that are activated in relation to dominant physical

[479] Robert McNeel & Associates, 2023.
[480] Ibid.

processes and scale conditions. When vegetation and evapotranspirative mechanisms play a determining role in outdoor thermal comfort, the workflow employs ENVI-met[481]. In this pathway, thermal comfort emerges from the interaction between plant canopies, soil moisture, radiative exchange, humidity, and airflow. ENVI-met is used for its capacity to represent these coupled surface–atmosphere processes at pedestrian level within a single modelling environment. Its integration into the computational framework is achieved through Morpho[482], which enables the parametric generation of simulation inputs, including geometry and boundary conditions, the execution of simulations, and the retrieval of result fields directly within Grasshopper. Through this bidirectional integration, ENVI-met operates as a native component of the workflow rather than as an external simulation step.

A second modelling pathway is adopted when vegetation does not constitute a primary driver of thermal comfort and when the assessment benefits from a configuration that is more detailed in architectural and component scales. In this pathway, Ladybug Tools[483] provides the framework for associating climatic inputs with geometry and for computing UTCI through a standardized and transparent formulation. Airflow is represented through a CFD solver that is compatible with Grasshopper and capable of producing spatially resolved, point-based outputs aligned with the sampling grids used for comfort evaluation. Within this methodological framework, Eddy3D[484] represents one such implementation, while other Grasshopper-compatible CFD environments can fulfil the same role provided they support equivalent probing-point or sampling strategies and return results in a form that can be reintegrated into the workflow.

Across both modelling pathways, simulation engines operate in the background of the computational framework. Radiative and thermodynamic calculations invoked through Ladybug Tools rely on established engines such as Radiance[485] and EnergyPlus, while CFD-based airflow simulations rely on solvers such as OpenFOAM[486]. These engines are not exposed directly at the methodological level; instead, they are called through interfaces that ensure consistent input preparation, execution control, and result handling within

[481] ENVI-met, 2023.
[482] https://github.com/AntonelloDN/Morpho.
[483] Ladybug Tools, 2023.
[484] Kastner et al. 2021.
[485] https://github.com/ladybug-tools/honeybee-radiance
[486] Chen et al., 2014

Grasshopper. This separation allows the workflow to benefit from validated simulation engines while maintaining a single, coherent operational logic.

Post-processing and result synthesis are likewise handled within the computational framework. Spatial outputs generated by simulations are mapped onto the evaluation domain and processed using the mathematical, logical, and data-management components available in Grasshopper. Statistical descriptors—such as distributional measures, frequency-based indicators, and aggregated metrics—can be computed directly within the parametric environment. Where tabular processing and graphical reporting are advantageous, external spreadsheet environments can be connected to Grasshopper through dedicated interfaces, allowing them to function as integrated components of the workflow. In this configuration, statistical analysis and visualization are treated as computational steps governed by the same procedural logic as modelling and simulation.

The evaluation domain and its associated sampling structure constitute the invariant interface across all operations. Regardless of the modelling pathway or simulation engine employed, microclimatic variables and comfort indicators are computed at identical spatial locations, aggregated according to declared temporal rules, and translated into outputs with stable semantic meaning. By grounding all operations within a single computational framework, the workflow ensures that differences between configurations arise from changes in spatial layout or boundary conditions, while the structure of the assessment remains constant and replicable.

4.5 UTCI variations as a metric for thermal resilience

At this stage, the methodological framework converges toward the definition of a synthetic criterion for comparative evaluation. Thermal fields generated across climatic conditions and spatial domains are interpreted through their relative variation, allowing differences in thermal response to be expressed in a compact and analytically tractable form. The change in UTCI under altered boundary conditions reframes thermal performance as a property emerging from the interaction between climate forcing and built configuration. Thermal resilience is thus articulated as a measurable attribute, suitable for consistent comparison across spatial arrangements, scales, and environmental settings.

4.5.1 Formal definition of ΔUTCI and resilience proxy

Within the methodological framework defined in this chapter, thermal resilience is assessed through the sensitivity of human thermal stress to a change in climatic boundary conditions, while the built configuration and the modelling framework are kept invariant. Thermal sensitivity is expressed through changes in the Universal Thermal Climate Index (UTCI) observed when the same spatial configuration is subjected to different climatic boundary conditions, evaluated at matched locations and times.

$UTCI_{cur}(x,t)$ and $UTCI_{fut}(x,t)$ identify the index values computed at the same spatial coordinates x and time step t, under baseline and future climatic conditions respectively. The underlying model geometry, the evaluation domain, and the computational workflow remain unchanged across these runs; climatic forcing is the only element that varies. The local thermal variation is then defined as:

$$\Delta UTCI(x,t) = UTCI_{fut}(x,t) - UTCI_{cur}(x,t)$$

This formulation yields a spatially and temporally resolved field that directly quantifies the change in thermal stress induced by altered climatic forcing. The sign of ΔUTCI retains physical meaning: positive values indicate an increase in thermal stress, while negative values indicate a reduction under identical interpretative conventions.

In this work, thermal resilience is operationalized through the capacity of a built configuration to limit the magnitude of ΔUTCI when exposed to future climatic conditions. Lower ΔUTCI values correspond to a more stable thermal response, indicating a reduced amplification of thermal stress under warming scenarios. Throughout the thesis, ΔUTCI is consistently reported as the difference between future and baseline conditions, establishing a common reference direction for comparison. Under projected warming, positive values are therefore expected and constitute the primary quantity against which relative performance is evaluated.

This differential formulation isolates the response of the built environment to changing climatic forcing from the absolute severity of background conditions. Thermal resilience can thus be expressed as a measurable and comparable attribute across spatial configurations, analytical scales, and environmental settings within a unified methodological framework.

4.5.2 Aggregation rules across space and time

The ΔUTCI field provides a spatially and temporally resolved description of thermal variation, whose interpretability depends on the adoption of explicit aggregation conventions. Comparison is therefore conducted through a controlled reduction of this field, designed to preserve both intensity and spatial structure while enabling consistent evaluation across configurations and climatic conditions.

Spatial aggregation is performed over the evaluation domain defined earlier in the chapter. The same set of sampling locations is retained across all simulations, ensuring that each aggregated value reflects differences in thermal response rather than changes in spatial reference. Temporal aggregation follows a fixed analytical window associated with peak summer conditions, selected to represent the period of maximum thermal load. Within this window, evaluation is anchored to a single reporting time after an appropriate spin-up period, so that transient effects related to initial conditions do not influence the comparison.

Within this framework, a compact set of comparative indicators is derived from the aggregated ΔUTCI field. The mean value over the evaluation domain captures the overall magnitude of thermal variation. Minimum and maximum values document the extent of peak behavior, providing information on localized amplification or mitigation of thermal stress. In parallel, the frequency distribution of ΔUTCI across the sampled points describes how thermal variation is spatially distributed, revealing whether changes are concentrated or diffuse. Considered together, these indicators support a reading of thermal resilience that accounts for both the intensity of change and its spatial articulation, without multiplying metrics beyond what is necessary for interpretation.

All aggregation choices are treated as methodological declarations rather than as adjustable parameters. The temporal reference, the wind representation adopted in the simulations, and the spatial sampling resolution are fixed and explicitly reported for each application of the workflow. Distribution plots are generated using the same point set employed for spatial mapping, maintaining coherence between statistical summaries and spatial representations. When multiple future climate horizons are considered, the indicator set can be computed

independently for each horizon, allowing relative performance to be examined as climatic severity increases.

4.5.3 Ranking and decision logic

Comparative outputs are interpreted through a ranking logic that translates aggregated ΔUTCI indicators into an ordered assessment of relative thermal resilience. The ordering is grounded in a primary measure of overall response, expressed by the mean ΔUTCI computed over the evaluation domain, which captures the dominant tendency of each configuration under altered climatic conditions.

This global reading is complemented by an explicit control of localized behavior. Maximum ΔUTCI values, together with the upper portion of the distribution, are examined to identify configurations in which an apparent improvement in average conditions coincides with the emergence of concentrated zones of elevated thermal stress. Such outcomes are not considered indicative of robust resilience, as they imply a redistribution rather than a mitigation of thermal burden.

When configurations exhibit comparable mean responses, attention shifts to the structure of the ΔUTCI distribution. A systematic shift toward lower values and a reduction in dispersion are interpreted as signs of a more homogeneous thermal response across the evaluated space. In this context, homogeneity is treated as a desirable property, reflecting a reduced sensitivity to localized amplification effects and a more stable performance under climatic forcing.

Through this layered reading, ranking emerges as a synthesis of magnitude, extremal behavior, and spatial consistency. The decision logic does not introduce additional metrics beyond those already defined, but articulates their combined interpretation into a coherent and reproducible ordering of relative performance.

4.5.4 Visualization protocol and reporting standards

The reporting of thermal resilience relies on a visualization protocol that combines spatial representations and statistical summaries within a unified analytical framework. Maps and

charts convey different but convergent aspects of the same dataset and are produced under shared assumptions, allowing spatial patterns and quantitative indicators to be interpreted as parts of a single comparative structure.

UTCI and ΔUTCI fields are associated with the three-dimensional model and rendered in plan views that preserve their spatial relationship with the evaluation domain. Statistical representations are generated from the identical set of sampled points, maintaining full correspondence between mapped patterns and numerical summaries. This alignment ensures that spatial gradients, localized effects, and overall tendencies are read consistently across visual and statistical outputs.

A set of fixed reporting conventions governs all visual material. Units, color scales, and legend ranges are held constant across comparative maps, and results are extracted at an identical reporting time. Summary statistics, including minimum, mean, and maximum ΔUTCI values, accompany each spatial representation together with the corresponding distribution plot. The joint presentation establishes a stable interpretative context and supports transparent comparison across configurations and climatic conditions.

A standardized figure structure is defined within the assessment framework to implement this visualization protocol. The combined use of baseline UTCI, future UTCI, the corresponding ΔUTCI map rendered with a fixed scale, and the associated distribution plot establishes a consistent visual grammar for comparative analysis. This structure ensures that spatial patterns, statistical summaries, and relative variations are interpreted under invariant representational conditions, independent of the specific configuration or climatic forcing being examined.

4.5.5 Limitations of ΔUTCI as resilience proxy

The adoption of ΔUTCI as a proxy for thermal resilience is grounded in a comparative reading of thermal stress under changing climatic boundary conditions. Its interpretative strength lies in the controlled evaluation of relative differences, while its scope is defined by a set of assumptions that shape how results should be understood. These conditions do not undermine the analytical value of the proxy, but delineate the domain within which comparisons remain meaningful and internally consistent.

A first group of limitations concerns the temporal framing of the assessment. ΔUTCI is evaluated within a specific analysis window and at a fixed reporting time corresponding to peak thermal load. This choice focuses the assessment on moments when resilience mechanisms are most critical, allowing differences between configurations to emerge clearly under demanding conditions. At the same time, it implies that the proxy characterizes sensitivity to extreme thermal forcing rather than long-term or averaged comfort conditions. Temporal choices are therefore treated as part of the analytical framing and are applied identically across all comparisons.

A second group of limitations relates to the representation of future climatic forcing. Weather-file morphing techniques embed uncertainty associated with climate projections, scenario assumptions, and statistical downscaling. In the adopted workflow, future EPW files generated with Meteonorm modify temperature, humidity, and radiative components while retaining baseline wind-speed values. This implies that potential long-term changes in large-scale wind regimes are not represented in the climatic forcing. Within a comparative framework, however, this assumption affects absolute comfort levels more than relative differences, as wind conditions remain invariant between baseline and future simulations. Local airflow patterns, shaped by geometry and spatial configuration, continue to differentiate the microclimatic response across configurations, preserving the internal coherence of ΔUTCI-based comparisons.

Additional limitations arise from the numerical representation of microclimatic processes. Airflow, radiation, and vegetation effects are resolved through models that rely on simplified physical formulations and parameterizations. Results are therefore sensitive to assumptions regarding wind boundary conditions, vegetation abstraction, radiative exchange, and spatial resolution. In the proposed methodology, these aspects are treated as controlled modelling choices: once defined, they are held constant across baseline and future scenarios as well as across all compared configurations. This procedural invariance constrains the influence of modelling uncertainty on comparative outcomes.

The use of UTCI as a human-centered index introduces further conditions of validity. UTCI represents thermal stress for a standardized reference subject under quasi-stationary conditions, incorporating limited behavioral adaptation and no long-term acclimatization. These characteristics shape the interpretation of absolute values but remain consistent across

all simulations. When applied to ΔUTCI, they allow relative changes in thermal stress to be interpreted coherently, even if individual perception or adaptive capacity is not explicitly modelled.

Taken together, these considerations define the analytical status of ΔUTCI within the thesis. The proxy supports a structured comparison of how different spatial configurations respond to altered climatic forcing under shared and explicitly stated assumptions. Its role is not to predict future comfort conditions in a deterministic sense, but to enable robust ranking and interpretation of relative thermal resilience within a controlled methodological framework.

5 Multi-scalar case studies

In order to test the illustrated methodology, three case studies,[487] based on different spatial scales, have been selected. For each of them, morphological configurations have been generated and compared under two temporal scenarios in order to assess their thermal-comfort resilience to climate change through the variation of the UTCI.

The first case study investigates the climate resilience of the municipal territory of Sassuolo (MO) at the urban meso-scale; the second focuses on the internal cloister of the Convent of San Sepolcro in Parma, corresponding to the building scale; the third analyzes selected façades of a new railway station in Xirbi (CL), representative of the building component scale.

For each case study, two reference climatological scenarios were considered: a current scenario based on historical weather data, and a future scenario selected to ensure a significant climatic delta for the specific scale and context under investigation. The future horizon corresponds to 2050 for the urban-scale case studies in Sassuolo and Xirbi, and to 2080 for the building-scale case study in Parma, reflecting differences in climatic sensitivity and response times across scales while remaining consistent with the same emissions pathway.

In both scenarios, three-dimensional models were prepared in Rhinoceros format and UTCI was computed for different configurations of the built environment, either as-existing or generated ad hoc by varying the morphological setup. Across all case studies, the analysis follows a consistent structure: for each scale, UTCI-based thermal comfort is assessed under baseline and future conditions, and the discussion focuses on the variation between scenarios rather than on absolute comfort values. To support a trans-scalar reading, the discussion of each case study concludes with a summary table that compares baseline and future UTCI conditions for each scale, making explicit how the same methodological framework can be interpreted coherently from the urban to the component level.

[487] The three case studies have been taken from real research assignments received from the Department of Architecture and Urban Planning of the University of Parma. Working group: Emanuele Naboni, Barbara Gherri, Marcello Turrini.

5.1 Urban scale: the city of Sassuolo and its districts

As discussed above, the global characteristics of climate change manifest differently by location: overheating is greater over land and at high latitudes. Furthermore, on land, they change further depending on geographical location. The present case study[488] is located at Sassuolo, Emilia Romagna Region, in Italy and aims to assess the behavior of climate change at the hyperlocal scale and evaluate the resilience of the built environment at the meso-scale according to territorial configurations[489].

5.1.1 Climate scenarios in Sassuolo.

Sassuolo is located in the Po Valley, Italy's largest plain, bordered by the Alps to the north, the Apennines to the south and west, and the Adriatic Sea to the east. Its municipal territory falls within the pre-Apennine belt, and its climate is humid subtropical, characterized by hot summers and cool winters, with frequent rainfall throughout the year.

For future scenario, the year 2050 with the IPCC scenario RCP 8.5 has been chosen. According to the climate projections, the increase in air temperature will lead to more frequent heat waves and extreme weather events, such as heavy rains and droughts. At a finer granularity, the air temperature increase to 2050 is reported in Figure 7.

As shown by the data, the increase in air temperature occurs mainly through concentrated heatwaves in January and in intermediate seasons (autumn and spring), while summer warming is more uniform, with a marked intensification in August during both day and night. This is critical because it prevents night cooling, confirming the topicalization of the climate.

[488] The opportunity to test the UTCI variations at meso-scale occurred as a consequence of a research project assigned to the Department of Engineering and Architecture by the industrial group IRIS Ceramica.

[489] The study has been published in the paper Chapter 39 Simulating Localized Delta Temperatures: A Methodology Workflow for Addressing the Hyperlocal Impacts of Climate Change (Emanuele Naboni, Marcello Turrini, and Barbara Gherri) https://doi.org/10.1007/978-981-99-8501-2_39

Apart from a few sporadic decreases in air temperature, mainly due to different cloudiness, peak increases of up to 8 °C are noted, resulting in air temperatures of up to over 40 °C for periods of several consecutive hours, repeated over several days.

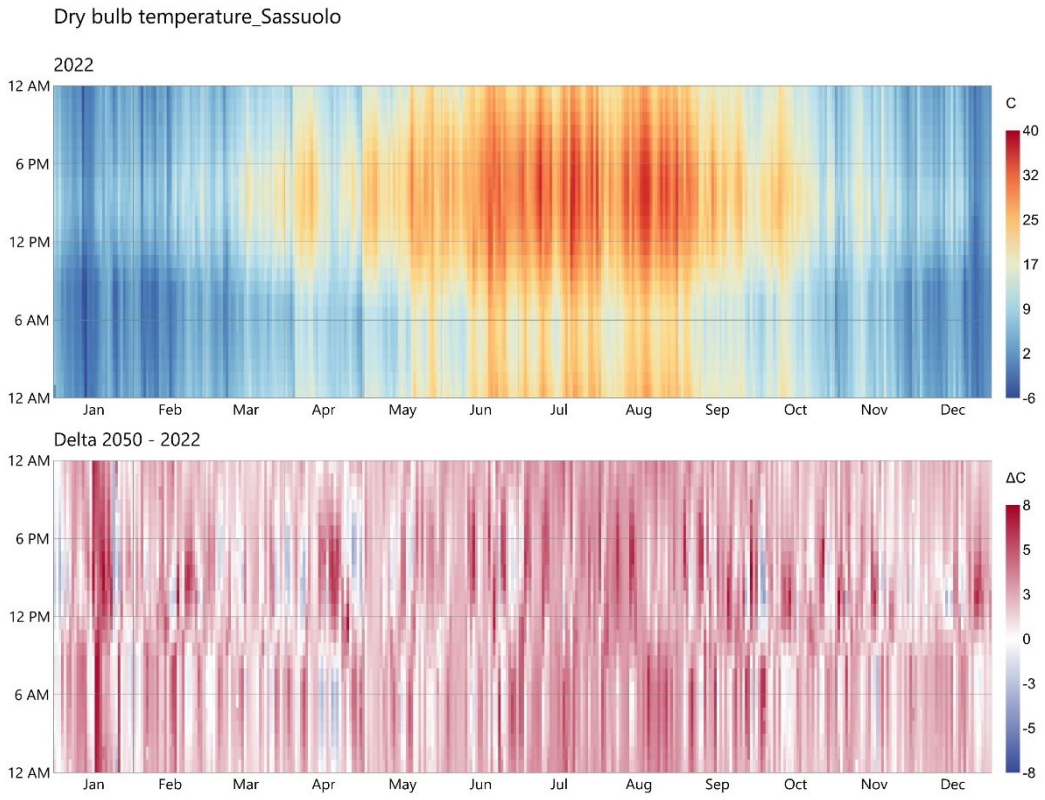

Figure 1. Hourly Heat Maps on air temperature. Sassuolo 2022, and Δ. There will be hours with temperatures increase higher than 8°C, in summer, bringing to a maximum of about 46°C, which is not happening in the current period. Chart made with Grasshopper and ladybug by the author. Copyright: Marcello Turrini, Emanuele Naboni, 2023

5.1.2 Identification of Configurations

Five homogeneous areas representative of the municipal territory of Sassuolo were identified, each defined as a 400 m × 400 m square. Each area represents a configuration to be used for the evaluation of UTCI variations. Figure 8 shows the location of the 5 configurations.

Figure 8. Sassuolo district and 5 selected configurations. UP_1-historical urban fabric. UP_2-modern urban fabric. UP_3-industrial area. UP_4-natural area. UP_5-agricultural area. Copyright: Marcello Turrini, Emanuele Naboni, Barbara Gherri 2022

Configuration UP_1-Historical urban fabric is representative of the historic center, with a compact urban fabric. The main open spaces are the central square, in the center of the area, and the large Piazza Martiri Partigiani on the west side. The Roman urban layout can be recognized, with the Cardo and Decumanus intersecting in the central square and dividing the entire area into four quadrants. There are narrow alleys in the north-south and east-west directions, and also two tree-lined avenues on the east side. The buildings are grouped mainly in blocks with inner courtyards. In the north-eastern part there are some less dense areas and open spaces treated with greenery. The buildings are mostly of load-bearing brick masonry and in the south-eastern part there are modern buildings with a reinforced concrete structure. The load bearing brick structure buildings are not thermically insulated, while the modern reinforced concrete structured ones can be both uninsulated and insulated with outer insulation layer. The pavements of open spaces are made of stone material and asphalt. Figure 9 on the left is a zoomed-in orthophoto map of the area.

Figure 9. On the left: Configuration UP_1-Historical urban fabric. On the right: Configuration UP_2-Modern urban fabric Source: Google Maps

Configuration UP_2-Modern urban fabric. is representative of the modern development of the city, with a lower density urban fabric. The buildings are isolated and arranged on a main north-south grid. In the center of the area there is a huge social building surrounded by open areas that are partially covered with trees and have permeable pavement as well as asphalt. In the north part of the area there is a park, partly covered with trees, with a meadow as pavement. There are many open spaces, due to the building sprawl. In the Figure 9 on the right is a zoomed-in orthophoto map of the area.

Configuration UP_3-Industrial area is located in the northern part of the municipal area. This configuration represents the typical industrial fabric of Sassuolo. It is characterized by large open spaces paved with asphalt on which are placed large industrial warehouses made of prefabricated reinforced concrete. There are a few small green areas with a few trees shading limited parts of the open space. In the Figure 10 on the left is a zoomed-in orthophoto map of the area.

Configuration UP_4-Natural area. This area includes part of the river Secchia and its immediate surroundings. Here the territory is characterized by a strong presence of natural elements, such as the river water, dense woodland on the left side of the river and some green glades on the right side. At this point, the river is crossed by a bridge and there is a small dam

that regulates the flow of the water. In the Figure 10 on the right is a zoomed-in orthophoto map of the area.

Figure 10. On the left: Configuration UP_3-Industrial area. On the right: Configuration UP_4-Natural area. Source: Google Maps

Configuration UP_5-Agricltural area. This homogeneous portion of land includes a piece of agricultural area. It is characterized by an almost total absence of shading elements. There are agricultural plots cultivated with different types of crops. A large asphalt road cuts the area in two, while a few small groups of rural houses are present in the western part. A paved parking area is present in the south-west part. In the Figure 11 is a zoomed-in orthophoto map of the area.

Figure 11. Configuration UP_5 - Agricultural area. Source: Google Maps

5.1.3 Processing of three-dimensional digital models

After the five configurations were identified, the three-dimensional models were derived in Rhinoceros (.3dm) format using the database available in the GIS portal of the Emilia Romagna Region[490]. From the portal it is possible to download vector files in .dxf format containing the simplified basic geometry of the buildings and additional information about elevation data and land use. The three-dimensional .dxf format can be fully imported into Rhinoceros without loss of information and quality.

After collecting the raw three-dimensional data for all five configurations, trees were positioned following visual cues taken directly from the orthophoto maps available on Google Maps. Trees were represented as simplified “lollipop” elements, consisting of a cylindrical trunk and an ellipsoidal crown. Given the analysis scale, tree sizes were not differentiated; a single tree model was used for all instances. A total height of 15 m, a crown diameter of 9 m, and a crown height of 11 m were assumed.

Pavements were then differentiated by material, using Google Maps Street View for each configuration. Depending on the configuration, material differentiation was simplified by

[490] https://geoportale.regione.emilia-romagna.it/download/download-data

grouping surfaces into asphalt, stone pavement, inner courtyard areas, permeable green pavements, water, and two types of agricultural crops.

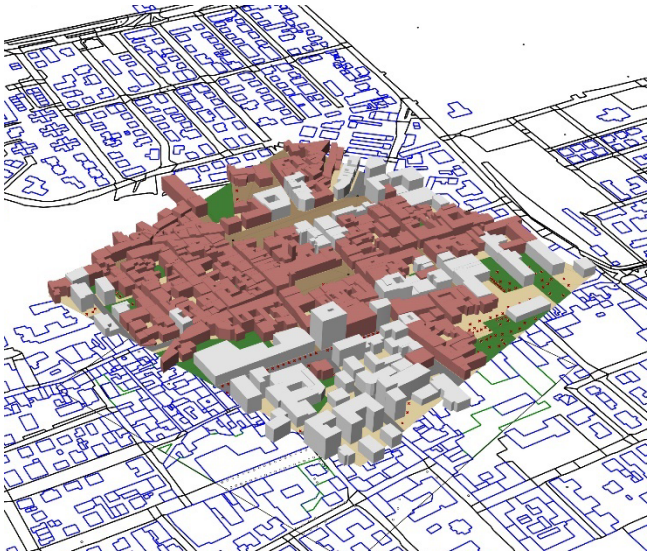

Figure 12. Building 3D models with Rhinoceros. Additional information was added to the GIS models, including tree positions (as point markers) and a material-based distinction between pavements and exterior building walls. Source: GIS database of Emilia Romagna Region, elaborated with Rhinoceros 3D. Copyright: Marcello Turrini, Emanuele Naboni, Barbara Gherri 2022

The buildings are differentiated by structural type, since, as seen in the chapter on the outdoor energy balance, the presence of exposed thermal masses or external insulation, as well as the color of the outermost layer, have an impact on the microclimate of open spaces. The distinction was made by proceeding by sight on Google Maps Street View, considering that the possibility of bias due to localized errors of interpretation would not alter the investigation of the entire configuration. Therefore, the masonry was distinguished into non-insulated load-bearing walls, non-insulated infills, isolated infills of renovated buildings, isolated infills of new buildings, residential prefabricated walls, and industrial prefabricated walls. Roofs structures are modelled as uninsulated reinforced concrete slabs, insulated reinforced concrete slabs and roofs with tiles.

In the pictures below, the complete three-dimensional models are shown, where the distinctions between the different floors can be recognized. Buildings were represented in a simplified manner while preserving their heights and retaining internal courtyards. The flooring materials are clearly separated, simplifying the details.

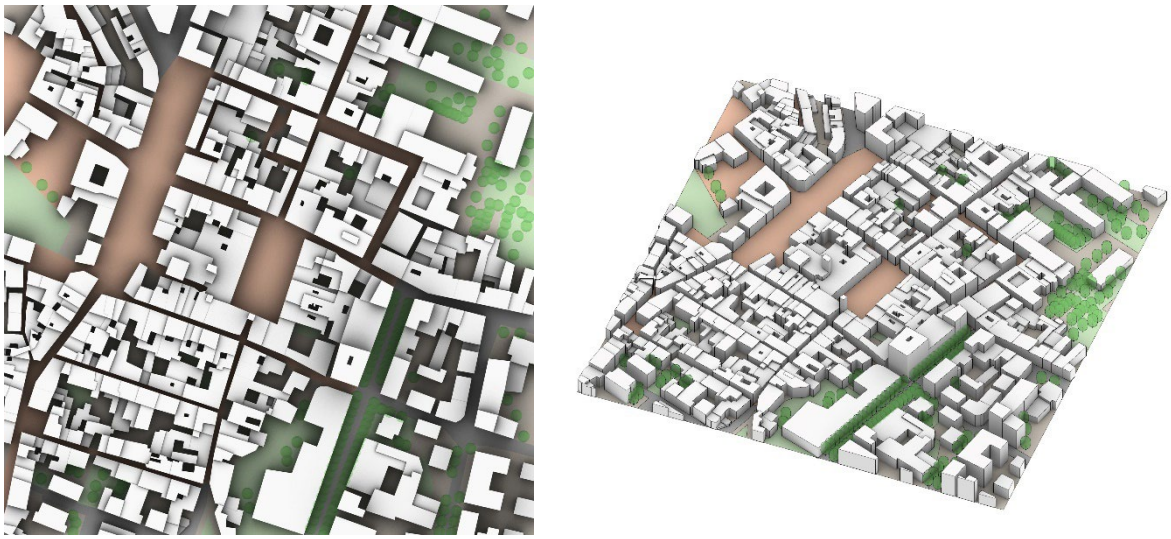

Figure 13. UP-1. Historical urban fabric. 3D model via Rhinoceros 3D. Copyright: Marcello Turrini, Emanuele Naboni, Barbara Gherri 2022

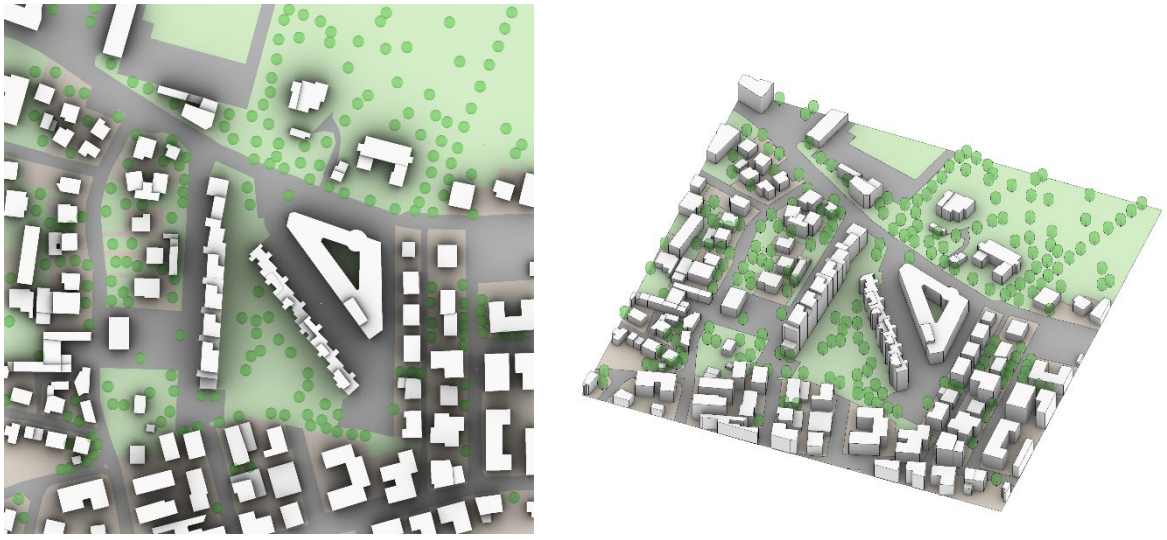

Figure 14. UP-2. Modern urban fabric. 3D model via Rhinoceros 3D. Copyright: Marcello Turrini, Emanuele Naboni, Barbara Gherri 2022

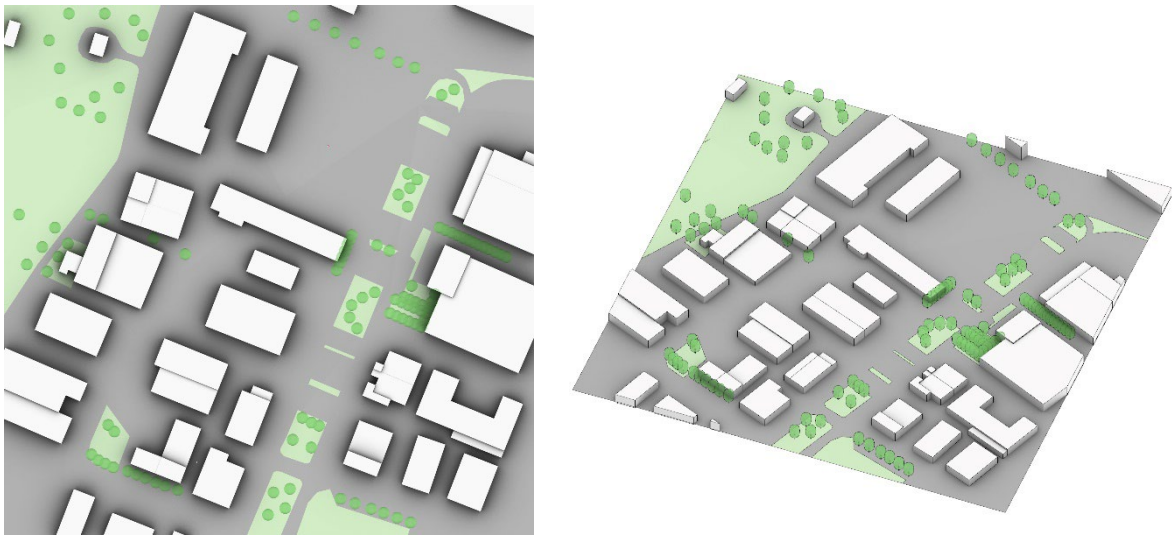

Figure 15. UP-3. Industrial area. 3D model via Rhinoceros 3D. Copyright: Marcello Turrini, Emanuele Naboni, Barbara Gherri 2022

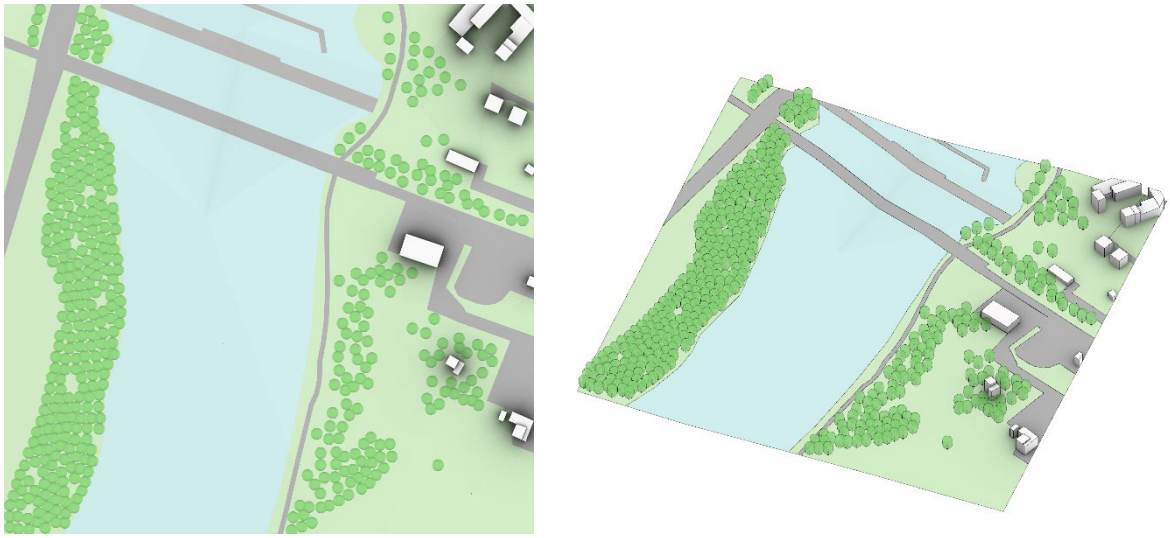

Figure 16. UP-4. Natural area. 3D model via Rhinoceros 3D. Copyright: Marcello Turrini, Emanuele Naboni, Barbara Gherri 2022

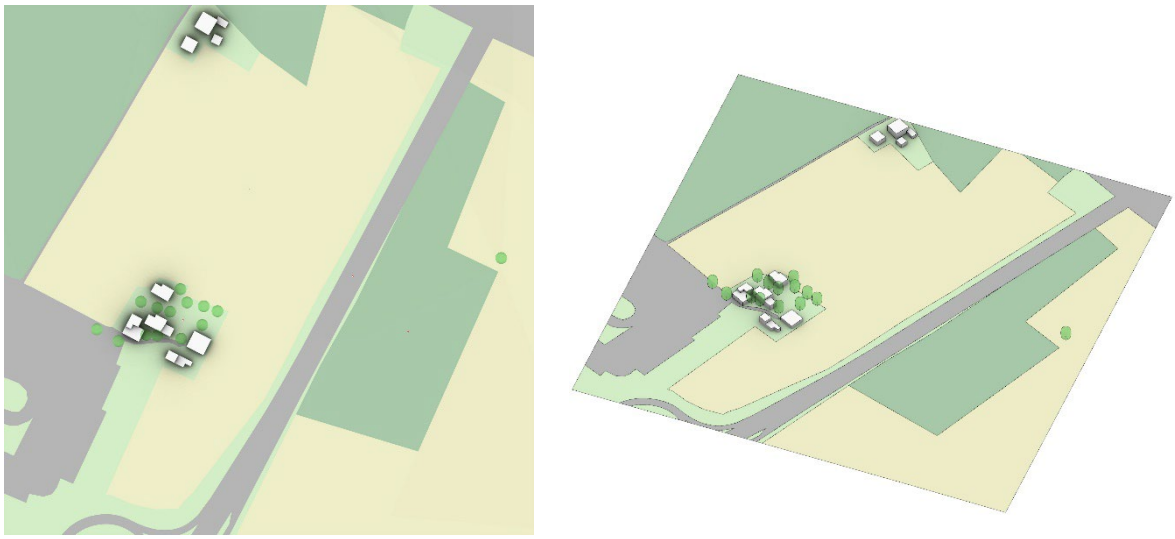

Figure 17. UP-5. Agricultural area. 3D model via Rhinoceros 3D. Copyright: Marcello Turrini, Emanuele Naboni, Barbara Gherri 2022

5.1.4 Preparation of the models for UTCI simulations

ENVI-met release 5 was selected as the simulation engine to compute UTCI. This choice was motivated by the fact that vegetation and water elements have a strong impact on comfort in all areas, and ENVI-met is currently the best software for capturing the contribution of these elements in calculating comfort in outdoor areas[491]. In addition, wind flow calculation is integrated into the software and can calculate temperature advection due to air movements over surfaces with different temperatures. Furthermore, ENVI-met can calculate vegetation evapotranspiration even under thermal stress, and this property is fundamental in comfort assessment. Finally, ENVI-met is able to calculate the movement of moist air masses from bodies of water or vegetation to surrounding areas, which is crucial in heterogeneous open spaces such as those analyzed.

The three-dimensional geometry used by ENVI-met is based on voxels, which are the reference units for all calculations. They consist of cubic units for three-dimensional parts and square element for flat surfaces. The thermodynamic quantities are calculated at their center point. Each voxel must be assigned the properties of the material it is made of. To transform

[491] Tsokaet al. 2018

the Rhinoceros model and make it compatible with ENVI-met, the Rhinoceros module "Grasshopper" combined with the "Morpho"[492] plug-in was used.

Workspace and location

Workspace and location were initialized by setting up the main folders for storing the binary simulation outputs using native Grasshopper components. The location was then set using the "Morpho Location" component by entering the geographical coordinates of Sassuolo (Figure 18).

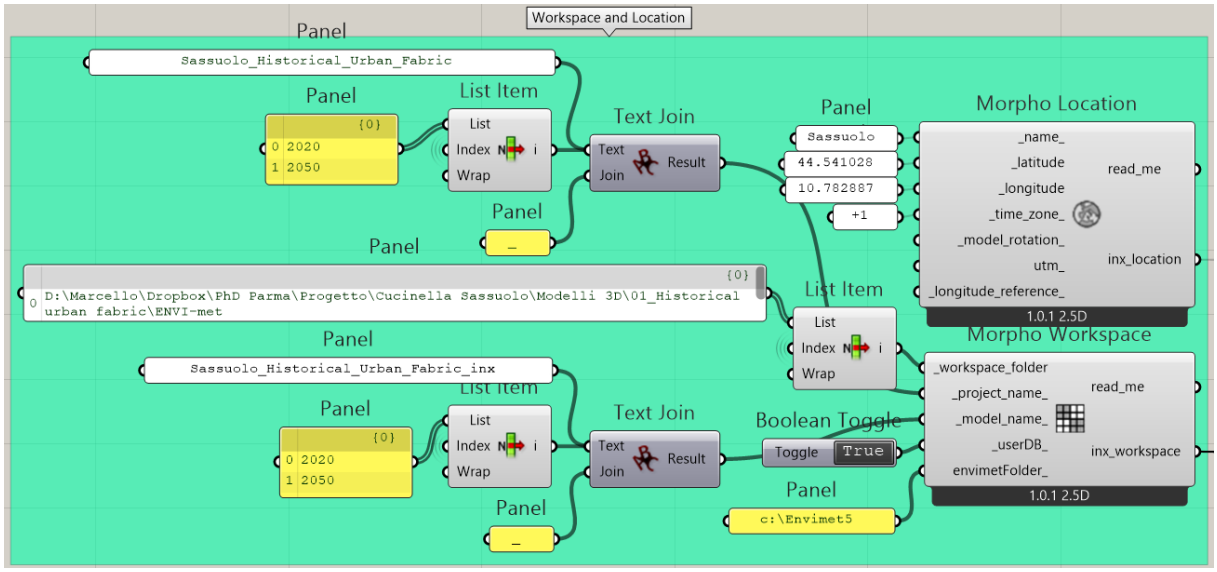

Figure 18. Grasshopper and Morpho components for workspace and location settings. Copyright: Marcello Turrini, Emanuele Naboni, Barbara Gherri 2022

Set up of the grid domain

Using the "Morpho grid size" component, a three-dimensional horizontal grid with 2.5 m resolution was applied to the 400 m × 400 m squares defining the configuration boundaries. The 2.5 m value corresponds to the calculation resolution, i.e., the side length of the cubic voxel used for the simulations. Starting from the third vertical voxel (7.5 m height), a telescopic vertical grid was adopted, with cells progressively increasing in size with height. This approach allowed to maintain a fine resolution close to the ground, where the phenomena most relevant

[492] https://github.com/AntonelloDN/Morpho

to urban comfort occur, and to reduce the total number of cells needed to reach high altitudes, thus optimizing calculation times. A domain control display was also included using the "Morpho Decompose Grid" component together with native Grasshopper components (Figure 19).

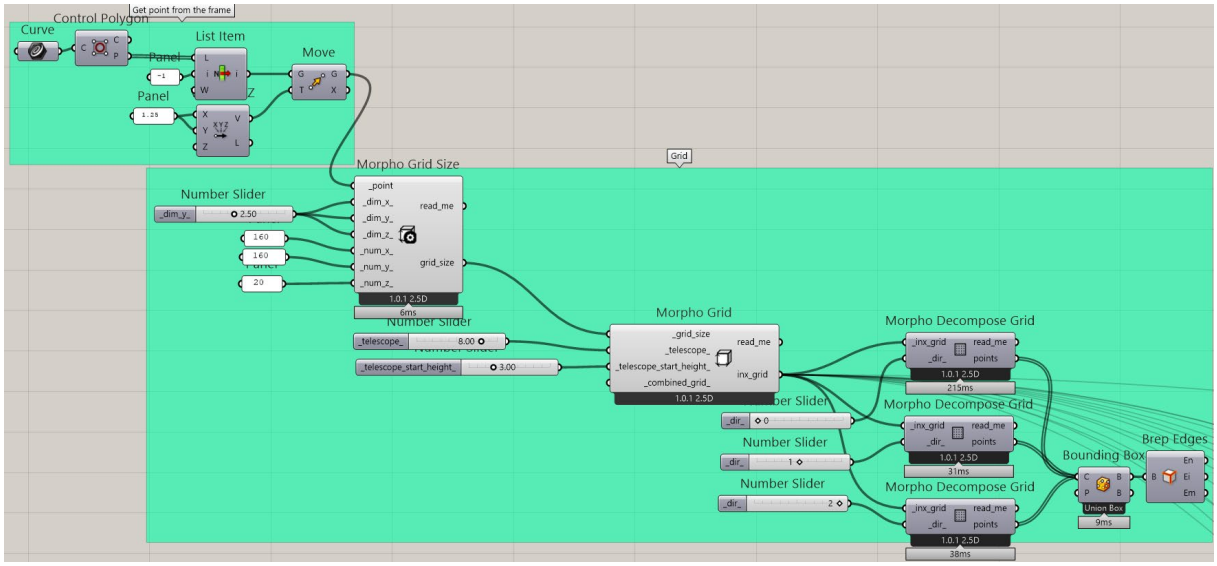

Figure 19. Morpho and Grasshopper components for grid domain setup. Copyright: Marcello Turrini, Emanuele Naboni, Barbara Gherri 2022

Geometry

To convert Rhinoceros building geometries into ENVI-met geometries, three components were used: a native Grasshopper mesh container holding the building mesh in Rhinoceros format; a GhPython script to project buildings to z = 0, eliminating geometric inaccuracies that could prevent import under conventional elevation settings[493]; and the "Morpho Facegroup" component, which converts solid geometry into a coherent group of voxelated faces for creating ENVI-met entities (Figure 20).

[493]
```
import Rhino as rh
result = []
for el in x:
    bbox = el.GetBoundingBox(False)
    min = bbox.Min
    zmove = rh.Geometry.Vector3d(0, 0, - min.Z)
    el.Translate(zmove)
    result.append(el)
a = result
```

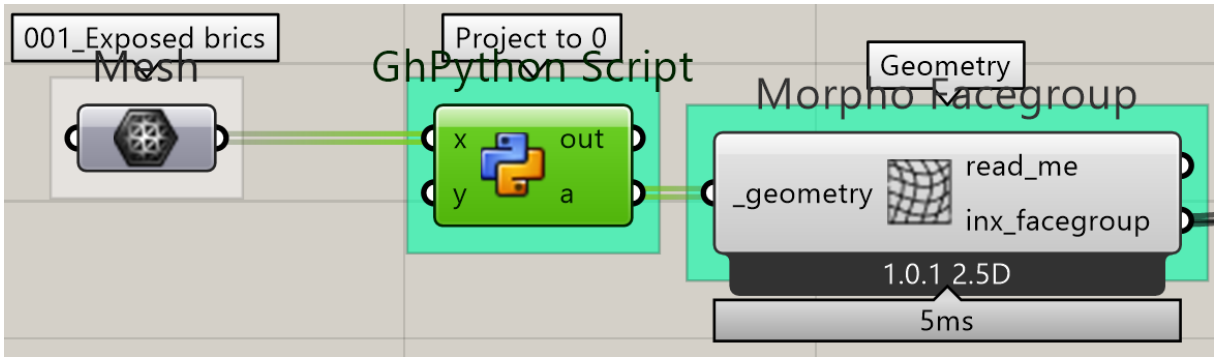

Figure 20. Components for transforming Rhinoceros objects into ENVI-met building objects. Copyright: Marcello Turrini, Emanuele Naboni, Barbara Gherri 2022

For geometric surfaces, the same method as for buildings was followed, with the addition of two components to adjust normals in accordance with ENVI-met criteria (Figure 21).

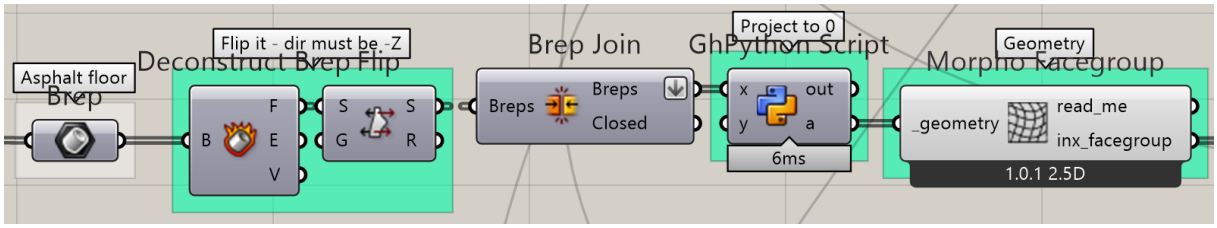

Figure 21. Components for transforming Rhinoceros objects into ENVI-met surface objects. Copyright: Marcello Turrini, Emanuele Naboni, Barbara Gherri 2022

Materials

Materials were added to the ENVI-met material database, assigning to each the stratigraphy and physical properties of each layer. The list of materials for buildings can be viewed in Table 4 and for surfaces in Table 5.

			m			%	%	%	%	J(KgK)	W/(mK)	Kg/m³	
001. Non insulated load bearing wall	**Layer**	**Material**	**Thickness**	**DB ID**	**DB Name**	**Abs.**	**Trans.**	**Refl.**	**Emis.**	**SH**	**TC**	**Dens.**	**Roof**
Exposed	Outside												*Tile*
	Layer 1	Bricks	0,125	*0000PB*	*Custom Brick: burned*	0,55	0	0,1	0,9	650	0,78	1900	
	Layer 2	Bricks	0,125	*0000PB*	*Custom Brick: burned*	0,55	0	0,1	0,9	650	0,78	1900	
ENVI-met database ID:	Layer 3	Plaster	0,02	*0100PL*	*Default Plaster*	0,5	0	0,5	0,9	850	0,6	1500	
001EXP	Inside	**Total thickness**	**0,27**							**U-Value**	**1,84**		
Dark	Outside												*Tile*
	Layer 1	Dark Plaster	0,02	*000PPD*	*Custom Plaster Dark*	0,7	0	0,2	0,9	850	0,87	1500	
	Layer 2	Bricks	0,25	*0000PB*	*Custom Brick: burned*	0,55	0	0,1	0,9	650	0,78	1900	
ENVI-met database ID:	Layer 3	Plaster	0,02	*0100PL*	*Default Plaster*	0,5	0	0,5	0,9	850	0,6	1500	
001DRK	Inside	**Total thickness**	**0,29**							**U-Value**	**1,76**		
Light	Outside												*Tile*
	Layer 1	Light Plaster	0,02	*000PPL*	*Custom Plaster Light*	0,35	0	0,55	0,9	850	0,87	1500	
	Layer 2	Bricks	0,25	*0000PB*	*Custom Brick: burned*	0,55	0	0,1	0,9	650	0,78	1900	
ENVI-met database ID:	Layer 3	Plaster	0,02	*0100PL*	*Default Plaster*	0,5	0	0,5	0,9	850	0,6	1500	
001LGT	Inside	**Total thickness**	**0,29**							**U-Value**	**1,76**		

002. Non insulated infill wall	**Layer**	**Material**	**Thickness**	**DB ID**	**DB Name**	**Abs.**	**Trans.**	**Refl.**	**Emis.**	**SH**	**TC**	**Dens.**	**Roof**
Dark	Outside												*Wet Roof*
	Layer 1	Dark Plaster	0,02	*000PPD*	*Custom Plaster Dark*	0,7	0	0,2	0,9	850	0,87	1500	
	Layer 2	Clay block	0,3	*010HCB*	*Hollow clay block*	0,6	0	0,4	0,9	1000	0,18	800	
ENVI-met database ID:	Layer 3	Plaster	0,015	*0100PL*	*Default Plaster*	0,5	0	0,5	0,9	850	0,6	1500	
002DRK	Inside	**Total thickness**	**0,335**							**U-Value**	**0,53**		
Light	Outside												*Wet Roof*
	Layer 1	Light Plaster	0,02	*000PPL*	*Custom Plaster Light*	0,35	0	0,55	0,9	850	0,87	1500	
	Layer 2	Clay block	0,3	*0000B1*	*Hollow clay block*	0,6	0	0,4	0,9	1000	0,18	800	
ENVI-met database ID:	Layer 3	Plaster	0,015	*0100PL*	*Default Plaster*	0,5	0	0,5	0,9	850	0,6	1500	
002LGT	Inside	**Total thickness**	**0,335**							**U-Value**	**0,53**		

003. Insulated infill wall Refurbished	**Layer**	**Material**	**Thickness**	**DB ID**	**DB Name**	**Abs.**	**Trans.**	**Refl.**	**Emis.**	**SH**	**TC**	**Dens.**	**Roof**
Dark	Outside												*Wall - Moderate Insulation*
	Layer 1	Dark Plaster	0,015	*000PPD*	*Custom Plaster Dark*	0,7	0	0,2	0,9	850	0,87	1500	
	Layer 2	Polystyrene	0,06	*010POL*	*Polystyrene*	0,6	0	0,4	0,9	1500	0,035	30	
ENVI-met database ID:	Layer 3	Clay block	0,24	*0100PL*	*Hollow clay block*	0,6	0	0,4	0,9	1000	0,18	800	
003DRK	Inside	**Total thickness**	**0,315**							**U-Value**	**0,31**		
Light	Outside												*Wall - Moderate Insulation*
	Layer 1	Light Plaster	0,015	*000PPL*	*Custom Plaster Light*	0,35	0	0,55	0,9	850	0,87	1500	
	Layer 2	Polystyrene	0,06	*010POL*	*Polystyrene*	0,6	0	0,4	0,9	1500	0,035	30	
ENVI-met database ID:	Layer 3	Clay block	0,24	*0100PL*	*Hollow clay block*	0,6	0	0,4	0,9	1000	0,18	800	
003LGT	Inside	**Total thickness**	**0,315**							**U-Value**	**0,31**		

004. Insulated infill wall New	**Layer**	**Material**	**Thickness**	**DB ID**	**DB Name**	**Abs.**	**Trans.**	**Refl.**	**Emis.**	**SH**	**TC**	**Dens.**	**Roof**
Dark	Outside												*Wall - Moderate Insulation*
	Layer 1	Dark Plaster	0,02	*000PPD*	*Custom Plaster Dark*	0,7	0	0,2	0,9	850	0,87	1500	
	Layer 2	Clay block	0,3	*0100PL*	*Hollow clay block*	0,6	0	0,4	0,9	1000	0,18	800	
ENVI-met database ID:	Layer 3	Polystyrene	0,05	*010POL*	*Polystyrene*	0,6	0	0,4	0,9	1500	0,035	30	
004DRK	Inside	**Total thickness**	**0,37**							**U-Value**	**0,30**		
Light	Outside												*Wall - Moderate Insulation*
	Layer 1	Light Plaster	0,02	*000PPL*	*Custom Plaster Light*	0,35	0	0,55	0,9	850	0,87	1500	
	Layer 2	Clay block	0,3	*0100PL*	*Hollow clay block*	0,6	0	0,4	0,9	1000	0,18	800	
ENVI-met database ID:	Layer 3	Polystyrene	0,05	*010POL*	*Polystyrene*	0,6	0	0,4	0,9	1500	0,035	30	
004LGT	Inside	**Total thickness**	**0,37**							**U-Value**	**0,30**		

005. Prefabricated Residential	**Layer**	**Material**	**Thickness**	**DB ID**	**DB Name**	**Abs.**	**Trans.**	**Refl.**	**Emis.**	**SH**	**TC**	**Dens.**	**Roof**
	Outside												*Wet Roof*
	Layer 1	Concrete	0,05	*0100C1*	*Concrete: heavyweight*	0,7	0	0,3	0,9	840	1,3	2000	
	Layer 2	Air gap	0,15	*0100AC*	*Air Custom*	0	1	0	0,96	1006	0,83	1,2041	
ENVI-met database ID:	Layer 3	Clay block	0,08	*010POL*	*Hollow clay block*	0,6	0	0,4	0,9	1000	0,18	800	
005PRE	Inside	**Total thickness**	**0,28**							**U-Value**	**1,17**		

006. Prefabricated Industrial	**Layer**	**Material**	**Thickness**	**DB ID**	**DB Name**	**Abs.**	**Trans.**	**Refl.**	**Emis.**	**SH**	**TC**	**Dens.**	**Roof**
	Outside												*Wet Roof*
	Layer 1	Concrete	0,065	*0100C1*	*Concrete: heavyweight*	0,7	0	0,3	0,9	840	1,3	2000	
	Layer 2	Mineral wool	0,07	*0100MW*	*Mineral wool*	0,6	0	0,4	0,9	830	0,04	100	
ENVI-met database ID:	Layer 3	Concrete	0,065	*0100C1*	*Concrete: heavyweight*	0,7	0	0,3	0,9	840	1,3	2000	
006PRE	Inside	**Total thickness**	**0,2**							**U-Value**	**0,49**		

Concrete Slab	**Layer**	**Material**	**Thickness**	**DB ID**	**DB Name**	**Abs.**	**Trans.**	**Refl.**	**Emis.**	**SH**	**TC**	**Dens.**
	Outside											
	Layer 1	Concrete	0,05	*0000C2*	*Concrete: lightweight*	0,7	0	0,3	0,9	840	0,2	620
	Layer 2	Concrete	0,1	*0000C2*	*Concrete: lightweight*	0,7	0	0,3	0,9	840	0,2	620
ENVI-met database ID:	Layer 3	Concrete	0,05	*0000C2*	*Concrete: lightweight*	0,7	0	0,3	0,9	840	0,2	620
0001CS	Inside	**Total thickness**	**0,2**							**U-Value**	**0,84**	

Wall - Moderate Insulation	**Layer**	**Material**	**Thickness**	**DB ID**	**DB Name**	**Abs.**	**Trans.**	**Refl.**	**Emis.**	**SH**	**TC**	**Dens.**
	Outside											
	Layer 1	Concrete	0,01	*0100F3*	*Moderate insulation*	0,42	0,13	0,45	0,9	1032,8	0,15	1686,9
	Layer 2	Concrete	0,12	*0100F3*	*Moderate insulation*	0,42	0,13	0,45	0,9	1032,8	0,15	1686,9
ENVI-met database ID:	Layer 3	Concrete	0,18	*0100F3*	*Moderate insulation*	0,42	0,13	0,45	0,9	1032,8	0,15	1686,9
0100F3	Inside	**Total thickness**	**0,31**							**U-Value**	**0,44**	

Tile	**Layer**	**Material**	**Thickness**	**DB ID**	**DB Name**	**Abs.**	**Trans.**	**Refl.**	**Emis.**	**SH**	**TC**	**Dens.**
	Outside											
	Layer 1	Tile	0,05	*010PR1*	*Custom Roofing: Tile*	0,7	0	0,2	0,9	800	0,84	1900
	Layer 2	Air	0,03	*010O2*	*Air*	0	1	0	0,96	1006	0,025	1,2041
ENVI-met database ID:	Layer 3	Wood	0,12	*0100PW*	*Custom Wood*	0,3	0	0,7	0,9	1470	0,14	1200
010PRT	Inside	**Total thickness**	**0,2**							**U-Value**	**0,43**	

Table 4. List of materials for buildings.

			m			m	%	%	m^3/m^3	m^3/m^3	m^3/m^3	m	$m/s \times 10^{-5}$	$J/(m^3 K) \times 10$		W/(mK)
Loamy Soil	**Layer**	**Material**	**Thickness**	**ID**	**name**	**z0 RL**	**Albedo**	**Emiss.**	**Water content at sat.**	**Water content at f.c.**	**Water content at w.p.**	**Matrix potential**	**Hydraulic conductivity**	**Volumetric heat capacity**	**C&A constant**	**Heat conductivity**
ENVI-met database ID:	Outside					0,015	0	0,98								
000000	Layer 1	Loam	4,5	*0000LE*	*Loam*				0,451	0,24	0,155	-0,478	7	1,212	5,39	0
Asphalt	**Layer**	**Material**	**Thickness**	**Database ID**	**Database name**	**z0 Roughness Length**	**Albedo**	**Emissivity**	**Water content at sat.**	**Water content at f.c.**	**Water content at w.p.**	**Matrix potential**	**Hydraulic conductivity**	**Volumetric heat capacity**	**C&A constant**	**Heat conductivity**
	Outside					0,01	0,2	0,9								
ENVI-met database ID:	Layer 1	Asphalt	0,3	*0000AB*	*Asphalt (With basalt)*				0	0	0	0	0	2,251	0	0,9
0100ST	Layer 2	Sand	4,2	*0000SL*	*Sandy loam*				0,43	0,195	0,114	-0,218	34,1	1,32	4,9	0
Stone road	**Layer**	**Material**	**Thickness**	**Database ID**	**Database name**	**z0 Roughness Length**	**Albedo**	**Emissivity**	**Water content at sat.**	**Water content at f.c.**	**Water content at w.p.**	**Matrix potential**	**Hydraulic conductivity**	**Volumetric heat capacity**	**C&A constant**	**Heat conductivity**
	Outside					0,01	0,3	0,9								
	Layer 1	Brick	0,03	*0000BR*	*Brick*				0	0	0	0	0	2	0	1
ENVI-met database ID:	Layer 2	Sand	0,01	*0000SD*	*Sand*				0,395	0,135	0,0068	-0,121	176	1,463	4,05	0
0100KK	Layer 3	Sand	4,46	*0000SL*	*Sandy loam*				0,43	0,195	0,114	-0,218	34,1	1,32	4,9	0
Semi-permeable floor	**Layer**	**Material**	**Thickness**	**Database ID**	**Database name**	**z0 Roughness Length**	**Albedo**	**Emissivity**	**Water content at sat.**	**Water content at f.c.**	**Water content at w.p.**	**Matrix potential**	**Hydraulic conductivity**	**Volumetric heat capacity**	**C&A constant**	**Heat conductivity**
	Outside					0,01	0,75	0,9								
	Layer 1	Smashed brick	0,03	*000CBS*	*Smashed brick*				0,39	0,135	0,0068	-0,12	176	2	4,05	0
	Layer 2	Sand	0,01	*0000SD*	*Sand*				0,395	0,135	0,0068	-0,121	176	1,463	4,05	0
ENVI-met database ID:	Layer 3	Sand	0,04	*000LS*	*Loamy sand*				0,41	0,15	0,075	-0,09	156,3	1,404	4,38	0
010CTB	Layer 4	Clay	4,42	*0000SL*	*Sandy clay*				0,426	0,31	0,219	-0,153	2,2	1,175	10,4	0
Water	**Layer**	**Material**	**Thickness**	**Database ID**	**Database name**	**z0 Roughness Length**	**Albedo**	**Emissivity**	**Water content at sat.**	**Water content at f.c.**	**Water content at w.p.**	**Matrix potential**	**Hydraulic conductivity**	**Volumetric heat capacity**	**C&A constant**	**Heat conductivity**
ENVI-met database ID:	Outside					0,01	0	0,96								
000000	Layer 1	Water	4,5	*0000WW*	*Water*				0	0	0	0	0	0	0	0

Grass	**CO2 fixation type**	**Plant height**	**Leaf type**	**Root zone depth**	**Transmittance**	**Albedo**
ENVI-met database ID:	C3	0,05	Gras	0,2	0,3	0,2
GRAS05						
Field 1	**CO2 fixation type**	**Plant height**	**Leaf type**	**Root zone depth**	**Transmittance**	**Albedo**
ENVI-met database ID:	C3	0,5	Gras	0,2	0,3	0,2
0100XY						
Field 2	**CO2 fixation type**	**Plant height**	**Leaf type**	**Root zone depth**	**Transmittance**	**Albedo**
ENVI-met database ID:	C3	0,25	Gras	0,2	0,3	0,2
0100XX						

Table 5. List of materials for surfaces.

Water

In ENVI-met, water is specified as specific soil material and is hence handled differently from the normal materials. All values are stored in the code and e.g. albedo changes over the course of the simulation depending on the sun height angle. The values cannot be changed in the manual settings. The only parameter left to define was the river depth, which was set to 3.0 m.

Trees

The trees are all considered to be of the same type, with cylindrical crowns. The trees are 15 m high and 9 m in diameter. They are considered deciduous, with foliage albedo of 0.18 and shortwave radiation transmittance of 0.30.

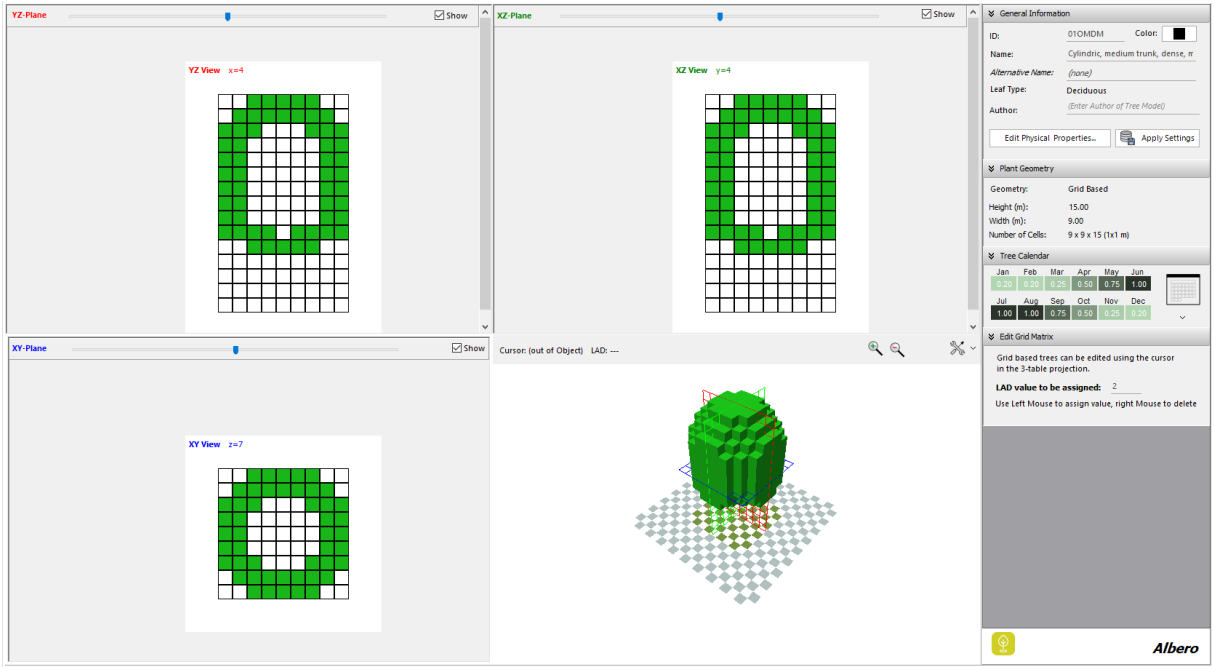

Figure 22. ENVI-met panel for tree configuration. The geometry is fully customizable, along with the foliage albedo data.

Day of Simulation

The day used for the simulations was identified by first selecting the hottest week of the year from the STAT file, a data format derived from EnergyPlus containing key statistics for the reference-year climate. For both 2022 and 2050, the hottest week was between August 17 and 23. Within that week, dry-bulb temperature and global horizontal radiation were compared to exclude days with significant differences in cloud cover between the two reference years. The graph in Figure 23 shows this comparison, which indicates that August 17 is the day of the week when radiation does not undergo sudden changes due to cloud cover, both in 2022 and in 2050, and that the temperature follows a continuous trend in both years. Therefore, August 17 was selected as the simulation day. The simulation was started at 6:00 a.m. on the previous day (August 16) to allow thermal masses to undergo a charging–discharging cycle and reach midnight on August 17—the actual start of the analysis—with an initialized energy state.

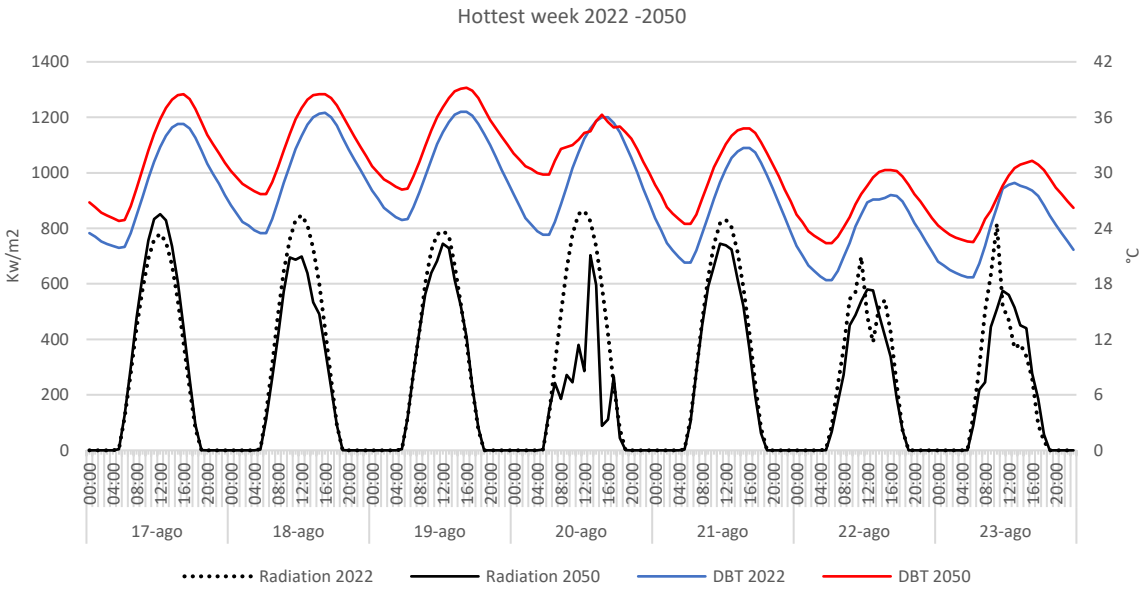

Figure 23. Comparison between Dry Bulb Temperature and Global Horizontal Radiation in 2022 and 2050 during the hottest week of the year. On August 17, radiation does not show significant differences in cloud cover.

Weather data

The EPW climate file was generated using Meteonorm, with Sassuolo set as the reference location. Since there is no weather station in Sassuolo, the software interpolated the temperature data from stations in Bologna (41 km), Piacenza (93 km), Florence/Peretola (98 km), Forlì (108 km), Ravenna (121 km), and Verona/Villafranca (94 km). The radiation data, on the other hand, is 100% satellite data.

The EPW file was also projected to 2050 using Meteonorm and the RCP 8.5 profile. The RCP 8.5 profile was selected to test the methodology under a high-end emissions pathway, ensuring a significant warming signal for comparative assessment.

The EPW files were then imported into ENVI-met, which generated FOX files—structured text files containing the forcing-variable values for each simulation timestep. Dry-bulb temperature, relative humidity, and radiation forcings were kept unchanged, whereas precipitation was excluded, as it is often not represented in EPW files. In addition, wind was kept constant in direction (135°) and speed (0.5 m/s). These values are representative of typical summer conditions for Sassuolo and were kept constant to avoid instability in the calculation model.

Extraction of results

After models and boundary conditions were set, simulations were launched using CPU parallelism to accelerate computation. Simulations covered an area of 160 hectares over 240 simulated hours, generating 95.5 GB of data. Total computation time across all simulated areas was approximately 732 hours, corresponding to an average speed of 0.65 simulated hours per hour of computation.

Morpho components were used to extract numerical data from the ENVI-met binary output files for all five configurations and both scenarios (2022 and 2050). Specifically, dry-bulb temperature, mean radiant temperature, relative humidity, and wind speed were extracted for each open-space surface voxel in both 2022 and 2050; these four microclimatic factors were then processed with Ladybug's "UTCI" component to compute UTCI for each voxel under both scenarios. These values were then mapped onto the three-dimensional models of each configuration using Ladybug's "Spatial Heatmap" component.

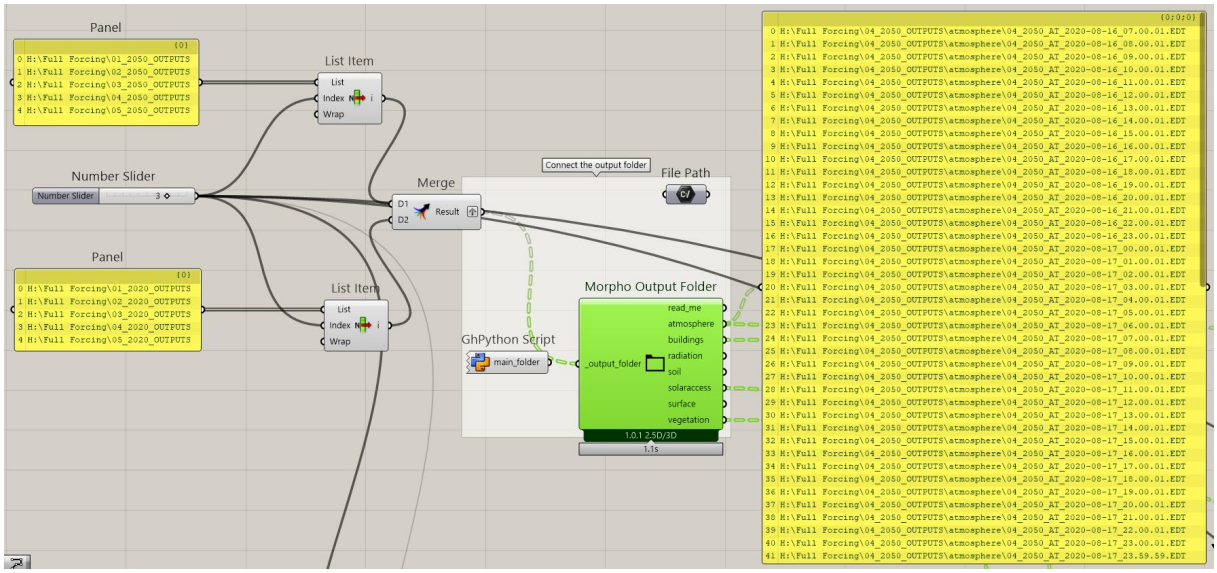

Figure 24. Sorting output files of ENVI-met with Morpho. Copyright: Marcello Turrini, Emanuele Naboni, Barbara Gherri 2022

Next, for each voxel, the 2050 UTCI was subtracted from the 2022 UTCI to obtain the variation, which was then mapped onto the three-dimensional models to link each spatial configuration with UTCI-variation values for visual assessment of climate-change resilience. Finally, for each configuration, the distribution of UTCI variations was calculated and plotted in Excel. Alongside the distribution, the mean UTCI-variation value for each configuration was

calculated using native Grasshopper components by dividing the sum of all values by the list length.

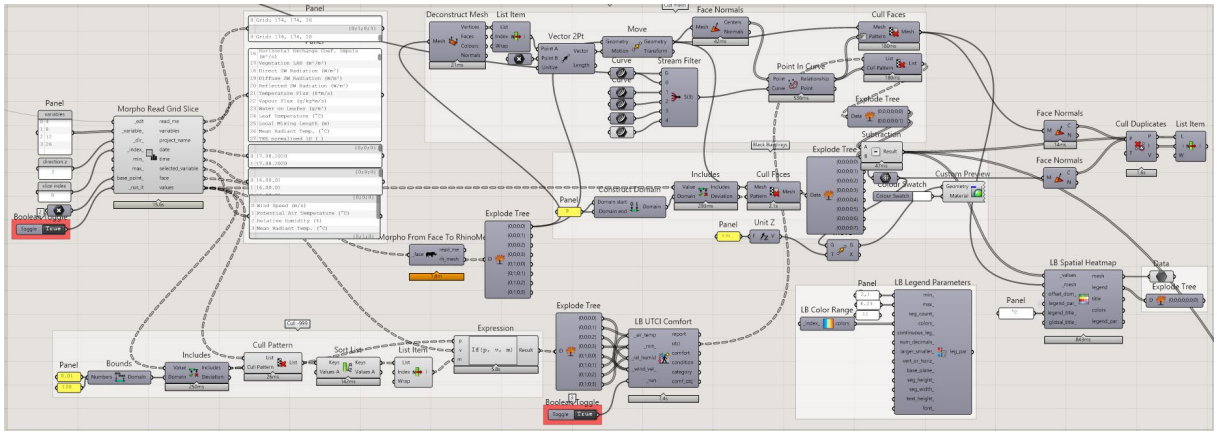

Figure 25. UTCI calculation for 2022 and 2050 with morpho, Ladybug and native Grasshopper components. Copyright: Marcello Turrini, Emanuele Naboni, Barbara Gherri 2022

The effect of pollutants and anthropogenic heat was not included in the UTCI calculation for simplicity.

5.1.5 UTCI Variation for Each Configuration

In the following sections, it is possible to observe the variation in UTCI for each configuration between current climate scenario and 2050. The reference time for evaluation was set at 4:00 pm, corresponding to the hottest period of the day. It is important and strategic that the legends of the results mapped for both scenarios are standardized, aligning the maximum and minimum values and the number of segments, for easier comparative reading of the results.

UP_1 – Historical Urban Fabric

The spatial distribution of UTCI within the historic urban fabric in the configuration UP_1 for August 17 at 4:00 p.m., under current and 2050 climate scenarios is shown in Figure 26. In the current scenario, UTCI values are largely confined to the strong heat stress category of the UTCI, between 32 and 38 °C, with a majority of areas remaining below 39 °C. The prevalence of narrow streets, high building density, and limited sky visibility create a microclimate

protected from direct solar radiation, helping to maintain relatively stable and tolerable thermal conditions during peak afternoon hours.

In the 2050 scenario, an overall increase in UTCI is visible across the domain, with the emergence of hotter areas in exposed suburbs and along some open courtyards. However, the central areas of the historic urban fabric still resist the transition to very strong thermal stress levels above 38 °C, and most of the built environment remains in the 40-45 °C range. Given that one of the hottest hours of the year is simulated, the relative containment of thermal amplification highlights the role of morphological compactness in modulating the urban microclimate, even under future warming.

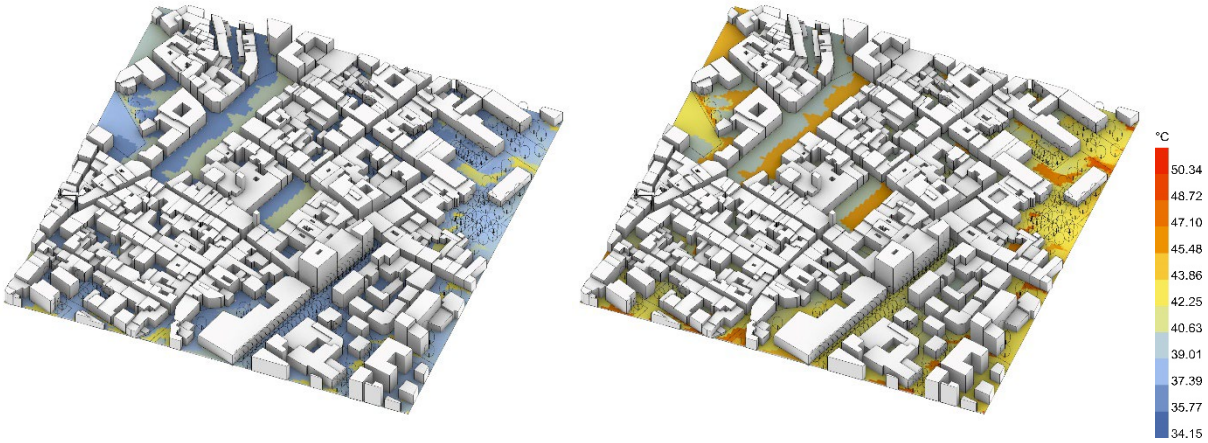

Figure 26. UP_1 - Historical Urban Fabric. UTCI on 17 August at 4:00 pm. 2022 on the left, 2050 on the right. Copyright: Marcello Turrini, Emanuele Naboni, Barbara Gherri 2022

The contrast between inner and peripheral areas is particularly evident: while perimeter spaces and large openings absorb more heat due to greater solar exposure, inner canyons and shaded alleys continue to act as thermal shelters. The persistence of these cooler micro-zones suggests that the historic urban fabric, although not always originally designed with climate

adaptation in mind, inherently possesses spatial characteristics that enhance passive thermal resilience.

Within the historical urban fabric, UTCI variation ranges mainly between 2.8 °C and 4.6 °C, with most values concentrated between 3.2 and 3.6 °C (Figure 27). These relatively low increases suggest that the historic fabric undergoes limited thermal amplification over time, especially when compared to more open or exposed urban morphologies. The presence of continuous shading, narrow street canyons, and a reduced sky view factor plays a crucial role in moderating the additional heat load introduced by future climate conditions.

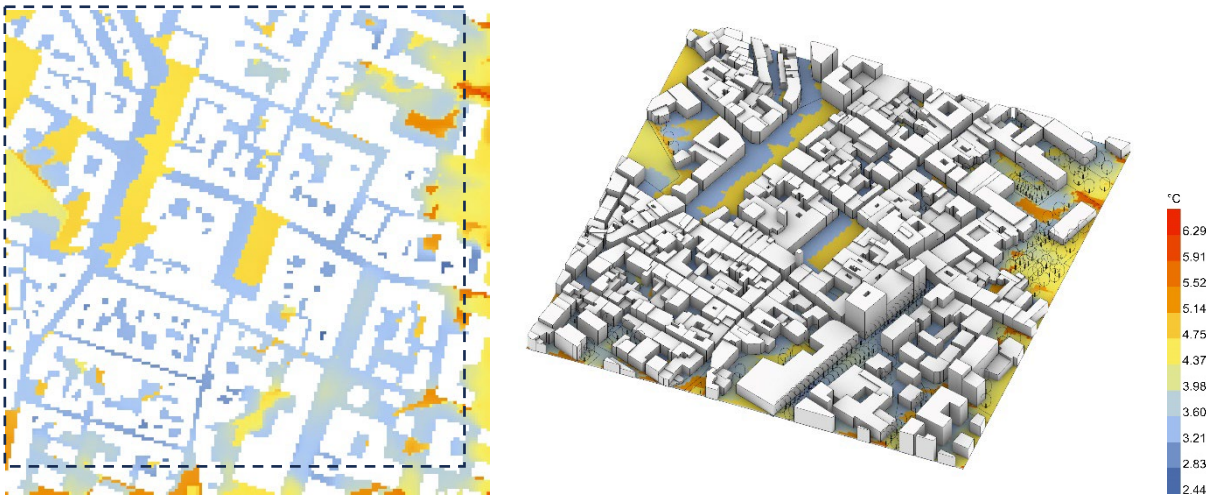

Figure 27. Variation in UTCI between 2022 and 2050 in the Configuration UP_1 – Historical urban fabric. The area within the dashed rectangle is the area actually used for numerical evaluation, as it is free from bias resulting from the edge effect of the CFD. Copyright: Marcello Turrini, Emanuele Naboni, Barbara Gherri 2022

Slightly higher values are observed along wider asphalt-paved streets and open courtyards, where solar penetration increases and wind exposure is more variable. However, even in these cases, the variation rarely exceeds 4.5 °C and there are no extreme hot spots. This spatial consistency highlights the morphological resilience of historic fabric, which inherently mitigates the impact of radiative forcing and maintains more favorable microclimatic performance.

Analysis of UTCI variations shows that shaded areas experience the smallest increases. In particular, in narrow alleys and small courtyards, UTCI varies by less than 3°C, while the air temperature variation derived from the EPW files is greater than 3°C. The asphalt-paved and unshaded areas show the greatest increase, exceeding 5°C.

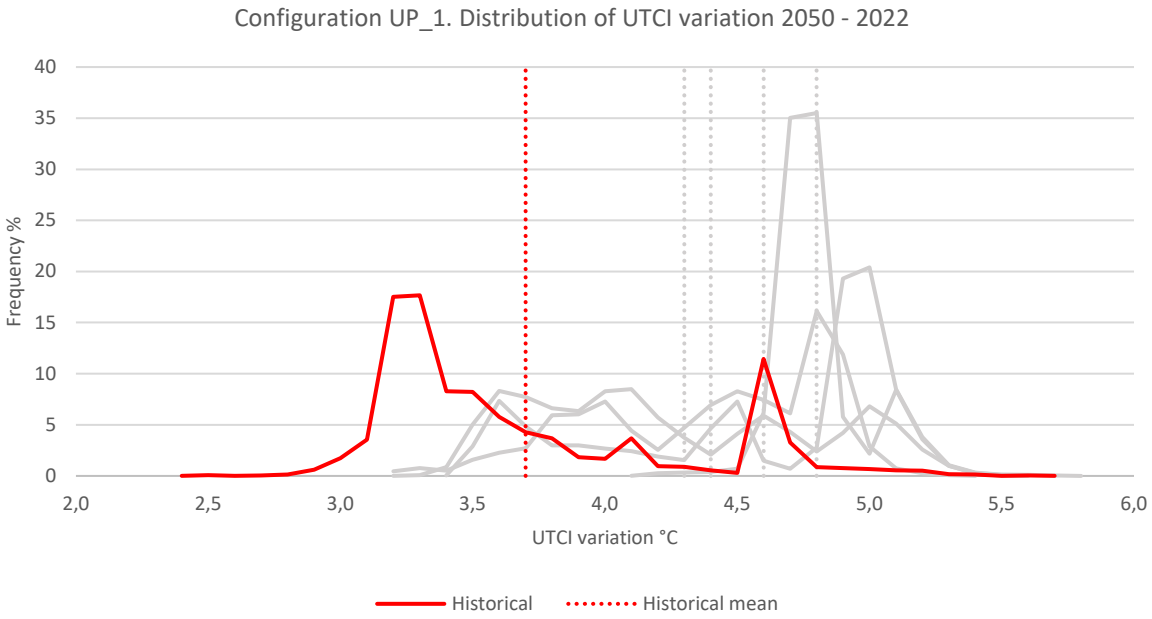

Figure 28. Distribution of UTCI variation in the UP_1 configuration between 2022 and 2050, referring to August 17 at 4:00 p.m. The red curve represents the relative frequency of UTCI variations, showing a peak around 3.3°C and an average of 3.7 °C, lower than the other configurations in gray. Copyright: Marcello Turrini, Emanuele Naboni, Barbara Gherri 2022

As shown in Figure 28, the distribution of UTCI variation for the UP_1 configuration shows a well-defined peak around 3.3 °C and an overall average lower than all other configurations analyzed. The limited dispersion and the presence of high frequencies at relatively low values indicate good thermal stability of the historic fabric and confirm its passive climate resilience, already observed in the spatial analysis. The morphological conditions of the historic center, with narrow streets, compact buildings, and widespread shading, act as effective mitigators of the increase in thermal stress expected in the future scenario.

Configuration UP_2 – Modern Urban Fabric

As displayed in Figure 29, the modern urban configuration shows a significant increase in heat stress between 2022 and 2050. In the 2022 scenario, shaded areas, mainly those adjacent to buildings and trees, remain in the “Strong heat stress” category, ranging between 38 and 46 °C UTCI. However, in the 2050 scenario, these same areas move upwards into the “Very high heat stress” range (46-50 °C), indicating a deterioration in thermal comfort even in partially

protected areas.

Asphalt-paved surfaces, already critical in 2022, deteriorate further in the 2050 projection. These areas consistently exceed 46 °C and in several places exceed 50 °C, falling into the “Extreme heat stress” category. This is particularly evident where solar exposure is prolonged, and vegetation is sparse.

The triangular courtyard in the center of the block performs relatively better, showing lower UTCI values than the surrounding exposed areas, but it too will tend to shift toward more stressful conditions by 2050. Overall, the spatial distribution highlights how fragmented vegetation and poorly organized building forms in modern settlements fail to provide effective mitigation against climate-induced heat amplification.

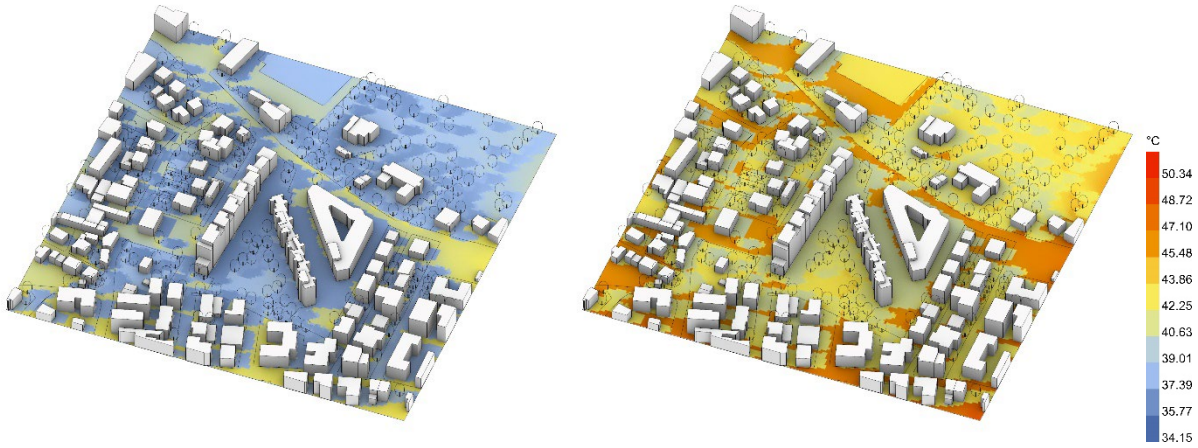

Figure 29. UP_2 - Modern Urban Fabric. UTCI on 17 August at 4:00 pm. 2022 on the left, 2050 on the right. Copyright: Marcello Turrini, Emanuele Naboni, Barbara Gherri 2022

Figure 30 shows the variation in UTCI for modern urban fabric (UP_2), highlighting the spatial distribution of the increase in heat stress expected between 2022 and 2050. The values mainly range between 3.9 and 5.5 °C, with some isolated areas exceeding 5.9 °C. These peaks are associated with asphalt-paved surfaces and open areas with high solar exposure and limited vegetation cover.

The central block enclosed by the triangular block shows a relatively lower increase, mostly between 3.0 and 4.0 °C, confirming the partial buffering capacity of semi-enclosed morphologies. However, the surrounding areas, including roads and parking lots, consistently show higher UTCI variation, indicating insufficient shading and thermal inertia.

Moreover, areas shaded by trees often show a greater variation in UTCI than those shaded by buildings. This counterintuitive result can be explained by the reduced evaporative capacity of trees at extreme temperatures, where stomatal closure limits evapotranspiration, combined with the aerodynamic resistance imposed by dense canopies, which hinders wind flow and convective cooling. As a result, areas shaded by trees can accumulate greater heat stress over time than well-ventilated architectural shade.

Overall, the delta map shows a heterogeneous but generally high level of vulnerability, with large portions of the urban fabric undergoing a transition to more intense heat stress conditions. The discontinuity in building layout and vegetation distribution appears insufficient to prevent significant thermal amplification, reinforcing the idea that morphological coherence and continuous shading are fundamental for future-proof urban design.

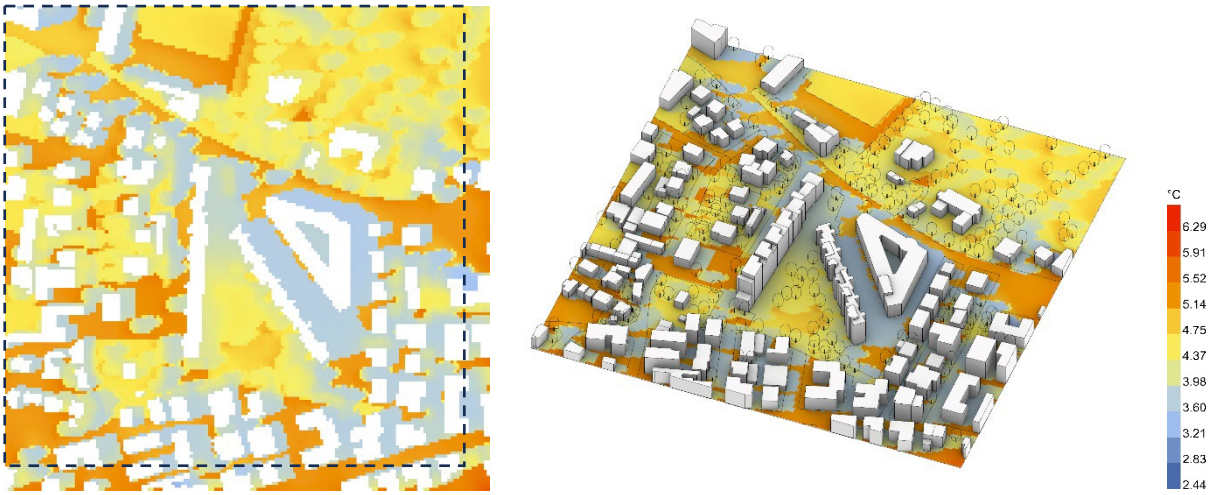

Figure 30. Variation in UTCI between 2022 and 2050 in the Configuration UP_2 – Modern urban fabric. The area within the dashed rectangle is the area actually used for numerical evaluation, as it is free from bias resulting from the edge effect of the CFD. Copyright: Marcello Turrini, Emanuele Naboni, Barbara Gherri 2022

The statistical distribution of the UTCI variation for the configuration UP_2, shown in the graph at Figure 31, further confirms the thermally unstable nature of modern urban fabrics. The frequency curve appears flat and dispersed, with no dominant mode, and covers a wide range from 3.3 to 5.6 °C. The average variation, indicated by the vertical dotted line, is around 4.3 °C, a value significantly higher than that observed in the historical configuration. This lack of established thermal behavior suggests heterogeneous performance in the urban fabric, probably determined by variable exposure, inconsistent vegetation patterns, and non-uniform building morphology.

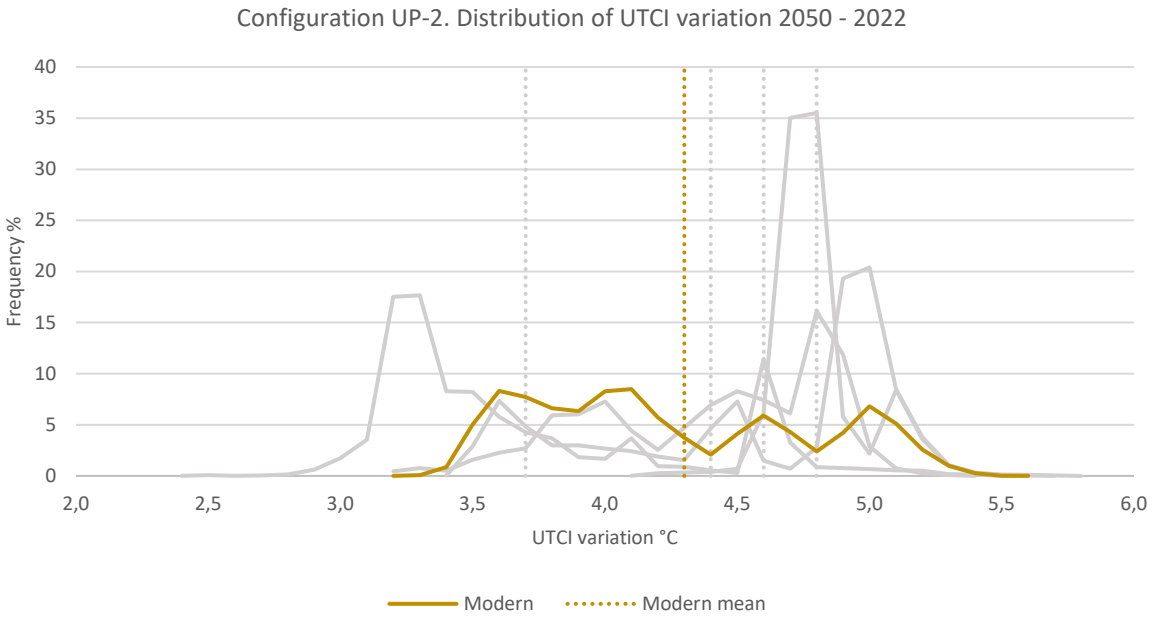

Figure 31. Distribution of UTCI variation for the configuration UP_2 - Modern urban fabric. The curve shows dispersed thermal behavior, with a mean value of around 4.3°C and no dominant peak, indicating uneven climate resilience. Copyright: Marcello Turrini, Emanuele Naboni, Barbara Gherri 2022

In particular, the absence of significant peaks in the distribution reflects the ineffectiveness of local mitigation elements, like scattered trees or isolated shading structures, in stabilizing thermal conditions. In contrast, the configuration has multiple minor peaks, probably corresponding to microclimatic niches where building form or vegetation provides temporary thermal relief. These data corroborate spatial observations, indicating a system that lacks the consistency necessary to withstand thermal amplification in a future climate scenario. In summary, UP_2 demonstrates moderate to low climate resilience, with localized performance dependent on fragmented design features rather than systematic urban morphology.

Configuration UP_3 – Industrial area.

Figure 32 shows the UTCI distribution in the industrial area (UP_3) for the reference date and time, comparing 2022 and 2050. In the 2022 scenario, UTCI values mainly range between 37 °C and 42 °C, corresponding to the “Strong heat stress” category. However, the open spaces between buildings and paved areas already have areas exceeding 43 °C, approaching the thresholds for “Extreme heat stress.”

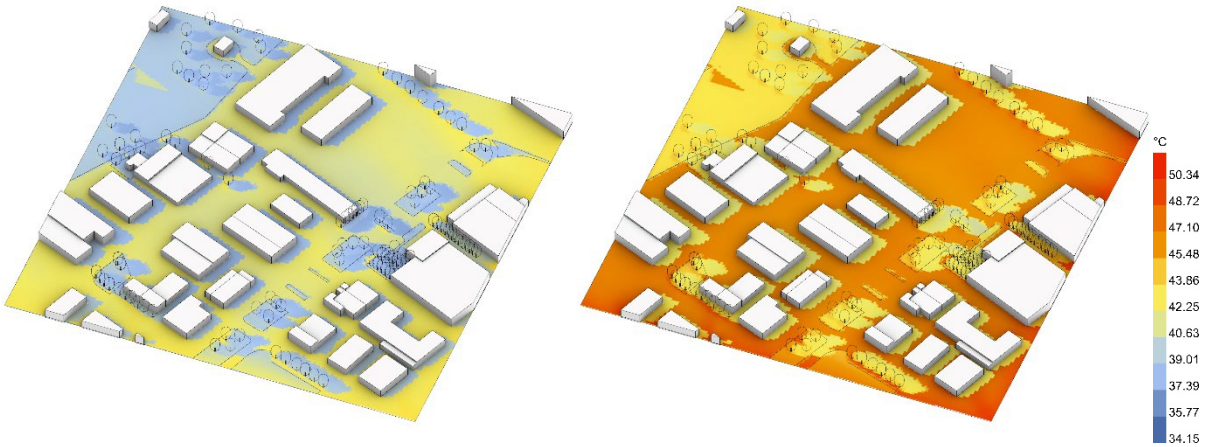

Figure 32. UP_3 – Industrial area. UTCI on 17 August at 4:00 pm. 2022 on the left, 2050 on the right. Copyright: Marcello Turrini, Emanuele Naboni, Barbara Gherri 2022

In the 2050 projection, the thermal landscape worsens considerably. The entire surface undergoes a substantial temperature change, with large areas exceeding 46 °C and several areas approaching 50 °C, falling into the “Extreme heat stress” category. In particular, the regularity and spacing of industrial buildings do not produce significant shading, and the limited presence of vegetation contributes minimally to mitigation.

The result is a uniformly overheated environment with little thermal heterogeneity, where radiation accumulation and low thermal inertia dominate the microclimate. These conditions highlight the critical vulnerability of industrial fabric to future climate stresses, particularly in areas characterized by sealed surfaces, low albedo, and limited airflow.

Figure 33 shows the variation in UTCI between 2022 and 2050 for the configuration UP_3 - Industrial area. Here, the UTCI variation ranges mainly between 4.3 and 5.9 °C, with large areas reaching or exceeding 5.5 °C. The spatial distribution is remarkably uniform, with no significant pockets of thermal buffering, indicating a widespread and constant intensification of heat stress throughout the industrial fabric.

This trend reflects the ineffectiveness of building morphology in mitigating future climate impacts. The low height of the buildings, the absence of continuous shading, and the prevalence of sealed and dark surfaces give rise to a system that accumulates and amplifies heat rather than dissipating it. Even the sparsest vegetated areas show values of high UTCI variation, confirming that the minimal green infrastructure in this configuration is not

sufficient to counterbalance radiative and convective loads under the expected climatic conditions.

The data suggest that the industrial fabric is not only thermally vulnerable in absolute terms, but also subject to high thermal amplification over time, making it a critical target for adaptive interventions.

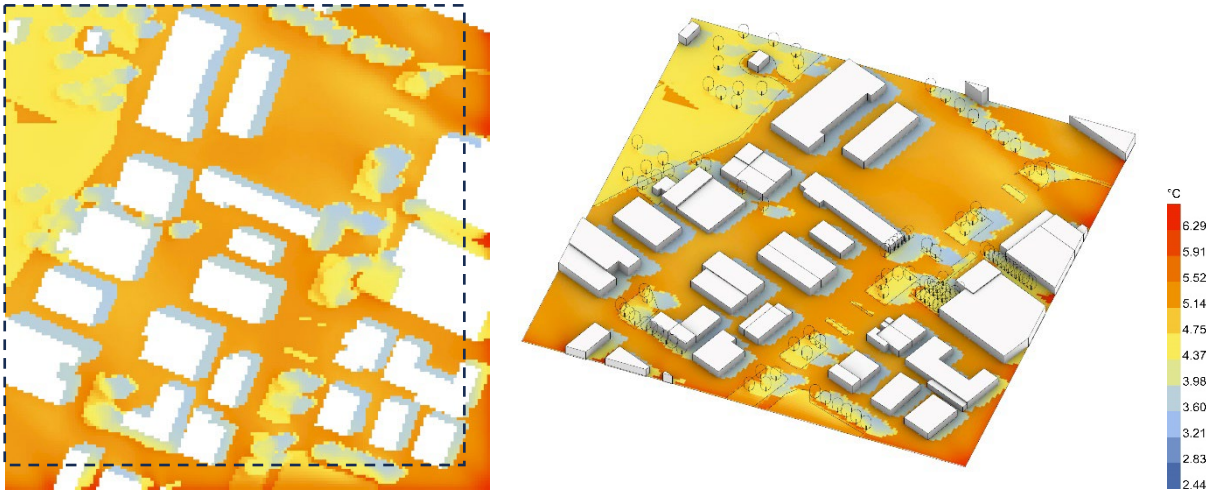

Figure 33. Variation in UTCI between 2022 and 2050 in the Configuration UP_3 – Industrial area. The area within the dashed rectangle is the area actually used for numerical evaluation, as it is free from bias resulting from the edge effect of the CFD. Copyright: Marcello Turrini, Emanuele Naboni, Barbara Gherri 2022

The frequency distribution of the UTCI variation for the UP_3 - Industrial area, shown in Figure 34, highlights a clearly asymmetrical trend, oriented towards higher temperature increases. The curve shows a clear peak between 4.9 and 5.0 °C, with a mean value slightly at 4.6 °C, making it one of the highest among all the configurations analyzed.

Unlike more resilient urban fabrics, the industrial distribution shows no variability in the lower range, apart from a small peak at 3.6 °C, that corresponds to a small green area on the north-west part of the area, confirming that no part of the proper industrial area experiences limited thermal intensification. The frequency density is compressed into a narrow band of high values, suggesting a systematically vulnerable microclimate, where structural characteristics offer minimal differentiation in thermal behavior.

This compact distribution is in line with the morphological characteristics of industrial fabric: large, isolated buildings, minimal shade coverage, and uniformly exposed ground surfaces. As a result, the entire area responds homogeneously to climatic stresses, with little

capacity to buffer or modulate incoming heat loads. These results reinforce the critical need for radical adaptation strategies in industrial areas, aimed at improving shading, surface albedo, and vegetation cover to increase future thermal resilience.

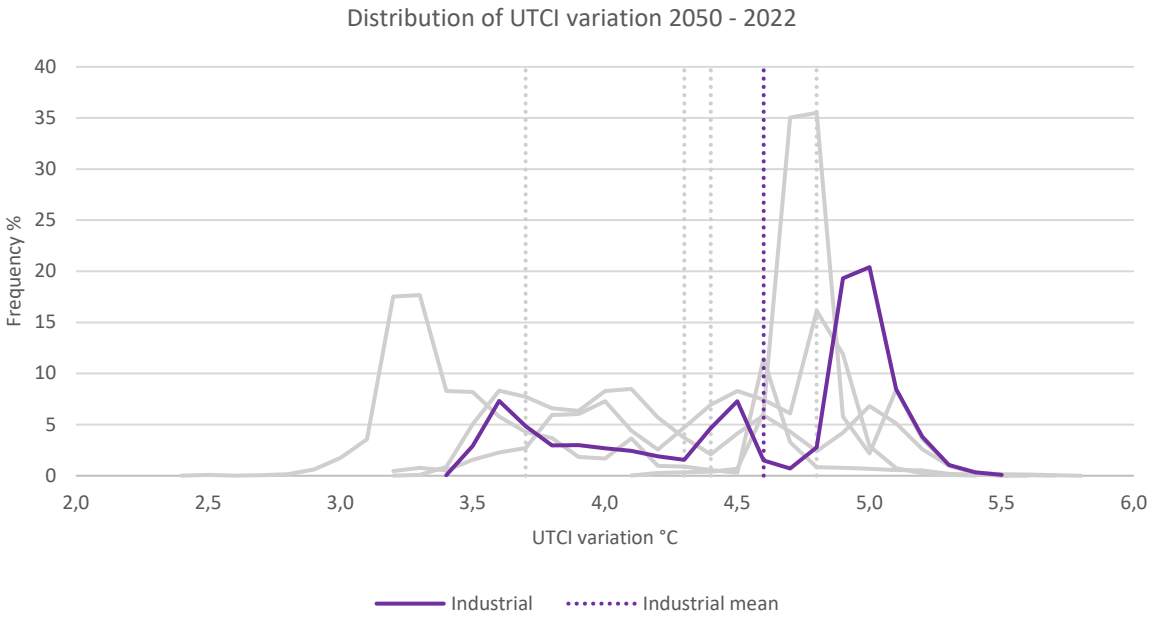

Figure 34. Distribution of UTCI variation for the UP_3 configuration. The curve shows a marked concentration between 4.9°C and 5.0°C, with a high mean value and low variability, indicative of low, diffuse, and uniform climate resilience.
Copyright: Marcello Turrini, Emanuele Naboni, Barbara Gherri 2022

Configuration UP_4 – Natural area

Figure 35 shows the spatial distribution of UTCI values in the configuration UP_4 - Natural area for the reference date and time, comparing the 2022 and 2050 scenarios. In the 2022 simulation, most of the domain remains in the Strong Heat Stress range, between 34 and 39 °C, with blue and light blue tones dominating especially along the river corridor and in the densely vegetated area to the west. The central water body contributes to localized cooling, while the forest cover on the left side provides constant shade and an evapotranspirative buffer.

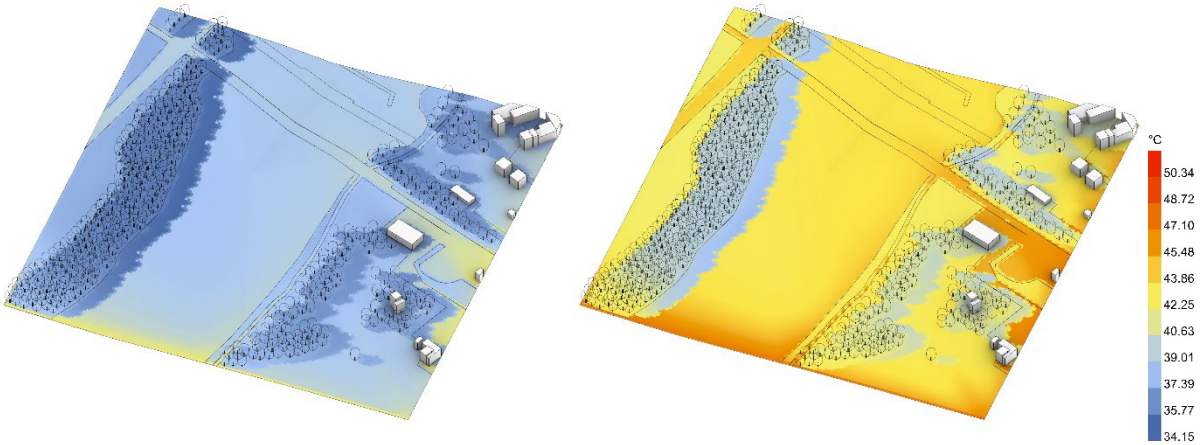

Figure 35. UP_4 – Natural area. UTCI on 17 August at 4:00 pm. 2022 on the left, 2050 on the right. Copyright: Marcello Turrini, Emanuele Naboni, Barbara Gherri 2022

In contrast, the 2050 scenario reveals a marked increase in temperature across the entire area. Most of the surfaces move from the 'Strong' to 'Very Strong' heat stress categories, above 40 °C, particularly in the clearing with sparse and dense tree cover on the eastern side, where the open ground and discontinuous shading allow for greater solar gain. The asphalt-paved road and bridge, which cut across the upper third of the frame from east to west, show high UTCI values, confirming the heat retention effect of paved infrastructure even in predominantly natural landscapes.

Despite the presence of natural elements, the map suggests that not all vegetated environments behave in the same way under warming conditions: dense, continuous vegetation combined with water surfaces provides effective thermal moderation, while fragmented or disordered groups of trees prove insufficient to counterbalance increasing heat loads. This highlights the need to distinguish between qualitative types of 'green' in resilience assessments, as their performance diverges significantly in high-stress scenarios.

The spatial distribution of UTCI variation for the configuration UP_4 - Natural area, as shown in Figure 36, mainly ranges between 3.8 °C and 5.5 °C, with higher values concentrated in the cleared areas and along the paved road corridor. In contrast, the riparian zone adjacent to the river and the densely vegetated western section show relatively lower increases, ranging between 2.8 and 4.0 °C, reflecting the buffering effect of the continuous canopy cover and latent cooling due to the presence of water.

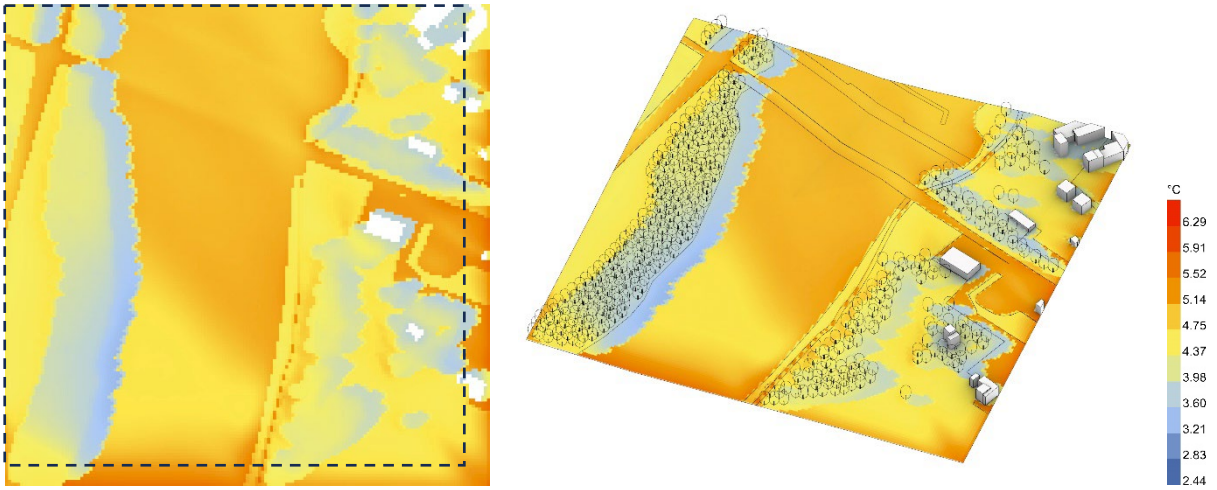

Figure 36. Variation in UTCI between 2022 and 2050 in the Configuration UP_4 – Natural area. The area within the dashed rectangle is the area actually used for numerical evaluation, as it is free from bias resulting from the edge effect of the CFD.
Copyright: Marcello Turrini, Emanuele Naboni, Barbara Gherri 2022

However, the difference between tree-shaded areas and those with open vegetation is clear: scattered groups of trees in the eastern sector show an unexpectedly high variation of UTCI, often comparable to that of adjacent bare surfaces. This suggests that fragmented vegetation does not possess the thermal inertia and microclimatic cohesion necessary to provide effective mitigation under future climate conditions. Furthermore, the road surface crossing the upper part of the domain shows a thermal amplification similar to that observed in fully built-up environments, highlighting the disproportionate impact of even minimal infrastructure within natural systems.

These results support the interpretation that the effectiveness of natural soil cover in mitigating heat depends not only on its presence, but also on its continuity, density, and interaction with local airflows and water bodies. Simply preserving green and blue infrastructures is not enough: spatial configuration and ecological structure are key in determining adaptive performance.

The statistical distribution of the UTCI variation for the configuration UP_4 - Natural area is characterized by a broad and irregular frequency profile, with values ranging from 3.2 °C to 5.4 °C, as shown in Figure 37. The curve has no dominant mode, but instead has multiple small peaks, particularly around 4.0 °C, 4.5 °C, and just below 5.0 °C. The mean value is at 4.4 °C, indicating a moderately high overall increase in heat stress.

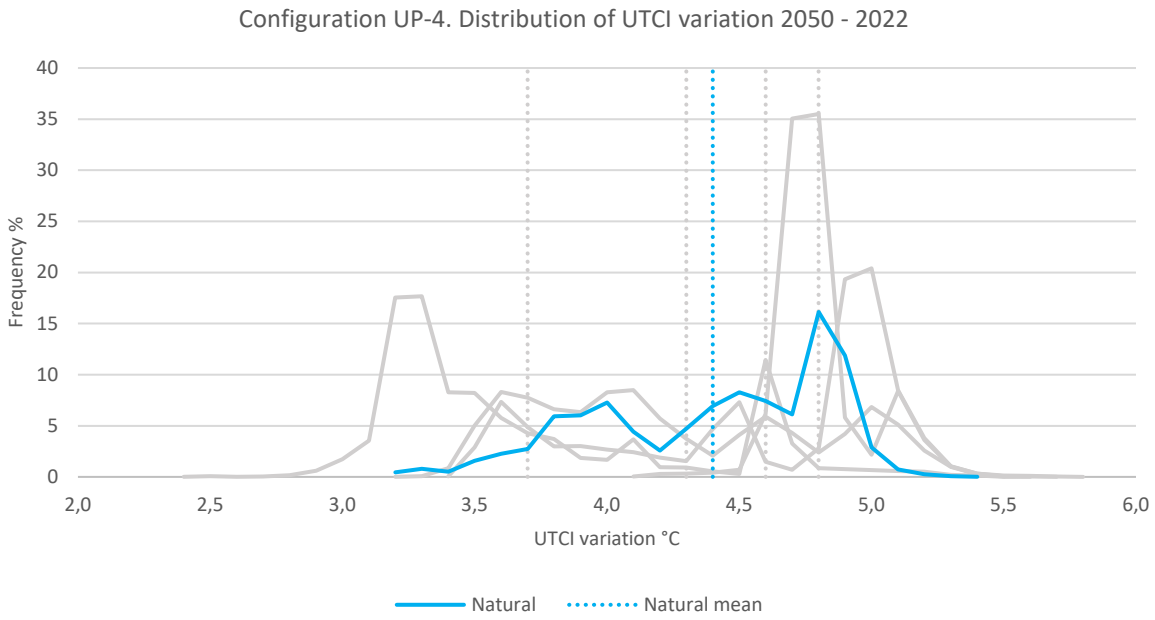

Figure 37. Distribution of UTCI variation for the configuration UP_4 - Natural area. The curve shows an irregular and multimodal profile, with an average of around 4.4°C, indicating a heterogeneous thermal response linked to internal variability in the soil, vegetation, and proximity to water. Copyright: Marcello Turrini, Emanuele Naboni, Barbara Gherri 2022

Compared to other configurations, the natural area is distinguished by its greater internal variability. This suggests that local environmental conditions, such as vegetation density, soil cover, and proximity to water bodies, introduce considerable spatial heterogeneity in the thermal response. The absence of a single prevailing peak, apart the slightly predominant peak of 4.8 °C corresponding to the water body of the river, reflects the diversification of thermal performance of different ecological zones within the same domain.

In particular, the lack of values in the lower range of variation below 3.3 °C implies that even the best-performing sub-zones experience a significant increase in UTCI, demonstrating that passive natural mitigation, while effective in relative terms, does not prevent absolute heat intensification in future climate projections. This supports the conclusion that natural areas require active improvement and structural continuity to serve as reliable climate buffers.

Configuration UP_5 – Agricultural area

The UTCI distribution for the configuration UP_5 - Agricultural area is shown in Figure 38, comparing 2022 and 2050 scenarios for a typical heat peak event on August 17 at 4:00 p.m. In the 2022 map, the landscape is predominantly under “Strong heat stress” in the UTCI scale, with UTCIs nearly 39 °C, especially in open fields and about 34 °C along road axis. The small group of buildings near the center, surrounded by sparse vegetation, appears slightly warmer but remains below 36 °C. The south and east edges of the area are clearly affected by CFD edge effects and are therefore excluded from the analysis.

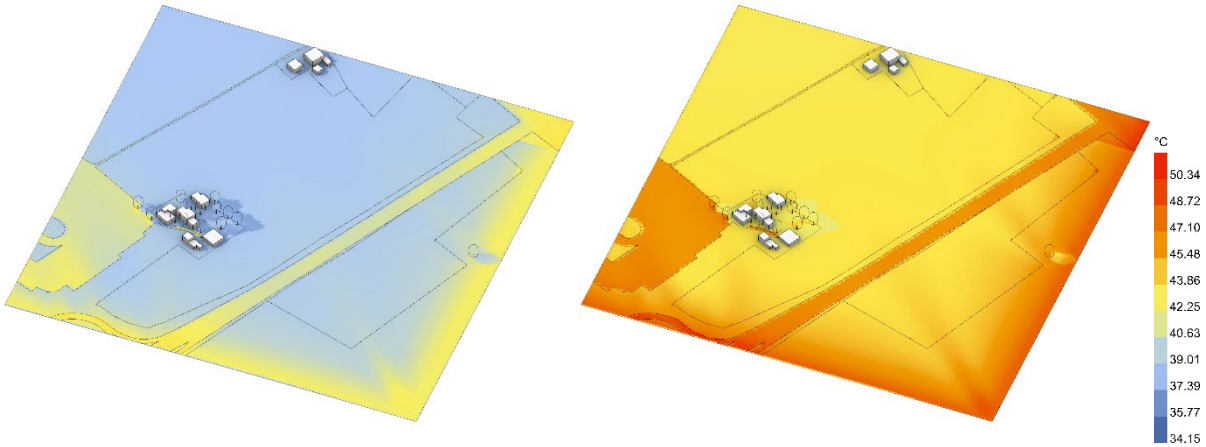

Figure 38. UP_5– Agricultural area. UTCI on 17 August at 4:00 pm. 2022 on the left, 2050 on the right. Copyright: Marcello Turrini, Emanuele Naboni, Barbara Gherri 2022

In the 2050 simulation (right), the entire domain undergoes a significant change in thermal conditions. UTCI values rise steadily above 42 °C, with large portions of the terrain, particularly the paved road and paring plot in the south-west part, reaching very strong thermal stress levels, above 45°C. The exposed nature of the area, minimal vegetation cover, and lack of structural shading contribute to this pronounced increase in heat stress.

The spatial uniformity of warming in the 2050 projections also reflects the limited microclimatic diversity of this type of land use. Unlike more complex urban or natural configurations, the agricultural fabric lacks elements capable of modulating the energy balance on a small scale. These results reinforce the urgency of considering adaptive strategies such as vegetative buffer zones, shaded infrastructure, and surface soil treatments even in non-urban landscapes, which are often overlooked in urban climate resilience planning.

Figure 39 illustrates the variation in UTCI between 2022 and 2050 for the UP_4 - Agricultural area. The analysis is limited to the central domain outlined by the dotted square in the left view, which omits peripheral pixels influenced by CFD boundary effects. Within this area, the variation in UTCI is consistently high, with the vast majority of the area showing values between 4.7 °C and 6 °C and large contiguous areas exceeding 5.5 °C.

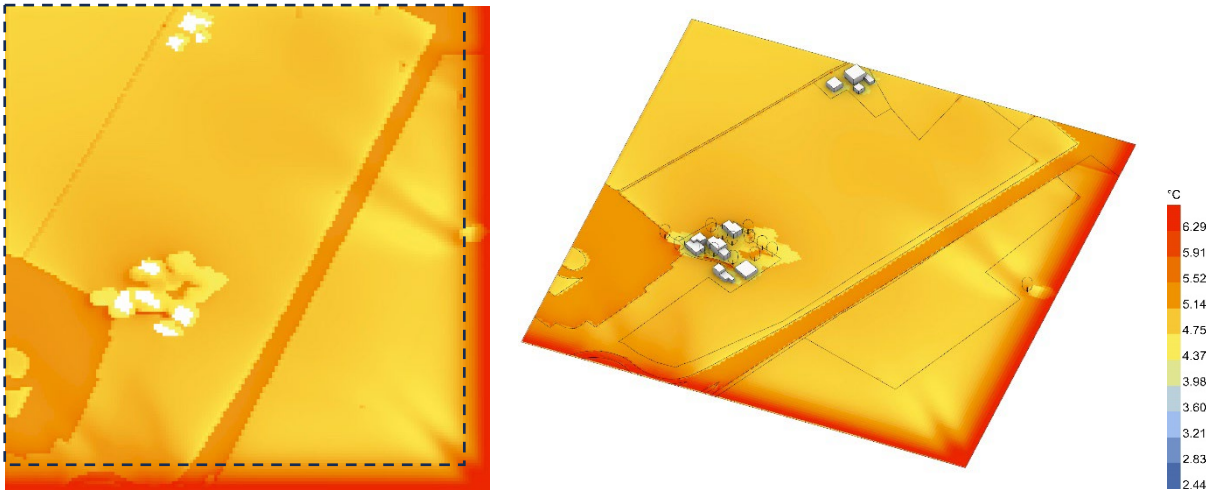

Figure 39. Variation in UTCI between 2022 and 2050 in the Configuration UP_5 – Agricultural area. The area within the dashed rectangle is the area actually used for numerical evaluation, as it is free from bias resulting from the edge effect of the CFD. Copyright: Marcello Turrini, Emanuele Naboni, Barbara Gherri 2022

The spatial uniformity of the variation confirms the intrinsic climatic exposure of the agricultural landscape, which lacks both vertical structure and significant vegetation complexity. The areas surrounding the small group of buildings offer no significant mitigation and show variations similar to those of completely exposed fields, demonstrating that planting isolated trees at low density is not sufficient to influence thermal dynamics under future climate conditions.

In particular, the road corridor and large parking plots have the highest UTCI variation values, reaching the upper limit of the scale used. This suggests that surface impermeability, low albedo, and high solar gain remain critical factors in heat amplification even in non-urban contexts.

Unlike more morphologically complex configurations, UP_5 does not provide localized thermal refuges, and the variation map reveals a homogeneous amplification of heat stress, raising serious concerns for human activity and well-being, besides ecosystem stability, and

infrastructure durability in peri-urban agricultural areas. These results underscore the need to reformulate resilience strategies to include rural and agricultural morphologies as integral parts of climate adaptation policies.

The statistical distribution of UTCI variation for the agricultural configuration (Figure 40) shows a highly concentrated curve, with a sharp peak between 4.7 °C and 4.8 °C and a total range from 4.1 °C to 5.8 °C. The mean value, indicated by the dotted line, is 4.8 °C, the highest among all the configurations considered.

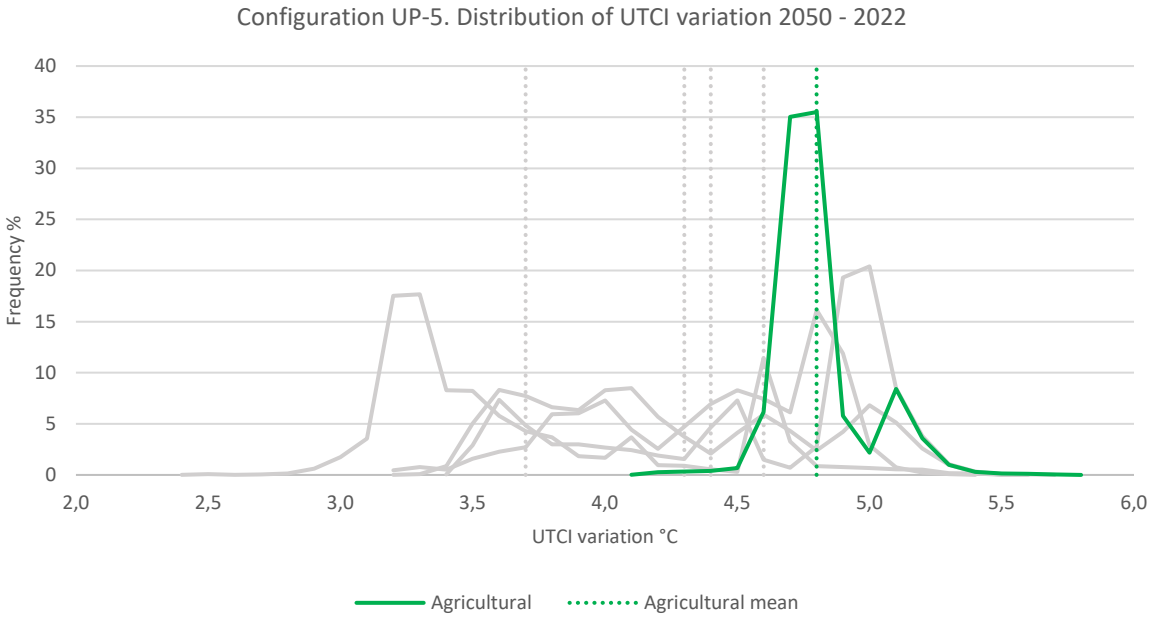

Figure 40. Distribution of UTCI variation for the configuration UP_5 - Agricultural area. The curve shows a very marked peak between 4.7°C and 4.8°C, with a mean value of 4.8°C and a limited range between 4.1 and 5.8°C, indicating high thermal homogeneity and low climate resilience. Copyright: Marcello Turrini, Emanuele Naboni, Barbara Gherri 2022

This distribution reflects the homogeneous and uniformly exposed nature of the agricultural landscape. The absence of morphological complexity, vegetation stratification, or significant shading elements results in a constant amplification of heat stress across almost the entire domain. Unlike other configurations with multimodal or dispersed profiles, UP_5 is characterized by microclimatic monotony, where virtually all areas experience a similar increase in perceived temperature.

The absence of values below 4.0 °C highlights the absence of thermal refuges and that even the most favorable areas within this configuration contribute significantly to the overall heat load. This singular, high-density peak reinforces the need to consider agricultural

environments as priority areas for climate adaptation, particularly where human work, food production, and ecological services are directly affected by extreme heat events.

5.1.6 Discussion

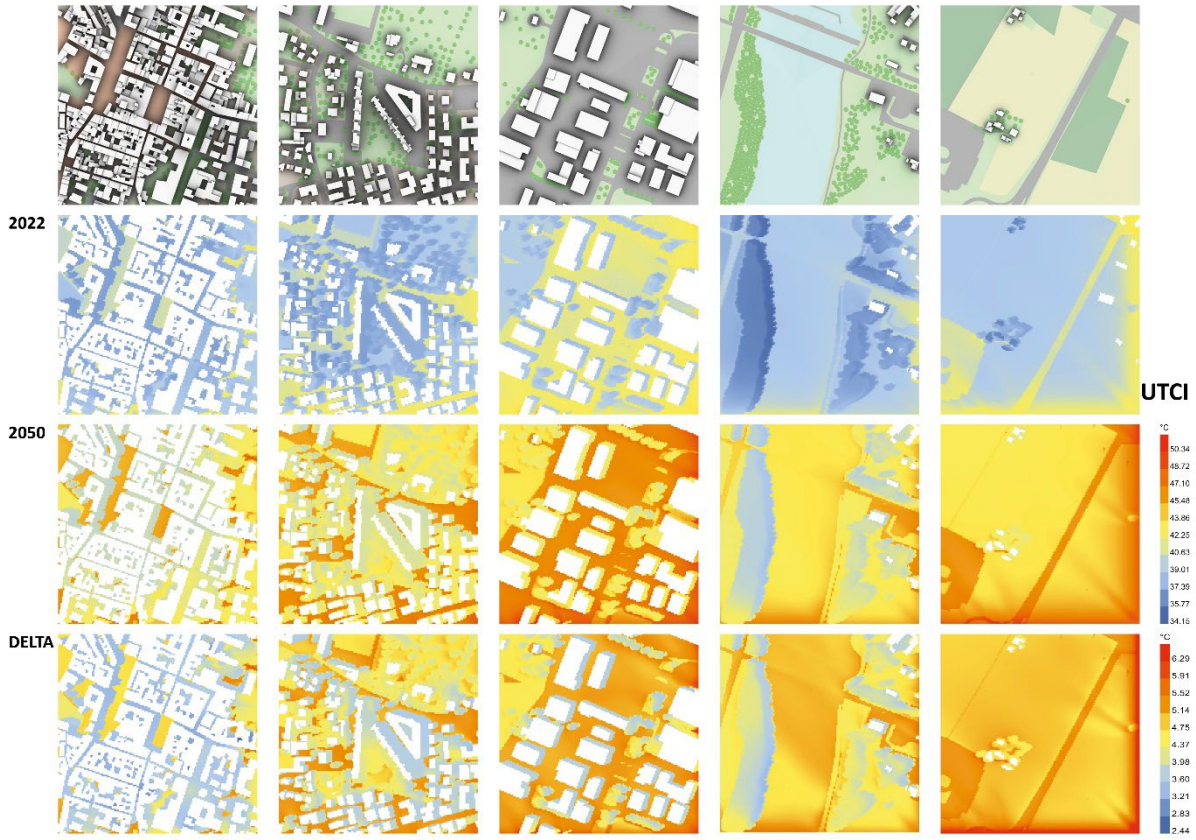

Figure 41. Summary comparison between the five morphological configurations analyzed (from left: historical urban fabric, modern urban fabric, industrial area, natural area, agricultural area), with visualization of the 3D models, the absolute UTCI values simulated for August 17 at 4:00 p.m. in the two scenarios (2022 and 2050), and the relative UTCI variation (delta). The figure highlights how the thermal response to climate change is strongly influenced by urban morphology: compact and shaded (historic) areas show limited increases, while more exposed and unmitigated (industrial, agricultural) areas show a marked and homogeneous increase in perceived heat stress. Copyright: Marcello Turrini, Emanuele Naboni, Barbara Gherri 2022

Applying the methodology to the urban mesoscale of Sassuolo showed that UTCI variation between current and future scenarios is a sensitive and robust indicator of the resilience of built environments to climate change. By simulating the thermal performance of five distinct morphological configurations in two climate scenarios, 2022 and 2050, with an RCP 8.5 profile, the study was able to generate differentiated thermal response profiles related to urban form, land use, and surface materiality.

Comparing the various configurations, the following performances emerge for each configuration.

Configuration UP_1 – The historic urban fabric showed the lowest average UTCI variation of approximately 3.7 °C, with a narrow distribution and a well-defined peak around 3.3 °C. The dense morphology, narrow alleys, and high surface-to-shadow ratio effectively limited thermal amplification, confirming the passive resilience of pre-modern urban forms. Even during peak hours, compactness and continuous shading provided a significant buffer, validating the potential of historic cores as thermal refuges.

Configuration UP_2 – The modern urban fabric showed a dispersed thermal response with an average of around 4.3 °C, with no clear trend and a variation between 3.3 and 5.6 °C. Inconsistent shading, exposure to solar radiation, and sparse vegetation contributed to a thermally unstable microclimate. In particular, areas shaded by trees performed worse than those shaded by buildings, due to reduced evapotranspiration at high temperatures and aerodynamic resistance to airflow, suggesting that the qualitative arrangement of vegetation is as important as its quantity.

Configuration UP_3 – The industrial area showed the highest level of uniform heat amplification, with UTCI variation closely concentrated between 4.9 and 5.0 °C. The frequency distribution showed a single dominant peak and virtually no low-variation zones, demonstrating the critical vulnerability of impervious, low-density industrial fabrics. The lack of vegetation, combined with large, paved surfaces and low building heights, generated uniform overheating with no local buffering effects.

Configuration UP_4 – The natural area showed a wide, multimodal distribution with an average of 4.4 °C, reflecting the high internal heterogeneity of natural environments. Dense wooded areas and water bodies showed lower variations, down to 2.8 °C, while barren areas and road surfaces exceeded 5.5 °C. The data support the idea that not all green infrastructure is thermally equivalent: continuity, structure, and interaction with hydrological characteristics are key to effective mitigation.

Configuration UP_5 – The agricultural area showed a very narrow and steep distribution, centered around 4.8 °C, with minimum values below 4.1 °C and a large portion above 5.5 °C. The homogeneity of land use, the absence of shading, and the presence of a large, paved road

produced a monotonous and amplified thermal response, with no microclimatic variations or thermal refuges throughout the domain. This confirms the extreme exposure of peri-urban agricultural areas to climate change, which is often overlooked in urban resilience strategies.

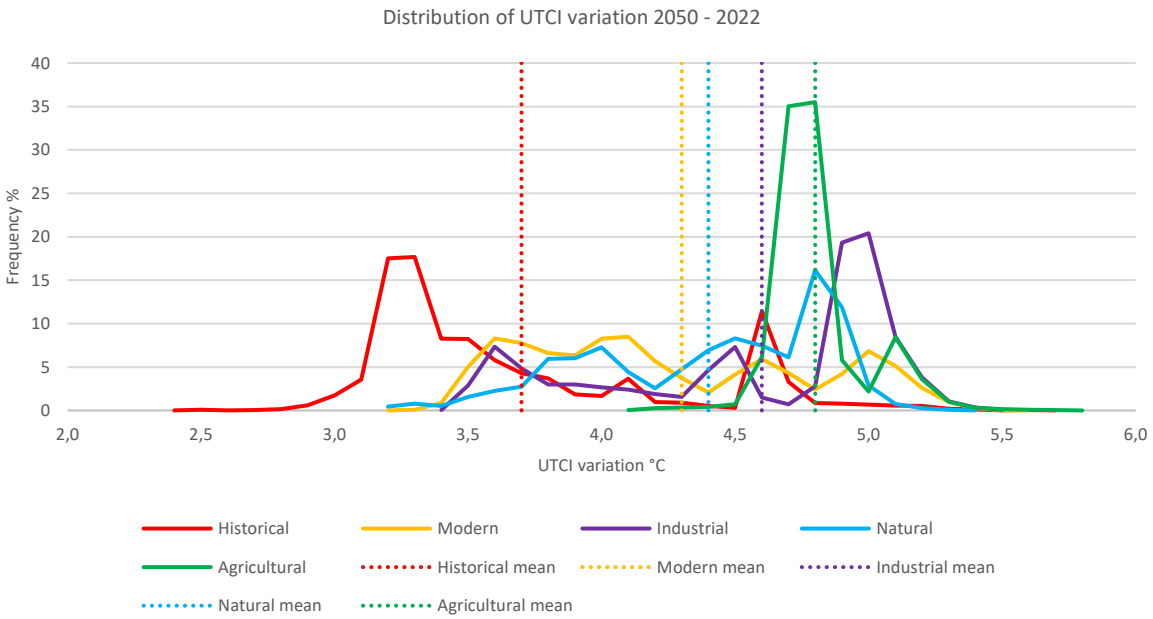

Figure 42. Statistical distribution of UTCI variation between 2022 and 2050 for the five morphological configurations analyzed. The curves represent the relative frequency of UTCI variation within each configuration, while the dotted lines indicate the average value for each case. The graph clearly shows the greater thermal resilience of the historic fabric, with a low average and concentrated distribution, compared to the marked vulnerability of the agricultural and industrial configurations, characterized by high peaks, low internal variability, and an average above 4.7°C. Copyright: Marcello Turrini, Emanuele Naboni, Barbara Gherri 2022

Methodological implications

The use of UTCI variation as a key metric in this study has proven capable of capturing the spatial heterogeneity of thermal dynamics at the meso-scale; highlighting morphological thresholds beyond which thermal resilience deteriorates; distinguishing between structural and surface mitigation mechanisms; and translating urban form into a measurable climate performance profile.

Furthermore, the method demonstrated excellent scalability, as it does not require calibration on absolute values and can be applied to any urban context or morphology, including historical, contemporary, industrial, natural, or agricultural areas. The workflow, based on thermodynamic simulations in two different time scenarios, 2022 and 2050, combined with the high-resolution voxel setting, data processing with Grasshopper, and post-

production work to exclude noise in some parts of the results, ensures both numerical stability and spatial accuracy, meeting the operational requirements for assessing resilience at the urban meso-scale.

Indicator	UP_1	UP_2	UP_3	UP_4	UP_5
Typology and key spatial traits	Compact blocks, narrow streets, reduced sky visibility, continuous architectural shade	Discontinuous building form, fragmented vegetation, open paved areas (roads/parking)	Low buildings, wide spacing, large sealed/dark surfaces, little vegetation	Continuous forest patches and water bodies, but also clearings and paved infrastructure	Open field with minimal vertical structure, sparse vegetation, limited shading; paved road/parking
Baseline UTCI	Mainly 32–38 °C, most areas < 39 °C	Shaded zones ~38–46 °C; exposed paved surfaces critical	Mainly ~37–42 °C; open/paved areas already > 43 °C	Mostly ~34–39 °C; cooler along river and forested zones	Predominantly ~34–39 °C (open fields ~39 °C; road axis ~34 °C)
Future UTCI	General increase; many areas ~40–45 °C, inner canyons relatively buffered	Shaded zones shift to ~46–50 °C; asphalt frequently > 46 °C and locally > 50 °C	Large areas > 46 °C, approaching ~50 °C	Many surfaces > 40 °C; clearings and road/bridge show high values	Values generally > 42 °C; road and parking areas reach > 45 °C
Mean ΔUTCI (°C)	≈ 3.7	≈ 4.3	≈ 4.6	≈ 4.4	≈ 4.8
ΔUTCI range (°C)	~2.8–4.6 (most values 3.2–3.6)	~3.3–5.6 (isolated peaks > 5.9)	~4.3–5.9 (large areas ≥ 5.5)	~2.8–5.5 (low near water/forest; high in clearings/road)	~4.7–6.0 (large areas ≥ 5.5)
Spatial response pattern	Narrow and stable; clear peak (~3.3 °C); limited hotspots	Dispersed, no dominant mode; multiple minor peaks	Very narrow and high; strong peak at 4.9–5.0 °C; spatially uniform	Multimodal; strong internal heterogeneity	Very narrow, steep, high; absence of low-ΔUTCI refuges
Main microclimatic drivers and design reading	Radiative buffering dominates: low SVF and continuous shade restrain MRT amplification and preserve pedestrian-level thermal shelters	Fragmentation effect: inconsistent shade leads to high MRT; tree shade may underperform architectural shade when evapotranspiration is constrained and canopy reduces wind; requires *systemic* greening	Uniform overheating: high surface temperatures and MRT with limited shade produce homogeneous ΔUTCI increase; priority levers are continuous shading, surface albedo, and structural greening	Quality of green matters: continuous canopy and water enable shading and evapotranspirative buffering; fragmented clearings and asphalt remain critical; resilience depends on continuity and hydrological coupling	Exposure-driven monotony: high sky exposure and lack of shading lead to strong, uniform MRT-driven amplification; adaptation requires *structured* shade (buffers, shaded routes, soil/surface strategy), not isolated low-density planting

Table 6 Comparative synthesis of the ΔUTCI-based assessment for the five urban-scale configurations in Sassuolo (UP_1–UP_5), evaluated at the selected peak-summer time slice under paired baseline and future climate scenarios (2022 vs 2050, RCP 8.5). The table summarizes absolute UTCI conditions, ΔUTCI magnitude, and internal variability within the defined evaluation domain, supporting a comparative interpretation of thermal resilience across different urban morphologies

.

5.1.7 Conclusions for urban scale applications

At the urban scale, the Sassuolo simulations confirm that the proposed workflow can distinguish, in a clear and operational manner, between urban morphologies that buffer climatic intensification and those that amplify it. By using ΔUTCI (2050–2022) as the central comparative indicator at peak summer conditions, resilience is framed not as the achievement of absolute comfort, but as the capacity of a district morphology to limit how strongly future forcing propagates into pedestrian-level thermal stress.

Across the five configurations, the results form a coherent gradient. The historic urban fabric (UP_1) exhibits the lowest mean amplification (≈ 3.7 °C) and a comparatively stable distribution, with most values concentrated between 3.2 and 3.6 °C and a clear dominant mode around 3.3 °C. In resilience terms, this indicates that compactness and pervasive architectural shading do not remove heat stress, but they measurably constrain the additional load imposed by the future scenario. The modern urban fabric (UP_2) shifts toward higher sensitivity, with a mean ΔUTCI of about 4.3 °C and a broad range (roughly 3.3–5.6 °C) with no dominant peak. This dispersed profile is an important conclusion in itself: it signals a morphology where microclimatic performance is spatially inconsistent, and where “good pockets” and critical hotspots coexist without forming a stable buffering structure.

At the exposed end of the spectrum, the industrial (UP_3) and agricultural (UP_5) configurations represent two forms of low resilience expressed through high, spatially uniform amplification. The industrial domain shows ΔUTCI values mainly between 4.3 and 5.9 °C, while its distribution is sharply concentrated around 4.9–5.0 °C, indicating a coherent, domain-wide sensitivity with limited internal moderation. The agricultural configuration reaches the highest mean ΔUTCI (≈ 4.8 °C) and shows a similarly concentrated behaviour, with a marked peak at 4.7–4.8 °C and an overall spread of approximately 4.1–5.8 °C. These two outcomes highlight a key planning message: when horizontal sealed surfaces dominate and structural shading is absent, future warming tends to translate into thermal stress amplification that is not only severe, but also difficult to escape spatially.

Finally, the natural area (UP_4) demonstrates that “green” is not automatically synonymous with resilience. Its mean ΔUTCI remains moderately high (≈ 4.4 °C) and the distribution is multimodal (about 3.2–5.4 °C), reflecting internal differentiation driven by canopy continuity, water adjacency, and local surface conditions. This matters at district scale because it suggests that the resilience value of natural and vegetated systems depends on their spatial coherence and functional continuity, rather than on their mere presence as land cover.

Overall, the urban scale case study shows that the methodology produces design-relevant evidence at planning resolution: it not only ranks morphologies by their average sensitivity, but also exposes whether a district offers thermally stable microclimates or instead evolves toward monotone, unavoidable amplification. In practice, this supports a shift from generic mitigation narratives toward targeted strategies that prioritize coherent shading structures, surface and material decisions, and continuous green–blue systems where they can operate as effective, spatially legible buffers under intensified summer conditions.

5.2 Building Scale: the case of the cloister of San Sepolcro in Parma.

A recurring element in Mediterranean architecture, and therefore in Italy, the internal cloister is an integral part of the building to which it belongs, both from a functional point of view, becoming a space for everyday life, and from a microclimatic point of view, mitigating the microclimate of the interior spaces. It is an intermediate space as a microclimatic buffer between indoor and outdoor microclimate. Therefore, working on a cloister, as in the case of San Sepolcro, is equivalent to working at the scale of the building. For this reason, this specific study [494] is introduced as the building-scale example for multiscale thermal-comfort assessment based on UTCI variations[495].

The study focuses on microclimatic adaptation to climate change in the cloister of the Convent of San Sepolcro in Parma. It is based on previous research on the surrounding urban block.[496]. The previous study highlighted potential overheating of the cloister by 2080[497], caused by intense solar radiation, poor ventilation, and high dry bulb temperatures. The new research examines mitigation strategies to reduce this overheating under future climate conditions.

[494] This study originates from a research assignment commissioned by the software house ENVI-met (Mainz, Germany) to the Department of Engineering and Architecture at the University of Parma. The assignment was part of the "ENVI-met World Tour" initiative, through which ENVI-met promoted research on urban climate adaptation and resilient urban development across different climate zones, using its microclimate simulation software. Working group: Emanuele Naboni, Barbara Gherri, Marcello Turrini, Rossella Siani.

[495] This work has been partially published in the article Naboni, E., R. Siani, M. Turrini, E. Touloupaki, B. Gherri, and F.D. Luca. 2023. 'Experiments on Microclimatically Adapt a Courtyard to Climate Change'. In. Vol. 1196. https://doi.org/10.1088/1755-1315/1196/1/012032 and discussed in the conference *IOP Conference Series Earth and Environmental Science* in 2022.

[496] Touloupaki, Eleftheria, Barbara Gherri, and Emanuele Naboni. 2023. 'A First Look at Italian Cloisters Resilience to a Changing Climate'. In *WILL CITIES SURVIVE? The Future of Sustainable Buildings and Urbanism in the Age of Emergency*, 2:644–49. Pontificia Universidad Católica de Chile. https://air.unipr.it/handle/11381/2940331.

[497] The end-of-century horizon (2080) is adopted in relation to the historical character of the San Sepolcro complex and its long expected lifespan, which extends beyond mid-century planning horizons.

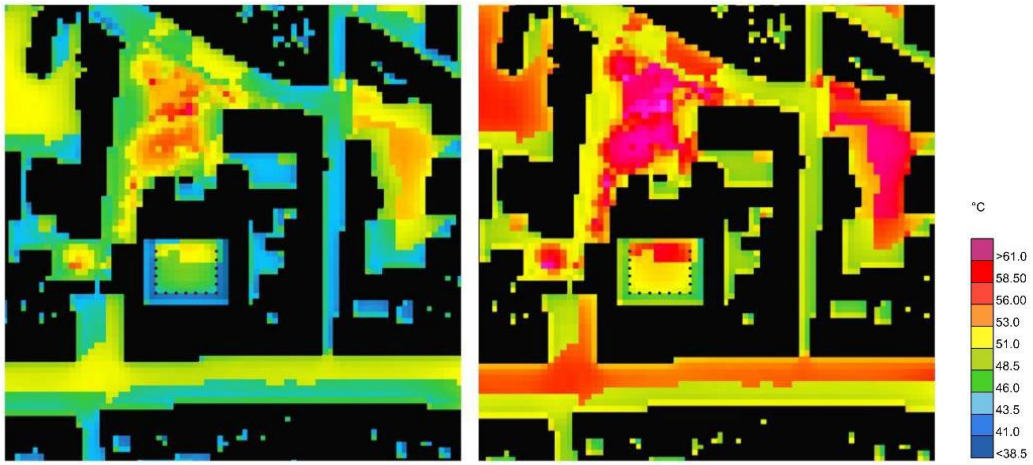

Figure 43. UTCI in the surrounding of the convent of San Sepolcro in Parma. Overheating problems related to climate change are evident, when the UTCI on august 5th 2080 at 3pm is higher than 50°C

5.2.1 Climate scenarios in Parma

Parma is located in the Po Valley and has a temperate, completely humid climate with hot summers (Cfa) according to the Köppen-Geiger climate classification system. The area is also characterized by a subcontinental climate according to regional classifications, with significant temperature variations between summer and winter. Analysis using the Johansson continentality index[498] places Parma in the transition zone between oceanic and continental climates, with index values just below the continental threshold. Moreover, the Kerner oceanicity index[499] confirms this continental trend, with values below 10, indicating a reduced maritime influence. The De Martonne aridity index[500], calculated on data from 1961-1990, classifies the region as semi-humid, with July identified as the driest month, an indicator of water stress in summer and a key factor in assessing the risk of overheating[501].

The dry bulb temperature profile for the city of Parma in the reference year 2022 shown in Figure 44 marks heat stress during the summer season. Between June and early September, maximum daily temperatures often exceed 32°C, with peaks reaching or exceeding 38°C during heat waves. Nighttime cooling is often limited, with minimum temperatures remaining above 68°F for several consecutive nights, giving rise to tropical nights. These conditions already pose

[498] Johansson, 1926
[499] Kerner, 1905
[500] De Martonne, 1926
[501] Nistor, 2016

a high risk of overheating, particularly in confined or poorly ventilated spaces, such as courtyards and historic cloisters, where heat retention is amplified by the geometry and materiality of the buildings.

Looking ahead to 2080, climate projections indicate a marked intensification of heat stress. Projected dry bulb temperatures show an average increase of 5-8°C during summer daytime hours, particularly from June to August. As a result, maximum daily temperatures are expected to regularly exceed 40°C, while early morning and evening values will also increase significantly. This reduction in temperature variations between day and night will limit the possibilities for passive nighttime cooling and exacerbate heat accumulation over time.

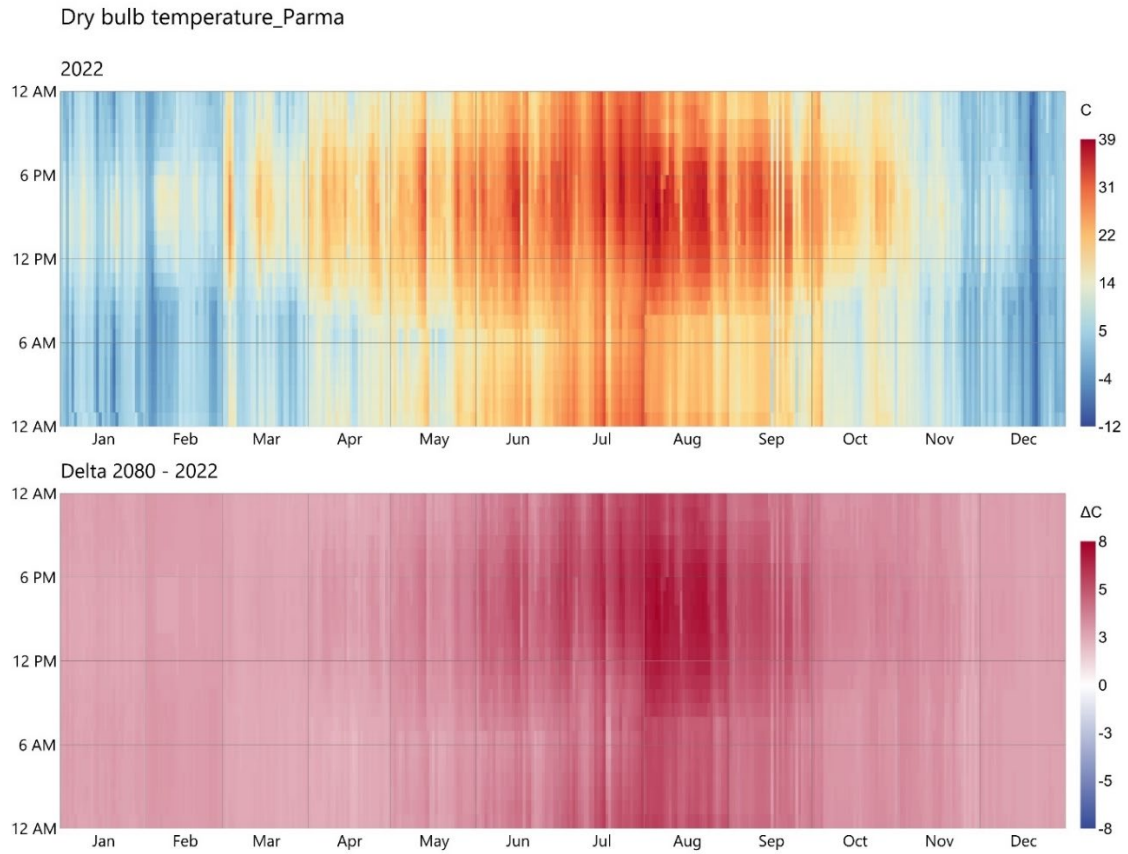

Figure 44. Hourly dry bulb temperature in Parma for the year 2022 (top) and projected temperature change for 2080 relative to 2022 (bottom), highlighting critical summer overheating and anticipated future intensification. Copyright: Marcello Turrini, Emanuele Naboni, 2023

Analysis of daytime wind speed profiles for a representative day in each month, as shown in Figure 45, reveals significant differences between current and future climatic conditions in Parma. In the reference year 2022, summer wind speeds typically range between 1 and 3 m/s, with limited variations during daylight hours. In contrast, projections for 2080 indicate a

significant increase in wind speeds during the same period, with average values often exceeding 3.5 m/s, particularly in the afternoon.

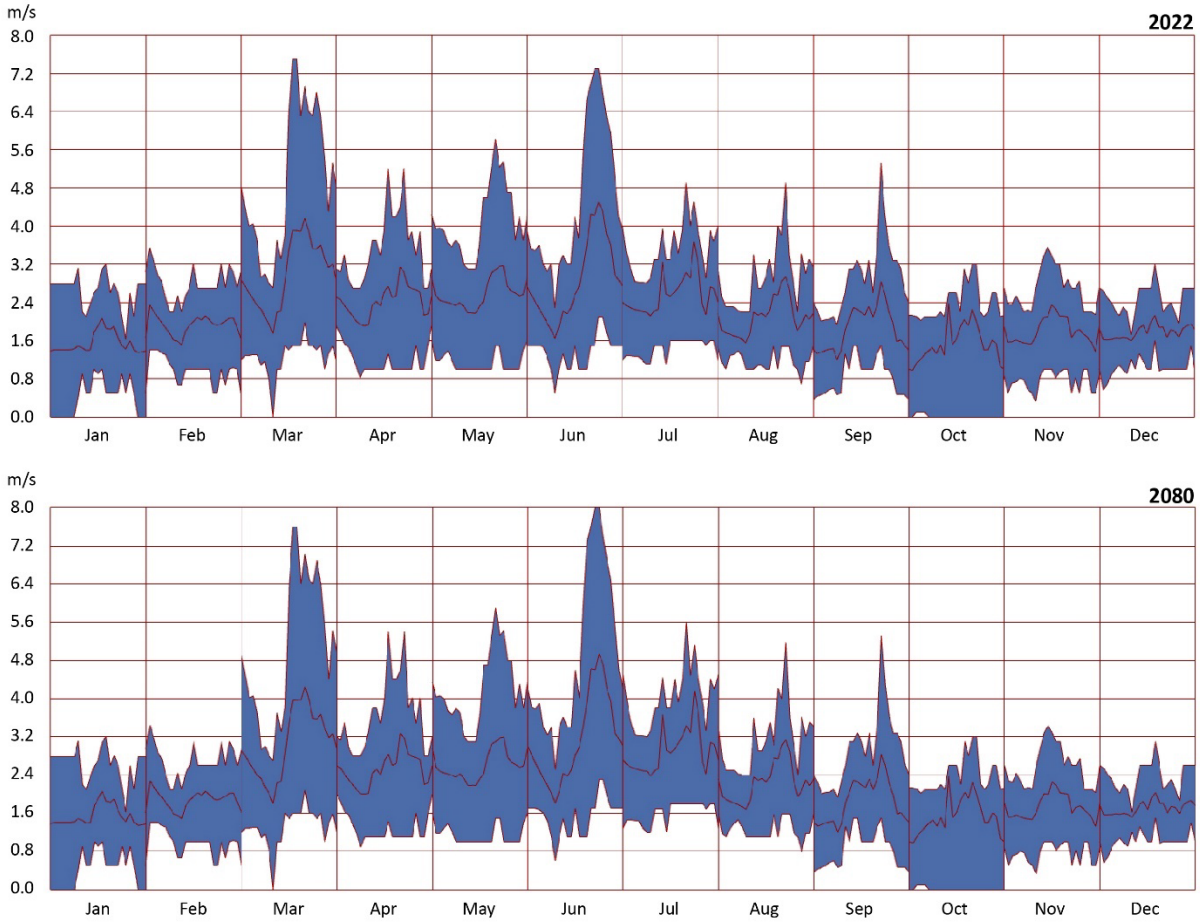

Figure 45. Hourly wind speed for a representative day of each month in Parma for 2022 (top) and 2080 (bottom). Each horizontal segment covers 24 hours, from 00:00 (left) to 24:00 (right), and represents the typical daily wind profile for that month. The red line shows the average wind speed, while the blue area indicates the daily range. In 2080, summer wind speeds will increase significantly during the hottest hours, potentially intensifying thermal discomfort due to increased convective heat. Copyright: Marcello Turrini, Emanuele Naboni, Barbara Gherri 2022

Although increased ventilation is often considered beneficial for microclimatic comfort, this assumption no longer applies when the ambient temperature exceeds the skin temperature threshold of approximately 33–35 °C, as observed in future summer conditions. In such circumstances, higher wind speeds can increase convective heat gain rather than promote cooling, especially when evaporative cooling is compromised by high humidity levels. This reversal of the typical thermoregulatory effect of wind exacerbates the risk of heat stress.

Relative humidity in Parma is high throughout the year, with peaks at night and in the early morning. Even in summer, relative humidity remains high, especially in the evening, when

values often exceed 70%. This prolonged humidity, combined with high temperatures, contributes to increased thermal discomfort, limiting the effectiveness of evaporative cooling mechanisms and increasing the sensation of heat.

5.2.2 Identification of Configurations

The monastic cloister adjacent to the Church of San Sepolcro in Parma, now known as the Chiostro delle Maestre Luigine, is an important architectural testimony to the stylistic change that took place in northern Italy at the end of the 15th century. Its construction has been attributed to the architect Ziliolo da Reggio and was dated between 1493 and 1495. The finely carved capitals and columns are attributed to Antonio Ferrari d'Agrate, important architect in the region at that time.

Figure 46. The cloister. Three porticoed galleries are on the sides facing north, east and west. A green pavement is in the entire area of the open space. A well is in the middle. Only some small edges on the northern part are the elevated vegetation. Copyright: Marcello Turrini, Emanuele Naboni, Barbara Gherri 2022

Today, the cloister is managed by the religious community of the Maestre Luigine. The layout is organized with porticoed galleries on three sides, while the southern side has no portico and is made by a closed masonry wall. In the center of the cloister there is a simple open-air garden, unpaved and covered with a layer of vegetation. The dense and traditional materials, like brick and stone, give the structure considerable thermal mass, mitigating

external temperature variations and promoting a more regulated internal thermal environment throughout the year.

In the Sassuolo ceramics-district case study, configurations were available as distinct territorial layouts and were therefore analyzed as-is, leveraging their spatial and microclimatic diversity. In the San Sepolcro convent and cloister case study, configurations were generated by ideal modifications of the existing building's geometric and physical layout, targeting the cloister's critical issues: overheating due to intense radiation, high dry-bulb temperature, and limited ventilation. This resulted in four configurations, hereafter referred to as SS_1 (Base case), SS_2 (Shading), SS_3 (Humidity), and SS_4 (Ventilation).

The configurations chosen are purely theoretical, intended solely for the purposes of this study, and do not take into account actual feasibility in terms of structural robustness, technical aspects, or preservation of the building's historical value.

Configuration SS_1 – Base case. This configuration considers the cloister as it is, with green permeable flooring, three porticoed sides and one side consisting of a completely infilled wall without portico. The central space is completely open to the sky, with perimeter walls in light-colored plastered brick and stone flooring in the porticoed areas (Figure 47).

Figure 47. Configuration SS_1 - Base case. Green permeable pavement, open to the sky, three porticoed sides. Rendering on the left by Armin Pirngruber. Source of the image on the right: https://internoverde.it/chiostro-delle-maestre-luigine/

Configuration SS_2 – Shading. This configuration includes a canopy system that blocks direct sunlight throughout the cloister, but does not obstruct radiation exchange with the sky or vertical ventilation. It consists of vertical prisms with a square base measuring 3 meters on each side, open at the bottom and top and joined together to form a single element. In this

way, solar rays inclined to the vertical are blocked by the side surfaces of the prisms, while in the vertical direction, exchanges with the sky are guaranteed by the openings.

The shading element was sized using a parametric generative workflow in Grasshopper (Galapagos) to optimize geometry dimensions, reducing material use while maximizing cloister shade. A high-albedo material was selected to limit overheating of the shading element and the consequent radiant heat emission toward the cloister (Figure 48).

Figure 48. Configuration SS_2 - Shading. Representation of the shading element on the cloister. Direct radiation, inclined with respect to the vertical, is blocked by the vertical elements, while radiative exchange with the sky and vertical ventilation is guaranteed. Renderings by Armin Pirngruber. Copyright: Marcello Turrini, Emanuele Naboni, Barbara Gherri, 2022

Configuration SS_3 – Humidity. The Cloister of San Sepolcro is currently characterized by a simple layer of grass covering the open area. The proposed configuration (Figure 49) involves the introduction of tall and low vegetation and the creation of a large pond occupying about one third of the total area. The vegetation selected consists of native deciduous species. Tree-species distribution was defined with reference to the northern portion of the cloister, which is more exposed to sunlight. The water feature is located in the southern third, which is shaded to prevent overheating.

Thanks to its high thermal inertia and its ability to promote evaporation, the water has a significant impact on thermal comfort. On the other hand, the vegetation, with its evapotranspirative effect, besides providing shade, contributes to humidity enhancement in the cloister. The combination of these two natural elements creates a synergistic system that defines a unique microclimate distinct from other configurations.

Figure 49. Configuration SS_3 - Humidity. Dense canopies of vegetation and water provide humidity to the cloister. Renderings by Armin Pirngruber. Copyright: Marcello Turrini, Emanuele Naboni, Barbara Gherri, 2022

Configuration SS_4 – Ventilation. This configuration considers the cloister open on the north side, at the level of the ground floor portico, to connect the interior of the cloister with the external area, allowing wind to flow inside it. The open part maintains the same rhythm of arches and columns as the other three sides of the cloister. Modifying the ventilation profile affects the perceived thermal comfort inside the cloister. This configuration is purely theoretical and is proposed to support microclimatic evaluation of potential alternative configurations. Therefore, and for its hypothetical implementation, it would be necessary to irreversibly alter parts of the building that could be crucial for its functionality and integrity from a historical point of view. The purely theoretical nature of this configuration is therefore emphasized (Figure 50).

Figure 50. Configuration SS_4 - Ventilation. The opening on the ground floor of the cloister connects the internal space to the outside, guaranteeing wind penetration. Renderings by Armin Pirngruber. Copyright: Marcello Turrini, Emanuele Naboni, Barbara Gherri, 2022

By acting on individual microclimatic factors, it becomes clear that these four configurations constitute a range of highly differentiated options. The methodology's ability to detect thermal-comfort resilience can therefore be tested through the variation in UTCI between the current scenario and the 2080 scenario across markedly different configurations.

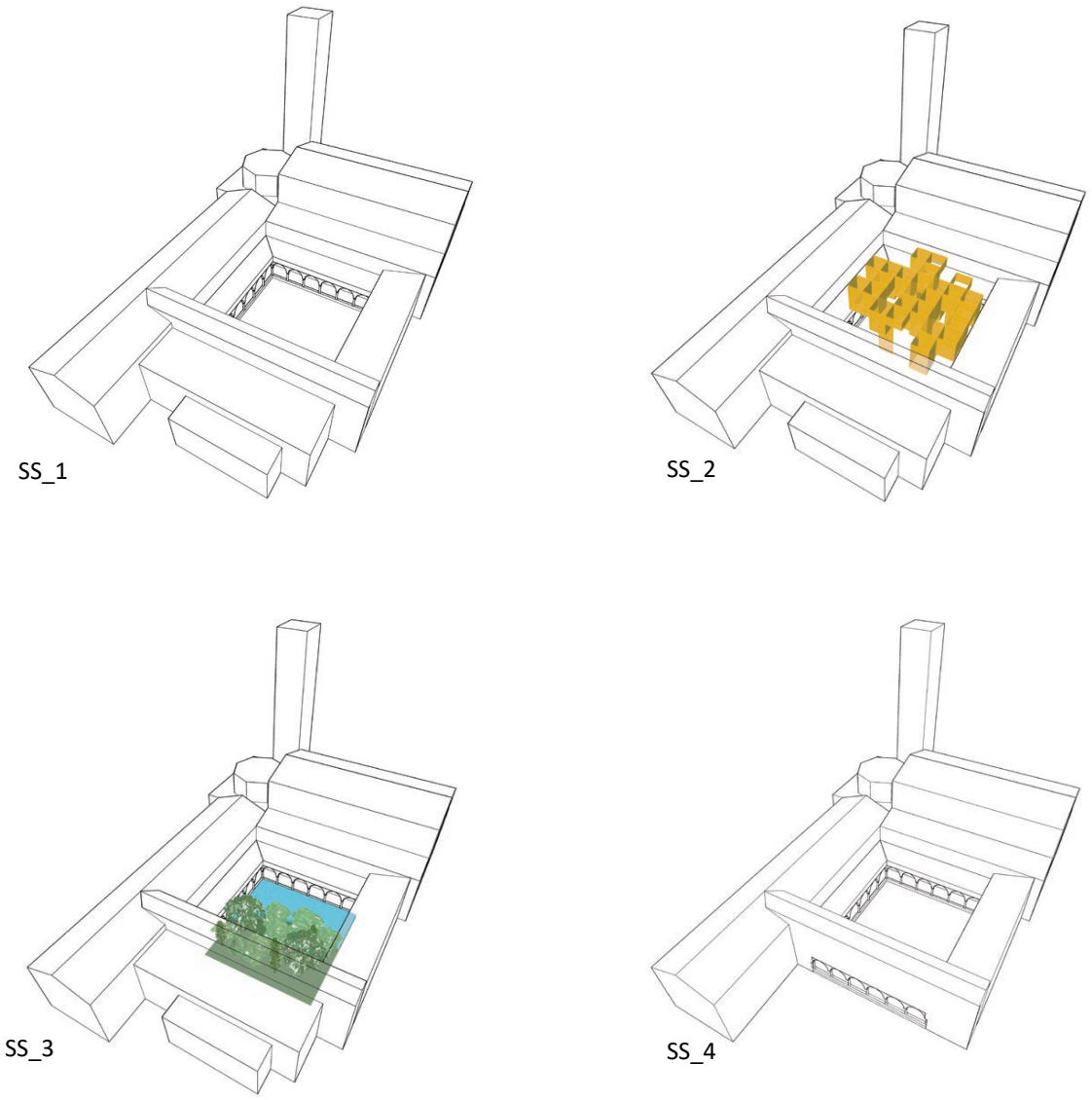

Figure 51. The four proposed configurations: SS_1 - Base case, SS_2 - Shading, SS_3 - Humidity, SS_4 - Ventilation. View from north. Copyright: Marcello Turrini, Emanuele Naboni, Barbara Gherri, 2022

5.2.3 Processing of three-dimensional digital models

In this case study, the convent 3D model was downloaded from OpenStreetMap[502] and further detailed in Rhinoceros using Google Maps 3D views as reference measurements. Surfaces and solids were separated by material to facilitate export to the simulation software. The model was further simplified by removing small elements (e.g., arcades and columns) and by flattening pitched roofs (Figure 52).

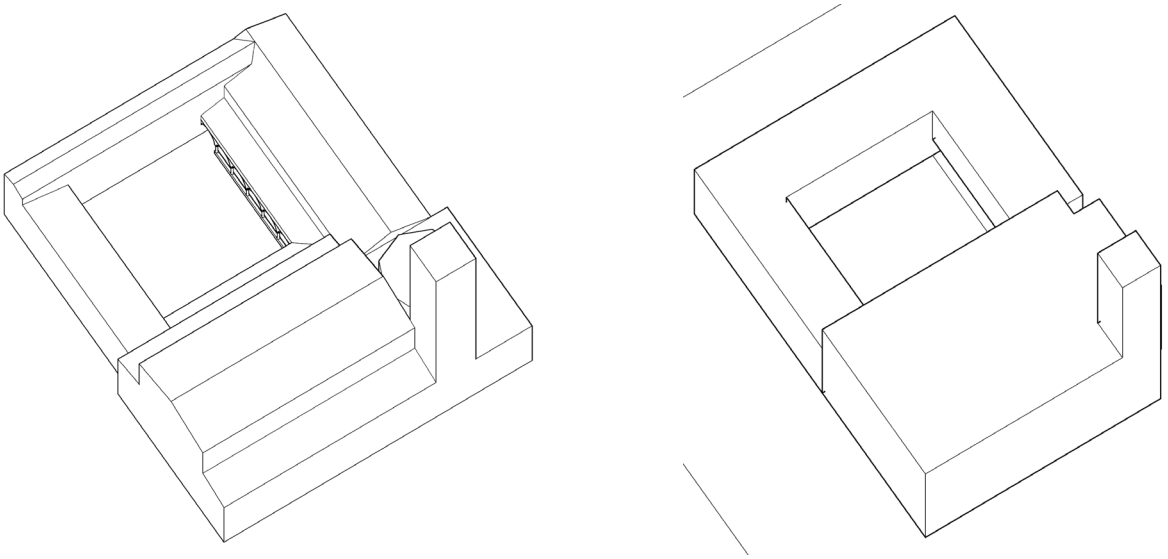

Figure 52. Detailed 3D model of the cloister (left) and simplified version for the simulations (right). Copyright: Marcello Turrini, Emanuele Naboni, Barbara Gherri, 2022

5.2.4 Preparation of the models for UTCI simulations

Given the need to simulate water and vegetation—and their contribution to overall humidity in the cloister—ENVI-met release 5 was selected as the simulation engine to compute UTCI for this case study as well. This setup allows realistic representation of vegetation evapotranspiration and pond evaporation.

To transform the Rhinoceros model and make it compatible with ENVI-met, the Rhinoceros module “Grasshopper” combined with the “Morpho” plug-in[503] was used.

[502] ‘OpenStreetMap’. n.d. OpenStreetMap. Accessed 12 April 2025. https://www.openstreetmap.org/.
[503] Ibid.

Workspace and location

Via the “morpho location” component, the coordinates of Parma where set up for solar radiation analysis, the time zone and the model rotation towards North. Using the “Morpho workspace” component, the project and model were named, customized material and tree databases were selected, and data-management folders were specified (Figure 53).

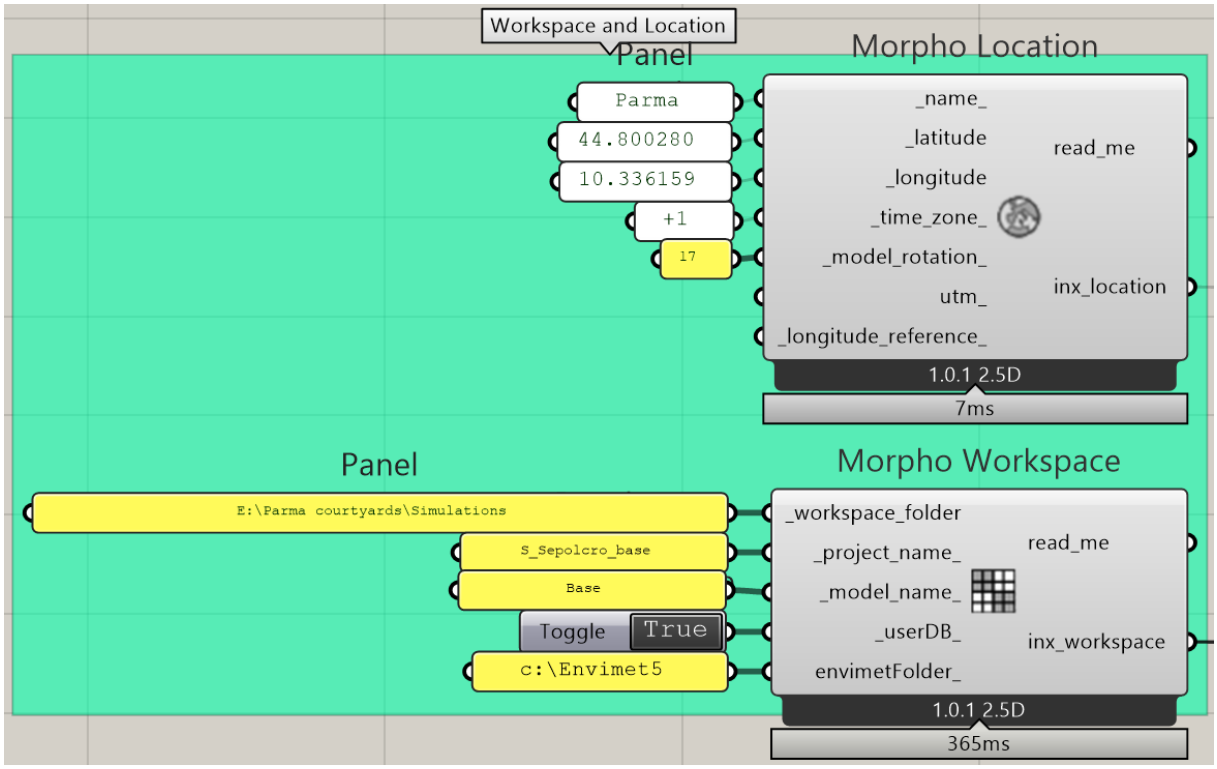

Figure 53. Grasshopper and Morpho components for workspace and location settings at the building scale. Copyright: Marcello Turrini, Emanuele Naboni, Barbara Gherri, 2022

Setup of the grid domain

The process is similar to that described in the previous case study in Sassuolo, with differences dictated by the much smaller size of the model. In this case, a grid size of 1 meter was chosen, the telescopic method was not applied for heights, and three nesting grids were applied to facilitate the transition between the condition outside the domain and its immediate surroundings, given the very small size of the model.

Geometry

Also in this case, the same methodology described for Sassuolo was used to convert the 3D model in Rhinoceros format into ENVI-met INX format, both for three-dimensional solids and paved surfaces.

Materials

ENVI-met material databases for buildings and surfaces were customized. The entire list can be seen in the Table 7 for buildings and in Table 8 and 9 for the pavements ad other horizontal surfaces.

			m	*%*	*%*	*%*	*%*	*J(KgK)*	*W/(mK)*	*Kg/m³*
WALL CONSTRUCTIONS	**Layer**	**Material**	**Thickness**	**Absorption**	**Transmission**	**Reflection**	**Emissivity**	**Specific Heat**	**Thermal Conductivity**	**Density**
0100BW Brick wall (exposed)	Outside									
Roughness length: 0.02	Layer 1	Bricks	0,12	0,55	0	0,1	0,9	650	0,78	1900
	Layer 2	Bricks	0,42	0,65	0	0.,35	0,9	840	0,90	1850
	Layer 3	Plaster	0,02	0,5	0	0,5	0,9	850	0,60	1500
	Inside	**Total thickness**	**0,56**					**U-Value**	**1,19**	
010SWL Brick wall (light stucco)	Outside									
Roughness length: 0.02	Layer 1	Light Plaster	0,02	0,35	0	0,55	0,9	850	0,87	1500
	Layer 2	Bricks	0,5	0,65	0	0.,35	0,9	840	0,90	1850
	Layer 3	Plaster	0,02	0,5	0	0,5	0,9	850	0,60	1500
	Inside	**Total thickness**	**0,54**					**U-Value**	**1,25**	
010SWD Brick wall (dark stucco)	Outside									
Roughness length: 0.02	Layer 1	Dark Plaster	0,02	0,7	0	0,2	0,9	850	0,87	1500
	Layer 2	Bricks	0,5	0,65	0	0.,35	0,9	840	0,90	1850
	Layer 3	Plaster	0,02	0,5	0	0,5	0,9	850	0,60	1500
	Inside	**Total thickness**	**0,54**					**U-Value**	**1,25**	
ROOF CONSTRUCTIONS										
010PRT Tiles	Outside									
Roughness length: 0.02	Layer 1	Tile	0,05	0,7	0	0,2	0,9	800	0,84	1900
	Layer 2	Air	0,03	0	1	0	0,96	1006	0,03	1,2041
	Layer 3	Wood	0,12	0,3	0	0,7	0,9	1470	0,14	1200
	Inside	**Total thickness**	**0,2**					**U-Value**	**0,43**	

Table 7. List of materials for buildings. Tab developed by the author

Water

As seen in the previous case-study in Sassuolo, water in ENVI-met is a special material, where all the most important values are hardcoded and change along with the boundary conditions, mostly the solar height. In the case of this study, a depth of 0.3 meters has been chosen for the water pond.

Trees

The local apple tree species was selected as the tall trees in the configuration SS_03, because its dimension is appropriate for the space of the cloister. Typical ENVI-met database values have been taken for it (Table 10).

			m	m^3/m^3	m^3/m^3	m^3/m^3	m	m/s	$J/(m^3K)$		W/(mK)
SOIL PROFILES	**Layer**	**Material**	**Thickness**	**W.C. at saturation**	**W.C. at field capacity**	**W.C. at wilting point**	**Matrix potential**	**Hydraulic conductivity**	**Volumetric heat cpacity**	**Clapp & Hornberger Constant**	**Thermal Conductivity**
010CTB Custom smashed brick	Outside										
z0 Roughness length: 0.01	Layer 1	Smashed bricks	0,03	0,395	0,135	0,0068	-0,121	176,00	2	4,05	0
Albedo: 0.75	Layer 2	Sand	0,01	0,395	0,135	0,0068	-0,121	176,00	1,463	4,05	0
Emissivity: 0.9	Layer 3	Loamy sand	0,04	0,41	0,15	0,075	-0,09	156,30	1,404	4,38	0
Surface is irrigated: False	Layer 4	Sandy clay	4,42	0,426	0,31	0,219	-0,153	2,20	1,175	10,4	0
Water mixing coefficient: 0.001											
Water turbidity/extintion: 2.1											
020CTB Custom granite	Outside										
z0 Roughness length: 0.01	Layer 1	Granite	0,02	0	0	0	0	0	2,35	0	4,61
Albedo: 0.1	Layer 2	Sandy clay	4,48	0,426	0,31	0,219	-0,153	2,20	1,175	10,4	0
Emissivity: 0.9											
Surface is irrigated: False											
Water mixing coefficient: 0.001											
Water turbidity/extintion: 2.1											
010RBR Custom brick road	Outside										
z0 Roughness length: 0.01	Layer 1	Basalt	0,08	0	0	0	0	0,00	2,386	0	1,73
Albedo: 0.8	Layer 2	Sand	0,02	0,395	0,135	0,0068	-0,121	176,00	1,463	4,05	0
Emissivity: 0.9	Layer 3	Sandy clay	4,4	0,426	0,31	0,219	-0,153	2,20	1,175	10,4	0
Surface is irrigated: False											
Water mixing coefficient: 0.001											
Water turbidity/extintion: 2.1		**Hedge**									
0100SL Unsealed soil	Outside										
z0 Roughness length: 0.015	Layer 1	Sandy loam	0,06	0,435	0,195	0,114	-0,218	34,1	1,32	4,9	0
Albedo: 0.2	Layer 2	Sandy clay	4,44	0,426	0,31	0,219	-0,153	2,20	1,175	10,4	0
Emissivity: 0.98											
Surface is irrigated: False											
Water mixing coefficient: 0.001											
Water turbidity/extintion: 2.1											
010PAR Asphalt road	Outside										
z0 Roughness length: 0.01	Layer 1	Asphalt (with basalt)	0,3	0	0	0	0	0	2,25	0	0,9
Albedo: 0.1	Layer 2	Sandy clay	4,2	0,426	0,31	0,219	-0,153	2,20	1,175	10,4	0
Emissivity: 0.9											
Surface is irrigated: False											
Water mixing coefficient: 0.001											
Water turbidity/extintion: 2.1											
0100WP Water pond	Outside										
z0 Roughness length: 0.01	Layer 1	Water	0,3				Algorithm driven				
Albedo: 0.1	Layer 2	Cement concrete	0,1	0	0	0	0	0,00	2,083	0	1,63
Emissivity: 0.9	Layer 3	Sandy clay	4,1	0,426	0,31	0,219	-0,153	2,20	1,175	10,4	0
Surface is irrigated: False											
Water mixing coefficient: 0.001											
Water turbidity/extintion: 2.1											

Table 8. List of materials for surfaces. Tab developed by the author

				$W/(m^2K)$	m	m			
VEGETATION	**CO2 fixation type**	**Leaf type**	**Albedo**	**Transmittance**	**Plant height**	**Root zone depth**	**LAD profile**	**RAD profile**	**Season profile**
0100H1 Hedge dense, 1m	C3	Deciduous	0,2	0,3	1	0,5	10*2,5	10*0,1	12*1,0
0100GR Grass 25cm	C3	Gras	0,2	0,3	0,25	0,2	10*0,3	10*0,1	12*1,0

Table 9. List of grass pavements and small vegetative elements. Tab developed by the author

			m	m	m		$W/(m^2K)$		g/m^2
TREES	**Alternative name**	**Leaf type**	**Plant width**	**Plant height**	**Root zone depth**	**Foliage sw. Albedo**	**Foliage sw. Trasmittance**	**Isoprene capacity**	**Leaf weight**
(Q) Apple tree (middle)	Malus domestica	Deciduous	6,6x7,13	8,14	2,5	0,18	0,3	12	100

Table 10. Tree type for configuration SS_3. Tab developed by the author

Day of simulation

The hottest day of the year in Parma is August 5, according to the stat file containing the statistics about the weather. It applies for both 2022 and 2080. The dry bulb temperature profile for that day is smooth, without gaps or jumps both for 2022 and for 2080, indicating that cloudiness does not alter the perfect correspondence between the two climate scenarios (Figure 54).

On this day, at 3:00 pm the highest temperature is reached, that is 39 °C in 2022 and the incredibly high value of 46.9 °C in 2080. Minimum temperatures for the two scenarios, in the same day, are also very high, 24 °C in 2022 and 29.6 °C in 2080, both at about 7:00 am.

Accordingly, August 5 was selected as the simulation day. The simulation was started at midnight on August 4 to allow model thermal masses to complete a charging–discharging cycle before the analysis period.

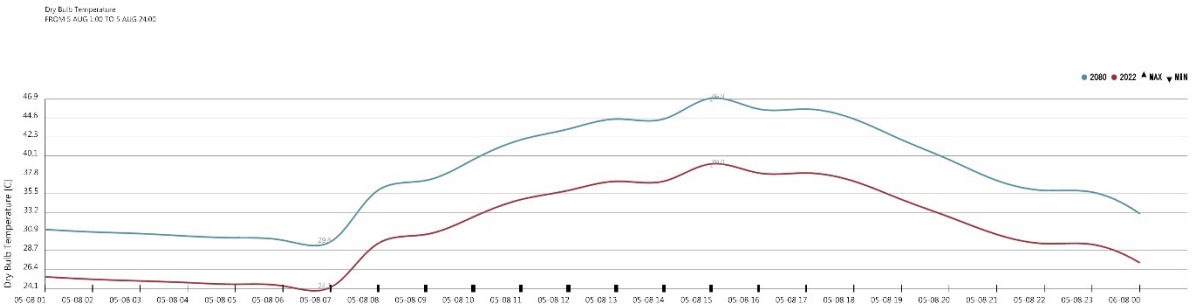

Figure 54. Dry bulb temperature in Parma on august 5th 2022 and 2080. Maximum temperature is 39 °C in 2022 and 46.9 in 2080, both at 3:00 pm. Copyright: Marcello Turrini, Emanuele Naboni, Barbara Gherri, 2022

Weather data for simulations.

Values taken from the EPW files of 2022 and 2080 have been taken to extract the FOX file used by ENVI-met to isolate the weather factors that are important for the simulation, i.e. dry bulb temperature, relative humidity and solar radiation it its shortwave direct and diffuse and longwave parts. Wind has not been forced, but kept constant to avoid instability in the calculations and a speed of 4 m/s and direction of 101° have been considered, as taken from the EPW data for that day of the year.

The summary graphs of the data contained in the FOX file (Figure 55) confirm what has already been seen in the climate analysis. In 2022, potential temperature peaks around 38°C with specific humidity between 12 and 16 g/kg; in 2080, the heat load increases and potential temperatures exceed 45°C, with specific humidity decreasing during peak hours to below 10 g/kg humidity during peak heating hours, falling below 10 g/kg. This indicates a drier environment with more intense heat in 2080. As for solar radiation, the direct component remains similar in both years, with a peak close to 700 W/m², but shortwave diffuse radiation increases in 2080, reaching values above 400 W/m², suggesting an increase in atmospheric turbidity. In addition, longwave radiation increases in 2080, with daytime values consistently above 460 W/m² compared to around 415 W/m² in 2022, indicating higher surface temperatures.

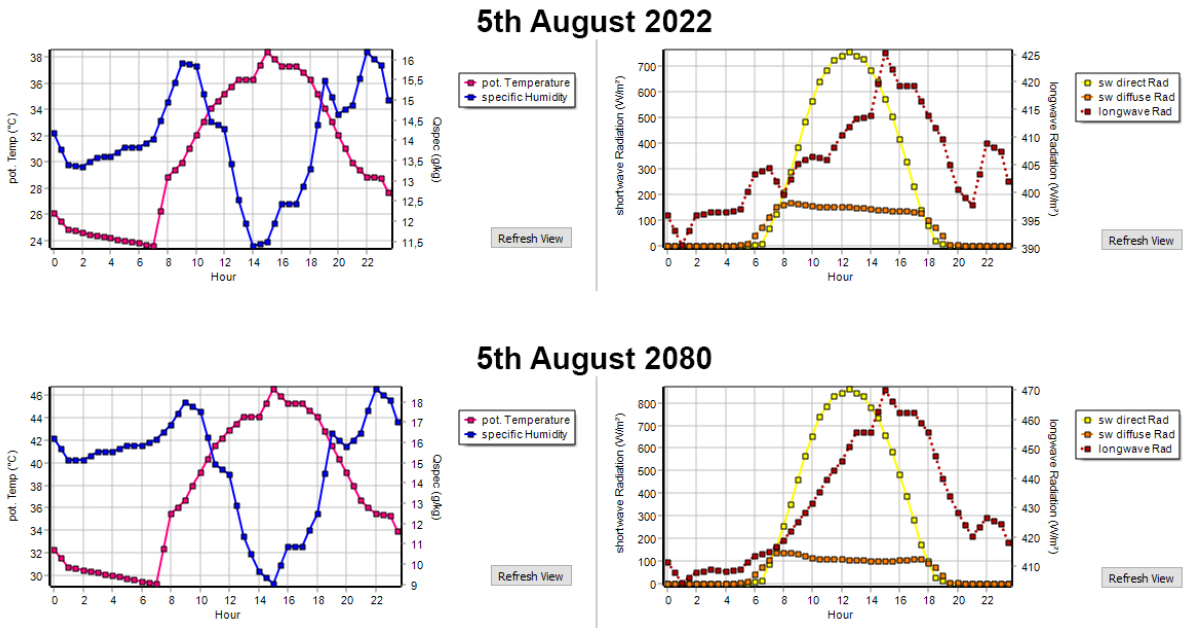

Figure 55. FOX file data for August 5th, 2022 – 2080: in 2080, temperatures exceed 45°C, specific humidity is lower, and diffuse radiation and longwave radiation are more intense than in 2022. Copyright: Marcello Turrini, Emanuele Naboni, Barbara Gherri, 2022

Extraction of results

Extraction of results. Results were extracted from the binary files and displayed as maps on the 3D model following the same procedure described for the Sassuolo case study. The simplicity of calculation due to the evident greater simplicity of the model considered in this work compared to the Sassuolo work allowed us to perform a further synthesis, namely mapping the maximum and minimum UTCI values using native Grasshopper components which, through indexing of the datasets, are able to assign a unique value to each face of the visualization meshes. Thanks to this property, it was possible to easily trace the face corresponding to the UTCI limit values and print them.

In this case too, ENVI-met has been used to simulate values for dry bulb temperature, mean radiant temperature, relative humidity, and wind velocity. The UTCI, that depends on these four microclimatic factors, has been calculated with the Ladybug component, consistently with the case study analyzed previously.

5.2.5 UTCI Variation for Each Configuration

The calculations of UTCI and the evaluation of its variations between 2022 and 2080 brought to the following analysis, where the resiliency to climate change of each configuration could be determined and discussed.

Configuration SS_1 – Base case

In the configuration SS_1, the UTCI maps in Figure 56, for August 5, indicate high levels of heat stress in current and future climate scenarios. In 2022, the maximum UTCI reaches 48.7 °C in the area exposed to direct solar radiation and paved with stone because it is under the portico. Here, the lower sky view factor does not mitigate the high temperatures. The minimum of 43.4 °C is found in the shaded area, with permeable grass paving and a large sky view factor. This places the area in the “very strong heat stress” category, confirming the overheating of the cloister detected in the preliminary assessment. The hottest area is located in the northern part of the cloister, adjacent to the unshaded masonry wall facing south and receiving direct solar radiation.

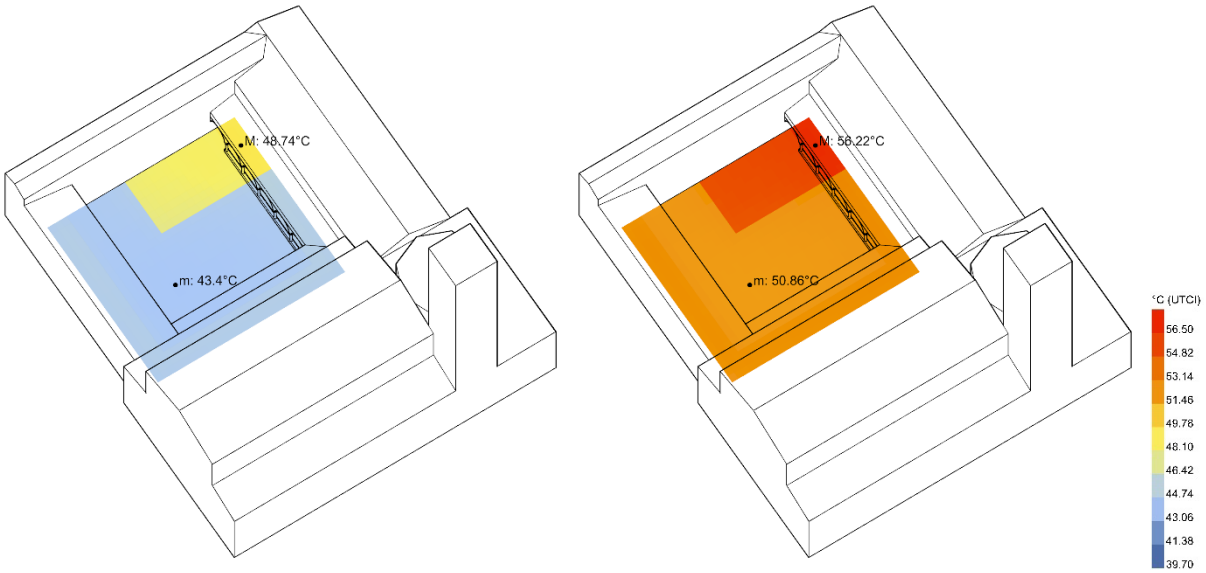

Figure 56. SS_1 – Base case. UTCI on 5 August at 3:00 pm. 2022 on the left, 2080 on the right. Copyright: Marcello Turrini, Emanuele Naboni, Barbara Gherri, 2022

In 2080, the thermal scenario worsens considerably. The maximum UTCI temperature rises to 58.2 °C and the minimum to 50.8 °C, placing the entire cloister in the “extreme heat stress”

category, above 46 °C UTCI. The permeable green surface area within the cloister is insufficient to counterbalance the increase in thermal force. The observed result is a cloister uniformly located in the extreme overheating range of UTCI, with different modulations and no effective microclimatic refuge under the conditions predicted for 2080 (Figure 56).

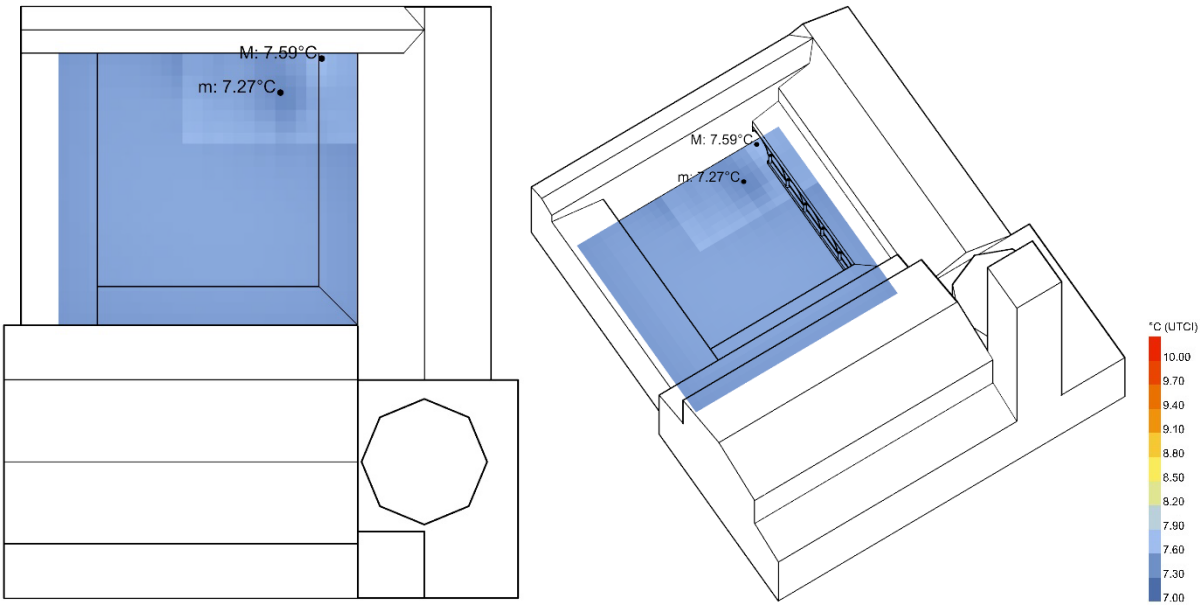

Figure 57. Variation in UTCI between 2022 and 2080 in the Configuration SS_1 – Base case. Maximum value (M) and minimum value (m) are shown. Copyright: Marcello Turrini, Emanuele Naboni, Barbara Gherri, 2022

The variation in UTCI in configuration SS_1 is almost uniformly amplified throughout the cloister, with values ranging closely between +7.27°C and +7.59°C (Figure 57). It can be seen that the area most affected by the increase corresponds to the northern sector, which is exposed to direct solar radiation and adjacent to the south-facing wall, which is not shaded. This is confirmed as the most thermally vulnerable part of the cloister. However, the minimum variation range in UTCI shows that the cloister, in its current form, does not generate spatial differences in thermal behavior based on future climate changes.

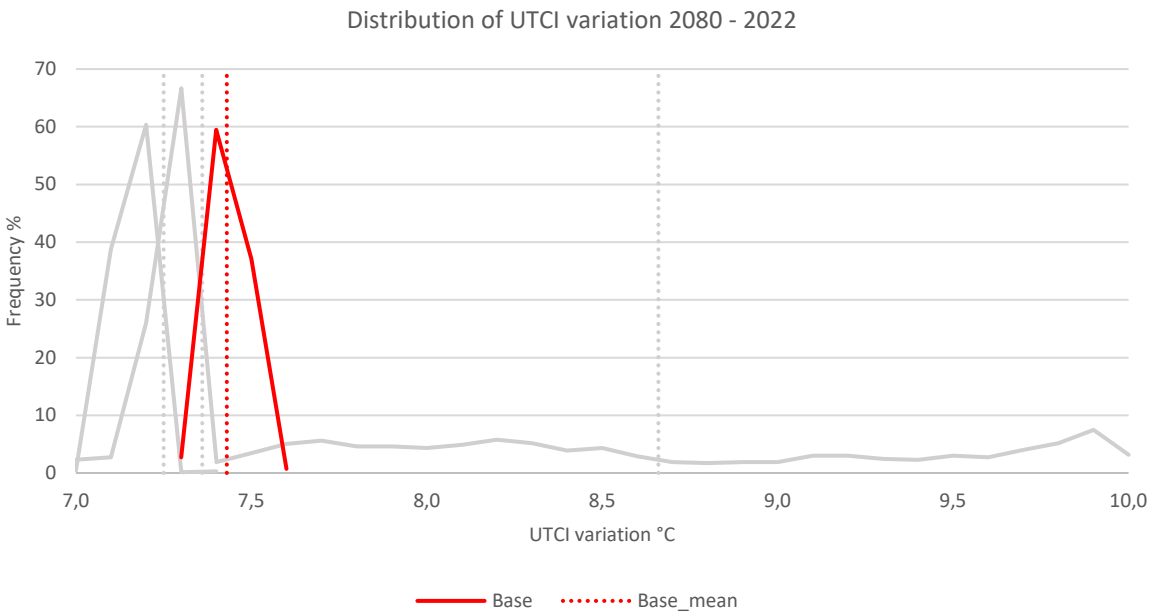

Figure 58. Distribution of UTCI variation for the configuration SS_1 – Base case. The curve shows a narrow distribution, with a peak around 7.4°C and a high frequency concentrated between 7.4°C and 7.5°C, indicating homogeneous thermal behavior and the lack of resilient microzones. Graph made by the author. Copyright: Marcello Turrini, Emanuele Naboni, Barbara Gherri, 2022

The statistical distribution of the UTCI variation for the SS_1 configuration further confirms the homogeneity and vulnerability observed in the spatial maps. The frequency curve shows a peak centered at 7.4 °C, with over 60% of sampled points within the narrow range 7.4–7.5 °C. The average variation is 7.43°C, as can be seen from the red dotted line. Furthermore, there is no “tail” at the bottom of the distribution, confirming that there are no thermal refuges, even in shaded areas or areas with vegetation cover (Figure 58).

Configuration SS_2 – Shading

In configuration SS_2, the introduction of a vertical rather than horizontal shading system significantly reduces exposure to direct solar radiation while preserving vertical solar radiation exchange and partial ventilation. In the 2022 scenario, Figure 59 shows UTCI between 42.2 and 45.3 °C (“very strong heat stress”), slightly lower than in configuration SS_1. This modest reduction confirms the selective impact of the geometric solar shading.

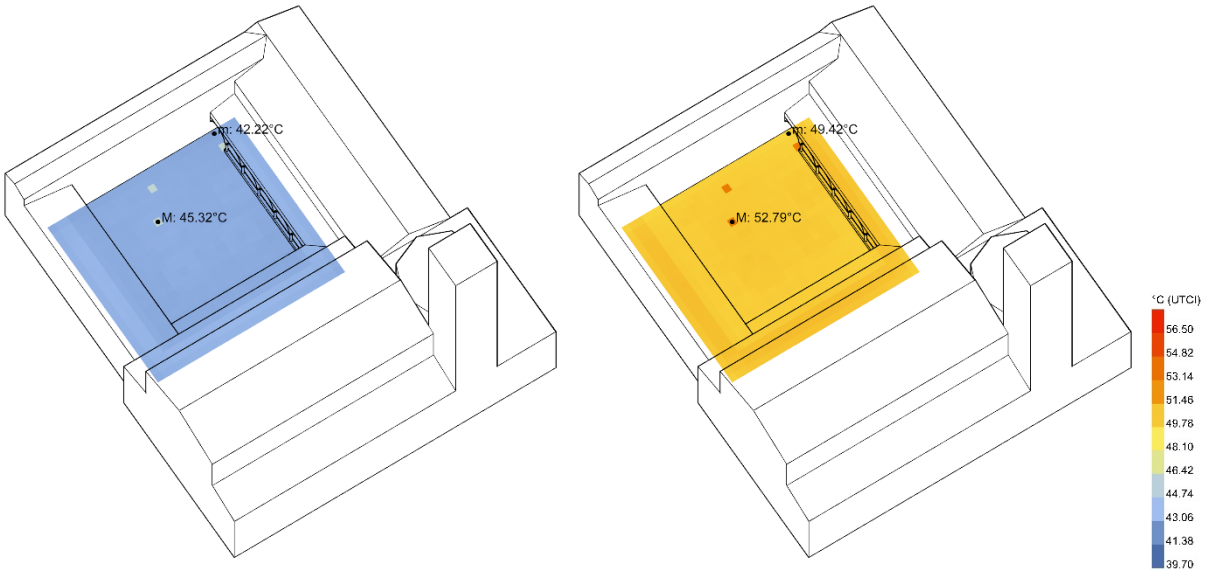

Figure 59. Absolute UTCI values for the configuration SS_2 – Shading. A uniform behavior can be observed in the entire surface of the cloister. Copyright: Marcello Turrini, Emanuele Naboni, Barbara Gherri, 2022

In the 2080 scenario, UTCI increases to 49.4–52.8 °C, placing the cloister in the "extreme heat stress" category. However, compared to SS_1, the mitigation provided by the shading system remains evident: the absolute UTCI values are lower, despite the identical boundary conditions. Along the base of the porticoed sides, a recurring thermal trend is observed: reduced ventilation, long-wave radiation accumulation, and very low sky view factor lead to higher values (Figure 59).

The variation in UTCI between 2080 and 2022 for SS_2 shown in Figure 60 confirms the ability of the vertical shading system to increase the thermal resilience of the cloister in future climatic conditions. Obviously, the UTCI variation remains high, between +7.13°C and +7.48°C, as it is measured during one of the hottest hours of the year and in a projection from the future of more than 50 years with the RCP 8.5 profile. However, the increase is marginally lower than that recorded in the SS_1 configuration. This subtle difference is significant from a morphological point of view, reflecting the effect of selective solar shading in a scenario where all other boundary conditions remain constant.

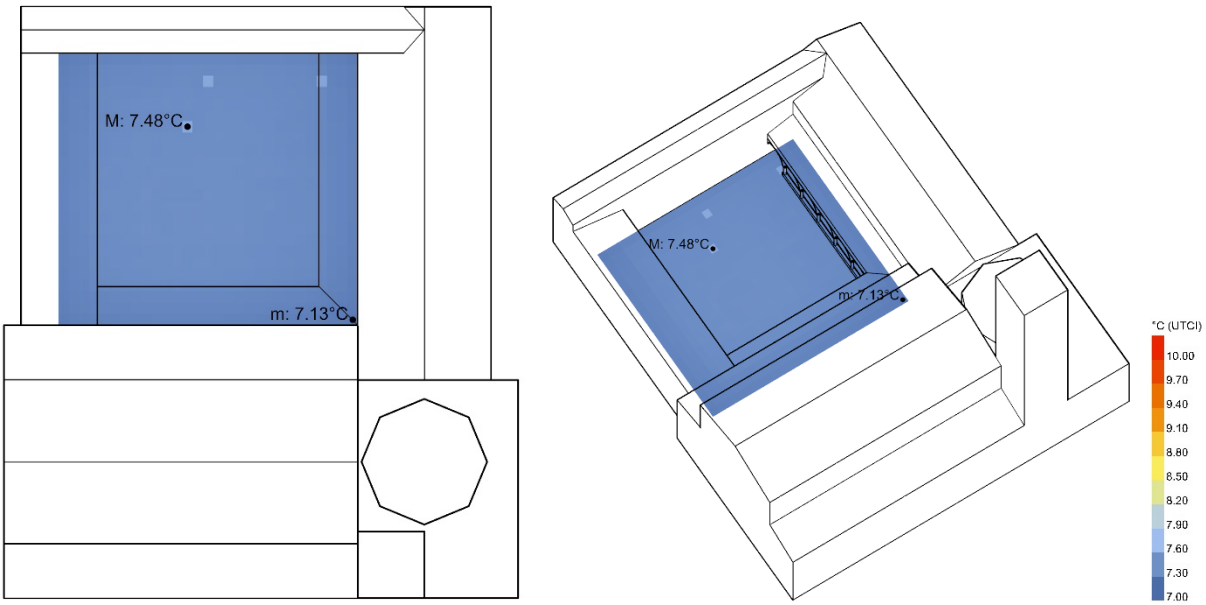

Figure 60. Variation in UTCI between 2022 and 2080 in the Configuration SS_2 – Shading. Maximum value (M) and minimum value (m) are shown. Copyright: Marcello Turrini, Emanuele Naboni, Barbara Gherri, 2022

The shading element in SS_2 acts as a uniform filter, reducing direct solar gain throughout the cloister. This results in slightly reduced thermal amplification, without hotspots. In particular, the perimeter walls of the cloister are also shaded, with a particular effect on the south-facing wall without a portico. As a result, long-wave radiation emission from the perimeter walls is also reduced.

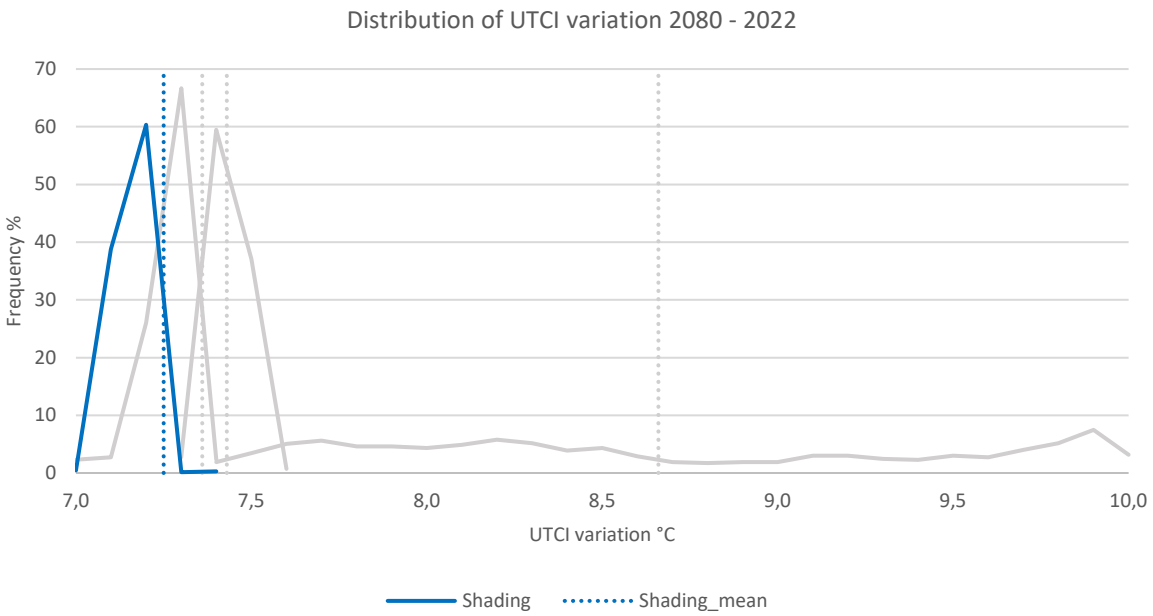

Figure 61. Distribution of UTCI variation for the SS_2 configuration - Shading. The curve shows a clear peak around 7.2°C, with the highest values between 7.1 °C and 7.2 °C. Graph made by the author. Copyright: Marcello Turrini, Emanuele Naboni, Barbara Gherri, 2022

The statistical distribution for the SS_2 - Shading configuration shows a concentration of variation values in the lower part of the x-axis, with the majority of values concentrated between 7.1°C and 7.2°C, and an average variation value of approximately 7.25°C. Compared to the SS_1 configuration, there is a small but measurable increase in climate resilience.

The curve shows a well-defined peak with no long tails, indicating climatic uniformity. This result suggests that a cloister shaded with a system that blocks direct radiation but ensures a good sky view factor without blocking vertical ventilation will overheat by 2080 under a severe climate change scenario, but has greater resilience characteristics than an unshaded cloister (Figure 61).

Configuration SS_3 – Humidity

The configuration SS_3 – Humidity is characterized by the ability to activate evapotranspiration and latent heat exchange with the presence of dense tall vegetation and a body of water. In this configuration, in the 2022 scenario, the maximum UTCI temperature reaches approximately 48.5 °C, while the minimum value is 43.4 °C, straddling the UTCI

categories “Very strong heat stress” and “Extreme heat stress.” These values are similar to those measured in the SS_1 - base case configuration, confirming that, under the climatic conditions of 2022, the generous presence of vegetation and water does not imply lower absolute heat stress at 3:00 p.m.

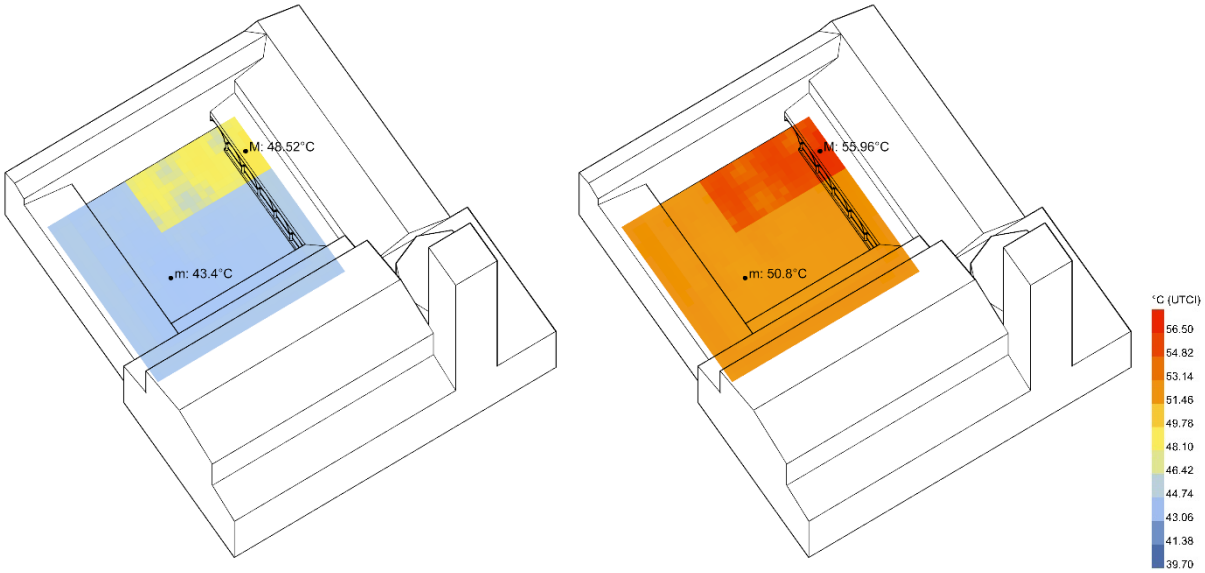

Figure 62. Absolute UTCI values for the configuration SS_3 – Humidity. A uniform behavior can be observed in the entire surface of the cloister. Copyright: Marcello Turrini, Emanuele Naboni, Barbara Gherri, 2022

In the 2080 scenario, the situation obviously becomes more critical. The maximum UTCI temperature rises to 55.9 °C, and the minimum reaches 50.8 °C, placing the cloister well within the UTCI category of “Extreme heat stress.” However, areas where direct radiation is blocked by tree canopy have slightly lower UTCI values, confirming that shading is the preferred option for increasing resilience. In fact, under conditions of high thermal stress, plants tend to reduce, if not eliminate, their evapotranspiration, decreasing the effectiveness of vegetation as a stress reliever in cases of greatest need. As a result, their intensive use is not effective.

Finally, the outline of the water body is completely undetectable in the color profile of the UTCI maps, both at present and in the future, confirming the lack of influence of its presence in the simulated climatic conditions (Figure 62).

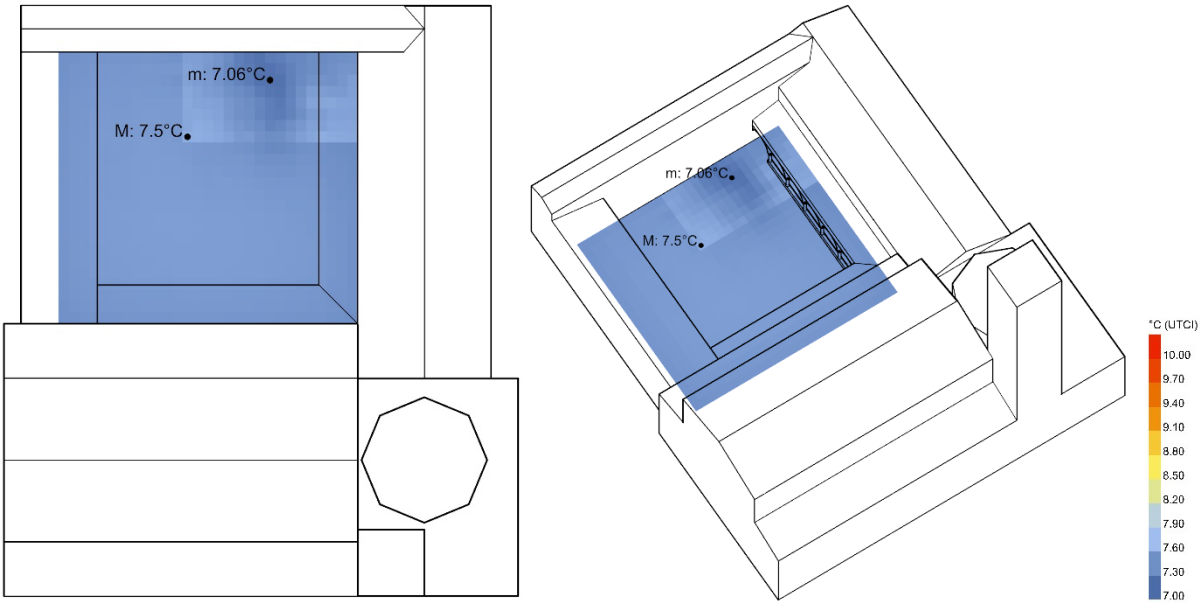

Figure 63. Variation in UTCI between 2022 and 2080 in the Configuration SS_3 – Humidity. Maximum value (M) and minimum value (m) are shown. Copyright: Marcello Turrini, Emanuele Naboni, Barbara Gherri, 2022

In the UTCI variation map shown in Figure 63, for the configuration SS_3 - humidity, it is possible to identify a range between 7.06 °C and 7.50 °C of UTCI increase between 2022 and 2080, with limited internal dispersion and a fairly constant thermal response throughout the cloister. A combined effect of vegetation and water surfaces would be expected, primarily modulating thermal dynamics through latent heat exchange and surface cooling. However, under the extreme thermal conditions in the background of the calculated simulations, the effectiveness of these mitigation mechanisms becomes limited.

Vegetation subject to high thermal stress can reduce or eliminate evapotranspiration, weakening its ability to dissipate heat. Similarly, the contribution of the water surface is not appreciated in a visible local reduction of UTCI variation across the entire simulated domain. Despite the ecological complexity of this configuration, variation remains spatially uniform and no clearly identifiable thermally distinct zones appear in the output maps, except for slightly more resilient areas beneath the tree canopy.

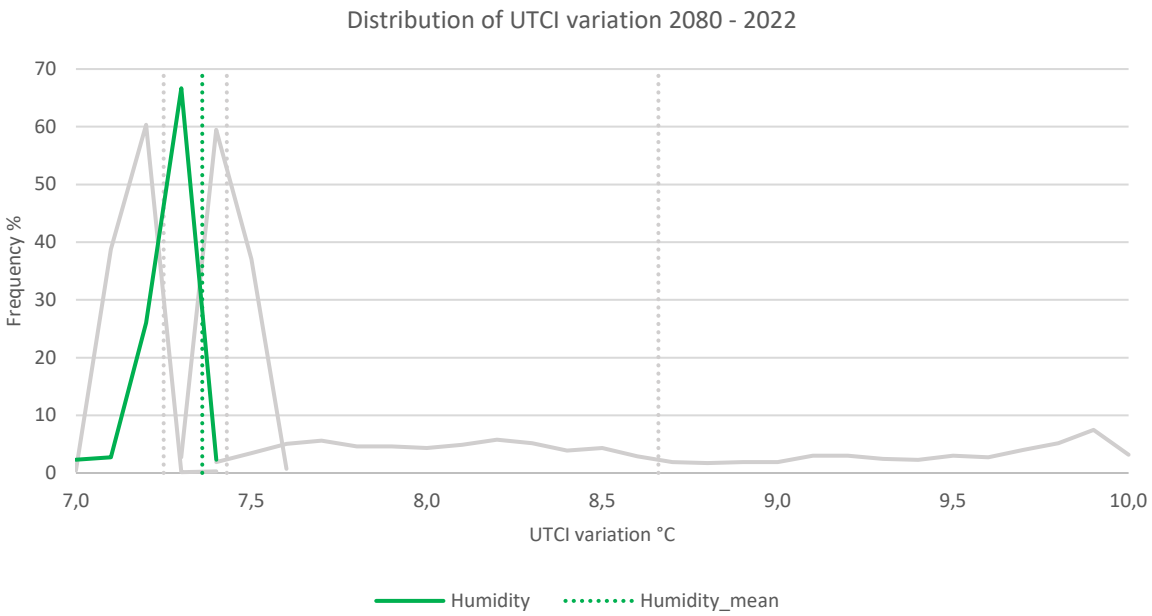

Figure 64. Distribution of UTCI variation for the configuration SS_3 - Humidity. The narrow curve, with a peak around 7.3°C, indicates a homogeneous and widespread thermal response without thermally privileged areas. Graph made by the author. Copyright: Marcello Turrini, Emanuele Naboni, Barbara Gherri, 2022

The statistical distribution of the UTCI variation for the configuration SS_3 - Humidity in Figure 64 shows a narrow peak concentrated between 7.2 °C and 7.3 °C. The average variation is approximately 7.36 °C, as indicated by the dotted line in the graph. This is indicative of a homogeneous distribution of variation throughout the cloister. This suggests that the biophysical mechanisms activated by the dense vegetation and the water surface operate in a diffuse manner, rather than generating microclimatic niches.

Configuration SS_4 – Ventilation

In configuration SS_4 (Ventilation), a ground-level opening was introduced along the north side of the cloister, connecting its interior with the exterior and allowing wind to enter directly.. This configuration microclimatically transforms the cloister space, promoting cross ventilation through the cloister and thus acting on the age of air.

In the 2022 scenario, the UTCI varies from 39.7 °C to approximately 46.8 °C (Figure 65). The thermal field is not uniform: the coldest areas occur along the southern and western edges,

while the warmest area is near the northern opening, where air enters the cloister at an initial speed of 1 m/s.

In the 2080 projection, thermal stress intensifies: the UTCI varies between 47.3 and 56.2 °C. The hottest point remains near the ventilation inlet. It is clear that the incoming air, rather than mitigating discomfort, introduces heat into the cloister. This result is consistent with microclimatic dynamics: when the air temperature exceeds the human skin temperature, which is typically around 33-35 °C, the wind ceases to remove heat from the human body and begins to add it, causing thermal discomfort. The highr is the air velocity, the higher is the thermal discomfort.

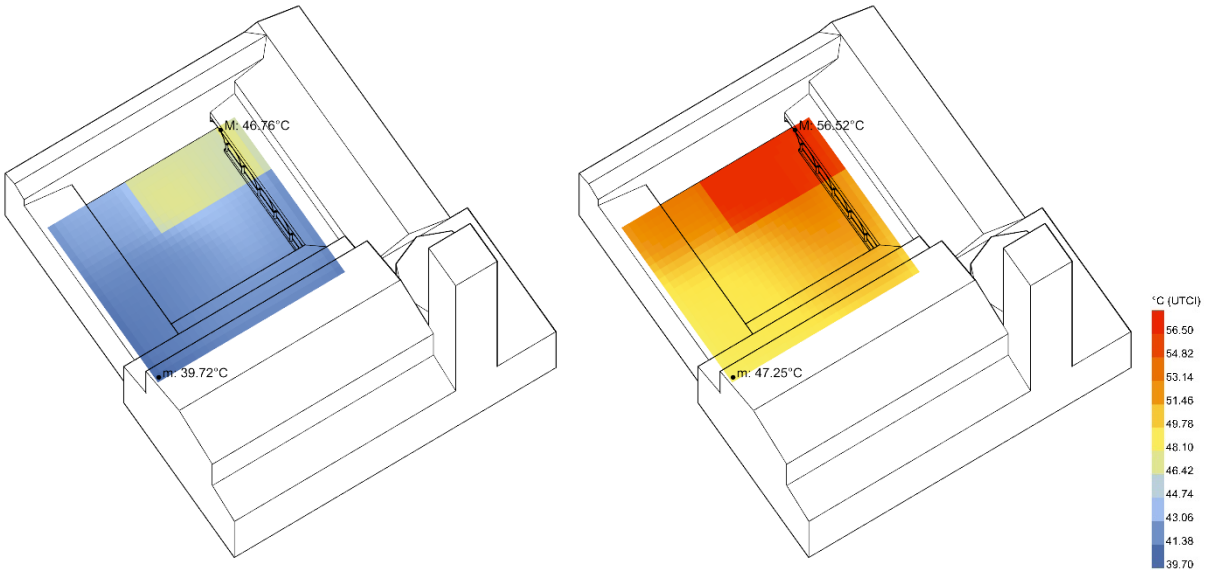

Figure 65. Absolute UTCI values for the configuration SS_4 – Ventilation. An asymmetrical behavior can be observed in the entire surface of the cloister, due to asymmetrical surface temperature of the pavement combined with wind flow. Copyright: Marcello Turrini, Emanuele Naboni, Barbara Gherri, 2022

The temperature gradient inside the cloister, in this case, derives only indirectly from shading: the air enters the cloister and passes over the part of the pavement surface affected by direct solar radiation, which is therefore warmer than the surrounding surfaces. This triggers turbulent motions that tend to mix the layers of air at different temperatures more quickly, with the result that the air speed increases[504]. This explains the asymmetrical nature

[504] Kim, Jae-Jin, and Jong-Jin Baik. 2001. 'Urban Street-Canyon Flows with Bottom Heating'. *Atmospheric Environment* 35 (20): 3395–3404. https://doi.org/10.1016/S1352-2310(01)00135-2.

of the UTCI in this configuration. The result is a heterogeneous UTCI field, in which the ventilation opening in combination with different surface temperatures introduces both warm air movement and thermal asymmetry, worsening comfort conditions.

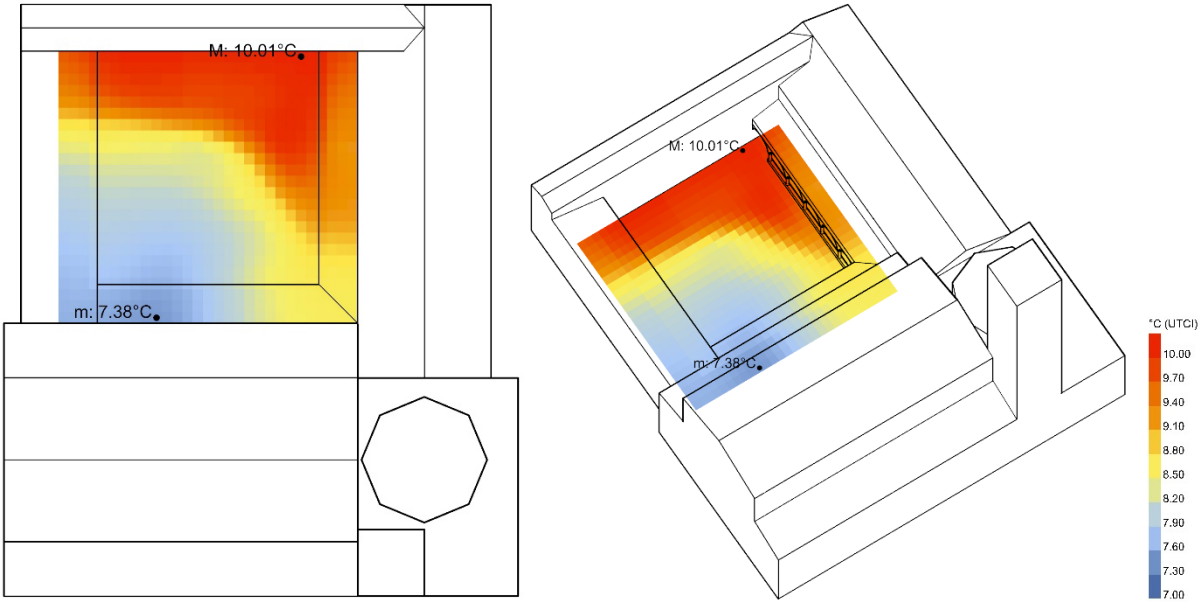

Figure 66. Variation in UTCI between 2022 and 2080 in the Configuration SS_4 – Ventilation. Maximum value (M) and minimum value (m) are shown. The asymmetric behavior is more evident here. Copyright: Marcello Turrini, Emanuele Naboni, Barbara Gherri, 2022

The UTCI variation map for the configuration SS_4 shows a marked spatial gradient, with delta values ranging from +7.38 °C to +10.01 °C (Figure 66). This reflects a highly heterogeneous thermodynamic response induced by the ventilation opening combined with an asymmetry in the surface temperature pattern within the cloister. The lowest increases are observed in the southern part of the cloister, while the highest amplification is concentrated near the northern opening, where outside air enters the cloister space.

This behavior induces higher wind speeds as the surface temperature asymmetry gradient increases, introducing a variation in air velocity within the cloister in the future projection. Consequently, in this case higher wind speeds correspond to greater discomfort, and a larger (worsening) UTCI variation is observed under the future scenario.

The statistical distribution for SS_4 in Figure 67 shows a broad profile ranging from 7.4 °C to 10 °C, with an average value close to 8.7 °C, denoting the extremely eterogeneous distribution of UTCI in the cloister. While an initial concentration of values is visible between 7.3 °C and 7.6 °C, the frequency gradually flattens and rises slightly up to 9.9 °C, where the frequency peak occurs, albeit not sharply pronounced. This result reflects the spatial asymmetry seen and explored in depth in the spatial and geometric analysis.

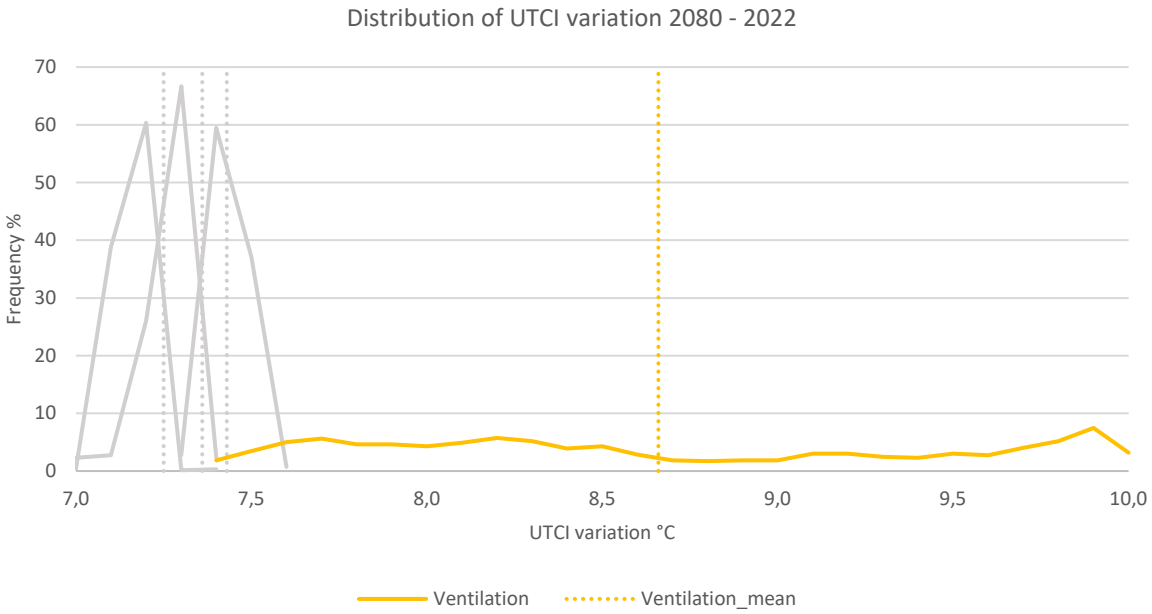

Figure 67. Distribution of UTCI variation for the configuration SS_4 – Ventilation. Wide distribution, with a long tail to the right and values up to 10°C. Graph made by the author. Copyright: Marcello Turrini, Emanuele Naboni, Barbara Gherri, 2022

This polarized behavior, which generates a high level of discomfort, highlights the complexity and risk of using ventilation as a passive mitigation strategy in extremely hot climates such as those likely to be found in Parma in 2080, where moving air may no longer act as a cooling agent as it does in temperate climates.

5.2.6 Discussion

The methodology applied to the building scale in the cloister of the Convent of San Sepolcro in Parma shows how the variation in UTCI between 2022 and 2080 serves as a sensitive indicator for assessing the resilience potential of each building configuration, regardless of its

origin or design intent. All four configurations, SS_1, SS_2, SS_3, and SS_4, while presenting similar levels of absolute thermal stress in 2080, reveal important differences when analyzing the variation of UTCI in its projection into the future by observing the spatial distribution and statistical behavior of the UTCI variation.

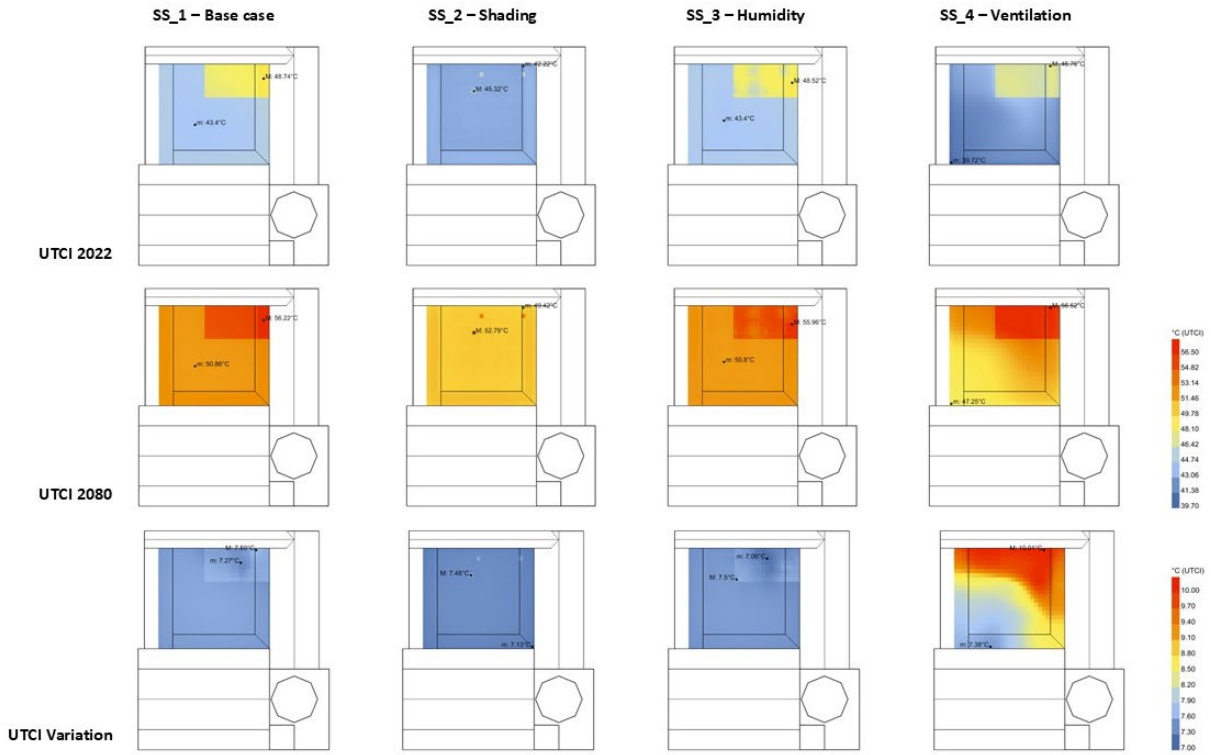

Figure 68. Summary comparison between the four morphological configurations analyzed (from left: SS_1-base case, SS_2-shading, SS_3-humidity, SS_4-ventilation), with visualization of the top views, the absolute UTCI values simulated for August 5 at 3:00 p.m. in the two scenarios (2022 and 2080), and the relative UTCI variation (delta). Copyright: Marcello Turrini, Emanuele Naboni, Barbara Gherri 2022

SS_1, which represents the most acknowledged and established model of the cloister, is highly susceptible to overheating in the future due to the strong direct radiation that heats the wall elements. The cloister SS_2, with its geometric shading system, reacts uniformly across its entire surface, revealing an effective reduction in UTCI variation and consequent high resilience to climate change. SS_3 proposes a cloister with a highly complex environment, with tall vegetation and a body of water, resulting in a compact distribution of overheating, with small mitigation effects located mainly under the canopy of the dense trees. SS_4 is a cloister that is connected to the outside area and allows air to penetrate at pedestrian level, ensuring greater ventilation. This type of cloister shows the widest range of variation and a distinct thermal gradient, highlighting the risk of using natural ventilation to mitigate overheating in

an environment where direct radiation has a strong impact, generating high surface temperatures (Figure 68).

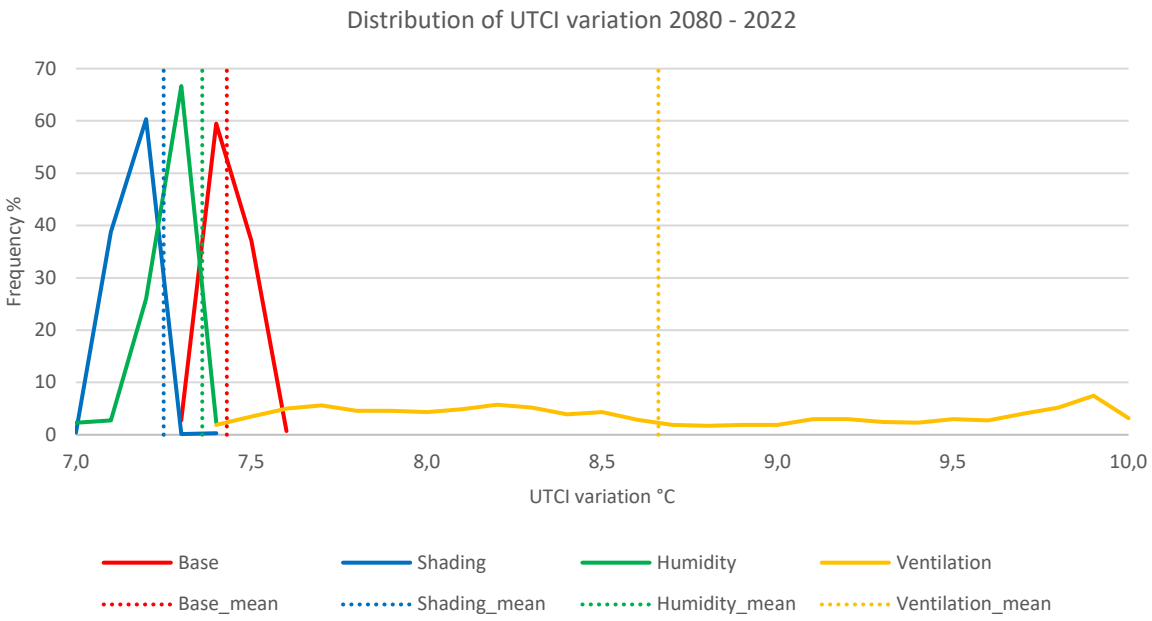

Figure 69. Statistical distribution of UTCI variations for the configurations. Graph by the author. Copyright: Marcello Turrini, Emanuele Naboni, Barbara Gherri, 2022

Statistical distributions (Figure 69), indicate that, at building scale, the methodology distinguishes both the intensity and the consistency of each configuration's thermal response cloister. While SS_2 and SS_3 are concentrated around lower delta values, around 7.2–7.3 °C, SS_4 shifts the average upwards, leading to variations of up to 10 °C. SS_1 has a distribution centered around 7.5 °C, with moderate internal variation.

Ultimately, this case study confirms that the methodology is suitable for assessing the climate change resilience of the built environment at the building scale, identifying differences in both the degree of future thermal stress and the spatial distribution of stress.

Indicator	**SS_1**	**SS_2**	**SS_3**	**SS_4**
Typology and key spatial traits	Existing cloister; 3 porticoes + 1 infilled south wall; open sky; green permeable ground, stone under porticoes	Vertical shading blocking direct sun; preserves sky exchange and partial ventilation	Dense tall vegetation + water body; increased "humidity/latent" intent + canopy shade	Ground-level opening on north side; promotes cross-ventilation through cloister
Baseline UTCI	≈43.4–48.7°C	≈42.2–45.3°C	≈43.4–48.5°C	≈39.7–46.8°C

Future UTCI	≈50.8–58.2°C	≈49.4–52.8°C	≈50.8–55.9°C	≈47.3–56.2°C
Mean ΔUTCI (°C)	≈7.43	≈7.25	≈7.36	≈8.7
ΔUTCI range (°C)	≈7.27–7.59	≈7.13–7.48	≈7.06–7.50	≈7.38–10.01
Spatial response pattern	Very narrow; peak ~7.4°C; >60% of points between 7.4–7.5; no low-value tail: uniform amplification	Narrow; clear peak ~7.2°C; values mostly 7.1–7.2; no long tails: stable shift to lower ΔUTCI	Narrow peak 7.2–7.3°C; largely uniform; minor canopy-related pockets; water signal weak: diffuse effect	Wide; long right tail up to 10°C; strong gradient toward inlet; peak near upper end: amplified heterogeneity
Main microclimatic drivers and design reading	Direct solar exposure + heated wall surfaces: strong radiative load; limited internal buffering: low resilience	Shortwave blocking reduces wall heating and longwave emission; but local longwave accumulation can persist in low-SVF zones: radiation-first resilience gain	Canopy shade helps locally; latent cooling not robust under extreme stress: condition-dependent resilience	Airflow imports hot air at peak; when air T > skin T, wind adds heat; increases ΔUTCI extremes and gradients: ventilation-first is threshold-dependent

Table 11. Comparative synthesis of the ΔUTCI-based assessment for the four building-scale configurations of the San Sepolcro cloister (SS_1–SS_4), evaluated at the selected peak-summer time slice under paired baseline and end-of-century climate scenarios (2022 vs 2080). The table summarizes absolute UTCI conditions, ΔUTCI magnitude, and internal variability within the cloister evaluation domain, supporting a comparative interpretation of the resilience of alternative microclimatic configurations.

5.2.7 Conclusions for building scale

The San Sepolcro cloister demonstrates, at building scale, that the proposed ΔUTCI-based workflow can translate complex microclimatic interactions into a set of comparative outputs that remain readable and design-actionable. The four configurations show that even within a constrained cloister typology, relatively small modifications to shading, humidity-related elements, or airflow pathways can produce distinct thermal-resilience behaviors when the space is evaluated consistently under baseline and future conditions.

Two complementary conclusions emerge when absolute UTCI and ΔUTCI are read together. First, the results make explicit that future peak conditions push the entire system toward severe thermal stress regardless of configuration. For example, the base case (SS_1) shifts from a 2022 range of approximately 43.4–48.7 °C to about 50.8–58.2 °C in the 2080 scenario. Second, and more importantly for design reasoning, the ΔUTCI layer shows that configurations still differ meaningfully in how strongly they transmit the future signal into the occupied domain. In SS_1, ΔUTCI remains tightly bounded (roughly 7.27–7.59 °C, mean ≈ 7.43 °C), indicating a relatively stable—if still stressed—response.

Among the adaptation variants, the shading configuration (SS_2) emerges as the most consistently resilient: it combines lower absolute UTCI values (about 42.2–45.3 °C in 2022 and 49.4–52.8 °C in 2080) with a relatively low and compact ΔUTCI field (approximately 7.13–7.48 °C, mean ≈ 7.25 °C). The humidity configuration (SS_3) also improves performance compared to the base case, reaching a mean ΔUTCI of about 7.36 °C (range ≈ 7.06–7.50 °C) while keeping absolute values lower than SS_1 in both scenarios. In contrast, the ventilation configuration (SS_4) illustrates the risk of increased sensitivity under intensified forcing: although its baseline UTCI can include relatively lower minima (around 39.7 °C in 2022), its future response becomes less stable, with ΔUTCI spanning approximately 7.38–10.01 °C and a higher mean near 8.7 °C.

The building-scale conclusion is therefore not that a single device “solves” cloister overheating, but that resilience depends on the robustness of the dominant adaptation logic. In this typology, interventions that structure the radiative environment tend to yield the most stable reductions in sensitivity, while approaches that rely primarily on airflow may deliver uneven benefits and can generate higher amplification under future boundary conditions. From a design perspective, this supports a hierarchy in which stable shading acts as a primary layer, complemented by moisture- and ventilation-related measures that are treated as qualified, context-dependent strategies rather than as universal guarantees of improvement.

Finally, the case study confirms the scalability of the workflow at architectural resolution. By preserving a coherent evaluation domain and by pairing baseline and future forcing under invariant settings, the method produces outputs that can support comparative design decisions in semi-open heritage spaces—where adaptation options are often constrained, but where the difference between “uniform stress” and “spatially moderated zones” remains crucial for usability and comfort.

5.3 Component Scale: The case of the railway station of Xirbi

Railway stations are hybrid spaces of passage. They are characterized by short-term use by users, with external and internal spaces usually connected due to the high mobility of passengers from the tracks to the waiting areas and ticket offices. The case of a bridge railway station in Sicily, in Xirbi, has been selected to test the methodology in a hot climate, in an indoor space that is not static, therefore without air conditioning and strongly connected to the outside.

The station examined has not been built, but is in the design phase. It consists of a single longitudinal structure, bridging the tracks, with a differentiated envelope: the long sides and the roof are made of a skin with differentiated transparency, which houses glass photovoltaic panels, and the two ends to the north and south are made of two glass closures. The floor is a reinforced concrete slab with a large opening over the tracks, which connects the external space with the internal space. There are also openings on the outer shell. Inside the station, there is an unconditioned waiting room with automatic ticket machines, while the staffed ticket offices and a small commercial area are enclosed in air-conditioned glass boxes[505].

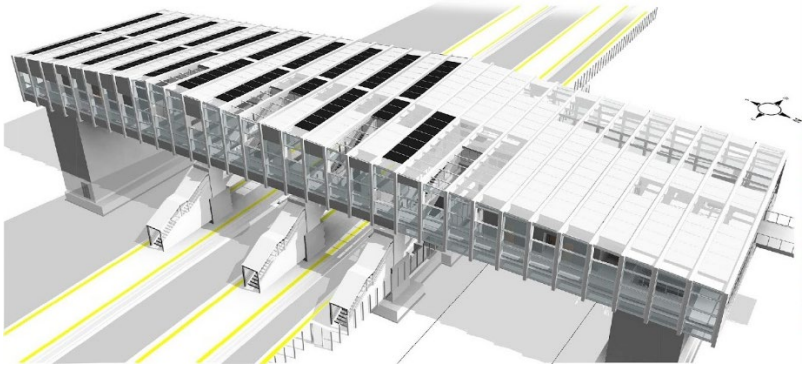

Figure 70. The building as a bridge station over the tracks. Source: ITALFERR

[505] This case study is an excerpt from a research project assigned to the Department of Engineering and Architecture at the University of Parma by the Italian company ITALFERR, Arch. M. Raffaele, M. Capobianchi. Working group: Emanuele Naboni, Marcello Turrini.

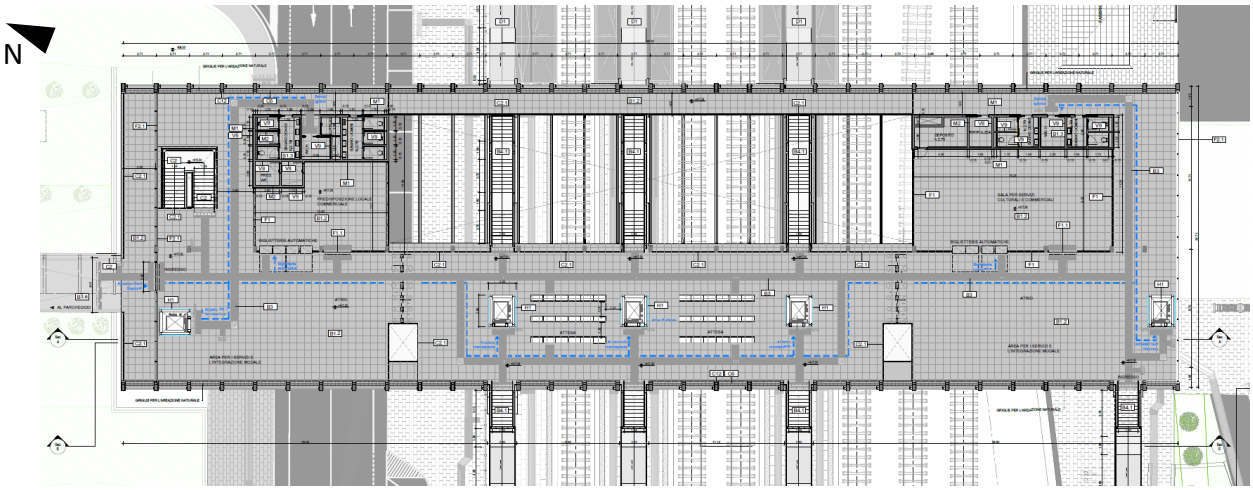

Figure 71. Plan of the station. A huge void over the tracks is in the central part, while two conditioned boxes for commercial use are on the left and the right side of the void. Source: ITALFERR

5.3.1 Climate scenarios in Xirbi

Xirbi is located in Sicily, in the province of Caltanissetta. The climate is hot, with summer temperatures currently exceeding 35 degrees on peak days in the early afternoon. When climate data are extrapolated to 2050 using the IPCC 8.5 scenario, the largest temperature increases occur in summer (up to 4°C), leading to August temperatures above 38°C (Figure 72).

Analyzing the hottest week of the year, from August 17 to 23, peak temperatures were recorded on August 18 and 19, at 3:00 p.m. While August 18 shows the highest peak in the current scenario, August 19 will record the peak in the 2050 scenario (Figure 73). This is due to the different cloud cover in the two selected scenarios. In fact, as can be seen in Figure 74, August 19 has 5/10 cloud cover during the daytime and afternoon hours, while August 18 has no cloud cover in either the current scenario or in 2050.

The simulation day was therefore chosen as August 18, due to this uniformity of solar radiation, which ensures that there is no bias between the UTCI in the current scenario and in 2050. The time chosen was 3:00 p.m., the hottest time of day, when critical conditions are most likely to cause heat-related illnesses.

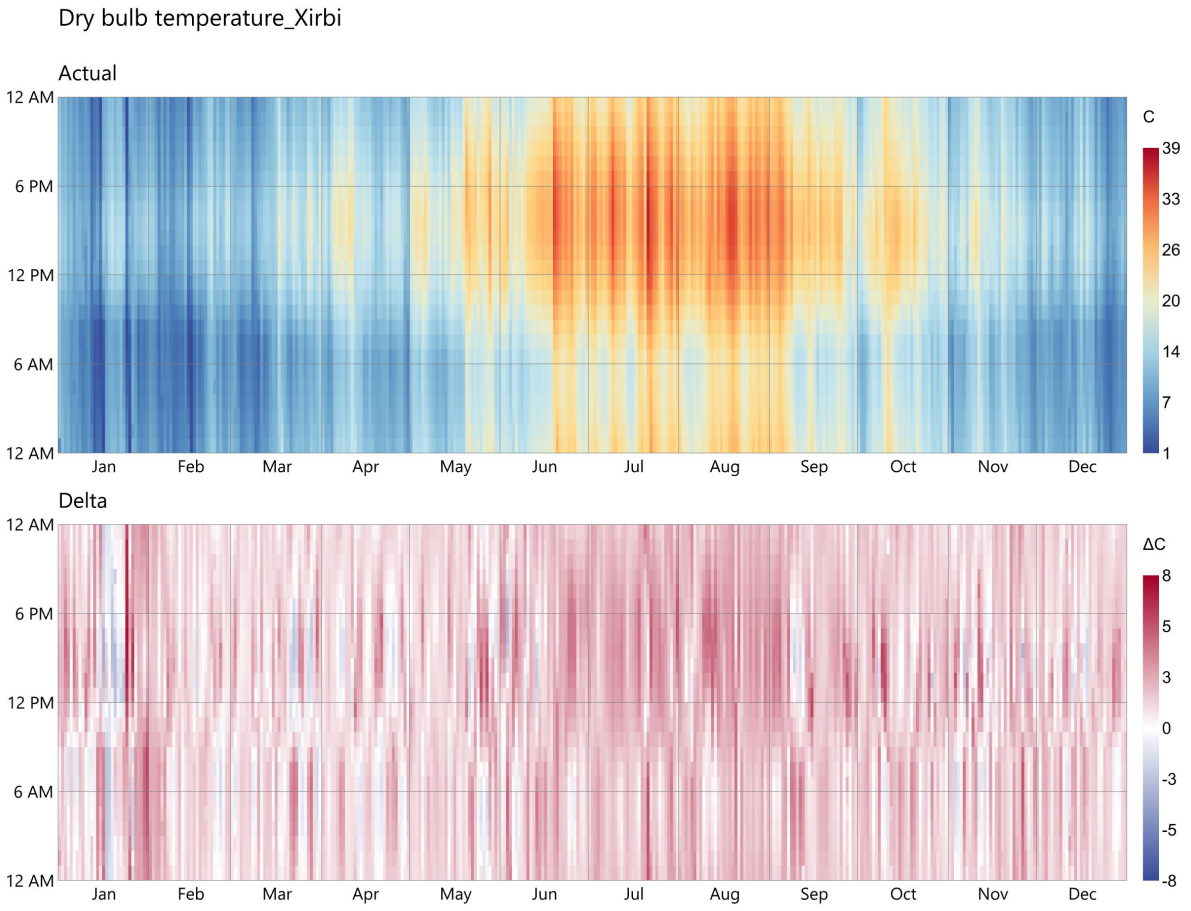

Figure 72. Dry bulb temperature in Xirbi. On top in the current scenario, below the delta between 2050 and current scenario. Graph by the author via Grasshopper and Ladybug Tools. Copyright: Marcello Turrini, Emanuele Naboni, 2023

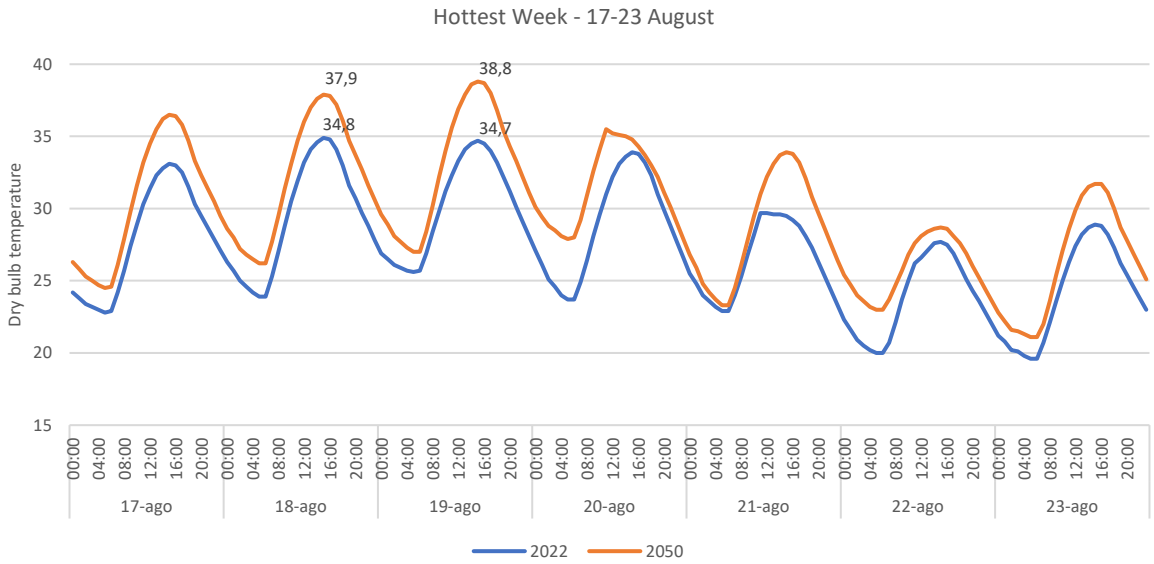

Figure 73. Dry bulb temperature analysis in the hottest week. Peaks are on August 18 and 19. Graph by the author. Copyright: Marcello Turrini, Emanuele Naboni,, 2022

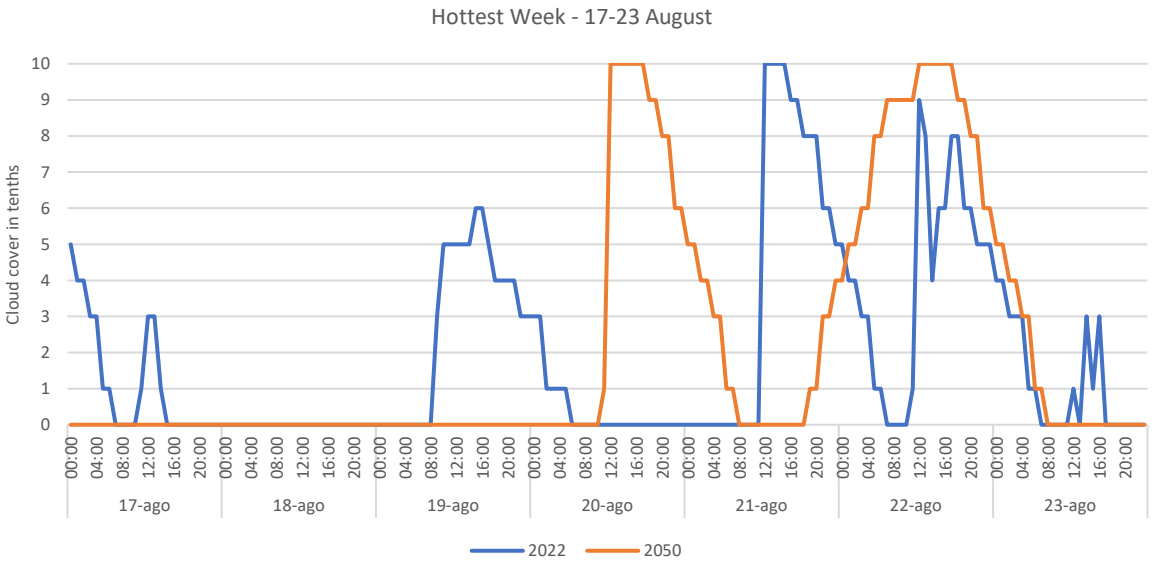

Figure 74. Cloud cover in the hottest week of Xirbi. August 18 is free of clouds both in the current and 2050 scenario. Graph by the author. Copyright: Marcello Turrini, Emanuele Naboni, 2022

5.3.2 Identification of Configurations

The challenge was to test the methodology in a hot climate to understand which strategy was best suited to this context. Inspiration was drawn from the north-south orientation of the building's main axis, which is aligned with the prevailing summer winds (Figure 75). It was therefore decided to test the resilience of a naturally ventilated building by varying the porosity of the wind inlets and outlets. Different configurations were then applied to the north and south glass facades. The reference scale is therefore that of the building component.

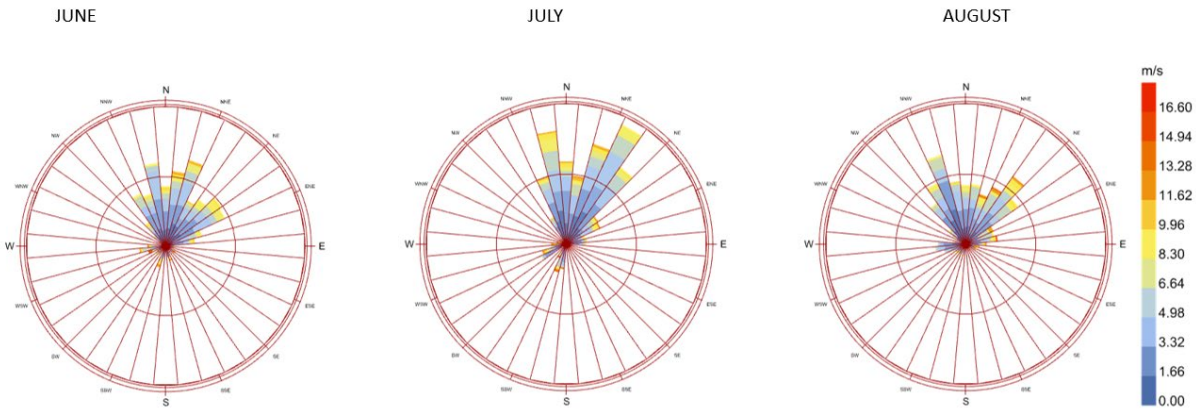

Figure 75. Wind velocity and direction in summer. The prevailing direction is from north. Copyright: Marcello Turrini, Emanuele Naboni, 2022

Five configurations were selected (Figure 76): XI1_All closed, which considers the façade completely closed; XI2_Above opened, with the upper part of the glazing open; XI3_Four opened, which considers the openings concentrated on one side of both glazing elements; XI4_alternated, which considers the two glazing elements with alternating open and closed modules; finally, configuration XI5_All opened, which considers the glazing elements completely open at all times.

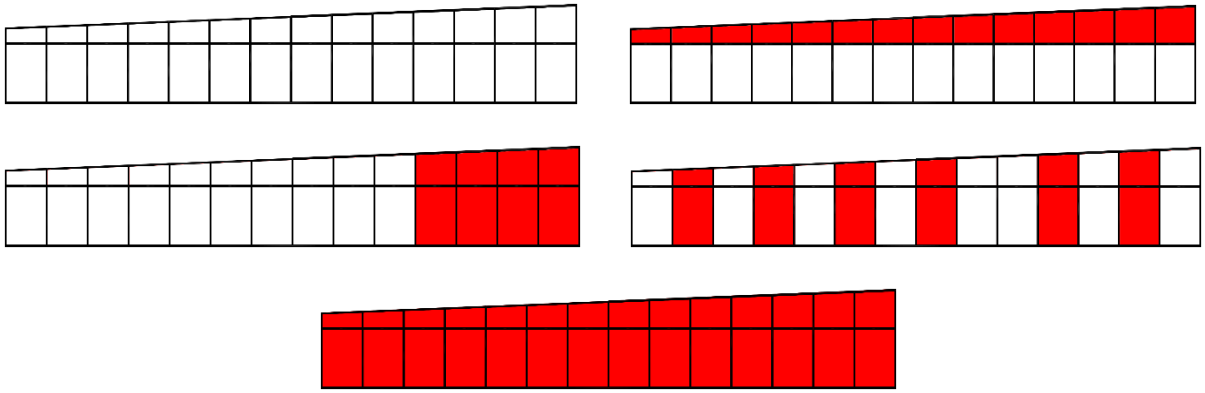

Figure 76. Variation of the two glass facades in the 5 configurations. The red part represents the opening. Copyright: Marcello Turrini, Emanuele Naboni, 2022

5.3.3 Processing of three-dimensional digital models

The three-dimensional Rhinoceros models were generated by importing the original models created in Revit. They were simplified to enable effective simulations without performing unnecessary calculations to capture overly minute details. The original transparent parts, the large opening in the floor, the two air-conditioned boxes, and the external escalators were retained for completeness. In addition, the internal elevator shafts that influence the internal wind flow were also modeled.

5.3.4 Preparation of the models to UTCI simulations

Microclimatic factor simulations were carried out using Honeybee, due to the absence of vegetation and bodies of water, which Honeybee is unable to simulate. Wind was simulated using Eddy3D. A grid of sensors was placed within the analyzed space, spaced 2 m apart. Wind speed and mean radiant temperature were resolved locally through simulation, while air temperature and relative humidity were taken from the external weather data, consistent with

the semi-outdoor and non-conditioned nature of the space. The simulation day chosen was August 18 at 3 PM, which is among the hottest hours of the year. The reference year was 2050, calculated with the RCP 8.5 profile.

5.3.5 UTCI variations for each configuration

Configuration XI_1 – All closed

The total closure of the two front glazed panels ensured that the air speed was kept at around 0.5 m/s (Figure 77), which is the minimum wind speed required to calculate the UTCI.

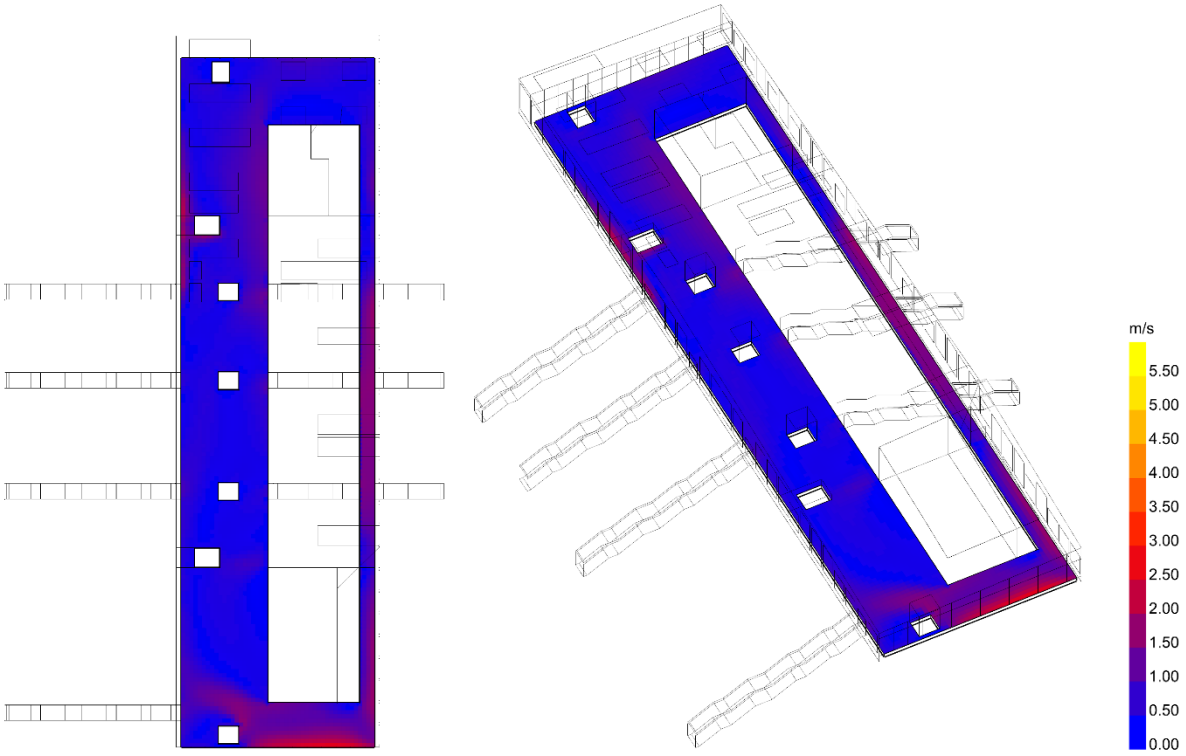

Figure 77 Wind simulation for configuration XI_1—The closure of the two facades keeps internal natural ventilation levels very low. Copyright: Marcello Turrini, Emanuele Naboni, 2022

Figure 78 shows the UTCI results at 2022 on the left and 2050 on the right. At 2022, a UTCI of “Strong heat stress” category can be seen throughout the building, with peaks at the envelope transparencies. At 2050 the whole building is in the very “strong heat stress” category with an almost constant UTCI of about 40 °C.

The variation in UTCI shown in figure 79 is kept around 3 °C over most of the building, showing a rather small change considering the extreme heat of the selected hour.

The statistical distribution of the variation of UTCI in the inner station space (Figure 80) shows uniformity over the entire inner surface, with a slight thing toward the highest values, which integrates the areas at the margin. The mean value is around 3 °C.

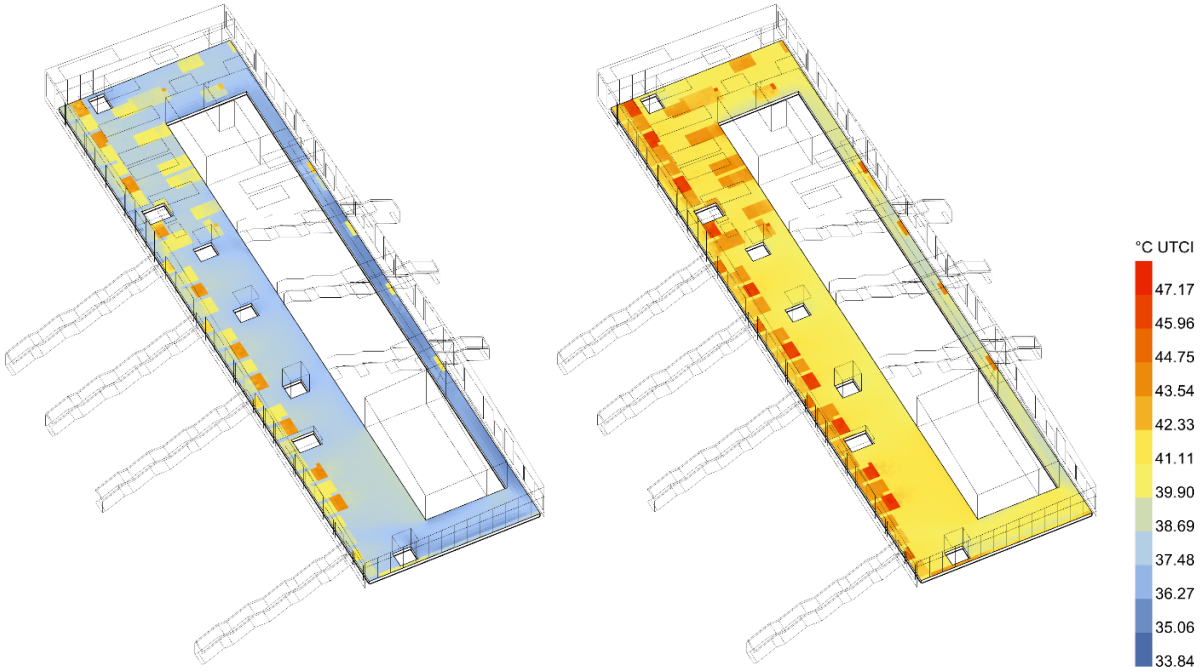

Figure 78. UTCI for configuration XI_1. 2022 on the left, 2050 on the right. Copyright: Marcello Turrini, Emanuele Naboni, 2022

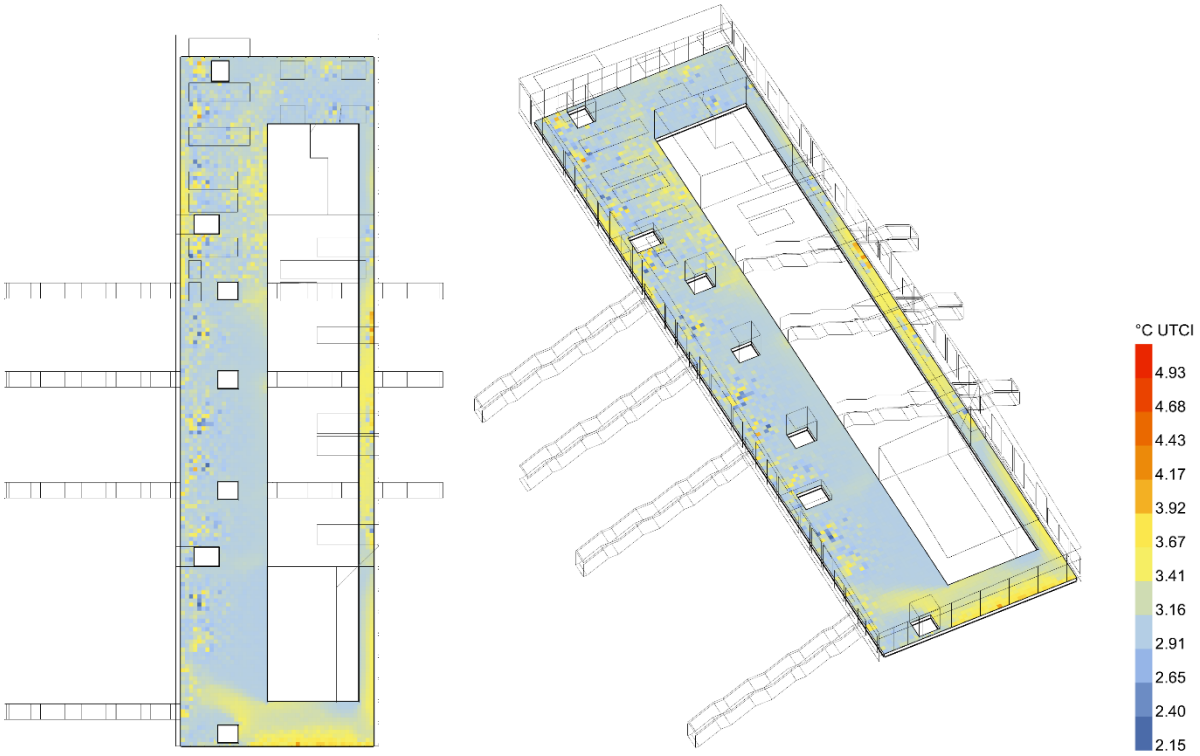

Figure 79. UTCI variation for the configuration XI_1. Copyright: Marcello Turrini, Emanuele Naboni, 2022

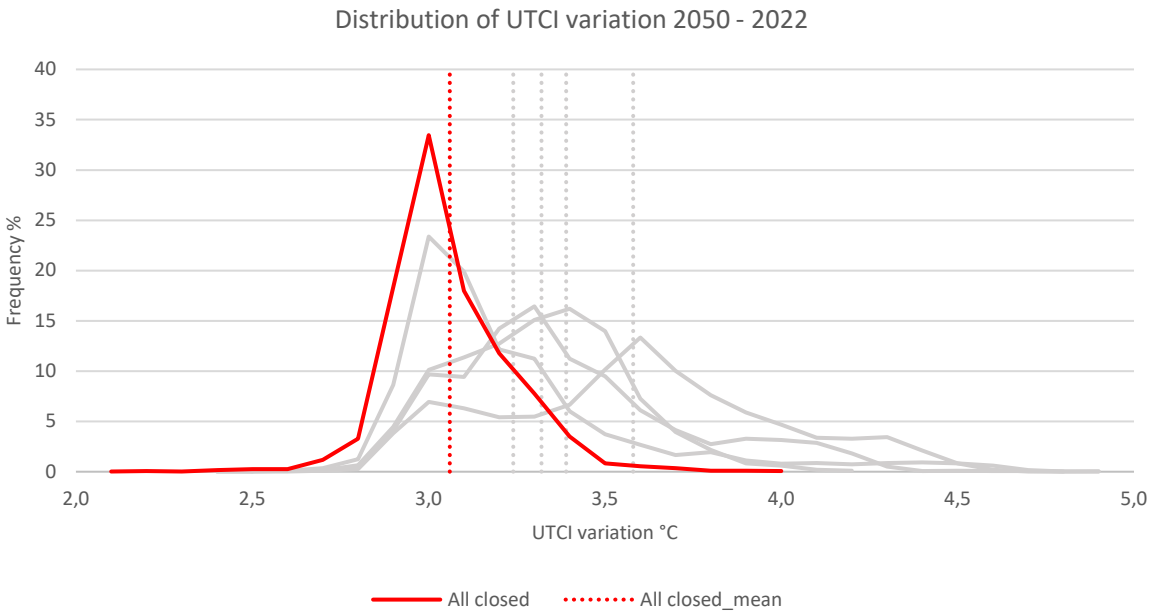

Figure 80. Statistical distribution of the UTCI variation for configuration XI_1. Copyright: Marcello Turrini, Emanuele Naboni, 2022

Configuration XI_2 – Above opened

The opening of the upper part of the two front glazed facades creates light air speed (Figure 81), that is stopped by the elevators in the central part and is more intense at some sharp corners. The wind velocity is between around 0.5 and 3 m/s.

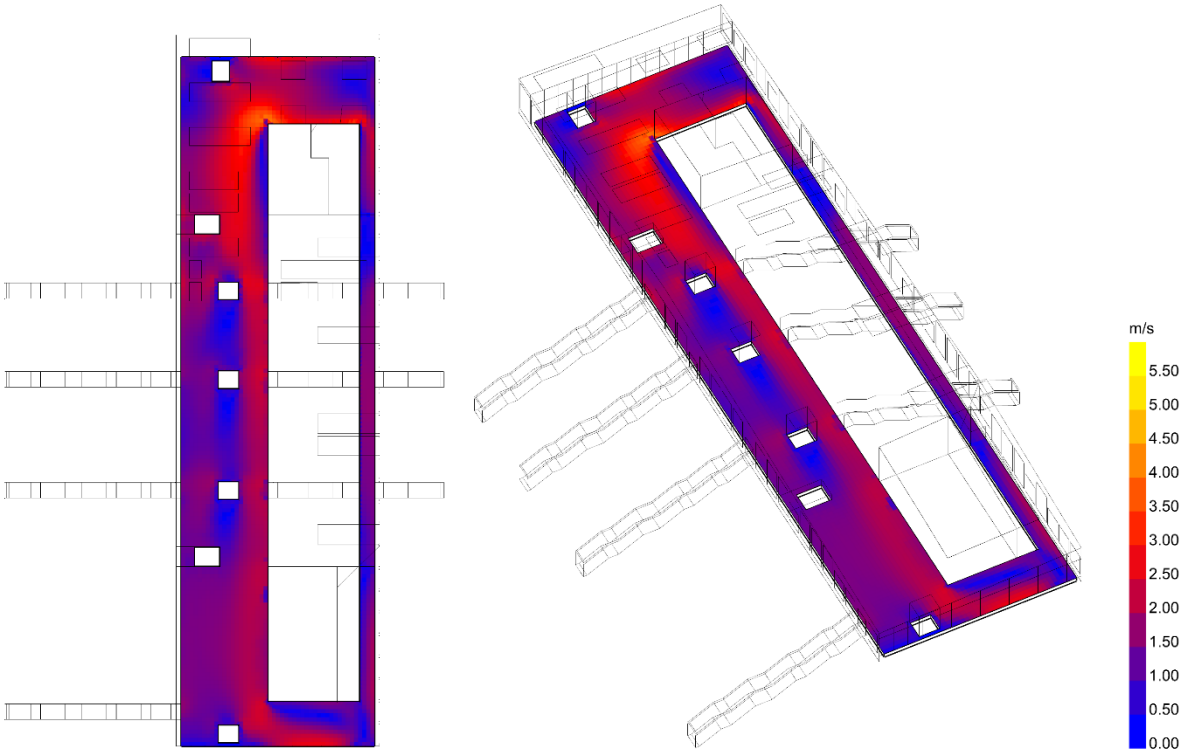

Figure 81. Wind flow for configuration XI_2. Copyright: Marcello Turrini, Emanuele Naboni, 2022

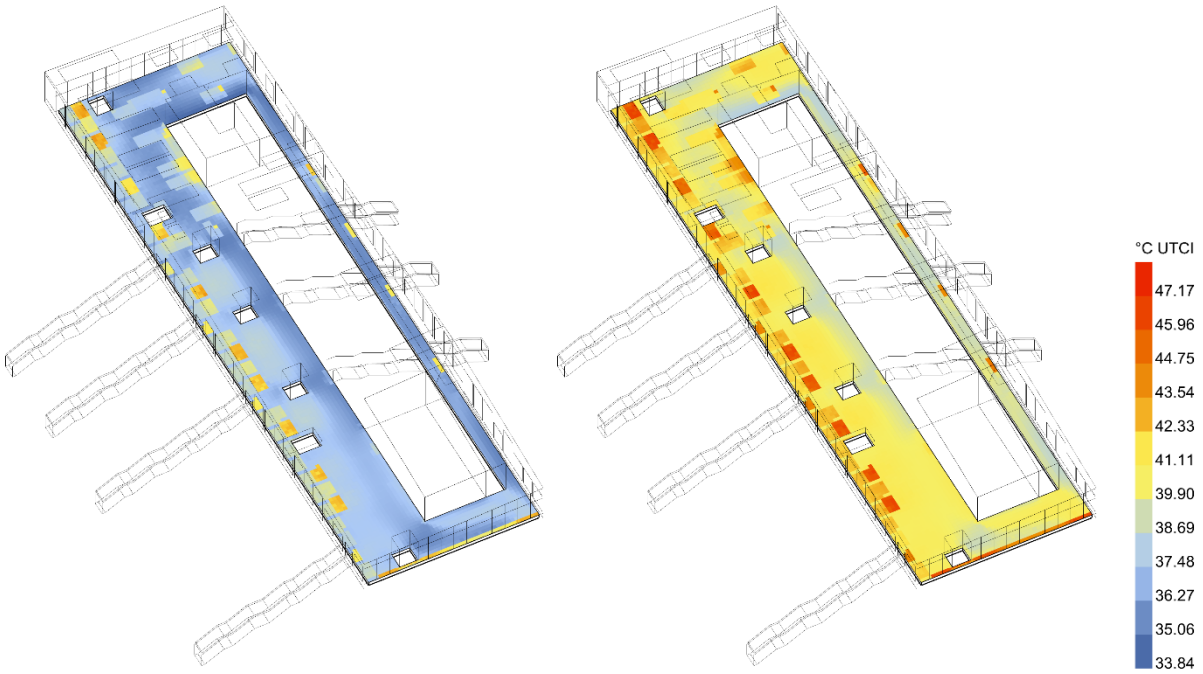

Figure 82. UTCI for configuration XI_2. 2022 on the left, 2050 on the right. Copyright: Marcello Turrini, Emanuele Naboni, 2022

Figure 82 shows the UTCI results at 2022 on the left and 2050 on the right, for configuration XI_2. In 2022, a UTCI of “Strong heat stress” category can be seen throughout the building, with peaks at the envelope transparencies, but slightly closed in comparison to configuration XI_1. In 2050 the whole building is in the very “strong heat stress” category with an almost constant UTCI of about 40 °C, with lower absolute values compared to XI_1.

The variation in UTCI in Figure 83 shows a higher grade compared to XI_2, with some peaks at around 4 °C. It seems that areas with higher wind velocity show a higher UTCI variation, that is less thermal resilience.

The statistical distribution of the variation of UTCI in the inner station space (Figure 84) shows a higher distribution of the UTCI variation, with a mean value of about 3.3 °C.

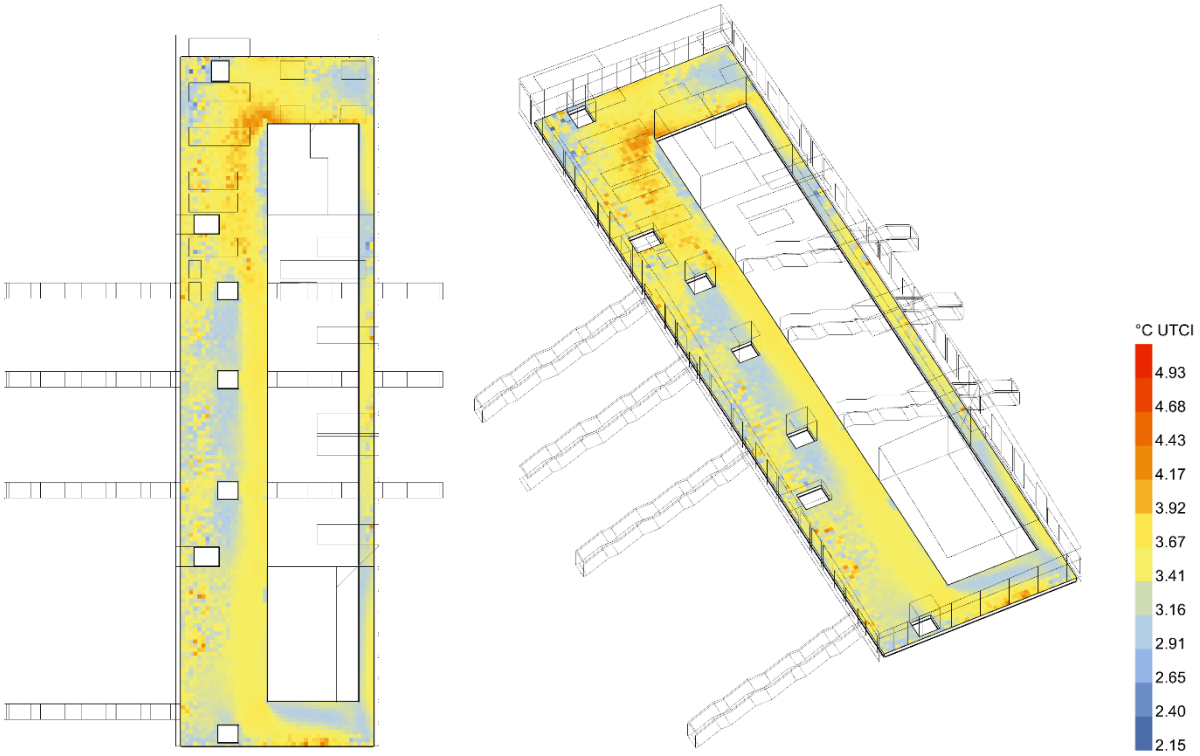

Figure 83UTCI variation for the configuration XI_2. Copyright: Marcello Turrini, Emanuele Naboni, 2022

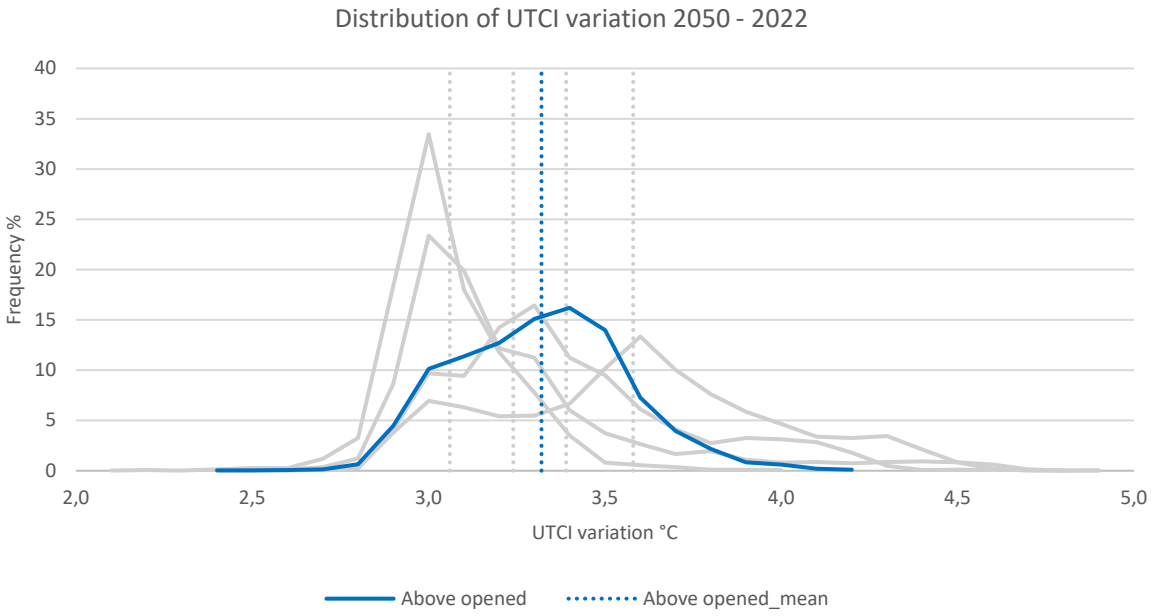

Figure 84. Statistical distribution of the UTCI variation for configuration XI_2. Copyright: Marcello Turrini, Emanuele Naboni, 2022

Configuration XI_3 – Four opened

The opening of one lateral part of the two front glazed facades creates higher air speed (Figure 85), that is concentrated near the inlet and the outlet. The wind velocity is between 0.5 and 5 m/s.

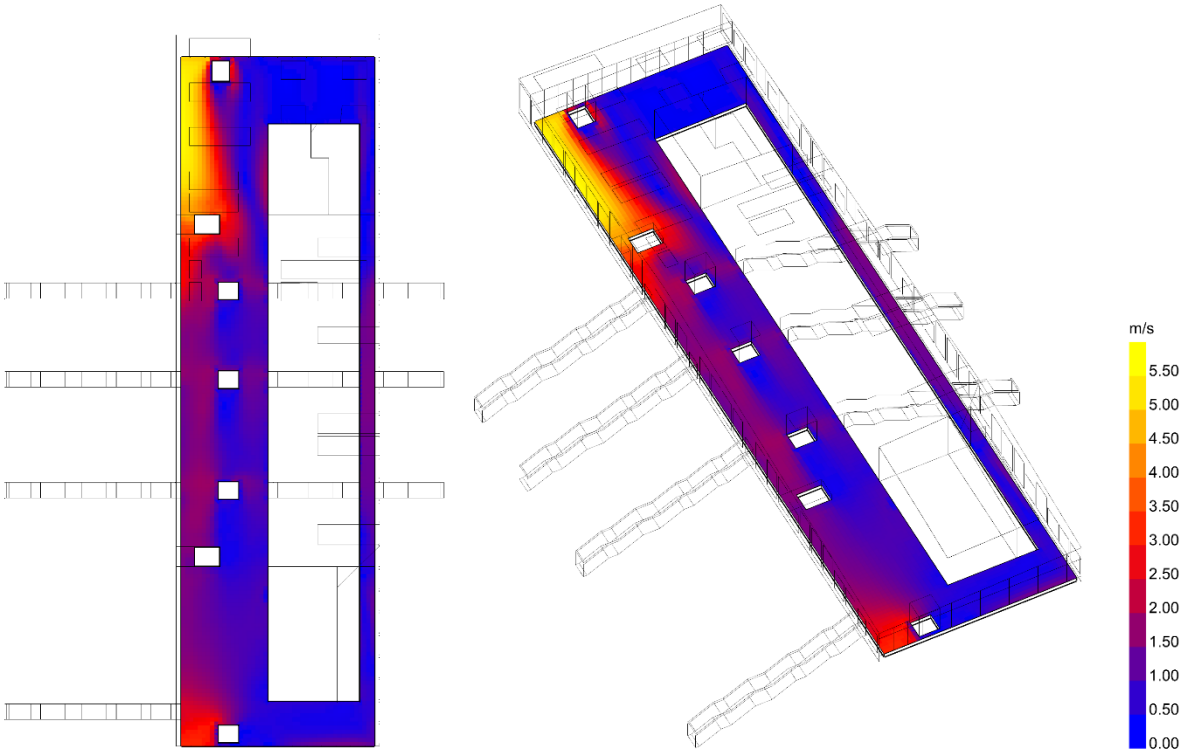

Figure 85. Wind flow for configuration XI_3. Copyright: Marcello Turrini, Emanuele Naboni, 2022

Figure 86 shows the UTCI results in 2022 on the left and 2050 on the right, for configuration XI_3. In 2022, a UTCI of “Strong heat stress” category can be seen throughout the building, with peaks at the envelope transparencies, but slightly lower, about 37 °C, in comparison to configuration XI_2. In 2050 the whole building is in the very “strong heat stress” category with an almost constant UTCI of about 40 °C, with lower absolute values compared to XI_2.

The variation in UTCI in Figure 87 shows a high grade in areas with higher wind velocity, confirming the findings in configuration XI_2.

The statistical distribution of the variation of UTCI in the inner station space (Figure 88) shows a uniform distribution of the UTCI variation, with a tail in the upper values showing the overheated spots. The mean value is about 3.2 °C.

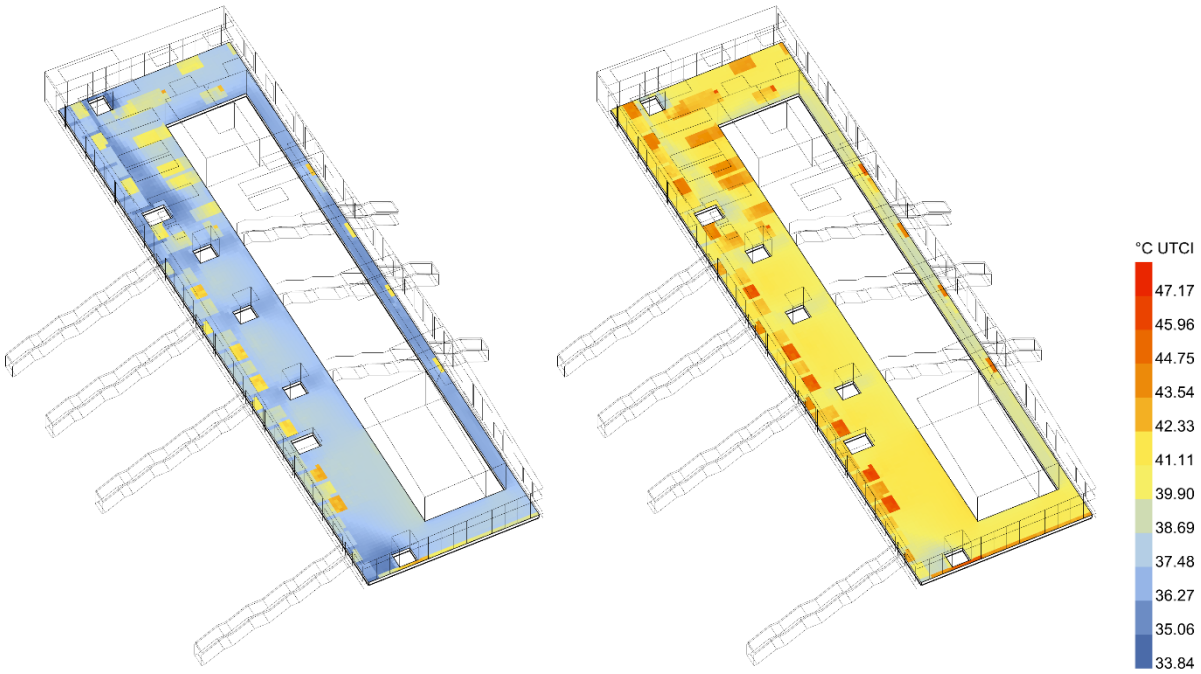

Figure 86. UTCI for configuration XI_3. 2022 on the left, 2050 on the right. Copyright: Marcello Turrini, Emanuele Naboni, 2022

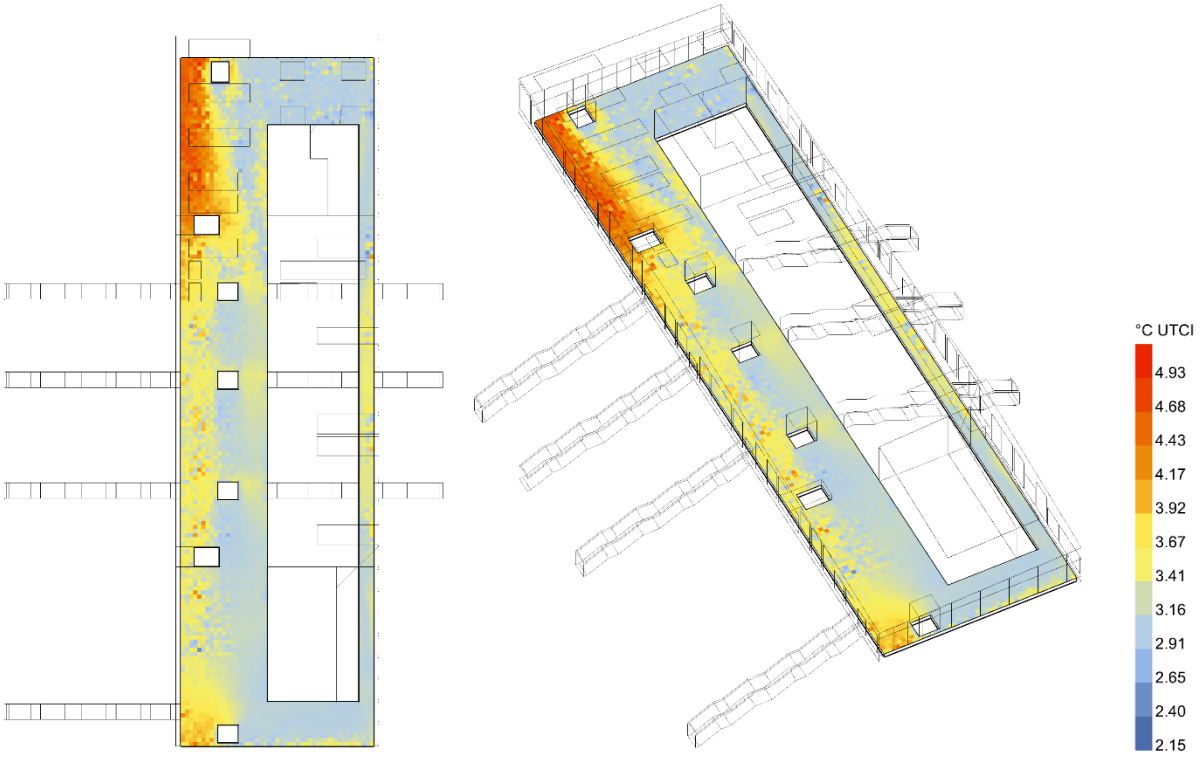

Figure 87. UTCI variation for the configuration XI_3. Copyright: Marcello Turrini, Emanuele Naboni, 2022

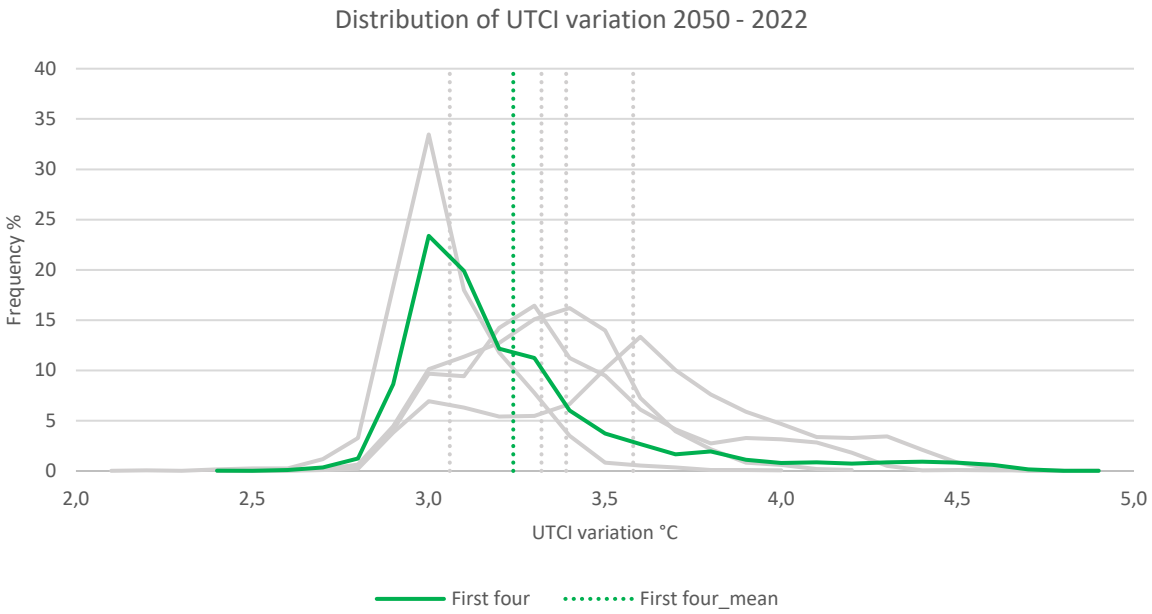

Figure 88. Statistical distribution of the UTCI variation for configuration XI_3. Copyright: Marcello Turrini, Emanuele Naboni, 2022

Configuration XI_4 – Alternated

The opening of alternated parts of the two front glazed facades creates higher air speed (Figure 89), that is distributing inside the building. The wind velocity is between 0.5 and 4 m/s.

Figure 90 shows the UTCI results in 2022 on the left and 2050 on the right, for configuration XI_4. In 2022, a UTCI of “Strong heat stress” category can be seen throughout the building, with peaks at the envelope transparencies, but slightly lower, with areas at about 35 °C. In 2050 the whole building is in the very “strong heat stress” category with an almost constant UTCI of about 39 °C.

The variation in UTCI in Figure 91 clearly shows a high grade in areas with higher wind velocity, with peaks of 4 °C

The statistical distribution of the variation of UTCI in the inner station space (Figure 92) shows a uniform distribution of the UTCI variation, with a tail in the upper values showing the overheated spots. The mean value is about 3.4 °C.

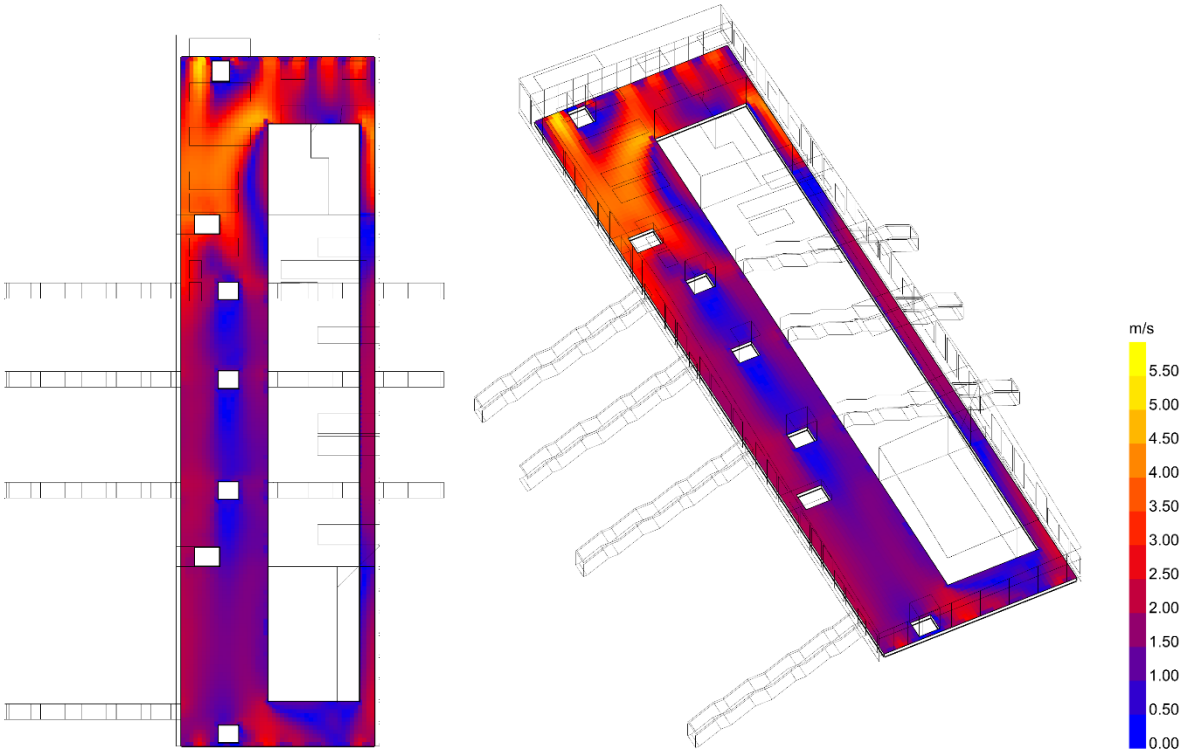

Figure 89. Wind flow for configuration XI_4. Copyright: Marcello Turrini, Emanuele Naboni, 2022

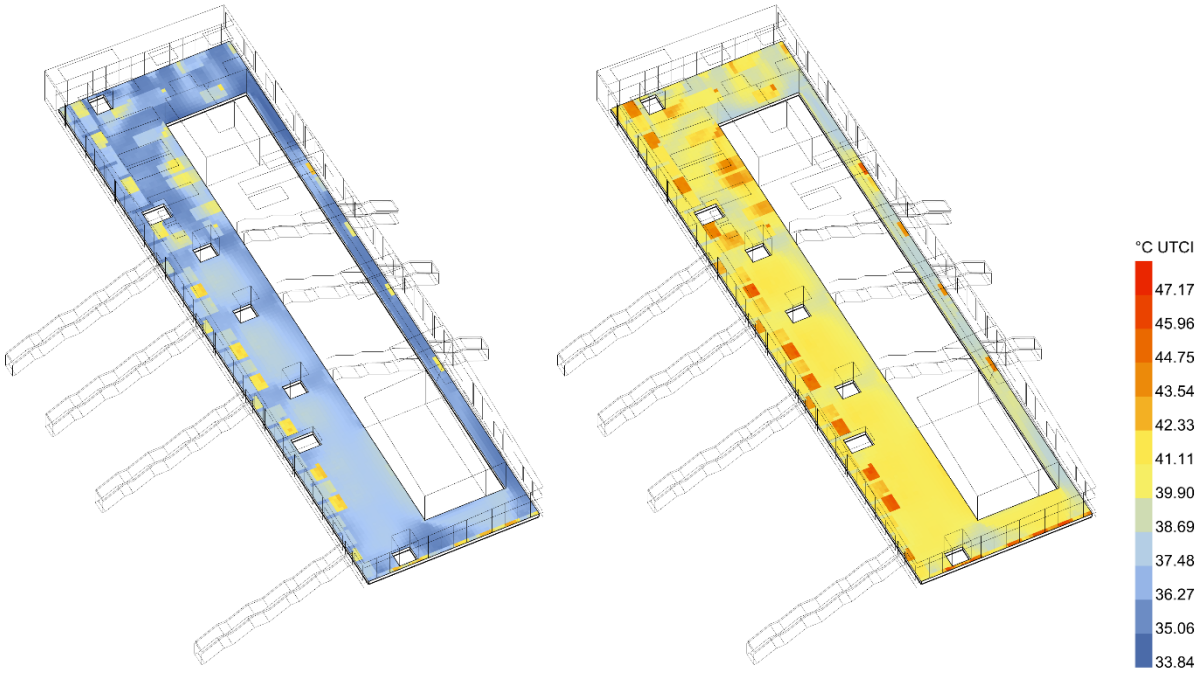

Figure 90. UTCI for configuration XI_4. 2022 on the left, 2050 on the right. Copyright: Marcello Turrini, Emanuele Naboni, 2022

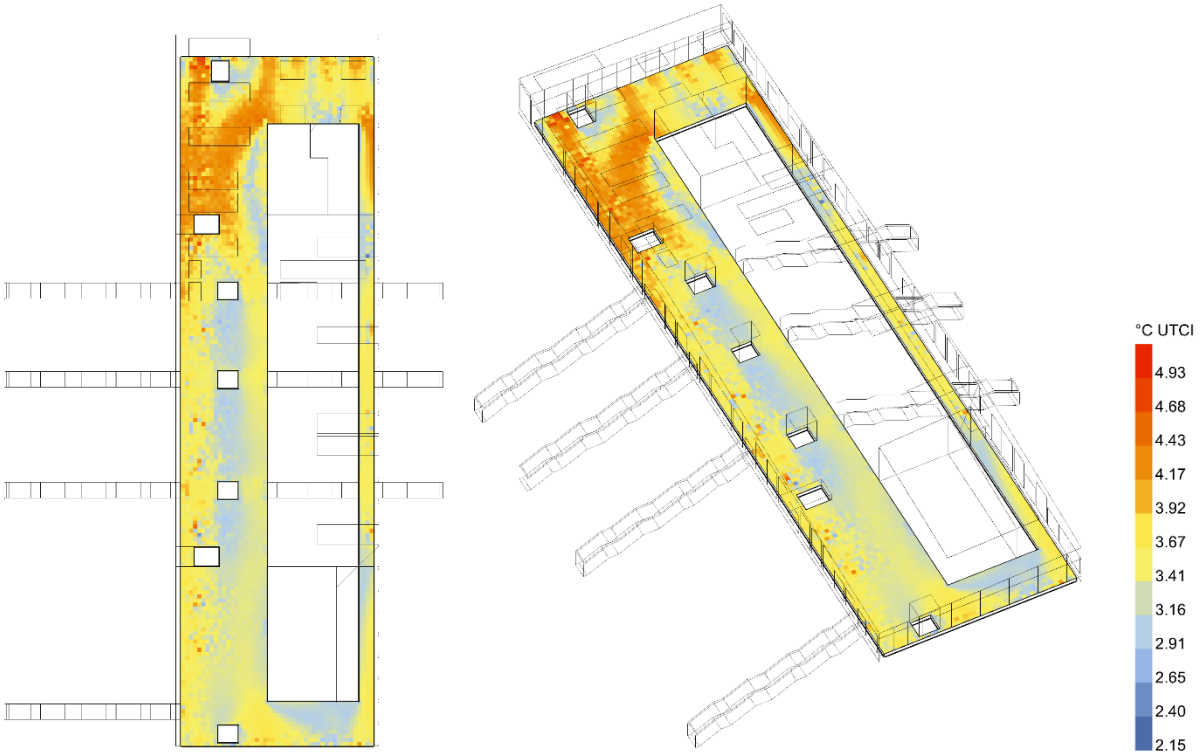

Figure 91. UTCI variation for the configuration XI_4. Copyright: Marcello Turrini, Emanuele Naboni, 2022

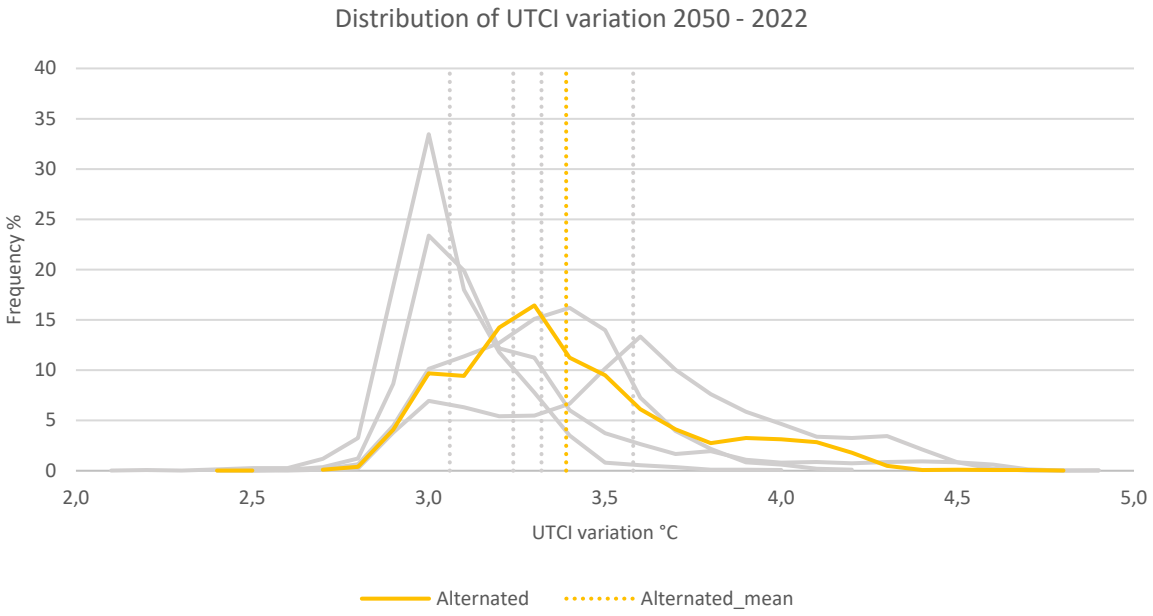

Figure 92. Statistical distribution of the UTCI variation for configuration XI_4. Copyright: Marcello Turrini, Emanuele Naboni, 2022

Configuration XI_5 – All opened

The opening of the entire front glazed facades creates a wind tunnel (Figure 93), In the whole internal space the wind speed is at about 3 m/s with peak areas at 5 m/s.

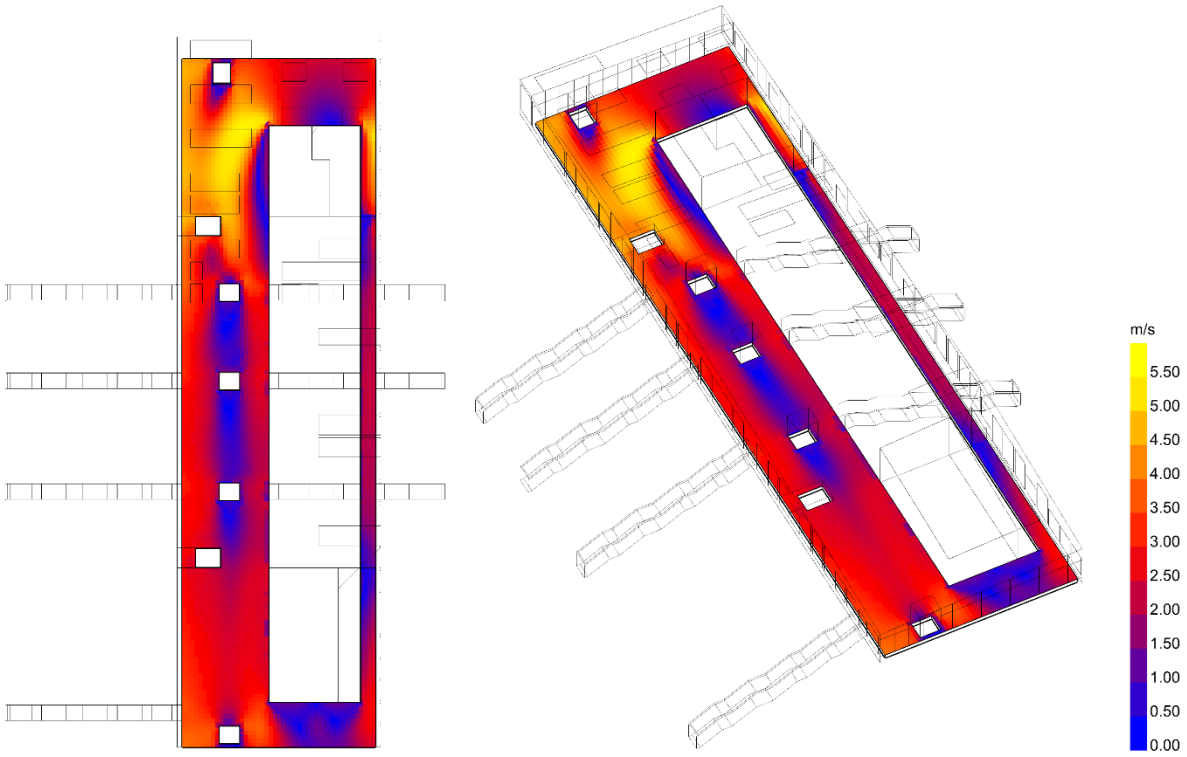

Figure 93. Wind flow for configuration XI_5. Copyright: Marcello Turrini, Emanuele Naboni, 2022

Figure 94 shows the UTCI results in 2022 on the left and 2050 on the right, for configuration XI_5. In 2022, a UTCI of “Strong heat stress” category can be seen throughout the building, although in this configuration the lowest temperatures are recorded. In 2050 the whole building is in the very “strong heat stress” category with lower UTCI areas of about 38 °C.

The variation in UTCI in Figure 95 clearly shows a very high grade of variation in the entire building, with peaks of 4.5 °C

The statistical distribution of the variation of UTCI in the inner station space (Figure 96) shows a flat profile distribution of the UTCI variation, with a peak near the average of 3.6 °C.

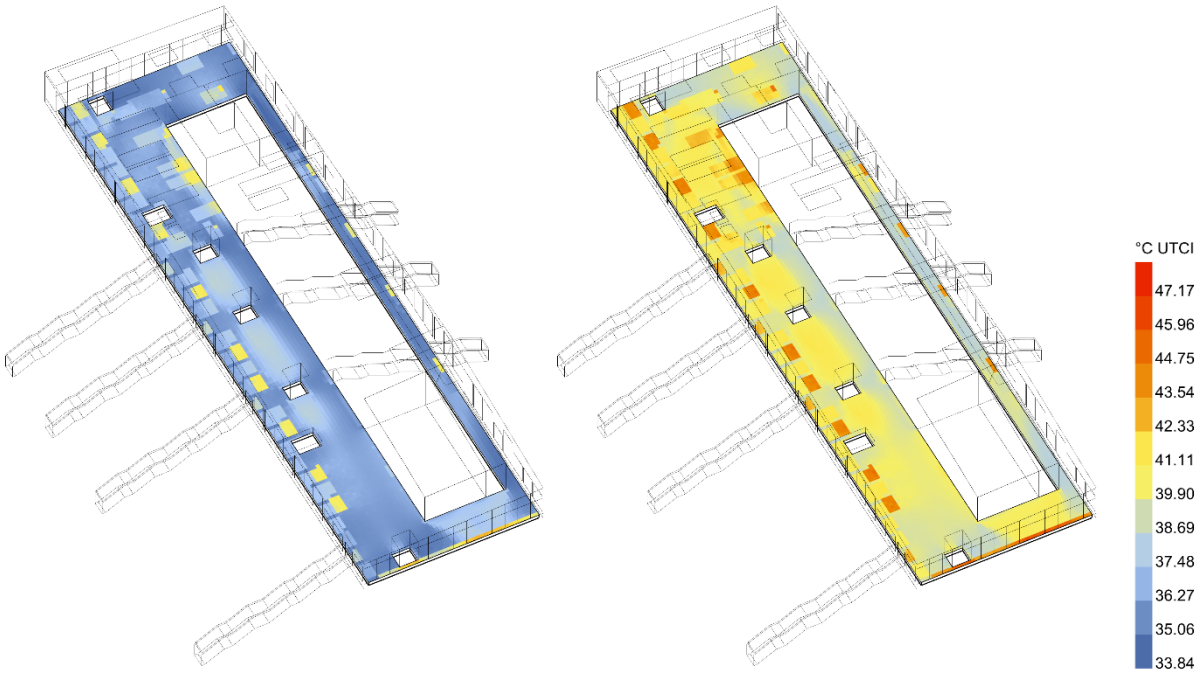

Figure 94. UTCI for configuration XI_5. 2022 on the left, 2050 on the right. Copyright: Marcello Turrini, Emanuele Naboni, 2022

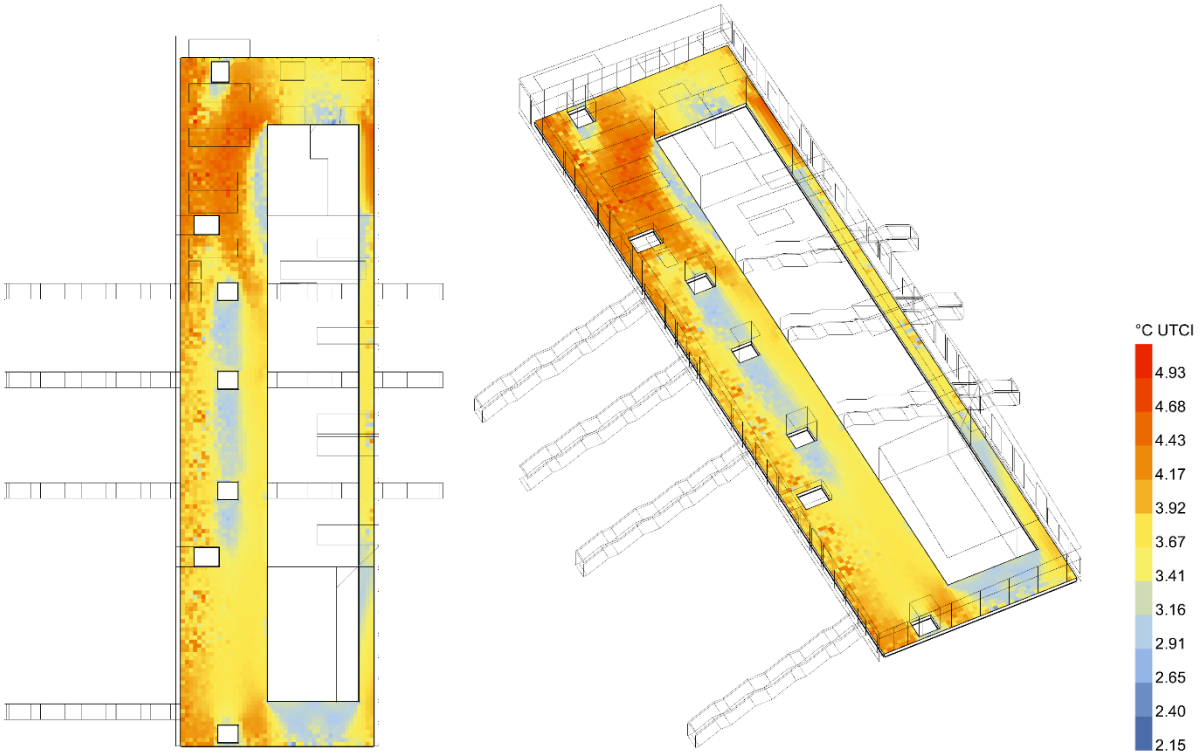

Figure 95UTCI variation for the configuration XI_5. Copyright: Marcello Turrini, Emanuele Naboni, 2022

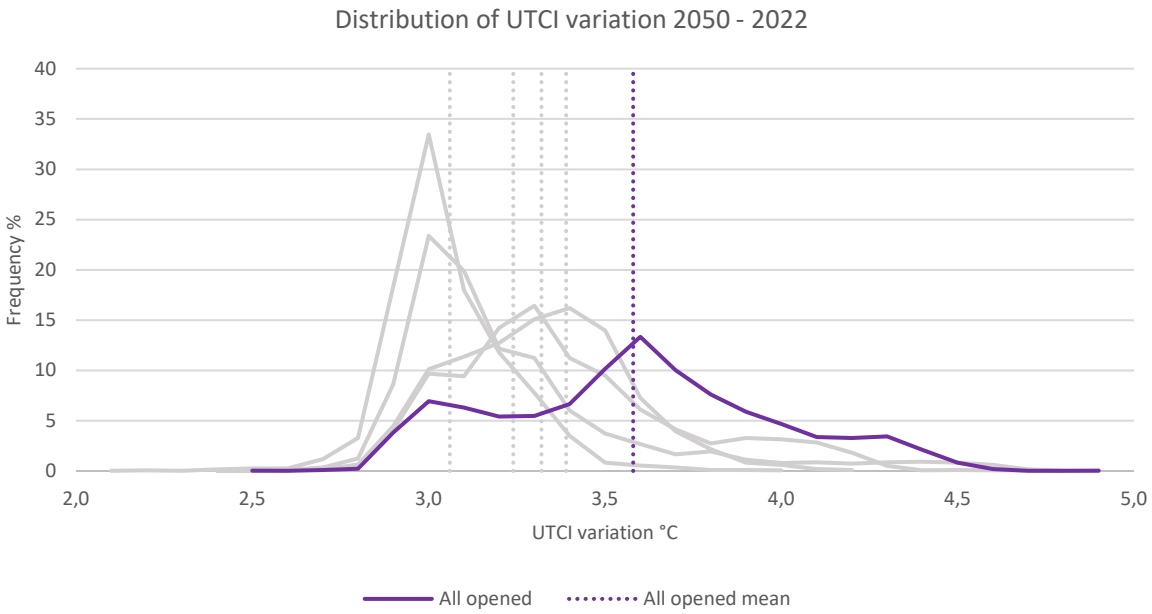

Figure 96. Statistical distribution of the UTCI variation for configuration XI_5. Copyright: Marcello Turrini, Emanuele Naboni, 2022

5.3.6 Discussion

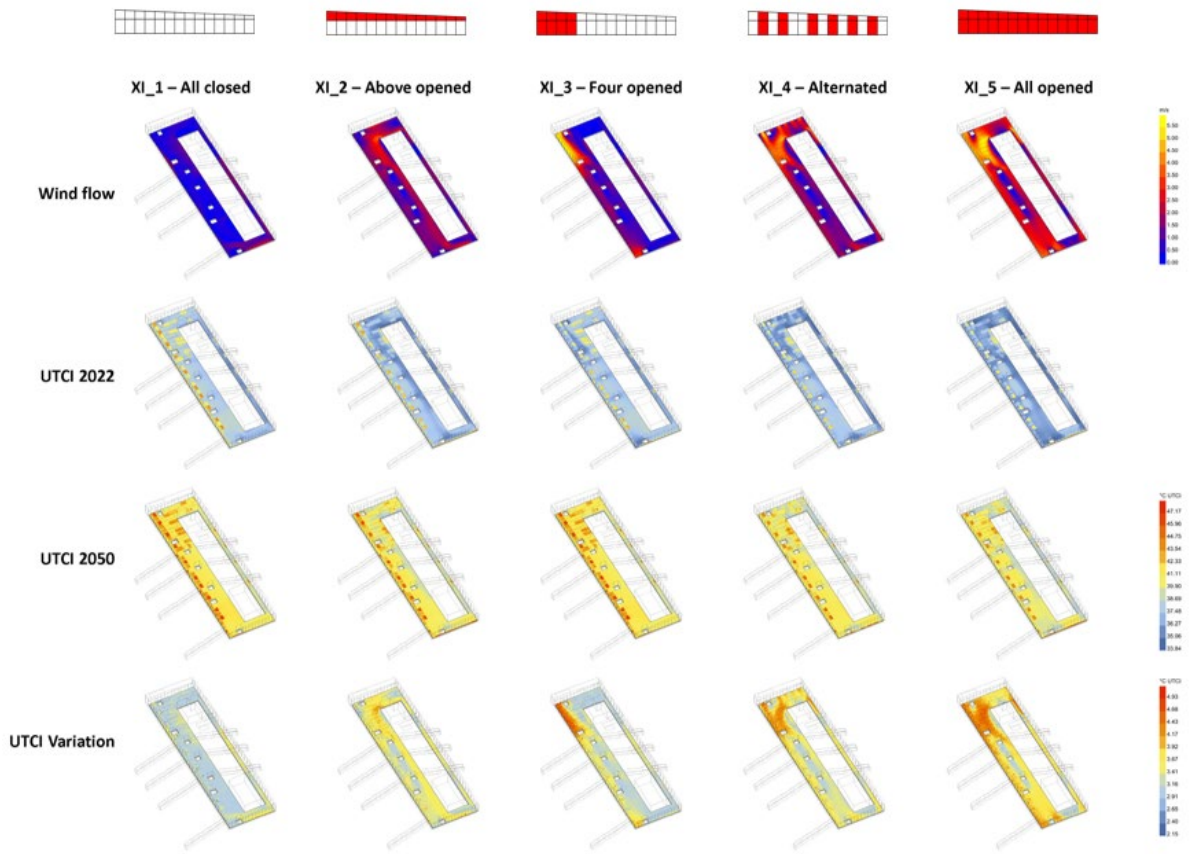

Figure 97. Comparison of the configurations. Copyright: Marcello Turrini, Emanuele Naboni, 2022

This case is emblematic of how the methodology is able to detect dual-valued behavior. While more porous and wind-permeable enclosures show lower absolute values in UTCI as porosity increases, resilience decreases, showing larger changes in UTCI in more wind-permeable configurations. This is an indicator on the impossibility of relying on natural ventilation in cases of extreme heat such as in Sicily in August, and suggests shifting the focus to lowering MRT by operating on envelope transparencies.

Also from the statistical distribution of the change in UTCI, a gradual shift from cuspidated curves to flatter curves that shift to higher values due to a greater distribution of thermal nonresilience is recognized.

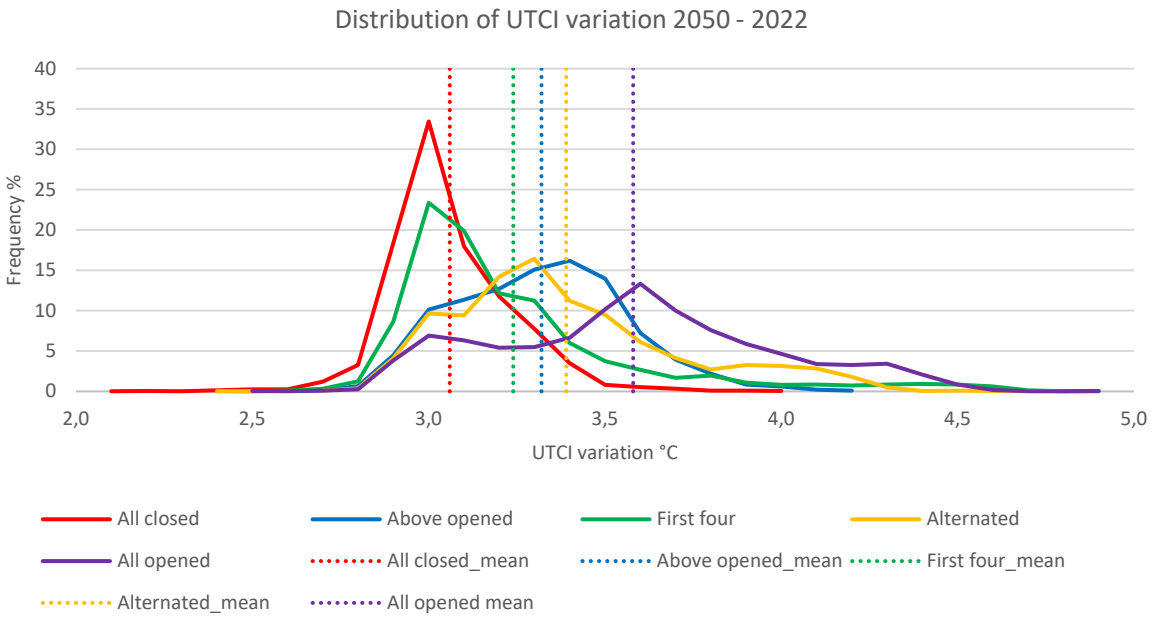

Figure 98. Statistical distribution of UTCI variations in all the configurations. Copyright: Marcello Turrini, Emanuele Naboni, 2022

Field	XI_1	XI_2	XI_3	XI_4	XI_5
Typology and key spatial traits	Fully sealed end façades; minimal indoor air movement; interior behaves as a weakly ventilated semi-indoor volume.	Upper façade portions open; limited but legible airflow pathways; ventilation remains partial and spatially uneven.	Concentrated openings promote stronger inflow/outflow paths; higher local air speeds near openings; spatially polarized ventilation.	Alternating open/closed modules distribute airflow more broadly than XI_3; ventilation is stronger and more spatially pervasive.	Fully open façades; “wind-tunnel” behaviour with sustained air movement across the occupied zone.
Baseline UTCI	Strong heat-stress regime across the interior; local peaks near transparent envelope areas.	Still in strong heat-stress regime; slightly lower absolute stress than the fully closed condition in ventilated zones.	Strong heat stress persists; locally lower UTCI where airflow is most effective.	Strong heat stress persists; comparatively cooler pockets appear where air movement penetrates deeper.	Lowest baseline UTCI among the set; broader interior areas benefit from airflow-driven relief.
Future UTCI	Very strong heat-stress regime, largely uniform; stress becomes less spatially differentiated.	Very strong heat stress throughout, with slightly reduced absolute levels where airflow is strongest.	Very strong heat stress throughout; local relief remains visible but overall severity increases.	Very strong heat stress throughout; comparatively lower absolute UTCI than the more sealed variants, yet still severe.	Very strong heat stress throughout; lowest future UTCI pockets occur in the most ventilated zones, though overall

Field	XI_1	XI_2	XI_3	XI_4	XI_5
					conditions remain critical.
ΔUTCI mean (°C)	≈ 3.0	≈ 3.3	≈ 3.2	≈ 3.4	≈ 3.6
ΔUTCI range (°C)	Approx. ~2.6–4.0 (mostly clustered near the mean).	Approx. ~2.8–4.2 (clear upper tail and local hotspots).	Approx. ~2.6–4.7 (uniform core with extended upper tail in high-flow areas).	Approx. ~2.6–4.7 (broad range; pronounced right tail).	Approx. ~2.8–4.8 (widest effective spread; persistent upper tail).
Spatial response pattern	Cuspidated, narrow distribution; limited spatial volatility; ΔUTCI field comparatively stable, with modest edge/margin hotspots.	Broader distribution; ΔUTCI increases where airflow is more intense; spatial sensitivity becomes more structured.	Uniform core + right tail: ΔUTCI rises at inlet/outlet-driven zones; stronger gradients emerge.	Flatter, right-skewed distribution: ΔUTCI heterogeneity increases; hotspots align with distributed high-velocity paths.	Flattest profile among variants: ΔUTCI is widely dispersed; high-sensitivity zones expand beyond immediate margins.
Main microclimatic drivers and design reading	Low ventilation reduces convective coupling with air-temperature forcing, producing a stable ΔUTCI response—yet at the cost of poor baseline conditions. Useful as a reference case showing that "stability" alone is not comfort.	Partial ventilation improves baseline locally but increases sensitivity where airflow dominates the heat balance. Indicates that ventilation benefits are conditional and spatially uneven.	Concentrated openings create strong local airflow pathways: baseline relief is localized, while ΔUTCI hotspots track high-flow zones, revealing threshold-dependence under warming.	Distributed ventilation improves local relief but produces stronger ΔUTCI dispersion, showing that enhanced airflow can amplify sensitivity under future heat.	Maximum porosity yields the greatest baseline relief but also the highest sensitivity and spatial instability. Design implication: keep operability, but govern openness by climatic thresholds; prioritize radiative control of transparent elements as the stable resilience backbone.

Table 12. Comparative synthesis of the ΔUTCI-based assessment for the five component-scale configurations of the Xirbi railway station (XI_1–XI_5), evaluated at the selected peak-summer time slice under paired baseline and future climate scenarios (2022 vs 2050). The table summarizes absolute UTCI conditions, ΔUTCI magnitude, and internal variability within the indoor evaluation domain, supporting a comparative interpretation of the thermal response associated with different envelope-porosity configurations

.

5.3.7 Conclusions for component scale.

At component scale, the Xirbi railway-station study tests the sensitivity of the workflow to envelope-level design variations by comparing five degrees of openness and porosity (XI_1 to XI_5) under paired baseline and future climatic conditions. The results confirm that the methodology remains responsive even when interventions are reduced to geometric and operational changes in the envelope, and that ΔUTCI can reveal trade-offs that would be difficult to identify through absolute comfort readings alone.

Quantitatively, the envelope variants exhibit a clear increase in sensitivity as openness grows. The most closed configuration (XI_1) yields a compact ΔUTCI distribution between roughly 2.9 and 3.2 °C, with an average around 3.0 °C, consistent with low internal variability. Intermediate configurations show progressively higher averages and broader spreads: XI_2 reaches a mean ΔUTCI of approximately 3.3 °C (range about 2.8–4.0 °C), XI_3 averages about 3.2 °C with a similarly wide span, and XI_4 rises to a mean close to 3.4 °C. The most open configuration (XI_5) shows the highest amplification, with most values concentrated between approximately 3.4 and 4.5 °C, a marked peak near 4.5 °C, and an average around 3.6 °C. In parallel, the airflow fields confirm that increased porosity produces higher local wind speeds—ranging from about 0.5 m/s in XI_1 up to peaks near 5 m/s in the most open variants—yet this aerodynamic benefit does not automatically translate into lower climate-change sensitivity.

The principal conclusion is therefore methodological and design-relevant: envelope openness can improve local ventilation and perceived comfort under some baseline conditions, while simultaneously increasing the coupling between the indoor microclimate and a warmer future exterior, thereby elevating ΔUTCI and expanding the upper tail of the distribution. In practical terms, this supports treating porosity as an adaptive capacity whose use should be governed by time-dependent and climate-dependent operating logic (for example, exploiting favorable cooling windows while limiting exposure when outdoor conditions are strongly adverse).

Overall, the component-scale case consolidates the validity of the workflow at the finest design resolution addressed in the thesis. It shows that the same comparative structure used at district and building level can be meaningfully applied to envelope decisions, producing

evidence that is both quantitative (means, ranges, tails) and spatially interpretable—precisely the combination required to support robust design choices under climate change.

6 Discussion

6.1 Synthesis of findings across scales

This chapter discusses the results presented in Chapter 5 by moving from *description* to *interpretation*, explaining why different spatial configurations exhibit different levels of thermal comfort resilience under climate change, and what those differences imply for design practice. The discussion adopts ΔUTCI as the central comparative lens, where resilience is interpreted as a configuration's capacity to limit the magnitude of thermal-stress change when exposed to modified climatic forcing.

6.1.1 Urban scale: Sassuolo and district morphologies

At the mesoscale, the Sassuolo case study shows that urban form governs not only the magnitude of outdoor thermal stress, but, more critically for climate adaptation, the *way in which climatic warming is translated into local thermal conditions*. Within the methodological framework adopted here, this translation is captured through the spatial field of ΔUTCI(x,t), computed at matched locations and times under invariant modelling assumptions. Thermal resilience is therefore interpreted as the capacity of an urban morphology to limit the amplification of heat stress when exposed to altered climatic forcing, rather than as the achievement of absolute comfort. Mean ΔUTCI values are read together with their dispersion and distribution structure, in order to distinguish between homogeneous amplification and spatially articulated responses.

Across the urban configurations, two contrasting resilience behaviors emerge, which are best understood in terms of *radiative control*. Morphologies characterized by extensive sky exposure, weak shading, and large horizontal sealed surfaces exhibit high and spatially uniform ΔUTCI values. In these conditions, the warming signal embedded in the future climate boundary conditions propagates almost directly to pedestrian level, producing a narrow and steep ΔUTCI distribution. The absence of internal variability indicates that the microclimatic system lacks buffering capacity: mean radiant temperature increases coherently across the domain, leaving little room for local moderation or the emergence of thermal refuges. This

behavior represents a critical failure mode for urban resilience, because thermal stress not only intensifies, but also becomes spatially monotonous.

By contrast, compact urban morphologies with reduced sky view factor and pervasive architectural shading show a more stable response to climate forcing. In these environments, ΔUTCI values are lower on average and more tightly clustered around a dominant mode, with limited extremes. Narrow streets, enclosed courtyards, and continuous façades act as a *radiative filter*, constraining shortwave exposure and moderating the increase in mean radiant temperature even under warmer boundary conditions. Importantly, this buffering effect does not eliminate heat stress in absolute terms, but it attenuates its amplification, preserving spatial differentiation at pedestrian level. In resilience terms, such morphologies demonstrate that urban form can decouple local thermal stress from the full magnitude of regional climatic warming.

Between these two extremes, intermediate behaviors highlight the role of *spatial coherence versus fragmentation*. Urban fabrics combining discontinuous building forms with scattered vegetation tend to display broad and multimodal ΔUTCI distributions. In these cases, local mitigation effects exist, but they are not systemically organized: pockets of reduced amplification coexist with highly exposed areas, resulting in thermally unstable patterns. A particularly instructive outcome is that zones shaded primarily by vegetation do not systematically outperform architecturally shaded areas in terms of ΔUTCI. This behavior can be explained by the climate sensitivity of evapotranspirative cooling—subject to reduced effectiveness under extreme heat and water stress—and by the aerodynamic resistance introduced by dense canopies, which can limit wind-driven relief at pedestrian level. These results suggest that greening strategies contribute to resilience only when conceived as coherent microclimatic systems, where shading, water availability, and airflow are jointly controlled.

Natural morphologies further illustrate the importance of internal heterogeneity. Where dense canopy cover and water bodies are continuous, ΔUTCI values are locally reduced, indicating effective buffering through combined radiative shielding and latent cooling. However, adjacent clearings and paved infrastructures exhibit amplification levels comparable to fully urbanized areas. This coexistence of low- and high-sensitivity zones produces wide ΔUTCI distributions, demonstrating that “green” is not thermally equivalent per se. Rather,

resilience depends on the continuity and structure of vegetated systems, and on their integration with hydrological and spatial configurations.

From a mechanistic perspective, the urban-scale results converge on the dominance of *mean radiant temperature control* as the primary driver of thermal resilience under peak summer conditions. While air temperature, humidity, and wind contribute to UTCI, the stability of MRT—shaped by geometry, surface exposure, and sky view factor—largely determines whether climatic warming translates into uniform stress amplification or into a buffered, spatially differentiated response. Because wind representation is held invariant between baseline and future simulations, differences in ΔUTCI can be attributed to morphological modulation of radiative exchange and microscale airflow rather than to changes in climatic input.

Overall, the Sassuolo case study indicates that urban resilience to climate change is strengthened by morphologies capable of maintaining robust radiative control under warming conditions, and weakened when mitigation relies primarily on mechanisms that are themselves climate-sensitive or spatially fragmented. At the district scale, resilience emerges not from isolated design features, but from the coherence of urban form in shaping radiative exposure and its translation into pedestrian-level thermal stress.

Read through the ΔUTCI lens, the district-scale evidence supports a clear distinction between robust and threshold-dependent adaptation logics. Configurations that provide continuous radiative control—via reduced sky view factor, persistent shading, and moderated surface heating—tend to stabilize the translation of future warming into pedestrian-level thermal stress. By contrast, approaches relying primarily on ventilation and evapotranspiration show higher sensitivity as thermal conditions intensify, with less predictable spatial responses. This hierarchy provides the conceptual bridge to the building-scale discussion, where the same mechanisms operate within a more controlled geometry.

6.1.2 Building scale: the cloister of San Sepolcro (Parma)

At the building scale, the cloister of San Sepolcro confirms, in a more controlled and spatially confined setting, the same conceptual principle observed at the urban scale: thermal resilience under climate change is governed less by absolute comfort levels than by the

capacity of spatial configuration to mediate how climatic warming is translated into local thermal stress. Within the methodological framework adopted, this mediation is captured through the spatial structure and dispersion of ΔUTCI, computed under invariant modelling assumptions and interpreted as a proxy for sensitivity to future climatic forcing rather than as a measure of comfort per se.

The cloister typology is particularly instructive because it operates as a transitional environment, where outdoor climatic forcing is filtered through architectural geometry before reaching the pedestrian domain. In this context, resilience emerges as a function of how geometry regulates radiative exchange, sky exposure, and air movement at human level. Configurations characterized by strong and continuous control of solar access exhibit a more stable ΔUTCI response, with limited spatial differentiation and restrained amplification under future climate conditions. This behaviour mirrors the “radiative buffering” observed in compact urban morphologies: when direct shortwave exposure is reduced and longwave re-radiation from heated surfaces is constrained, the warming signal embedded in future boundary conditions is partially decoupled from perceived thermal stress.

Conversely, configurations that rely primarily on mechanisms whose effectiveness is contingent on climatic thresholds display less stable behaviour. In particular, strategies that prioritize increased air movement introduce a marked spatial variability in ΔUTCI, revealing a sensitivity to future conditions that is not evident when considering absolute UTCI alone. When ambient air temperatures approach or exceed skin temperature, convective exchange may shift from a cooling to a heating mechanism, and ventilation becomes a vector for thermal amplification rather than mitigation. At the building scale, this produces pronounced gradients in ΔUTCI within the same spatial domain, indicating a redistribution—and in some areas an intensification—of thermal stress under warming scenarios.

Intermediate behaviors further clarify the distinction between local mitigation and resilience. Configurations that introduce vegetation and moisture increase microclimatic complexity and generate spatial differentiation, but their overall ΔUTCI response remains governed by radiative conditions. While shaded zones under dense canopy may exhibit locally reduced amplification, the global sensitivity of the cloister to climatic forcing is only marginally altered unless radiative control is both continuous and robust. This confirms that evapotranspiration-based mechanisms, although valuable for spatial quality and local relief,

do not by themselves guarantee resilience under extreme warming if their performance is climate-dependent.

From a mechanistic standpoint, the building-scale results reinforce the central role of mean radiant temperature as the dominant driver of thermal resilience in semi-enclosed environments. Geometry that limits sky view factor and shields surfaces from direct solar loading stabilizes MRT and, in turn, limits the magnitude and spatial variability of ΔUTCI. By contrast, configurations that expose internal spaces to increased radiative or convective fluxes amplify the sensitivity of thermal stress to future climatic conditions. As at the urban scale, resilience therefore emerges not from isolated mitigation features, but from the coherence of the spatial system in regulating radiative exchange at human level.

Overall, the San Sepolcro case study demonstrates that, even at the building scale, resilience to climate change is best interpreted as the stability of thermal response rather than as the achievement of comfort. The cloister confirms that architectural form can either dampen or magnify the translation of climatic warming into perceived stress, depending on whether radiative control is treated as a primary design driver or subordinated to mechanisms that lose effectiveness under extreme conditions. In this sense, the building-scale findings align directly with the urban-scale evidence and support a unified, cross-scalar reading of thermal resilience grounded in ΔUTCI.

Read through the ΔUTCI lens, the cloister case study allows a clear distinction to be drawn between adaptation strategies that remain robust under climatic intensification and those whose effectiveness is intrinsically threshold-dependent. As already observed at the urban scale, configurations that primarily operate on radiative exchange—by limiting direct shortwave exposure and moderating longwave re-radiation from heated surfaces—tend to stabilize the thermal response of space under future conditions. In contrast, strategies that rely on enhanced airflow or evapotranspiration exhibit a more fragile behavior when background temperatures rise, as their underlying physical mechanisms can weaken or even reverse under extreme heat.

Read through the ΔUTCI lens, the cloister case study confirms the same robustness hierarchy already observed at the urban scale. Radiation-first strategies—limiting direct shortwave exposure and moderating longwave re-radiation—stabilize the thermal response of

semi-open spaces under climatic intensification. Ventilation-first strategies, conversely, remain condition-dependent and can amplify stress as ambient temperatures approach physiological thresholds, increasing ΔUTCI dispersion and internal gradients. From a design perspective, resilience therefore emerges when radiative control is treated as a primary driver, while airflow and evapotranspiration are integrated as secondary levers within their domains of validity.

6.1.3 Component scale: the Xirbi railway station envelope

At the component scale, the Xirbi railway-station case study isolates, in a highly controlled manner, how a single design lever—envelope porosity and operability—can reshape the relationship between climatic forcing and perceived thermal stress.This relationship is not read primarily through absolute UTCI severity, but through the spatial field of ΔUTCI under invariant modelling assumptions. Resilience is therefore interpreted as the capacity of the envelope configuration to limit the magnitude and spatial volatility of ΔUTCI within the occupied domain, preserving a predictable thermal response under future boundary conditions.

The key outcome at this scale is the emergence of a dual-valued behaviour that is structurally consistent with the cross-scalar logic developed in this chapter: configurations that improve baseline conditions do not necessarily improve resilience. In Xirbi, increasing envelope openness can lower baseline heat stress locally—particularly where airflow penetrates effectively—yet it tends to increase climate-change sensitivity, expressed as a broader and higher ΔUTCI distribution and as more pronounced spatial gradients. In other words, porosity may act as a short-term relief mechanism while simultaneously amplifying the extent to which the future climatic signal is translated into thermal-stress change. This finding is not a paradox, but a direct consequence of how convective exchange interacts with boundary conditions under extreme heat.

Mechanistically, the case clarifies why ventilation-first logics become fragile in peak summer conditions. Greater porosity increases pedestrian-level air movement and strengthens the coupling between UTCI and air temperature, because convective heat exchange scales with wind speed. As background temperatures rise, this coupling becomes increasingly unstable: when ambient air approaches (and in critical windows may exceed) skin temperature, the convective pathway shifts from a reliable cooling channel to a marginal—or even adverse—

mechanism. In ΔUTCI terms, the consequence is not simply a uniform increase, but a redistribution of sensitivity: locations that are most “ventilated” in the baseline scenario are also those that exhibit stronger amplification under future forcing. The component-scale model therefore makes explicit a general design warning already implicit in the urban and building-scale results: ventilation can reduce stress in the present and still produce lower resilience if its effectiveness depends on thermal conditions that are precisely those most altered by climate change.

At the same time, the Xirbi case does not reduce thermal resilience to airflow alone. Even in an unconditioned, semi-open indoor environment, radiative conditions remain decisive for perceived stress, because mean radiant temperature (MRT) governs the radiative load on the body and is strongly influenced by envelope transparency, surface heating, and the balance between solar access and longwave exchange. The envelope here is not merely a “porous boundary”; it is a radiative system. This is why the component-scale evidence aligns tightly with the chapter’s broader interpretation: strategies that stabilize radiative exchange—by controlling solar transmission, moderating surface temperatures, and reducing persistent radiative exposure—provide a more robust foundation for resilience than strategies that rely primarily on increasing airflow during already hot periods.

A direct design implication follows: at the component scale, resilience is best supported by treating operability as an *adaptive* mechanism rather than as a fixed performance state. Envelope openings should remain operable, but their use should be governed by climatic thresholds and time-dependent logic (e.g., favoring airflow when outdoor air can plausibly act as a cooling resource, and limiting porosity when convective exchange is unlikely to be beneficial). Conversely, solar-control features—such as selective transparency, external or integrated shading of critical glazed areas, and radiatively “quiet” surface strategies—should be conceived as stable, always-on components of the envelope, because their effectiveness does not rely on a narrow range of ambient conditions. In this hierarchy, airflow becomes a secondary, qualified lever: valuable for spatial quality and perceived freshness when conditions allow, but insufficient as the primary resilience strategy under extreme warming.

Read through the ΔUTCI lens, the Xirbi station therefore consolidates a cross-scalar principle that becomes particularly legible at the component scale: the most reliable resilience gains arise when design acts on mechanisms whose performance does not degrade as heat

intensifies. Configurations centered on radiative control remain comparatively robust under climatic intensification, whereas configurations that privilege ventilation as a dominant adaptation logic expose a threshold-dependence that manifests as increased sensitivity and spatial instability. In this sense, the component-scale evidence does not merely add detail to the thesis; it sharpens its design meaning by showing, at the finest scale, how “better baseline comfort” can coexist with lower resilience if the intervention logic is anchored to climate-sensitive mechanisms.

6.1.4 Cross-scale synthesis: recurring mechanisms and scale-specific effects

The purpose of the three case studies is to validate a single comparative logic for thermal-comfort resilience across the urban–building–component continuum. In this work, resilience is treated as a measurable sensitivity: the extent to which a spatial configuration amplifies or dampens the translation of climatic forcing into human-perceived thermal stress. The ΔUTCI lens is central precisely because it shifts the analytical focus from absolute comfort categories to response stability under altered boundary conditions, allowing configurations to be ranked and interpreted even when absolute stress remains severe.

Across scales, the evidence converges on a consistent hierarchy of microclimatic drivers. The most robust resilience behaviors are associated with stable radiative control, meaning a geometry–material–shading system that limits shortwave exposure and moderates the longwave environment experienced at pedestrian level. This is coherent with the structure of UTCI itself: while air temperature, humidity, and wind contribute to thermal stress, the spatial variability that differentiates design variants at microclimatic resolution is often dominated by mean radiant temperature (MRT), which is strongly shaped by sky exposure, shading continuity, and surface heating. In other words, resilience emerges where a configuration reduces the degree to which warming “locks into” MRT-driven amplification, producing a more controlled ΔUTCI field and preserving legible spatial differences in exposure.

The urban case makes this mechanism visible through the contrast between homogeneous amplification and structured heterogeneity. In exposed, weakly-shaded morphologies, the future signal propagates almost uniformly across the evaluation domain: ΔUTCI becomes spatially monotonous, indicating that the outdoor environment offers few microclimatic

“degrees of freedom” for adaptation. Conversely, compact fabrics and other radiatively buffered morphologies act as a filter: reduced sky view and pervasive shading do not eliminate heat stress, but they limit its amplification and preserve spatial differentiation. Importantly, this is not simply a matter of “more shade is better”, but of coherence: when shading and surface strategies operate as a continuous system, the thermal response becomes more stable; when mitigation relies on fragmented elements, the ΔUTCI field tends to become dispersed and less predictable.

At the building scale, the cloister confirms the same principle in a constrained environment where geometry directly structures radiation, longwave trapping, and air movement at human level. Because the domain is semi-enclosed, small morphological modifications can produce disproportionately meaningful shifts in how the warming signal is translated into local stress. The cross-scale insight is not that cloisters behave like districts, but that the same resilience logic applies: “radiation-first” configurations—those that prioritize stable solar control and limit radiative loading of surfaces—tend to stabilize the response, whereas “ventilation-first” approaches introduce a more condition-dependent behavior. This is not a dismissal of airflow as a design lever, but a qualification of its epistemic status under heat extremes: when ambient temperatures approach physiological thresholds, convection may cease to provide relief and can become a mechanism of heat gain. Under those conditions, the apparent benefit of ventilation in baseline comfort can coexist with reduced resilience, expressed as wider ΔUTCI dispersion and stronger internal gradients.

At the component scale, the station-envelope study expresses the same trade-off through a particularly clear “dual-valued” behavior. Increasing porosity and operability can improve baseline conditions in some areas by enhancing air movement, yet the same strategy can reduce resilience by increasing sensitivity to future forcing. The building component becomes an interface that can either buffer or transmit climatic stress depending on whether it primarily regulates radiative exchange (solar control, transparency management, reduction of longwave re-radiation) or whether it depends mainly on airflow mechanisms whose effectiveness is threshold-dependent. Read cross-scale, the key point is that the resilience ranking changes when the evaluation shifts from immediate comfort to robustness under climatic intensification.

Vegetation- and moisture-based strategies occupy an intermediate position across the three scales: they can generate meaningful local mitigation and increase microclimatic richness, but their resilience contribution is contingent on climatic and ecological constraints and on their spatial continuity. In the urban domain, the effectiveness of “green” depends on structure, continuity, and hydrological coupling; at the building scale, vegetation may improve specific sub-areas without necessarily stabilizing the overall sensitivity of the domain; and at component scale, evapotranspiration is largely secondary to envelope radiation and airflow in determining the resilience signal. The cross-scale implication is that greening cannot be treated as a uniform substitute for radiative design: it contributes to resilience when conceived as a functional system, radiatively coherent, hydrologically supported, and aerodynamically compatible, rather than as a scattered geometric addition.

This cross-scalar consistency matters also in relation to the international methodological gap mapped in Chapter 1. Reviews point to scale heterogeneity, metric fragmentation, and toolchain inhomogeneity as major barriers to comparability and operational uptake. The results presented here speak back to those barriers in a focused way: the same resilience logic, interpreting change through ΔUTCI under declared invariances, remains readable across a district, a cloister, and a building component, even though the geometric representations, dominant physical processes, and modelling pathways necessarily differ by scale. The novelty is therefore not the use of UTCI per se, nor the use of future weather files per se, but the fact that a consistent comparative construct can be maintained across heterogeneous design scales, enabling a unified interpretation of resilience mechanisms rather than three unrelated assessments.

A final clarification is necessary regarding cross-case comparability and the role of future horizons. The case studies operate in different climatic contexts and, in practice, adopt different future reference years (e.g., mid-century versus late-century), depending on data availability and on the requirements of the applied research settings from which they originate. This choice does not undermine the internal validity of the results, because resilience rankings are always derived within each case study through internally consistent baseline–future pairs and invariant modelling assumptions.

However, this also implies that ΔUTCI values are not intended to be interpreted as absolute, directly comparable quantities across cases. A larger ΔUTCI in one study does not automatically

indicate lower resilience than a smaller ΔUTCI in another study if the underlying climatic forcing differs in magnitude. In this framework, ΔUTCI does not function as a universal scalar of resilience, but as a diagnostic indicator whose meaning emerges from relative patterns rather than from raw numerical values.

Accordingly, the assessment of thermal-comfort resilience developed is qualitative–comparative in nature, even though it is grounded in quantitative simulations. Resilience is inferred from how configurations behave relative to one another within the same climatic horizon, from the structure and dispersion of ΔUTCI fields, and from the recurrence of mechanism-based hierarchies across scales. The analytical focus therefore lies on identifying robust versus fragile design logics—such as the consistent stabilizing role of radiative buffering and the threshold-dependent behavior of ventilation and evapotranspiration—rather than on ranking cases by ΔUTCI magnitude alone.

Within this interpretative stance, the use of a later horizon can be understood as a form of stress testing: it explores whether the same design logics remain valid as climatic forcing approaches physiological limits and as some mitigation mechanisms risk losing effectiveness or reversing their role. Crucially, this stress-test reading reinforces the qualitative objective of the method, which is to reveal how and why different configurations respond under intensification. Under this framing, the adoption of different future horizons becomes methodologically explicit and fully compatible with a cross-scale synthesis grounded in comparable causal mechanisms.

6.2 Contribution to knowledge

The contribution of this thesis can be articulated along three tightly interrelated dimensions: a conceptual reframing of thermal resilience as a property of sensitivity rather than of absolute comfort; a methodological framework that enables consistent comparison across architectural scales through a unified metric and invariant workflow; and a set of empirically grounded insights that clarify how different design logics respond to climatic intensification when assessed through that framework.

The first contribution lies in the operational clarification of thermal resilience. By defining resilience through the spatial field of ΔUTCI—computed as the difference between future and baseline UTCI values at matched locations and times under invariant modelling conditions—the thesis establishes resilience as a comparative property of the built environment. This choice moves the assessment away from categorical comfort thresholds and toward the analysis of how strongly thermal stress is amplified under changing climatic forcing. In doing so, resilience is treated not as an aspirational state to be achieved, but as a measurable sensitivity that can be evaluated, ranked, and interpreted even in contexts where absolute thermal stress remains high. This reframing enables a more precise discussion of adaptation, because it distinguishes configurations that are intrinsically robust from those whose apparent performance depends on favorable boundary conditions.

The second contribution is methodological and directly addresses gaps identified in the international literature. Existing studies frequently analyze thermal comfort at a single scale, adopt heterogeneous comfort metrics, or rely on workflows that change substantially between urban, building, and component applications. Such fragmentation limits comparability and reduces the transferability of findings. The framework developed here responds to these limitations by enforcing a set of declared invariances: the same comfort index (UTCI), the same interpretation through ΔUTCI, consistent spatial sampling logic, and a coherent workflow structure are maintained across all case studies. While modelling tools and geometric resolutions necessarily adapt to scale-specific phenomena, the assessment logic remains unchanged. As a result, the framework enables meaningful multi-scalar comparison, and provides a structured way to interpret results across heterogeneous spatial domains without resorting to ad hoc normalization or scale-dependent metrics.

The third contribution concerns the translation of climatic and microclimatic analysis into design-relevant knowledge. The thesis establishes an explicit and implementable chain linking scenario-based climate data, microclimate simulation, a human heat-balance index, and the interpretation of design alternatives. Within this chain, UTCI functions as a common physiological reference, while ΔUTCI provides the comparative layer through which resilience is assessed. The workflow is designed to be operational rather than purely demonstrative: it can be applied at early design stages, accommodates different modelling environments, and

remains transparent in its assumptions and outputs. The method supports design exploration activating alternative simulation pathways, while preserving internal consistency.

Taken together, these contributions position the thesis within the current state of the art demonstrating how existing tools and models can be assembled into a standardized, multi-scalar assessment framework centered on thermal-comfort resilience. A distinguishing aspect is the ability to read urban districts, architectural spaces, and building components through the same interpretative lens, and to extract comparable insights about robustness, sensitivity, and threshold behavior under warming. In this sense, the thesis advances the field by shifting the focus from isolated performance evaluations toward a coherent methodology for assessing how design decisions mediate the impact of climate change on human thermal experience across scales.

6.3 Limitations and uncertainties

A comparative assessment of thermal-comfort resilience gains credibility when it declares, with the same clarity as its results, the conditions under which those results hold. Resilience is evaluated through ΔUTCI fields computed at matched locations and times under invariant modelling settings, using baseline–future climate pairs prepared consistently within each case study. This section consolidates the main limitations and uncertainties by distinguishing their primary effect on: (i) absolute UTCI levels, (ii) comparative ranking among configurations, and (iii) transferability of the evidence to other climates and modelling contexts.

6.3.1 Uncertainties shaping absolute UTCI values

Climatic forcing and weather-file generation. Wind forcing is a specific limitation of the present implementation. In the EPW generation/morphing procedure adopted (Meteonorm), wind is not substantially modified between baseline and future files and is therefore retained approximately unchanged. In addition, in the microclimate simulations wind was treated as a controlled boundary input (kept constant in speed/direction for the simulated day) to ensure numerical stability and preserve strict baseline–future comparability. As a consequence, the computed UTCI/ΔUTCI fields do not represent potential future changes in synoptic wind

regimes, and the results should be read as the morphological translation of changes in temperature–humidity–radiation under invariant wind forcing.

Microclimate model form and parameterization. Absolute UTCI levels are influenced by the fidelity with which microclimatic drivers, particularly mean radiant temperature (MRT) and wind at pedestrian level, are resolved by the selected toolchains. The modelling environments used in the thesis rely on physical formulations and parameterizations that inevitably abstract complex processes, including vegetation–air coupling, soil moisture dynamics, radiative exchange, and turbulence. The resulting microclimatic variables (DBT, RH, wind speed, MRT) provide a physically grounded basis for comparative comfort assessment across configurations; at the same time, their absolute values remain sensitive to assumptions about surface properties, canopy characterization, boundary conditions, and numerical settings.

UTCI interpretative boundaries. UTCI provides a standardized physiological reference that enables consistent interpretation of thermal stress across outdoor and transitional environments. Absolute UTCI values, however, remain tied to the conventions embedded in the index: a reference subject, standardized activity assumptions, and a quasi-stationary modelling logic with limited behavioral adaptation and no explicit long-term acclimatization. These characteristics are treated here as part of the fixed interpretative layer that makes results comparable across configurations and scales, while keeping absolute readings anchored to a defined physiological convention. UTCI stress categories serve communication and interpretation; continuous UTCI values remain the analytical basis used throughout the workflow.

6.3.2 Uncertainties that can influence comparative ranking

The thesis derives rankings within each case study by comparing configurations under the same baseline–future forcing pair and under invariant modelling settings, sampling geometry, and decision rules. This internal consistency strongly constrains spurious ranking shifts induced by changes in workflow rather than by changes in spatial configuration. Within this comparative structure, three levels of uncertainty deserve explicit distinction because they interact differently with ranking robustness.

Level 1 — Climatic uncertainty (models and scenarios). The uncertainty associated with climate projections and scenario choice primarily governs the absolute severity of future stress. When configurations are compared internally within a single case study—using the same future EPW and the same boundary forcing for all variants—climatic uncertainty tends to affect the absolute ΔUTCI levels more than the relative ordering among configurations, especially when the comparison is driven by geometry-dependent mechanisms that remain active across plausible warm-season futures. Ranking robustness still benefits from scenario exploration, and the methodological framework is compatible with repeating the same comparative procedure under alternative scenario pathways and time horizons to verify stability of the ordering.

Level 2 — Microclimate model uncertainty (materials, vegetation, turbulence, boundary conditions). The uncertainty associated with microclimate and airflow modelling can influence both values and spatial patterns, because it acts directly on the variables that shape UTCI and on the emergence of hotspots, gradients, and sheltered zones in the evaluation domain. In comparative terms, this uncertainty becomes most consequential when competing configurations exhibit small performance differences. Under those conditions, ranking is strengthened by reading not only mean ΔUTCI but also distribution structure and extremal behaviour, as already embedded in the thesis' decision logic. Model sensitivity therefore motivates a "signal strength" interpretation: large and spatially coherent ΔUTCI separations support robust ordering; narrow separations invite explicit sensitivity testing of the parameters most likely to shift MRT and wind patterns (e.g., vegetation attributes, surface radiative properties, turbulence settings, and boundary-condition definitions).

Level 3 — Temporal sampling uncertainty (choice of day and hour). The temporal framing of the assessment—selection of a representative extreme summer period and extraction at a peak afternoon reporting hour after a spin-up—supports a clear stress-test condition in which resilience mechanisms become legible. Temporal sampling also interacts directly with ranking because microclimatic drivers can reorganize across hours and across hot days with different radiation and humidity profiles. Ranking robustness can be further qualified through verification across a small set of strategically chosen time slices (e.g., morning/afternoon contrast, and a short sequence of representative hot days), while preserving the same spatial sampling and modelling assumptions. Within the comparative logic of the thesis, such checks

function as a robustness layer: they test whether a configuration's resilience behavior is stable across plausible high-stress temporal realizations, and whether apparent improvements rely on narrow time-specific conditions.

Taken together, these three uncertainty levels position the work clearly as an applied comparative methodology: one that delivers internally coherent rankings under declared invariances, and that identifies where additional sampling and sensitivity work increases confidence when performance differences are small.

6.3.3 Limitations that condition transferability to other climates and contexts

Cross-case comparability and horizon differences. The three case studies operate in different climatic contexts and, where required by the underlying research settings, may adopt different future reference horizons. The workflow is designed so that rankings are derived within each case study through internally consistent baseline–future pairs and invariant modelling conditions. Transferability across cases therefore occurs primarily through mechanisms and response structures—how radiative control, ventilation, and evapotranspirative effects translate into ΔUTCI patterns—while direct comparison of ΔUTCI magnitude across cases remains conditioned by differences in climatic forcing and horizon severity.

Toolchain dependence across scales. A multi-scalar thesis necessarily adapts modelling pathways to dominant processes and available resolution at each scale. The methodology preserves comparability through invariant definitions (evaluation domain, sampling logic, UTCI computation, ΔUTCI interpretation, ranking rules), while toolchains differ in the way they resolve vegetation processes, radiation, and airflow. Transferability of the workflow to other contexts therefore benefits from maintaining the declared invariances while selecting the simulation pathway that best matches the physical drivers of the site and the design questions being asked.

Climate- and ecology-specific constraints. The evidence synthesized in Chapter 6 highlights robust causal mechanisms—particularly the stabilizing role of radiative control under peak heat—across the studied contexts. Applying the same design inferences to climates with different limiting factors (e.g., regimes dominated by hot-humid conditions, monsoon

dynamics, or strong synoptic winds) calls for re-running the same comparative workflow with boundary conditions that represent those regimes and with modelling assumptions suitable for local vegetation and water constraints. In this sense, the thesis provides a transferable method and a mechanism-based interpretative hierarchy; its application to new climates proceeds through the same workflow steps that make the present cases comparable and replicable.

6.4 Implications for design and climate adaptation

Heat adaptation emerges as a design responsibility that can be addressed with methodological continuity across the urban–building–component continuum. The contribution that enables this continuity is the comparative workflow formalized in Chapter 4: by defining an explicit evaluation domain at human exposure level, keeping the sampling locations invariant, and applying paired baseline–future climatic forcing to pre-defined configurations, the method translates heterogeneous design questions into a shared analytical language. This procedural coherence is what makes it possible to reach a high level of *intra-scalar synthesis*—within each case study—while also allowing insights to remain cross-readable across scales.

Within this framework, the implications for climate-adaptive design are derived through a dual reading that remains consistent throughout the thesis. Absolute UTCI fields under baseline and future scenarios establish the severity of heat stress and the operational space for use, comfort, and protection. ΔUTCI complements this reading by operationalizing resilience as sensitivity: it quantifies, point by point within a stable spatial reference, how much additional thermal stress results from climatic warming under controlled modelling assumptions. The methodological decision to preserve UTCI as a continuous variable directly supports this comparative intent: numerical values sustain rigorous ranking across variants, while categorical bands remain a communicative layer for interpreting severity. In the same spirit, synthesis relies on a compact, reproducible indicator set—means, extrema, and distribution structure—so that both the magnitude of change and its spatial articulation become legible as design-relevant signals.

Because the workflow holds key modelling choices constant across variants and scenarios, it becomes possible to generalize across cases while keeping the interpretation anchored to the same thermo-physiological and microclimatic mechanisms. Across the three case studies, the evidence consolidates into a hierarchy of adaptation logics that the method renders visible through the combined reading of maps and distributions. Radiative control emerges as the most consistently stabilizing driver of resilience under warming, largely because mean radiant temperature is strongly governed by geometry, sky exposure, and surface heating and is a dominant contributor to UTCI during peak summer conditions. Configurations characterized by continuous shading—at district level through compactness and reduced sky view, at building level through cloister geometry, and at component level through solar-control strategies applied to transparent elements—tend to shift ΔUTCI distributions downward and reduce dispersion, indicating a more predictable thermal response under intensified climatic boundary conditions.

Ventilation-oriented strategies can contribute substantially to perceived relief when boundary conditions support convective heat loss, and the thesis clarifies the physiological constraint that governs their reliability as summers intensify. Convective exchange depends on both air movement and the temperature gradient between the body and surrounding air; when air temperatures approach typical skin temperatures, increased air movement can lose its cooling capacity and contribute to heat gain. The comparative method makes this condition explicit at design level: in several variants, higher openness or permeability improves baseline UTCI locally while increasing ΔUTCI and sharpening spatial gradients under future forcing. This pattern supports a precise implication that remains valid across scales: ventilation is most effective as an adaptive resource when it is controllable and time-dependent, embedded in operability logics that activate air paths during favorable windows and moderate them during extreme heat.

Vegetation and water-related strategies emerge as powerful contributors to local comfort quality and to the creation of microclimatic diversity, and the workflow helps specify the conditions under which they contribute to resilience as well. Their performance depends on canopy structure, shading continuity, and hydrological support, because evapotranspirative cooling responds to plant stress and water availability during the most demanding periods. In the building-scale case study, mitigation concentrates under canopy zones; at urban scale, the

interpretation points to the vulnerability of evapotranspirative cooling under future dryness. Read through ΔUTCI distributions, these strategies often broaden the range of responses, producing valuable refuges alongside more exposed areas, unless they are conceived as coherent microclimatic systems that couple shading, adequate soil-water regimes, and aerodynamic compatibility. When these conditions are embedded in design, greening becomes a durable spatial resource for refuge-making and for improving the equity of thermal exposure across the lived domain of the project.

Table 13 aligns three dimensions that emerge jointly from the assessment: the dominant microclimatic mechanisms shaping thermal resilience, the corresponding design levers through which those mechanisms are addressed, and the type of evidence produced by the workflow that supports interpretation. In this way, the table clarifies how quantitative outputs are meant to be interpreted when moving from analytical comparison to design reasoning. The table therefore functions as a synthetic interpretative framework, linking physical mechanisms, design action, and reading of results across scales within a single, coherent structure.

Scale	Primary resilience levers	Adaptive levers	Interpretative focus
Urban	Radiative buffering through form: canyon geometry and sky-view control; continuous architectural shading; surface strategies that reduce radiative loading and surface overheating	Ventilation as urban air management: permeability and wind access where synoptic and local winds provide cooling; vegetation and water as continuous systems with maintained water availability	Absolute UTCI to locate heat-stress severity and exposure hotspots; ΔUTCI mean + dispersion to distinguish homogeneous amplification from buffered, spatially articulated responses; maps + distributions to identify whether “cooler pockets” behave as reliable refuges
Building	Cloister shading logic: geometries and elements that stabilize MRT at pedestrian level; surface and material choices that limit radiative re-loading	Porosity and ventilation pathways: controlled openings and air paths tuned to time-of-day; vegetation as localized relief with canopy shading and viable moisture regimes	Absolute UTCI to understand whether the space remains usable at peak periods; ΔUTCI structure to read whether the intervention stabilizes the future response across the whole cloister or concentrates gains in limited sub-areas
Component	Solar-control envelope strategies: transparency management; shading of critical glazed/translucent areas; radiatively “quiet” surfaces that reduce persistent exposure	Operability rules for porosity: openings as an adaptive mechanism governed by climatic thresholds (heatwave vs night cooling windows)	Absolute UTCI to verify immediate comfort impacts; ΔUTCI gradients to detect whether increased openness improves current conditions while amplifying sensitivity to future warming; distribution tails to locate emerging hotspots

Table 13. Cross-scale design levers for heat adaptation, synthesized from the three case studies and structured through the thesis' UTCI–ΔUTCI workflow. For each scale of intervention, the table summarizes primary resilience levers and adaptive levers linked to the dominant mechanisms observed, and specifies the key readings the workflow prompts designers to interpret.

Finally, the thesis supports a multi-criteria design culture for climate adaptation in which resilience is treated as both an environmental and a spatial concern. Exposed configurations can produce ΔUTCI fields that are high and spatially uniform, signaling a monotone amplification of thermal stress; other configurations lower averages while introducing concentrated hotspots. The workflow provides a practical basis for navigating both outcomes by maintaining a stable evaluation domain across design iterations and interpreting mean change together with extremal behavior and distribution structure. This encourages iterative design trajectories that combine reduced absolute stress where feasible, lower sensitivity to future climatic forcing, and legible spatial patterns capable of sustaining accessible thermal refuges.

6.5 Research and practical recommendations

The evidence synthesized here supports a set of recommendations that are directly actionable because they are embedded in the methodological workflow itself and have been exercised across multiple spatial scales and configurations. The central recommendation is to treat the methodology as a transferable analytical protocol: a traceable sequence of procedures that links climate forcing to microclimate simulation, UTCI computation, and ΔUTCI-based comparative interpretation within an explicit and invariant evaluation domain. This procedural continuity enables robust comparative analysis across predefined spatial configurations and ensures methodological consistency across scales, while keeping interpretation grounded in the same thermophysiological logic that links microclimatic drivers to human thermal stress.

For research applications, the workflow supports replication and extension to new contexts through a stable set of methodological commitments, while allowing context-specific calibration of inputs and modelling assumptions required to reflect local climatic, geometric, and environmental conditions. First, each study benefits from making the baseline–future climate pairing fully transparent: weather-file provenance, scenario definition, and the selection of the heat-stress analysis period become explicit inputs of the method, and their

documentation preserves traceability of the climatic forcing driving all subsequent outputs. Second, the definition of configurations as pre-specified inputs—geometry, materials, vegetation attributes, and operability assumptions—supports a clear causal reading because differences in outcomes can be attributed to differences in spatial and material structure under invariant modelling settings. Third, comparability is operationalized spatially through the evaluation domain and sampling strategy: fixed sampling coordinates at human exposure level, consistently applied across baseline and future runs and across all variants, provide the reference frame within which ΔUTCI(x,t) becomes a meaningful comparative field. Fourth, the analytical layer remains grounded in continuous UTCI values computed from the same microclimatic variables (air temperature, humidity, wind speed, and mean radiant temperature), enabling pointwise differencing and the construction of distribution-based descriptors; stress categories then support interpretation and communication as a subsequent layer, keeping the analytical sensitivity of the method intact. Finally, research reporting gains clarity when it follows the output structure already demonstrated in the thesis: paired UTCI maps (baseline and future), ΔUTCI maps in the same spatial reference, and a compact set of distribution descriptors (central tendency, dispersion, and extremes) that are sufficient to support ranking and mechanism-based interpretation.

For practice, the workflow can be adopted directly as an early-stage decision-support scaffold that remains consistent across design scales and across iterative design development. The operative step is to define, at the outset, the evaluation domain and sampling grid as stable comparators: these act as the project's reference instrument, allowing successive design iterations to be assessed under the same spatial and interpretative frame. In this applied setting, each design cycle benefits from a minimum comparative set that keeps the exploration legible: a base case and a small number of variants that isolate distinct microclimatic levers (radiative control, controlled ventilation/porosity, and vegetated or water-related strategies where relevant). Interpretation remains strongest when it combines absolute UTCI severity with ΔUTCI as the resilience proxy: absolute values describe usability and exposure during critical periods, while ΔUTCI reveals how strongly thermal stress amplifies under future boundary conditions and whether amplification is spatially uniform, gradient-driven, or concentrated in hotspots. This dual reading supports decisions that attend simultaneously to peak-risk management and to the spatial equity of outdoor comfort, since

a similar mean change can correspond to very different exposure patterns across the lived domain.

The cross-scale findings of this thesis translate into a pragmatic hierarchy for design action within the workflow. Radiative control emerges as the most reliable stabilizer of the thermal response under warming, because mean radiant temperature is the principal driver of spatial differentiation in UTCI during peak summer conditions. Accordingly, design iterations that introduce coherent shading systems, manage sky-view exposure, and control radiative loading of key surfaces tend to produce more stable ΔUTCI fields and more predictable distributions. Ventilation and porosity function effectively as adaptive resources when their operation is structured in time and aligned with boundary conditions that support convective relief; operability rules and exposure-aware use scenarios can therefore be encoded as explicit configuration parameters and evaluated within the same comparative domain. Vegetation and moisture-related measures contribute most consistently when they operate as continuous microclimatic systems—providing organized shading and locally moderated radiant environments—so that their benefits appear as structured patterns in UTCI and as spatially legible reductions in ΔUTCI, rather than as fragmented, isolated effects.

This methodology aligns naturally with planning and design processes when it is framed as a set of procedural deliverables. During concept design, the workflow supports option screening through simplified but simulation-ready massing and surface assumptions, a clearly defined evaluation domain at human exposure level, and rapid comparison of a base case with a small number of variants under baseline–future paired forcing. During schematic design, refinements in geometry, shading devices, surface strategies, and vegetation layout are tested through the same sampling framework, allowing the design team to confirm whether resilience gains remain spatially coherent as the project definition increases. During design development, the method supports formal documentation of resilience evidence: assumptions and parameters are consolidated, outputs are packaged through consistent maps and distribution descriptors, and the comparative logic becomes a transparent record that can be integrated into performance briefs and adaptation narratives. Across all phases, the stable spine of the protocol maintains continuity between design intent and performance evidence, and it keeps the methodological contribution of the thesis operational at every scale where climate-adaptive decisions are made.

6.6 Final remarks

This discussion consolidates the thesis' key outcome as a methodological contribution: a comparative workflow that makes the impact of climate change readable at the level where design decisions operate, namely the lived microclimate and the corresponding human thermal stress. By keeping the evaluation domain explicit and invariant, and by translating climatic forcing into microclimatic variables that feed a physiologically grounded index, the method creates a stable analytical frame in which design alternatives can be interpreted with clarity. The use of ΔUTCI as a comparative field strengthens this frame further, because it expresses resilience as a measurable sensitivity: it shows where, and by how much, thermal stress amplifies under future boundary conditions, while preserving the spatial structure that matters for comfort, access, and exposure.

Across the different spatial scales explored in the thesis, the same interpretative hierarchy becomes visible when results are read through maps and distributions together. Radiative control emerges as the most robust stabilizer of the thermal response under summer peak conditions. The mechanism is consistently linked to the behavior of mean radiant temperature at pedestrian level, shaped by geometry, sky exposure, shading continuity, and surface heating. Configurations that impose coherent radiative buffering tend to yield ΔUTCI fields that are lower and more spatially controlled, supporting a predictable response under climatic intensification. This is a practical outcome as much as a theoretical one: it provides designers with a lever that remains effective precisely in the conditions where heat stress becomes most critical.

Ventilation-oriented strategies also retain a clear role within this hierarchy. The thesis clarifies how airflow contributes to relief when convective exchange supports heat loss, and how its effectiveness evolves with the boundary conditions that accompany extreme heat. Within the comparative lens adopted here, ventilation becomes especially meaningful when it is treated as an operable resource: its benefits are strongest when openings, permeability, and air paths are organized to respond to time-dependent opportunities for cooling. This operational framing connects microclimatic physics to design intent and to the way spaces are actually used, offering a pathway to adaptive performance that can be represented explicitly in the evaluation protocol.

Vegetation and moisture-related measures complement these levers by shaping microclimatic diversity and enabling the formation of local refuges. The thesis' evidence supports their strongest contribution when they are conceived as coherent systems: continuous canopy structure, viable moisture regimes, and aerodynamic compatibility become the conditions through which local mitigation is translated into stable patterns of exposure. In this reading, resilience is expressed not only as a reduction in mean amplification, but also as the emergence of legible spatial gradients and protected zones within the evaluation domain—an aspect that matters directly for the equity of thermal experience in public and semi-public space.

A further outcome of this chapter is the consolidation of an interpretative discipline for microclimate results. The method encourages readings that combine absolute UTCI severity with ΔUTCI-based sensitivity, and it places emphasis on distribution structure—dispersion, tails, and spatial organization—alongside mean values. This analytic stance supports design reasoning that remains attentive to hotspots and to uneven exposure, and it strengthens the capacity of the workflow to inform decisions under realistic conditions where severe heat may remain present even when resilience improves.

The following chapter brings this discussion to a formal closure by consolidating the thesis' outcomes and clarifying their scope and conditions of validity. Building on the interpretative framework developed here, it draws together the methodological, empirical, and conceptual strands of the work into a coherent concluding synthesis.

7 Conclusions

The structure of this section reflects the dual role played by the research questions and the research objectives in guiding the work. Each research question is addressed explicitly, and the corresponding response is articulated by drawing together the methodological framework developed in Chapter 4, the empirical evidence generated through the multi-scalar case studies presented in Chapter 5, and the interpretative synthesis discussed in Chapter 6. Within the same structure, the objectives that shaped the operational development of the research are also brought to closure. Rather than being restated as a separate checklist, these objectives are addressed through the results themselves, and their fulfillment is articulated in terms of consolidated outcomes, validated procedures, and design-relevant interpretations.

This organization is intended to make explicit the coherence between what the research set out to achieve and what it ultimately establishes. By aligning each research question with the objectives it encompasses, the section clarifies how conceptual framing, methodological choices, and empirical testing converge into a consistent set of conclusions. The responses that follow therefore operate at two complementary levels: they provide direct answers to the research questions, and they demonstrate how the associated objectives are met through the combined reading of theory, method, and cross-scale evidence.

7.1 Responses to the research questions

This chapter brings the thesis to a close by returning explicitly to the research questions formulated in Chapter 1 and consolidating their answers on the basis of:

- the comparative methodological framework developed in Chapter 4,
- the empirical evidence generated through the three multi-scalar case studies in Chapter 5
- the interpretative synthesis and boundary conditions articulated in Chapter 6.

The research was motivated by a clearly identified gap in the international literature: thermal-comfort adaptation under climate change is typically addressed through scale-specific methods and heterogeneous metrics, limiting comparability and weakening the transferability of results across the urban–building–component continuum. The conclusions resolve this gap

not by introducing additional analytical layers, but by stabilizing a single comparative construct—ΔUTCI under declared invariances—and demonstrating its consistency, limits of validity, and interpretative value across heterogeneous architectural scales.

7.1.1 Addressing RQ1: multi-scalar assessment of thermal-comfort resilience

Research Question 1 asked how a quantitative–qualitative, designer-oriented methodology based on local UTCI variations can be developed and validated to assess thermal-comfort resilience to climate change across multiple architectural scales.

The thesis answers this question by operationalizing thermal-comfort resilience as sensitivity to climatic intensification. Resilience is expressed through the spatial field of ΔUTCI, computed between baseline and future scenarios at matched locations and reporting times under invariant modelling conditions. Within this framing, resilience is not treated as an absolute comfort target, but as a comparative property that describes how strongly climatic warming propagates to human thermal stress through spatial and material configuration.

Across the urban, building, and component scales, the methodology retains a single comparative logic while adapting modelling pathways to dominant physical processes. At the urban scale, vegetation- and surface-driven microclimatic interactions are resolved through ENVI-met; at the building and component scales, radiation, airflow, and envelope effects are resolved through a Ladybug-centered workflow integrating thermodynamic solvers and CFD. In all cases, comparability is ensured by the invariances formalized in Chapter 4: fixed evaluation domains at human exposure level, consistent spatial sampling, aligned reporting times, and standardized post-processing that produces paired UTCI fields, ΔUTCI fields, and compact distribution descriptors.

Validation is provided through three case studies deliberately selected to span the urban–building–component continuum. Within each case study, ΔUTCI functions as an internal comparative indicator: configurations are ranked and interpreted under a single baseline–future pairing, while cross-scale synthesis relies on recurring mechanisms rather than on direct comparison of absolute ΔUTCI magnitudes across different climatic horizons.

At the urban scale (Sassuolo), the method discriminates clearly among morphologies and land-use patterns. Compact historic fabric exhibits the lowest average ΔUTCI and the most concentrated distributions, while exposed industrial and agricultural configurations show higher and more spatially uniform amplification. Natural areas display intermediate behavior, characterized by higher internal heterogeneity. Read comparatively, these results clarify that vegetation contributes to resilience when it operates as a coherent microclimatic system—radiatively effective, hydrologically supported, and spatially continuous—rather than as a fragmented mitigation layer.

At the building scale (the cloister of San Sepolcro in Parma), the methodology remains sensitive at architectural resolution. Configurations dominated by radiative control show restrained and spatially coherent ΔUTCI responses, while ventilation-driven configurations exhibit wide distributions and pronounced gradients, with ΔUTCI values extending up to approximately 10 °C. This behavior aligns with the thermophysiological mechanisms discussed in Chapter 3: as ambient air temperatures approach skin-temperature thresholds, convective exchange loses reliability as a cooling pathway. In resilience terms, ventilation emerges as effective when treated as a controllable and time-dependent resource.

At the component scale (Xirbi railway station), the methodology captures a systematic trade-off between present-day mitigation and future sensitivity. Increasing envelope porosity lowers baseline UTCI locally by enhancing airflow, yet increases ΔUTCI, with mean values rising from approximately 3.0 °C to 3.6 °C across configurations. This dual behavior makes explicit that operability can simultaneously improve current comfort and intensify coupling to future climatic forcing. The method renders this trade-off legible at the scale where envelope decisions are made, framing operability as an adaptive mechanism whose effectiveness depends on boundary conditions and control logic.

Taken together, the three applications confirm that a quantitative–qualitative methodology based on local UTCI variations can be applied consistently across heterogeneous architectural scales, producing comparable evidence about resilience mechanisms and supporting interpretation that remains directly legible to design practice.

Alongside closing the first research question, the work consolidates the objectives that structured its operational development and brings them to a coherent closure. It establishes,

in a unified framework, the physiological and thermodynamic mechanisms that govern thermal comfort across indoor, outdoor, and transitional conditions, and confirms their relevance for design-oriented assessment under climate stress. This grounding provides a stable interpretative basis for the use of a heat-stress index within spatially complex environments, where comfort is shaped by the combined action of radiative, convective, and regulatory processes.

The thesis substantiates the use of UTCI and of ΔUTCI by consolidating its theoretical justification and by formalizing the interpretative conventions that make comparative assessment possible. The systematic application of the methodology to three real case studies at the urban, building, and component scales confirms its validity across different geometries, exposure conditions, and modelling resolutions, and demonstrates its capacity to retain internal coherence while remaining scale-independent.

The work ultimately translates these results into design-relevant interpretative criteria. The resulting interpretation links ΔUTCI spatial fields, distributional behavior, and extreme values directly to the underlying physical mechanisms, articulating a clear hierarchy of climate-adaptive strategies and providing a robust basis for informed decision-making. This synthesis completes the objectives associated with the first research question by integrating theoretical understanding, methodological consistency, and actionable design interpretation within a single comparative construct.

Research question	Methodological foundations	Empirical validation	Cross-scale synthesis, contribution and scope
RQ1: How can a quantitative–qualitative, designer-oriented methodology based on local UTCI variations be developed and validated to assess the thermal-comfort resilience of the built environment across urban, building and building component scales under current and future climate conditions? **OB1**: Develop and validate a single quantitative–qualitative methodology to measure thermal-comfort resilience to climate change across the three project scales: urban, building, and component. **OB1.1**: Identify physiological and thermodynamic mechanisms that, indoors and outdoors, influence thermal comfort. **OB1.2**: Validate through the literature the feasibility of UTCI variations as an indicator of thermal-comfort resilience and justify the selection of UTCI as the core thermal comfort index. **OB1.3**: Apply the methodology to real case studies at three different scales (urban, building and component) to test and refine it under realistic design constraints. **OB1.4**: Derive design-relevant interpretative criteria to translate ΔUTCI outputs into actionable guidance for climate-adaptive strategies.	**Addresses OB1.1–OB1.2 and frames OB1.4**: • UTCI rationale and interpretative conventions; ΔUTCI definition as a comparative construct (baseline–future, declared invariances). • Thermophysiological and thermodynamic framing for interpreting stress pathways and threshold effects. • Workflow logic: fixed evaluation domains, consistent spatial sampling, aligned reporting times, standardized post-processing and descriptors (paired UTCI fields, ΔUTCI fields, distributions).	**Addresses OB1.3**: Urban scale: Sassuolo; Building scale: San Sepolcro cloister; Component scale: Xirbi station envelope.	**Addresses OB1.4 and consolidates OB1**: • Cross-scale mechanisms and hierarchy (e.g., radiative control as a stable driver; threshold-dependent behaviors for ventilation and vegetation-related pathways). • Design-relevant interpretative criteria: reading resilience through the combined structure of spatial fields and distributions and making trade-offs legible at the scale of decision. • Scope conditions for comparative validity: interpretation anchored to declared invariances and scenario pairing discipline.

Table 14. Alignment between Research Question 1 and the related research objectives.
The table synthesizes how the objectives associated with Research Question 1 are addressed through the methodological foundations of the thesis, empirically validated across the three case studies, and consolidated into a cross-scale interpretative framework. It clarifies the correspondence between the development of the ΔUTCI-based methodology, its multi-scalar application, and the resulting contribution to the understanding of thermal-comfort resilience in the built environment.

7.1.2 Addressing RQ2: operational robustness and replicability

Research Question 2 asked which operational procedures, modelling tools, and assessment mechanisms are required to implement the methodology in a robust and replicable manner.

The thesis answers this question by formalizing a complete operational workflow designed for methodological transparency and early-stage decision support. The workflow is structured around two organizing principles: traceability of climatic forcing and comparability through declared invariances.

Traceability is achieved through standardized baseline–future EPW packages generated and documented consistently within each case study. Comparability is achieved by fixing the evaluation domain, spatial sampling, reporting times, and post-processing rules so that differences in outputs can be attributed to spatial configuration and climatic forcing rather than to procedural variation.

Operationally, the workflow integrates:

- acquisition of baseline climate data and generation of scenario-consistent future EPW files through climate morphing;
- geometric modelling with scale-appropriate abstraction rules;
- microclimate simulation and UTCI computation at invariant sampling points;
- standardized post-processing that yields aligned maps and distributional descriptors.

A key procedural decision is the explicit separation between numerical evaluation and interpretative communication. Continuous UTCI values are retained throughout computation, aggregation, and ranking, preserving analytical resolution for pointwise differencing and distribution-based interpretation. Stress categories are introduced only after analysis as a communicative layer, supporting dialogue with non-specialist stakeholders without constraining comparative sensitivity.

The resulting workflow relies on traceable climate inputs, declared invariances, and standardized deliverables, enabling reproducible application across contexts and adaptation to different scales without altering its comparative logic. In design-oriented applications, this structure supports option screening, controlled comparison among limited sets of variants,

and progressive refinement while maintaining continuity between design intent and performance evidence.

In doing so, the thesis fulfils the second set of operational objectives by delivering a complete and internally coherent digital workflow for multi-scalar ΔUTCI assessment. The workflow brings together geometry handling, future-climate data generation, microclimate and thermodynamic simulation, and UTCI computation within a single comparative logic, ensuring that results remain traceable and consistent across scales and configurations.

It identifies a stable and interoperable suite of modelling tools and establishes clear procedures for future-climate processing, geometric abstraction, definition of evaluation domains, spatial sampling, and post-processing of results. These procedures are documented in a form that supports repetition under comparable assumptions and transparent adaptation to different design contexts. The workflow's internal consistency is verified through its full deployment across the three case studies, where identical methodological settings enable controlled comparison despite differences in scale, geometry, and modelling pathways.

As a result, the thesis delivers operational guidelines that support confident re-application of the method in other research and design contexts, preserving comparability while allowing flexibility in tool choice and project scale. This completes the operational objectives associated with the second research question by translating methodological rigor into a reproducible and transferable assessment framework.

Research question	Methodological foundations	Empirical validation	Cross-scale synthesis, contribution and scope
RQ2: Which operational procedures, modelling tools and assessment mechanisms are needed to implement the methodology in a robust and replicable manner? **OB2**: Develop and validate a complete operational digital workflow so that the proposed method can be implemented in a robust, repeatable way with a consistent suite of available tools at the urban, building and component scales. **OB2.1**: Identify appropriate software tools for three-dimensional geometric modelling, acquisition of current and future climate data, microclimatic and thermal simulation, and UTCI calculation. **OB2.2**: Develop and document detailed and repeatable operating procedures for data collection, climate processing, microclimate simulation, and ΔUTCI calculation, ensuring methodological transparency and future replicability. **OB2.3**: Verify the overall consistency and reliability of the workflow through its complete application to the selected case studies and produce operational guidelines to facilitate future use in other contexts.	**Addresses OB2.1–OB2.2**: • Climate inputs and baseline–future pairing; traceability of climatic forcing through standardized EPW packages and scenario morphing. • Geometric modelling and scale-appropriate abstraction rules. • Computational framework, sampling and post-processing rules to preserve comparability via declared invariances.	**Addresses OB2.3**: Full workflow implementation across the three case studies, including consistent sampling, UTCI computation, and comparable outputs (maps + distributional descriptors).	**Addresses OB2.3 and consolidation of OB2**: • Robustness and uncertainty framing for ranking and interpretation (separation between numerical evaluation and communicative categorization). • Design-facing deliverables and operational guidelines enabling repeatable application in other contexts when assumptions and pairing logic are handled consistently.

Table 15. Alignment between Research Question 2 and the related research objectives.
The table summarizes how the objectives linked to Research Question 2 are fulfilled through the definition of operational procedures, the selection and integration of modelling tools, and the implementation of a robust and replicable workflow. It highlights the empirical verification of the workflow across scales and its contribution in terms of methodological transparency, repeatability, and transferability to other design and research contexts.

7.2 Concluding synthesis

Taken as a whole, the thesis demonstrates that climate adaptation in the built environment cannot be assessed meaningfully through isolated measures or single-scale reasoning. Heat exposure emerges from linked decisions across urban morphology, architectural space, and envelope configuration, and its future amplification depends on how these decisions mediate the translation of climatic forcing into human thermal stress.

The comparative framework developed here supports this understanding by stabilizing the evaluation domain and interpreting change through ΔUTCI as a measure of sensitivity. Within this frame, resilience is read through the combined structure of spatial fields and distributions, rather than through absolute comfort categories alone. This approach allows robust identification of trade-offs, clarifies threshold-dependent behaviors, and avoids false confidence in strategies whose apparent effectiveness depends on boundary conditions that are themselves altered by climate change.

This comparative framing also clarifies the practical and epistemic implications of the work. The stabilization of how climate-driven change is interpreted at the level of human thermal stress allows design decisions to be evaluated not only against present-day conditions, but in terms of their robustness under intensifying climatic forcing. This perspective is particularly relevant in contexts where absolute comfort cannot be ensured and where the critical issue becomes the degree to which different configurations amplify or attenuate future stress. Read in this way, the use of ΔUTCI shifts the focus from isolated performance indicators to sensitivity, trade-offs, and threshold effects, providing a shared basis for comparison across the urban–building–component continuum.

7.3 Scope, transferability, and outlook

The conclusions are bounded by the assumptions made explicit in the methodology and discussed in Chapter 6, including uncertainty in future climatic forcing, model-form abstractions in microclimate simulation, standardized UTCI subject conventions, and a focus on representative extreme-heat periods. Within these bounds, ΔUTCI-based comparison provides internally coherent ranking and interpretation across configurations.

While the case studies are context-specific, the transferable outcome of the thesis is the assessment logic itself: a traceable climate-input procedure, an invariance-based comparative workflow, and a comfort-centered resilience proxy that can be re-applied to other climates, morphologies, and design problems when baseline–future pairing and modelling assumptions are handled consistently.

Within this framing, the value of the proposed approach lies in its capacity to operate under conditions of uncertainty without collapsing into indeterminacy. The comparative logic based on invariant evaluation domains and paired baseline–future scenarios does not eliminate uncertainty in climate projections or microclimate modeling, but renders its effects legible and comparable across design alternatives. This makes the framework particularly suited to contexts where decisions must be taken despite incomplete information, allowing relative robustness and vulnerability to be assessed consistently. As a result, the method supports transfer through the reapplication of a stable assessment logic that can accommodate different climates, morphologies, and modeling environments while preserving interpretative coherence.

Building on this foundation, the following chapter outlines future research directions that extend the framework toward dynamic-exposure comfort representations, accelerated exploration through surrogate modelling, and targeted microclimate calibration, without altering the comparative structure established in this work.

8 Future developments

This thesis has developed a comparative, multi-scalar framework to assess thermal resilience of the built environment under climate change through spatially explicit ΔUTCI fields. A central strength of the work is methodological control: the evaluation domain and sampling strategy are held invariant across baseline and future climates, so that differences can be interpreted as climate-driven shifts and morphology-driven modulations rather than artefacts of changing procedures. Building on this backbone, future work should aim to make the framework more representative of lived exposure, more scalable for design-space exploration and uncertainty analysis, and more credible for decision support through empirical grounding.

The thesis outlook identifies three priority directions: dynamic exposure representations, accelerated analysis through surrogate modelling, and microclimate calibration. The following sections consolidate these directions into a concise research agenda, and briefly indicate two additional extensions—scenario uncertainty propagation and indoor–outdoor coupling—that become feasible once the three priorities are addressed.

8.1 Dynamic-exposure comfort

The thesis evaluates thermal resilience through spatial snapshots of UTCI under controlled conditions. This choice is coherent with the comparative logic of ΔUTCI mapping, yet it remains a static proxy for a phenomenon that is inherently dynamic: heat stress is experienced as an accumulation over time, shaped by daily rhythms, short-term adaptation (e.g., shade-seeking), and movement between micro-environments. Future work can therefore extend the framework from “comfort at a location and time” toward “exposure across time and trajectories”, while preserving the thesis’ core requirement of comparability.

A direct and thesis-consistent step is to replace single-hour descriptors with time-integrated exposure metrics derived from UTCI time series, such as degree-hours above a threshold (or other exceedance-based constructs). This approach has already been operationalized in the biometeorological literature through cumulative UTCI-based heat-stress exposure measures that explicitly combine intensity and duration into a single interpretable descriptor. The advantage for resilience assessment is that interventions with similar peak effects may diverge

strongly when evaluated over realistic exposure windows, particularly where radiative control reduces peaks but does not fully mitigate prolonged stress[506].

A second extension concerns movement and route structure. In many urban contexts, thermal risk and discomfort are driven by repeated short trips (to transit, school, services) rather than by long stationary exposure. Recent evidence shows that heat stress (quantified via UTCI) can affect pedestrian route choice behavior and perceived walking distance, with implications for accessibility and equity[507]. From a resilience perspective, this suggests that the importance of a hotspot depends not only on its intensity, but also on whether it lies on unavoidable paths, bottlenecks, or destinations.

Methodologically, a dynamic-exposure extension can be implemented without abandoning the thesis' comparative discipline. A small set of standardized exposure scenarios can be defined—e.g., representative routes, schedules, and activity levels—and then evaluated consistently under baseline and future climates. Resilience can remain a difference metric: not only ΔUTCI(x), but ΔE where E is an exposure descriptor computed along trajectories or over time (e.g., cumulative exceedance, time above severe-stress categories, peak UTCI along a path). Crucially, the behavioral assumptions must remain explicit and invariant across the compared climates and design configurations, so that differences remain attributable and interpretable.

8.2 Accelerated exploration through surrogate modelling

A recurring barrier to multi-scalar thermal resilience assessment is computational cost. High-resolution urban microclimate simulations are often too slow to support systematic exploration of design alternatives, robust sensitivity testing, or the propagation of uncertainty across climate scenarios. This limits the practical uptake of microclimate-informed resilience assessment, and tends to confine studies to a small number of configurations.

A promising pathway is the integration of surrogate models—data-driven emulators trained on high-fidelity simulations—to accelerate repeated evaluation while keeping the physics-

[506] Sadeghi et al., 2021.
[507] Basu et al., 2024.

based model as the reference for training and verification. Recent work has demonstrated the feasibility of such approaches for urban microclimate assessment, showing that machine learning-based metamodels trained on high-fidelity simulations can substantially reduce computational cost while preserving sensitivity to morphological and climatic variation, when applied within a declared domain of validity[508]. Importantly, surrogates do not replace the thesis framework; they can be used to scale it. Once trained under a controlled modelling setup, a surrogate can support rapid screening, optimization, and uncertainty exploration while preserving the same output structure needed for ΔUTCI mapping and resilience ranking.

Recent research demonstrates the feasibility and potential magnitude of this acceleration in design-oriented microclimate contexts. For instance, surrogate models trained on CFD-generated datasets have been shown to reduce prediction time from hours to fractions of a second for key pedestrian-level variables (e.g., local air temperature and wind velocity), while maintaining accuracy in the same order as the reference simulations[509]. For a comparative resilience framework, this matters because it enables an expanded experimental space: more morphological variants, more mitigation strategies, and—critically—more climate inputs.

For surrogate integration to remain coherent with the thesis logic, three methodological requirements are decisive:

1. Consistency across comparisons. Surrogates must be applied identically across baseline and future climates and across competing design options, so that surrogate error does not introduce systematic ranking bias.
2. Documented validity domain. The surrogate should have a clearly defined training domain (geometry ranges, boundary conditions, climatic envelopes) and diagnostics to detect extrapolation. This is essential if the surrogate is later used for scenario ensembles.
3. Hybrid workflows. A practical research direction is to combine fast surrogates for broad exploration with targeted high-fidelity simulations for confirmation, refinement, and active learning. In this configuration, computational effort is

[508] Manapragada et al., 2026.
[509] Zhao et al., 2024.

allocated where it matters most, that is on high sensitivity, high uncertainty, or decision-critical trade-offs.

In short, surrogate modelling is not a methodological detour. If implemented with transparency and error control, it is a direct enabler for transforming a rigorous comparative method into a scalable resilience instrument.

8.3 Microclimate calibration and empirical credibility

The thesis' comparative strategy is designed to reduce interpretive ambiguity under uncertainty; nonetheless, credibility becomes increasingly important when results are used beyond methodological demonstration—particularly for real projects, policy applications, or inter-city comparisons. Microclimate models are sensitive to boundary conditions, surface optical properties, material thermal behavior, vegetation parameterization, and turbulence/radiation schemes. Without calibration and validation, systematic biases may persist in absolute UTCI fields and may sometimes affect relative gradients, especially where interventions act through radiative processes.

Future work should therefore develop targeted calibration protocols aligned with the thesis' controlled-comparison ethos: calibration improves the realism of the shared modelling setup, and the calibrated configuration is then used invariantly across baseline and future climates strengthening comparability.

Validation studies already indicate where calibration effort is most valuable. Mean radiant temperature and the underlying radiative fluxes are often dominant drivers of outdoor thermal stress patterns, and they are also where models can show substantial errors under extreme conditions. Seasonal validation work has shown that common tools (including ENVI-met and RayMan [510]) can exhibit large MRT errors—particularly under extreme heat, complex morphology, or engineered shade—highlighting the need for in-situ checks and the risk of using unvalidated simulations in morphological extremes [511]. More recent work has also demonstrated that, with empirically constrained inputs (e.g., albedo calibration and cloud

[510] Matzarakis, 2007
[511] Crank et al., 2020.

parameterization), ENVI-met can model diurnal MRT with improved accuracy and without systematic shaded-area bias in a dense subtropical context—again pointing to calibration as a decisive lever for reliability[512].

A thesis-consistent calibration agenda can be structured around three practical layers:

- Forcing consistency. Validate the meteorological forcing used for simulation periods against local observations where possible, and document any adjustments.
- Radiation and surface properties. Prioritize parameters that dominate radiative load and MRT (albedo, emissivity, shading geometry representation), because these strongly shape UTCI gradients and the apparent effectiveness of shade-based interventions.
- Vegetation and aerodynamics. Where nature-based strategies are assessed, calibrate vegetation optical/aerodynamic parameters and verify wind behavior at pedestrian height, since ventilation and shading can interact in non-trivial ways.

Finally, calibration should be paired with uncertainty communication. Even limited measurement campaigns can support error bounds and sensitivity ranges that indicate how robust design rankings remain under plausible parameter variation. This is a practical step toward decision relevance: not only “what improves resilience”, but “how confident we are that it does”.

8.4 Closing outlook

Once dynamic exposure, surrogate acceleration, and calibration are in place, two further extensions become both feasible and strategically important. First, resilience assessment can incorporate scenario ensembles rather than a single future pathway, translating climate uncertainty into distributions of ΔUTCI and exposure metrics, in line with the IPCC framing of climate risk under multiple plausible futures[513]. Second, the framework can evolve toward whole-exposure resilience by coupling outdoor microclimate fields with indoor performance and energy use, recognizing that people experience heat across indoor–outdoor sequences

[512] Schöneberger et al., 2024
[513] IPCC, 2023.

and that buildings and microclimate interact bidirectionally. Recent work on two-way coupling between ENVI-met and EnergyPlus illustrates both the feasibility and the benefits of explicitly accounting for microclimate feedback when quantifying building energy performance under changing conditions[514]. These directions do not replace the thesis framework; they extend its comparative logic toward decisions that must be robust under uncertainty and meaningful across the full lived domain of thermal exposure.

[514] Pasandi et al., 2025

9 References

This rational index re-organizes all references cited throughout the thesis into a thematic structure that mirrors the conceptual architecture of the work: from climate-system fundamentals and future scenarios, to heat-related health risks, human thermophysiology, thermal-comfort metrics, microclimate–built-environment mechanisms, modelling toolchains, and design-oriented resilience frameworks. To preserve transparency and traceability, the same reference is intentionally repeated in every section where it provides a substantive contribution.

9.1 Climate System Fundamentals and Climate Change Scenarios

9.1.1 Physical basis of climate change

Etminan, M., G. Myhre, E. J. Highwood, and K. P. Shine. 2016. 'Radiative Forcing of Carbon Dioxide, Methane, and Nitrous Oxide: A Significant Revision of the Methane Radiative Forcing'. Geophysical Research Letters 43 (24): 12,614-12,623. https://doi.org/10.1002/2016GL071930.

Feldman, D. R., W. D. Collins, P. J. Gero, M. S. Torn, E. J. Mlawer, and T. R. Shippert. 2015. 'Observational Determination of Surface Radiative Forcing by CO2 from 2000 to 2010'. Nature 519 (7543): 339-43. https://doi.org/10.1038/nature14240.

Forster, Piers, Trude Storelvmo, Kyle Armour, William Collins, Jean-Luis Dufresne, David Frame, Daniel J. Lunt, et al. 2021. ‘The Earth’s Energy Budget, Climate Feedbacks, and Climate Sensitivity’. In Climate Change 2021: The Physical Science Basis. https://doi.org/10.1017/9781009157896.001.

Harries, John, Helen Brindley, Pretty Sagoo, and Richard Bantges. 2001. 'Increases in Greenhouse Forcing Inferred from the Outgoing Longwave Radiation Spectra of the Earth in 1970 and 1997'. Nature 410 (April):355-57. https://doi.org/10.1038/35066553.

Kiehl, Jeffrey, and Kevin Trenberth. 1997. 'Earth's Annual Global Mean Energy Budget'. Bulletin of the American Meteorological Society 78 (February). https://doi.org/10.1175/1520-0477(1997)078<0197:EAGMEB>2.0.CO;2.

Myhre, Gunnar, Eleanor J. Highwood, Keith P. Shine, and Frode Stordal. 1998. 'New Estimates of Radiative Forcing Due to Well Mixed Greenhouse Gases'. Geophysical Research Letters 25 (14): 2715-18. https://doi.org/10.1029/98GL01908.

Schmidt, Gavin A., Reto A. Ruedy, Ron L. Miller, and Andy A. Lacis. 2010. 'Attribution of the Present-Day Total Greenhouse Effect'. Journal of Geophysical Research: Atmospheres 115 (D20). https://doi.org/10.1029/2010JD014287.

Trenberth, Kevin E., John T. Fasullo, and Jeffrey Kiehl. 2009. 'Earth's Global Energy Budget'. Bulletin of the American Meteorological Society 90 (March). https://doi.org/10.1175/2008BAMS2634.1.

9.1.2 Emission pathways, SSPs and future climate scenarios

Cooley, S., D. Schoeman, L. Bopp, P. Boyd, S. Donner, D.Y. Ghebrehiwet, S.-I. Ito, W. Kiessling, P. Martinetto, E. Ojea, M.-F. Racault, B. Rost, and M. Skern-Mauritzen. 2022. Ocean and Coastal Ecosystems and their Services Supplementary Material. In:Climate Change 2022: Impacts, Adaptation, and Vulnerability. Contribution of Working Group II to the Sixth Assessment Report of the Intergovernmental Panel on Climate Change [H.-O. Pörtner, D.C. Roberts, M. Tignor, E.S. Poloczanska, K. Mintenbeck, A. Alegría, M. Craig, S. Langsdorf, S. Löschke, V. Möller, A. Okem, B. Rama (eds.)]. Available from https://www.ipcc.ch/report/ar6/wg2/.

Eyring, Veronika, Sandrine Bony, Gerald A. Meehl, Catherine A. Senior, Bjorn Stevens, Ronald J. Stouffer, and Karl E. Taylor. 2016. 'Overview of the Coupled Model Intercomparison Project Phase 6 (CMIP6) Experimental Design and Organization'. Geoscientific Model Development 9 (5): 1937-58. https://doi.org/10.5194/gmd-9-1937-2016.

Gasparrini, Antonio, Yuming Guo, Francesco Sera, Ana Maria Vicedo-Cabrera, Veronika Huber, Shilu Tong, Micheline de Sousa Zanotti Stagliorio Coelho, et al. 2017. 'Projections of Temperature-Related Excess Mortality under Climate Change Scenarios'. The Lancet. Planetary Health 1 (9): e360-67. https://doi.org/10.1016/S2542-5196(17)30156-0.

IPCC. 2021. Index. In: Climate Change 2021: The Physical Science Basis. Contribution of Working Group I to the Sixth Assessment Report of the Intergovernmental Panel on Climate Change [Masson-Delmotte, V., P. Zhai, A. Pirani, S.L. Connors, C. Péan, S. Berger, N. Caud, Y. Chen, L. Goldfarb, M.I. Gomis, M. Huang, K. Leitzell, E. Lonnoy, J.B.R. Matthews, T.K. Maycock, T. Waterfield, O. Yelekçi, R. Yu, and B. Zhou (eds.)]. Cambridge University Press, Cambridge, United Kingdom and New York, NY, USA, pp. 2339 -2391.

IPCC. 2022. Climate Change 2022: Impacts, Adaptation and Vulnerability. Contribution of Working Group II to the Sixth Assessment Report of the Intergovernmental Panel on Climate Change [H.-O. Pörtner, D.C. Roberts, M. Tignor, E.S. Poloczanska, K. Mintenbeck, A. Alegría, M. Craig, S. Langsdorf, S. Löschke, V. Möller, A. Okem, B. Rama (eds.)]. Cambridge University Press. Cambridge University Press, Cambridge, UK and New York, NY, USA, 3056 pp., doi: https://doi.org/10.1017/9781009325844.

IPCC. 2023. Climate Change 2023: Synthesis Report. Contribution of Working Groups I, II and III to the Sixth Assessment Report of the Intergovernmental Panel on Climate Change [Core Writing Team, H. Lee and J. Romero (eds.)]. IPCC, Geneva, Switzerland, pp. 35-115, doi: 10.59327/IPCC/AR6-9789291691647.

Meinshausen, M., Nicholls, Z. R. J., Lewis, J., Gidden, M. J., Vogel, E., Freund, M., Beyerle, U., Gessner, C., Nauels, A., Bauer, N., Canadell, J. G., Daniel, J. S., John, A., Krummel, P. B., Luderer, G., Meinshausen, N., Montzka, S. A., Rayner, P. J., Reimann, S., Smith, S. J., van den Berg, M., Velders, G. J. M., Vollmer, M. K., and Wang, R. H. J. 2020. ‘The shared socio-economic pathway (SSP) greenhouse gas concentrations and their extensions to 2500’. Geosci. Model Dev. 13: 3571-3605. https://doi.org/10.5194/gmd-13-3571-2020.

9.1.3 Observational evidence and large-scale climate trends

Cooley, S., D. Schoeman, L. Bopp, P. Boyd, S. Donner, D.Y. Ghebrehiwet, S.-I. Ito, W. Kiessling, P. Martinetto, E. Ojea, M.-F. Racault, B. Rost, and M. Skern-Mauritzen. 2022. Ocean and Coastal Ecosystems and their Services Supplementary Material. In:Climate Change 2022: Impacts, Adaptation, and Vulnerability. Contribution of Working Group II to the Sixth Assessment Report of the Intergovernmental Panel on Climate Change [H.-O. Pörtner, D.C. Roberts, M. Tignor, E.S. Poloczanska, K. Mintenbeck, A. Alegría, M. Craig, S. Langsdorf, S. Löschke, V. Möller, A. Okem, B. Rama (eds.)]. Available from https://www.ipcc.ch/report/ar6/wg2/.

De Martonne, Emmanuel. Une nouvelle fonction climatologique: L. 1926. ‘indice d’. aridité. La Météorologie 2: 449-458.

ENEA. 2023. 'Rapporto Annuale sull'Efficienza Energetica 2023'. ENEA - Dipartimento Unità per l'efficienza energetica. 14 December 2023.

European Green Deal. 2019. Communication from the Commission to the European Parliament, the European Council, the Council, the European Economic and Social Committee and the Committee of the Regions (COM(2019) 640 final).

Feldman, D. R., W. D. Collins, P. J. Gero, M. S. Torn, E. J. Mlawer, and T. R. Shippert. 2015. 'Observational Determination of Surface Radiative Forcing by CO2 from 2000 to 2010'. Nature 519 (7543): 339-43. https://doi.org/10.1038/nature14240.

IPCC. 2021. Index. In: Climate Change 2021: The Physical Science Basis. Contribution of Working Group I to the Sixth Assessment Report of the Intergovernmental Panel on Climate Change [Masson-Delmotte, V., P. Zhai, A. Pirani, S.L. Connors, C. Péan, S. Berger, N. Caud, Y. Chen, L. Goldfarb, M.I. Gomis, M. Huang, K. Leitzell, E. Lonnoy, J.B.R. Matthews, T.K. Maycock, T. Waterfield, O. Yelekçi, R. Yu, and B. Zhou (eds.)]. Cambridge University Press, Cambridge, United Kingdom and New York, NY, USA, pp. 2339 -2391.

IPCC. 2022. Climate Change 2022: Impacts, Adaptation and Vulnerability. Contribution of Working Group II to the Sixth Assessment Report of the Intergovernmental Panel on Climate Change [H.-O. Pörtner, D.C. Roberts, M. Tignor, E.S. Poloczanska, K. Mintenbeck, A. Alegría, M. Craig, S. Langsdorf, S. Löschke, V. Möller, A. Okem, B. Rama (eds.)]. Cambridge University Press. Cambridge University Press, Cambridge, UK and New York, NY, USA, 3056 pp., doi:10.1017/9781009325844.

IPCC. 2023. Climate Change 2023: Synthesis Report. Contribution of Working Groups I, II and III to the Sixth Assessment Report of the Intergovernmental Panel on Climate Change [Core Writing Team, H. Lee and J. Romero (eds.)]. IPCC, Geneva, Switzerland, pp. 35-115, doi: 10.59327/IPCC/AR6-9789291691647.

IPCC. 2023. Climate Change 2023: Synthesis Report. Contribution of Working Groups I, II and III to the Sixth Assessment Report of the Intergovernmental Panel on Climate Change. IPCC, Geneva.

IPCC. 2023. Climate Change 2023: Synthesis Report. Intergovernmental Panel on Climate Change.

Johansson, Oscar V. 1926. Über die Asymmetrie der meteorologischen Schwankungen. Commentationes Physico-Mathematicae 3, no. 1. Helsingfors: Societas Scientiarum Fennica.

Kautz, Lisa-Ann, Olivia Martius, Stephan Pfahl, Joaquim G. Pinto, Alexandre M. Ramos, Pedro M. Sousa, and Tim Woollings. 2022. 'Atmospheric Blocking and Weather Extremes over the Euro-Atlantic Sector - a Review'. Weather and Climate Dynamics 3 (1): 305-36. https://doi.org/10.5194/wcd-3-305-2022.

Keeling, Ralph F., Heather D. Graven, Lisa R. Welp, Laure Resplandy, Jian Bi, Stephen C. Piper, Ying Sun, Alane Bollenbacher, and Harro A. J. Meijer. 2017. 'Atmospheric Evidence for a Global Secular Increase in Carbon Isotopic Discrimination of Land Photosynthesis'. Proceedings of the National Academy of Sciences 114 (39): 10361-66. https://doi.org/10.1073/pnas.1619240114.

Kerner, Friedrich von. Thermisodromen: Versuch einer kartographischen Darstellung des jährlichen Ganges der Lufttemperatur. Mitteilungen der k. k. Geographischen Gesellschaft in Wien 6, no. 3. 1905.

Lazoglou, Georgia, Alexandros Papadopoulos-Zachos, Pantelis Georgiades, George Zittis, Kondylia Velikou, Errikos Michail Manios, and Christina Anagnostopoulou. 2024. 'Identification of Climate Change Hotspots in the Mediterranean'. Scientific Reports 14 (1): 29817. https://doi.org/10.1038/s41598-024-80139-1.

Manning, Andrew C., and Ralph F. Keeling. 2006. 'Global Oceanic and Land Biotic Carbon Sinks from the Scripps Atmospheric Oxygen Flask Sampling Network'. Tellus B 58 (2): 95-116. https://doi.org/10.1111/j.1600-0889.2006.00175.x.

Nistor, Mărgărit M. 2016. 'Spatial Distribution of Climate Indices in the Emilia-Romagna Region'. Meteorological Applications 23 (2): 304-13. https://doi.org/10.1002/met.1555.

Robine, Jean-Marie, Siu Lan K. Cheung, Sophie Le Roy, Herman Van Oyen, Clare Griffiths, Jean-Pierre Michel, and François Richard Herrmann. 2008. 'Death Toll Exceeded 70,000 in Europe during the Summer of 2003'. Comptes Rendus Biologies 331 (2): 171-78. https://doi.org/10.1016/j.crvi.2007.12.001.

9.2 Heat, Human Health and Well-Being

9.2.1 Heat stress as a public-health risk

Ballester, Joan, Marcos Quijal-Zamorano, Raúl Fernando Méndez Turrubiates, Ferran Pegenaute, François R. Herrmann, Jean Marie Robine, Xavier Basagaña, Cathryn Tonne, Josep M. Antó, and Hicham Achebak. 2023. 'Heat-Related Mortality in Europe during the Summer of 2022'. Nature Medicine 29 (7): 1857-66. https://doi.org/10.1038/s41591-023-02419-z.

Centers for Disease Control and Prevention (CDC). 1984. 'Heat-Related Mortality - Latium Region, Italy, Summer 1983'. Morbidity and Mortality Weekly Report (MMWR) 33 (37): 518-521. https://www.cdc.gov/mmwr/preview/mmwrhtml/00000000.htm.

Italian Ministry of Health and National Centre for Disease Prevention and Control. 2018. Results of the Heat-Health Warning Systems (HHWWS) and the Daily Mortality Surveillance

System (SiSMG) and Emergency Department Visits - Summer 2017: Summary Report. Rome: Ministry of Health. https://www.salute.gov.it/imgs/C_17_pubblicazioni_2654_allegato.pdf.

Kovats, Sari, and Shakoor Hajat. 2008. Heat Stress and Public Health: A Critical Review. Annual Review of Public Health 29 (February):41-55. https://doi.org/10.1146/annurev.publhealth.29.020907.090843.

Orsetti, Eleonora, Nicola Tollin, Martin Lehmann, Vanessa Agudelo Valderrama, and Jordi Morató. 2022. 'Building Resilient Cities: Climate Change and Health Interlinkages in the Planning of Public Spaces'. International Journal of Environmental Research and Public Health 19 (3): 1355. https://doi.org/10.3390/ijerph19031355.

World Health Organization, Regional Office for Europe. 2008. Heat-Health Action Plans: Guidance. Copenhagen: World Health Organization. ISBN 978-92-890-7191-8.

World Health Organization. 2018. WHO Housing and Health Guidelines. Geneva: World Health Organization. ISBN 978-92-4-155037-6.

World Health Organization, Regional Office for Europe. 2021. Heat and Health in the WHO European Region: Updated Evidence for Effective Prevention. Copenhagen: World Health Organization. ISBN 978-92-890-5540-6.

9.2.2 Epidemiological evidence and vulnerability patterns

Alessandrini, Ester, Stefano Zauli Sajani, Fabiana Scotto, Rossella Miglio, Stefano Marchesi, and Paolo Lauriola. 2011. 'Emergency Ambulance Dispatches and Apparent Temperature: A Time Series Analysis in Emilia-Romagna, Italy'. Environmental Research 111 (8): 1192-1200. https://doi.org/10.1016/j.envres.2011.07.005.

Baccini, Michela, Annibale Biggeri, Gabriele Accetta, Tom Kosatsky, Klea Katsouyanni, Antonis Analitis, H. Ross Anderson, et al. 2008. 'Heat Effects on Mortality in 15 European Cities'. Epidemiology 19 (5): 711. https://doi.org/10.1097/EDE.0b013e318176bfcd.

Ballester, Joan, Marcos Quijal-Zamorano, Raúl Fernando Méndez Turrubiates, Ferran Pegenaute, François R. Herrmann, Jean Marie Robine, Xavier Basagaña, Cathryn Tonne, Josep M. Antó, and Hicham Achebak. 2023. 'Heat-Related Mortality in Europe during the Summer of 2022'. Nature Medicine 29 (7): 1857-66. https://doi.org/10.1038/s41591-023-02419-z.

Centers for Disease Control and Prevention (CDC). 1984. 'Heat-Related Mortality - Latium Region, Italy, Summer 1983'. Morbidity and Mortality Weekly Report (MMWR) 33 (37): 518-521. https://www.cdc.gov/mmwr/preview/mmwrhtml/00000000.htm.

Gasparrini, Antonio, Yuming Guo, Francesco Sera, Ana Maria Vicedo-Cabrera, Veronika Huber, Shilu Tong, Micheline de Sousa Zanotti Stagliorio Coelho, et al. 2017. 'Projections of Temperature-Related Excess Mortality under Climate Change Scenarios'. The Lancet. Planetary Health 1 (9): e360-67. https://doi.org/10.1016/S2542-5196(17)30156-0.

Italian Ministry of Health and National Centre for Disease Prevention and Control. 2018. Results of the Heat-Health Warning Systems (HHWWS) and the Daily Mortality Surveillance System (SiSMG) and Emergency Department Visits - Summer 2017: Summary Report. Rome: Ministry of Health. https://www.salute.gov.it/imgs/C_17_pubblicazioni_2654_allegato.pdf.

Klepeis, N.E., Nelson, W.C., Ott, W.R., Robinson, J.P., Tsang, A.M., Switzer, P., Behar, J.V., Hern, S.C., Engelmann, W.H. 2001. 'The National Human Activity Pattern Survey (NHAPS): A resource for assessing exposure to environmental pollutants'. Journal of Exposure Analysis and Environmental Epidemiology 11: 231-252. https://doi.org/10.1038/sj.jea.7500165.

Martínez-Solanas, Èrica, Marcos Quijal-Zamorano, Hicham Achebak, Desislava Petrova, Jean-Marie Robine, François R Herrmann, Xavier Rodó, and Joan Ballester. 2021. 'Projections of Temperature-Attributable Mortality in Europe: A Time Series Analysis of 147 Contiguous Regions in 16 Countries'. The Lancet Planetary Health 5 (7): e446-54. https://doi.org/10.1016/S2542-5196(21)00150-9.

Michelozzi, P, Luigi Bisanti, Antonio Russo, Ennio Cadum, Moreno Demaria, M D'Ovidio, Giuseppe Costa, and Carlo Perucci. 2005. 'The Impact of the Summer 2003 Heat Waves on Mortality in Four Italian Cities'. Euro Surveillance: Bulletin Européen Sur Les Maladies Transmissibles = European Communicable Disease Bulletin 10 (August):161-65. https://doi.org/10.2807/esm.10.07.00556-en.

Michelozzi, Paola, Francesca De' Donato, Matteo Scortichini, Manuela De Sario, Federica Asta, Nera Agabiti, Ranieri Guerra, Annamaria de Martino, and Marina Davoli. 2016. '[On the increase in mortality in Italy in 2015: analysis of seasonal mortality in the 32 municipalities included in the Surveillance system of daily mortality]'. Epidemiologia E Prevenzione 40 (1): 22-28. https://doi.org/10.19191/EP16.1.P022.010.

Stafoggia, Massimo, Francesco Forastiere, Daniele Agostini, Annibale Biggeri, Luigi Bisanti, Ennio Cadum, Nicola Caranci, et al. 2006. 'Vulnerability to Heat-Related Mortality: A Multicity, Population-Based, Case-Crossover Analysis'. Epidemiology 17 (3): 315. https://doi.org/10.1097/01.ede.0000208477.36665.34.

9.2.3 Climate change, urbanization and health impacts

Aghamohammadi, Nasrin, and Mat Santamouris, eds. 2022. Urban Overheating: Heat Mitigation and the Impact on Health. Advances in Sustainability Science and Technology. Singapore: Springer Nature. https://doi.org/10.1007/978-981-19-4707-0.

Basu, Rounaq, Nicola Colaninno, Aziz Alhassan, and Andres Sevtsuk. 2024. 'Hot and Bothered: Exploring the Effect of Heat on Pedestrian Route Choice Behavior and Accessibility'. Cities 155 (December): 105435. https://doi.org/10.1016/j.cities.2024.105435.

Harlan, Sharon L., Anthony J. Brazel, G. Darrel Jenerette, Nancy S. Jones, Larissa Larsen, Lela Prashad, and William L. Stefanov. 2007. 'In the Shade of Affluence: The Inequitable Distribution of the Urban Heat Island'. In Equity and the Environment, 15:173-202. Emerald Group Publishing Limited. https://doi.org/10.1016/S0196-1152(07)15005-5.

Mavrogianni, Anna, Ioanna Tsoulou, Clare Heaviside, Eleni Oikonomou, Giorgos Petrou, Phil Symonds, Mike Davies, Jonathon Taylor, Ai Milojevic, and Paul Wilkinson. 2022. 'Urban Overheating and Impact on Health: An Introduction'. In Urban Overheating: Heat Mitigation and the Impact on Health, edited by Nasrin Aghamohammadi and Mat Santamouris, 1-20. Singapore: Springer Nature. https://doi.org/10.1007/978-981-19-4707-0_1.

Orsetti, Eleonora, Nicola Tollin, Martin Lehmann, Vanessa Agudelo Valderrama, and Jordi Morató. 2022. 'Building Resilient Cities: Climate Change and Health Interlinkages in the Planning of Public Spaces'. International Journal of Environmental Research and Public Health 19 (3): 1355. https://doi.org/10.3390/ijerph19031355.

Romanello, Marina, Alice McGushin, Claudia Di Napoli, Paul Drummond, Nick Hughes, Louis Jamart, Harry Kennard, et al. 2021. 'The 2021 Report of the Lancet Countdown on Health and Climate Change: Code Red for a Healthy Future'. The Lancet 398 (10311): 1619-62. https://doi.org/10.1016/S0140-6736(21)01787-6.

Santamouris, M. 2020. 'Recent Progress on Urban Overheating and Heat Island Research. Integrated Assessment of the Energy, Environmental, Vulnerability and Health Impact. Synergies with the Global Climate Change'. Energy and Buildings 207 (January):109482. https://doi.org/10.1016/j.enbuild.2019.109482.

9.3 Human Thermophysiology and Thermal Comfort

9.3.1 Human heat balance and thermoregulation

Bergman, T.L., Lavine, A.S., Incropera, F.P., and DeWitt, D.P. 2011. Fundamentals of Heat and Mass Transfer (7th ed.). John Wiley & Sons.

Campbell, Gaylon S., and John M. Norman. 1998. An Introduction to Environmental Biophysics. Springer. https://doi.org/10.1007/978-1-4612-1626-1.

Luo, M., Zhou, X., Zhu, Y., Sundell, J. "Revisiting an Overlooked Parameter in Thermal Comfort Studies, the Metabolic Rate." Energy and Buildings 118 (2016): 152-159. https://doi.org/10.1016/j.enbuild.2016.02.041.

Mazdeyasna, Siavash, Pejman Ghassemi, and Quanzeng Wang. 2023. ‘Best Practices for Body Temperature Measurement with Infrared Thermography: External Factors Affecting Accuracy’. Sensors 23 (18): 8011. https://doi.org/10.3390/s23188011.

Togawa, T. 1989. ‘Non-Contact Skin Emissivity: Measurement from Reflectance Using Step Change in Ambient Radiation Temperature’. Clinical Physics and Physiological Measurement: An Official Journal of the Hospital Physicists' Association, Deutsche Gesellschaft Fur Medizinische Physik and the European Federation of Organisations for Medical Physics 10 (1): 39-48. https://doi.org/10.1088/0143-0815/10/1/004.

Çengel, Y.A., and Boles, M.A. 2014. Thermodynamics: An Engineering Approach (8th ed.). McGraw-Hill Education.

9.3.2 Physiological limits, adaptation and acclimatization

Ahima, Rexford S. 2020. ‘Global Warming Threatens Human Thermoregulation and Survival’. The Journal of Clinical Investigation 130 (2): 559-61. https://doi.org/10.1172/JCI135006.

Kenney, W. L., and J. L. Hodgson. 1987. ‘Heat Tolerance, Thermoregulation and Ageing’. Sports Medicine (Auckland, N.Z.) 4 (6): 446-56. https://doi.org/10.2165/00007256-198704060-00004.

Sadeghi, Mahsan, Richard de Dear, Geoffery Morgan, Mattheos Santamouris, and Bin Jalaludin. 2021. 'Development of a Heat Stress Exposure Metric - Impact of Intensity and Duration of Exposure to Heat on Physiological Thermal Regulation'. Building and Environment 200 (August): 107947. https://doi.org/10.1016/j.buildenv.2021.107947.

Sawka, M.N., Wenger, C.B., and Pandolf, K.B. 2011. ‘Thermoregulatory Responses to Acute Exercise-Heat Stress and Heat Acclimation’. In Comprehensive Physiology, edited by R. Terjung. Hoboken, NJ, USA: John Wiley & Sons, Inc. https://doi.org/10.1002/cphy.cp040109.

9.3.3 Thermal stress and perception mechanisms

Basu, Rounaq, Nicola Colaninno, Aziz Alhassan, and Andres Sevtsuk. 2024. 'Hot and Bothered: Exploring the Effect of Heat on Pedestrian Route Choice Behavior and Accessibility'. Cities 155 (December): 105435. https://doi.org/10.1016/j.cities.2024.105435.

Cabanac, M. 1971. ‘Physiological Role of Pleasure’. Science 173 (4002): 1103-7. https://doi.org/10.1126/science.173.4002.1103.

Cabanac, M. 2011. "Heat Stress and Behavior." In Comprehensive Physiology, edited by R. Terjung. Hoboken, NJ, USA: John Wiley & Sons, Inc. https://doi.org/10.1002/cphy.cp040113.

Cohen, Pninit, Oded Potchter, and Andreas Matzarakis. "Human Thermal Perception of Coastal Mediterranean Outdoor Urban Environments." Applied Geography 37 (2013): 1-10. https://doi.org/10.1016/j.apgeog.2012.11.001.

Heschong, L. 1979. Thermal Delight in Architecture. MIT Press.

Klepeis, N.E., Nelson, W.C., Ott, W.R., Robinson, J.P., Tsang, A.M., Switzer, P., Behar, J.V., Hern, S.C., Engelmann, W.H. 2001. ‘The National Human Activity Pattern Survey (NHAPS): A resource for assessing exposure to environmental pollutants’. Journal of Exposure Analysis and Environmental Epidemiology 11: 231-252. https://doi.org/10.1038/sj.jea.7500165.

9.4 Thermal Comfort Indices and Assessment Metrics

9.4.1 Evolution of thermal comfort indices

Blazejczyk, Krzysztof, Peter Bröde, Dusan Fiala, George Havenith, Ingvar Holmér, Gerd Jendritzky, Bernhard Kampmann, and Anna Błażejczyk. 2010. ‘Principles of the New Universal Thermal Climate Index (UTCI) and Its Application to Bioclimatic Research in European Scale’. Miscellanea Geographica 14: 91-102. https://doi.org/10.2478/mgrsd-2010-0009.

Brauner, Neima, and M. Shacham. 1995. 'Meaningful Wind Chill Indicators Derived from Heat Transfer Principles'. International Journal of Biometeorology 39 (1): 46-52. https://doi.org/10.1007/BF01320893.

Brown, R.D., Gillespie, T.J. 1986. ‘Estimating Outdoor Thermal Comfort Using a Cylindrical Radiation Thermometer and an Energy Budget Model’. International Journal of Biometeorology 30 (1): 43-52. https://doi.org/10.1007/BF02192058.

Bröde, Peter, Dusan Fiala, Krzysztof Blazejczyk, et al. 2009. CALCULATING UTCI EQUIVALENT TEMPERATURE. January 1.

Crank, Peter J., Ariane Middel, Melissa Wagner, Dani Hoots, Martin Smith, and Anthony Brazel. 2020. 'Validation of Seasonal Mean Radiant Temperature Simulations in Hot Arid Urban Climates'. Science of The Total Environment 749 (December): 141392. https://doi.org/10.1016/j.scitotenv.2020.141392.

Friedlingstein, Pierre, Michael O'Sullivan, Matthew W. Jones, Robbie M. Andrew, Dorothee C. E. Bakker, Judith Hauck, Peter Landschützer, et al. 2023. 'Global Carbon Budget 2023'. Earth System Science Data 15 (12): 5301-69. https://doi.org/10.5194/essd-15-5301-2023.

Höppe, P. 1999. ‘The Physiological Equivalent Temperature - a Universal Index for the Biometeorological Assessment of the Thermal Environment’. International Journal of Biometeorology 43 (2): 71-75. https://doi.org/10.1007/s004840050118.

Martínez-Solanas, Èrica, Marcos Quijal-Zamorano, Hicham Achebak, Desislava Petrova, Jean-Marie Robine, François R Herrmann, Xavier Rodó, and Joan Ballester. 2021. 'Projections of Temperature-Attributable Mortality in Europe: A Time Series Analysis of 147 Contiguous Regions in 16 Countries'. The Lancet Planetary Health 5 (7): e446-54. https://doi.org/10.1016/S2542-5196(21)00150-9.

Matzarakis, A., Mayer, H. 1996. ‘Another Kind of Environmental Stress: Thermal Stress’. WHO Newsletter 18: 7-10.

Matzarakis, A. 2008., Amelung, B. "Physiological Equivalent Temperature as Indicator for Impacts of Climate Change on Thermal Comfort of Humans." In Seasonal Forecasts, Climatic Change and Human Health, edited by Thomson, M.C., Garcia-Herrera, R., Beniston, M., 161-172. Springer. https://doi.org/10.1007/978-1-4020-6877-5_10.

Mavrogianni, Anna, Ioanna Tsoulou, Clare Heaviside, Eleni Oikonomou, Giorgos Petrou, Phil Symonds, Mike Davies, Jonathon Taylor, Ai Milojevic, and Paul Wilkinson. 2022. 'Urban Overheating and Impact on Health: An Introduction'. In Urban Overheating: Heat Mitigation and the Impact on Health, edited by Nasrin Aghamohammadi and Mat Santamouris, 1-20. Singapore: Springer Nature. https://doi.org/10.1007/978-981-19-4707-0_1.

OFCM. 2003. Report on Wind Chill Temperature and Extreme Heat Indices: Evaluation and Improvement Projects (FCM-R19-2003). Office of the Federal Coordinator for Meteorological Services and Supporting Research. https://weather.missouri.edu/gcc/OFCMWindchillReport.pdf.

Osczevski, R.J., Bluestein, M. 2005. ‘The New Wind Chill Equivalent Temperature Chart’. Bulletin of the American Meteorological Society 86 (10): 1453-1458. https://doi.org/10.1175/BAMS-86-10-1453.

Pickup, J. 2000., de Dear, R. "An Outdoor Thermal Comfort Index (OUT_SET*) - Part I - The Model and Its Assumptions." In de Dear, R., Kalma, J., Oke, T., Auliciems, A. (Eds.),

Biometeorology and Urban Climatology at the Turn of the Millennium, 279-283. World Meteorological Organization.

Thom, E.C. "The Discomfort Index." Weatherwise 12(2) (1959): 57-61. https://doi.org/10.1080/00431672.1959.9926960.

9.4.2 Physiological and meteorological foundations of comfort metrics

ASHRAE. 2010. ANSI/ASHRAE Standard 55-2010: Thermal Environmental Conditions for Human Occupancy. ASHRAE.

ASHRAE. 2017. ANSI/ASHRAE Standard 55-2017: Thermal Environmental Conditions for Human Occupancy. Atlanta, GA: American Society of Heating, Refrigerating and Air-Conditioning Engineers.

Avantaggiato, M., Ladisa, G., Lapenna, L., Capozzoli, A. "Unlocking thermal comfort in transitional spaces: A field study in three Italian shopping centres." Building and Environment 188 (2021): 107428. https://doi.org/10.1016/j.buildenv.2020.107428.

Brown, R.D., Gillespie, T.J. 1986. 'Estimating Outdoor Thermal Comfort Using a Cylindrical Radiation Thermometer and an Energy Budget Model'. International Journal of Biometeorology 30 (1): 43-52. https://doi.org/10.1007/BF02192058.

Bruse, M. 2000. "Assessing Thermal Comfort in Urban Environments Using an Integrated Dynamic Microscale Biometeorological Model System." Proceedings of the AMS Conference (AugDavis_3urban). https://ams.confex.com/ams/AugDavis/techprogram/paper_15005.htm.

Chatzidimitriou, Angeliki, and Simos Yannas. 2016. 'Microclimate Design for Open Spaces: Ranking Urban Design Effects on Pedestrian Thermal Comfort in Summer'. Sustainable Cities and Society 26 (October): 27-47. https://doi.org/10.1016/j.scs.2016.05.004.

de Dear, R.J., Brager, G.S. 2002. 'Thermal comfort in naturally ventilated buildings: revisions to ASHRAE Standard 55'. Energy and Buildings 34 (6): 549-561. https://doi.org/10.1016/S0378-7788 (02)00005-1.

Desogus, G., Di Benedetto, S., Ricciu, R. "The use of adaptive thermal comfort models to evaluate the summer performance of a Mediterranean earth building." Energy and Buildings 104 (2015): 350-359. https://doi.org/10.1016/j.enbuild.2015.07.020.

Diz-Mellado, E., Nikolopoulou, M., López-Cabeza, V.P., Rivera-Gómez, C., Galán-Marín, C. "Extending the adaptive thermal comfort models for courtyards." Building and Environment 203 (2021): 108094. https://doi.org/10.1016/j.buildenv.2021.108094.

Diz-Mellado, E., Tablada, A., Gaitan, C., Soriano, C. "Thermal comfort thresholds for enclosed transitional spaces: in-between courtyards of the Mediterranean area." Urban Climate 47 (2023): 101369. https://doi.org/10.1016/j.uclim.2023.101369.

Diz-Mellado, Eduardo, Marialena Nikolopoulou, Victoria Patricia López-Cabeza, Carlos Rivera-Gómez, and Carmen Galán-Marín. 2023. 'Cross-Evaluation of Thermal Comfort in Semi-Outdoor Spaces According to Geometry in Southern Spain'. Urban Climate 49 (May): 101491. https://doi.org/10.1016/j.uclim.2023.101491.

Diz-Mellado, Eduardo, Victoria Patricia López-Cabeza, Carlos Rivera-Gómez, and Carmen Galán-Marín. 2023. 'Seasonal Analysis of Thermal Comfort in Mediterranean Social Courtyards: A Comparative Study'. Journal of Building Engineering 78 (November): 107756. https://doi.org/10.1016/j.jobe.2023.107756.

Fanger, P. 1970. O. Thermal Comfort: Analysis and Applications in Environmental Engineering. Danish Technical Press.

Fanger, P.O. 1970. Thermal Comfort. Analysis and Applications in Environmental Engineering.

Hendriks, Eefje, Noorullah Kuchai, Carolina Pereira Marghidan, and Anna Conzatti. 2025. 'Adapting Housing Design Tools for Indoor Thermal Comfort to Changing Climates'. Sustainability 17 (6): 2511. https://doi.org/10.3390/su17062511.

International Organization for Standardization (ISO). 2005. ISO 7730:2005 - Ergonomics of the Thermal Environment: Analytical Determination and Interpretation of Thermal Comfort Using Calculation of the PMV and PPD Indices and Local Thermal Comfort Criteria. Geneva: ISO.

Ji, Yuchen, Jusheng Song, and Pengyuan Shen. "A Review of Studies and Modelling of Solar Radiation on Human Thermal Comfort in Outdoor Environment." Building and Environment 214 (2022): 108891. https://doi.org/10.1016/j.buildenv.2022.108891.

Johansson, Erik. "Influence of Urban Geometry on Outdoor Thermal Comfort in a Hot Dry Climate: A Study in Fez, Morocco." Building and Environment 41(10) (2006): 1326-38. https://doi.org/10.1016/j.buildenv.2005.05.022.

Kastner, Patrick, and Timur Dogan. 2021. 'Eddy3D: A Toolkit for Decoupled Outdoor Thermal Comfort Simulations in Urban Areas'. Building and Environment 212 (December): 108639. https://doi.org/10.1016/j.buildenv.2021.108639.

López-Cabeza, V.P., Galán-Marín, C., Rivera-Gómez, C., Roa-Fernández, J. "Albedo influence on the microclimate and thermal comfort of courtyards under Mediterranean hot summer climate conditions." Sustainable Cities and Society 81 (2022): 103872. https://doi.org/10.1016/j.scs.2022.103872.

Luo, M., Zhou, X., Zhu, Y., Sundell, J. "Revisiting an Overlooked Parameter in Thermal Comfort Studies, the Metabolic Rate." Energy and Buildings 118 (2016): 152-159. https://doi.org/10.1016/j.enbuild.2016.02.041.

Martinelli, L., Lin, T.-P., Matzarakis, A. "Assessment of the Influence of Daily Shadings Pattern on Human Thermal Comfort and Attendance in Rome during Summer Period." Building and Environment 92 (2015): 30-38. https://doi.org/10.1016/j.buildenv.2015.04.013.

Matzarakis, A. 2008., Amelung, B. "Physiological Equivalent Temperature as Indicator for Impacts of Climate Change on Thermal Comfort of Humans." In Seasonal Forecasts, Climatic Change and Human Health, edited by Thomson, M.C., Garcia-Herrera, R., Beniston, M., 161-172. Springer. https://doi.org/10.1007/978-1-4020-6877-5_10.

Mayer, Helmut, Jutta Holst, Paul Dostal, Florian Imbery, and Dirk Schindler. 2008. 'Human Thermal Comfort in Summer within an Urban Street Canyon in Central Europe'. Meteorologische Zeitschrift 17 (3): 241-50. https://doi.org/10.1127/0941-2948/2008/0285.

Morales, Richard Dean, Amaryllis Audenaert, and Stijn Verbeke. 2025. 'Thermal Comfort and Indoor Overheating Risks of Urban Building Stock - A Review of Modelling Methods and Future Climate Challenges'. Building and Environment 269 (February):112363. https://doi.org/10.1016/j.buildenv.2024.112363.

Nasrollahi, Nazanin, Yasaman Namazi, and Mohammad Taleghani. "The Effect of Urban Shading and Canyon Geometry on Outdoor Thermal Comfort in Hot Climates: A Case Study of Ahvaz, Iran." Sustainable Cities and Society 65 (2021): 102638. https://doi.org/10.1016/j.scs.2020.102638.

Nicol, J.F., Humphreys, M.A. 2002. 'Adaptive thermal comfort and sustainable thermal standards for buildings'. Energy and Buildings 34 (6): 563-572. https://doi.org/10.1016/S0378-7788 (02)00006-3.

Nicol, J.F., Humphreys, M.A., and Roaf, S. 2012. Adaptive Thermal Comfort: Principles and Practice. Routledge.

Nikolopoulou, M., Baker, N., Steemers, K. 2001. 'Thermal Comfort in Outdoor Urban Spaces: Understanding the Human Parameter'. Solar Energy 70 (3): 227-35. https://doi.org/10.1016/S0038-092X(00)00093-1.

Nikolopoulou, M., Steemers, K. 2003. 'Thermal comfort and psychological adaptation as a guide for designing urban spaces'. Energy and Buildings 35 (1): 95-101. https://doi.org/10.1016/S0378-7788 (02)00084-1.

Nikolopoulou, M., Lykoudis, S. "Thermal Comfort in Outdoor Urban Spaces: Analysis across Different European Countries." Building and Environment 41(11) (2006): 1455-70. https://doi.org/10.1016/j.buildenv.2005.05.031.

Pickup, J. 2000., de Dear, R. "An Outdoor Thermal Comfort Index (OUT_SET*) - Part I - The Model and Its Assumptions." In de Dear, R., Kalma, J., Oke, T., Auliciems, A. (Eds.), Biometeorology and Urban Climatology at the Turn of the Millennium, 279-283. World Meteorological Organization.

Vellei, Matteo, Andrea Peretti, Stefano Le Dréau, Elena De Carli, and Stefano P. Corgnati. "The Influence of Relative Humidity on Adaptive Thermal Comfort." Building and Environment 126 (2017): 1098-1111. https://doi.org/10.1016/j.buildenv.2017.10.005.

9.4.3 UTCI: theoretical background, assumptions and domain of validity

Blazejczyk, Krzysztof, Peter Bröde, Dusan Fiala, George Havenith, Ingvar Holmér, Gerd Jendritzky, Bernhard Kampmann, and Anna Błażejczyk. 2010. 'Principles of the New Universal Thermal Climate Index (UTCI) and Its Application to Bioclimatic Research in European Scale'. Miscellanea Geographica 14: 91-102. https://doi.org/10.2478/mgrsd-2010-0009.

Blazejczyk, Krzysztof, Yoram Epstein, Gerd Jendritzky, Henning Staiger, and Birger Tinz. 2012. 'Comparison of UTCI to Selected Thermal Indices'. International Journal of Biometeorology 56 (3): 515-535. https://doi.org/10.1007/s00484-011-0453-2.

Bröde, Peter, Dusan Fiala, Krzysztof Blazejczyk, et al. 2009. CALCULATING UTCI EQUIVALENT TEMPERATURE. January 1.

Bröde, P., D. Fiala, K. Blazejczyk, Y. Epstein, I. Holmér, G. Jendritzky, B. Kampmann, B. Richards, and H. Rintamäki. 2012. 'Deriving the Operational Procedure for the Universal Thermal Climate Index (UTCI)'. International Journal of Biometeorology 56 (3): 481-494. https://doi.org/10.1007/s00484-011-0454-1.

Błażejczyk, Krzysztof, and Magdalena Kuchcik. 2021. 'UTCI Applications in Practice (Methodological Questions)'. Geographia Polonica 94 (2): 153-165. https://doi.org/10.7163/gpol.0198.

Fiala, D., Havenith, G., Bröde, P., Kampmann, B., Jendritzky, G. 2012. 'UTCI-Fiala Multi-Node Model of Human Heat Transfer and Temperature Regulation'. International Journal of Biometeorology 56 (3): 429-441. https://doi.org/10.1007/s00484-011-0424-7.

Havenith, G., Fiala, D., Błażejczyk, K., Richards, M., Bröde, P., Holmér, I., Rintamäki, H., Benshabat, Y., Jendritzky, G. 2012. 'The UTCI-Clothing Model'. International Journal of Biometeorology 56 (3): 461-470. https://doi.org/10.1007/s00484-011-0451-4.

Jendritzky, G., R. de Dear, and G. Havenith. 2012. 'UTCI-Why Another Thermal Index?'. International Journal of Biometeorology 56 (3): 421-428. https://doi.org/10.1007/s00484-011-0513-7.

Psikuta, A., Fiala, D., Laschewski, G., Jendritzky, G., Richards, M., Błażejczyk, K., Mekjavic, I.B., Rintamäki, H., de Dear, R., Havenith, G. 2012. 'Validation of the Fiala Multi-Node Thermophysiological Model for UTCI Application'. International Journal of Biometeorology 56 (3): 443-460. https://doi.org/10.1007/s00484-011-0450-5.

9.4.4 Limitations and comparative use of thermal comfort indices

Blazejczyk, Krzysztof, Yoram Epstein, Gerd Jendritzky, Henning Staiger, and Birger Tinz. 2012. 'Comparison of UTCI to Selected Thermal Indices'. International Journal of Biometeorology 56 (3): 515-535. https://doi.org/10.1007/s00484-011-0453-2.

Błażejczyk, Krzysztof, and Magdalena Kuchcik. 2021. 'UTCI Applications in Practice (Methodological Questions)'. Geographia Polonica 94 (2): 153-165. https://doi.org/10.7163/gpol.0198.

Diz-Mellado, Eduardo, Marialena Nikolopoulou, Victoria Patricia López-Cabeza, Carlos Rivera-Gómez, and Carmen Galán-Marín. 2023. 'Cross-Evaluation of Thermal Comfort in Semi-Outdoor Spaces According to Geometry in Southern Spain'. Urban Climate 49 (May): 101491. https://doi.org/10.1016/j.uclim.2023.101491.

Farajzadeh, Hassan, Mohammad Saligheh, Bohloul Alijani, and Andreas Matzarakis. 2015. 'Comparison of Selected Thermal Indices in the Northwest of Iran'. Natural Environment Change 1 (1): 1-20.

9.5 Microclimate, Built Environment and Heat-Exchange Mechanisms

9.5.1 Urban form, geometry and radiative environments

Alexandri, Eleftheria, and Phil Jones. "Temperature Decreases in an Urban Canyon due to Green Walls and Green Roofs in Diverse Climates." Building and Environment, Part Special: Building Performance Simulation 43(4) (2008): 480-93. https://doi.org/10.1016/j.buildenv.2006.10.055.

ASHRAE. 1997. ASHRAE Handbook-Fundamentals. American Society of Heating, Refrigerating and Air-Conditioning Engineers.

Assimakopoulos, V.D, H.M ApSimon, and N Moussiopoulos. 2003. 'A Numerical Study of Atmospheric Pollutant Dispersion in Different Two-Dimensional Street Canyon Configurations'. Atmospheric Environment 37 (29): 4037-49. https://doi.org/10.1016/S1352-2310 (03)00533-8.

Aynsley, R.M., Melbourne, W., Vickery, B.J. 1977. Architectural Aerodynamics. Applied Science Publishers, London.

Brager, G.S., de Dear, R.J. 1998. 'Thermal adaptation in the built environment: a literature review'. Energy and Buildings 27 (1): 83-96. https://doi.org/10.1016/S0378-7788 (97)00053-4.

Brown, R.D., Gillespie, T.J. 1986. 'Estimating Outdoor Thermal Comfort Using a Cylindrical Radiation Thermometer and an Energy Budget Model'. International Journal of Biometeorology 30 (1): 43-52. https://doi.org/10.1007/BF02192058.

Brown, Robert D. 2010. Design With Microclimate: The Secret to Comfortable Outdoor Space. Island Press.

Calama-González, C., et al. "Thermal insulation impact on overheating vulnerability reduction in Mediterranean dwellings." Heliyon 9(5) (2023): e16102. https://doi.org/10.1016/j.heliyon.2023.e16102.

Chatzidimitriou, Angeliki, and Simos Yannas. 2016. 'Microclimate Design for Open Spaces: Ranking Urban Design Effects on Pedestrian Thermal Comfort in Summer'. Sustainable Cities and Society 26 (October): 27-47. https://doi.org/10.1016/j.scs.2016.05.004.

Crank, Peter J., Ariane Middel, Melissa Wagner, Dani Hoots, Martin Smith, and Anthony Brazel. 2020. 'Validation of Seasonal Mean Radiant Temperature Simulations in Hot Arid Urban Climates'. Science of The Total Environment 749 (December): 141392. https://doi.org/10.1016/j.scitotenv.2020.141392.

Cui, Zhiqiang, Xiaoming Cai, and Chris J. Baker. 2004. 'Large-Eddy Simulation of Turbulent Flow in a Street Canyon'. Quarterly Journal of the Royal Meteorological Society 130 (599): 1373-94. https://doi.org/10.1256/qj.02.150.

de Dear, R.J., Arens, E., Hui, Z., Oguro, M. 1997. 'Convective and radiative heat transfer coefficients for individual human body segments'. International Journal of Biometeorology 40 (3): 141-156. https://doi.org/10.1007/s004840050035.

Diz-Mellado, Eduardo, Marialena Nikolopoulou, Victoria Patricia López-Cabeza, Carlos Rivera-Gómez, and Carmen Galán-Marín. 2023. 'Cross-Evaluation of Thermal Comfort in Semi-

Outdoor Spaces According to Geometry in Southern Spain'. Urban Climate 49 (May): 101491. https://doi.org/10.1016/j.uclim.2023.101491.

Djedjig, Rabah, Emmanuel Bozonnet, and Rafik Belarbi. 2015. ‘Experimental Study of the Urban Microclimate Mitigation Potential of Green Roofs and Green Walls in Street Canyons’. International Journal of Low-Carbon Technologies 10 (1): 34-44. https://doi.org/10.1093/ijlct/ctt019.

Djedjig, Rabah, Emmanuel Bozonnet, and Rafik Belarbi. "Modeling Green Wall Interactions with Street Canyons for Building Energy Simulation in Urban Context." Urban Climate 16 (2016): 75-85. https://doi.org/10.1016/j.uclim.2015.12.003.

Gartland, Lisa. 2012. Heat Islands: Understanding and Mitigating Heat in Urban Areas. Earthscan.

Givoni, B. 1998. Climate Considerations in Building and Urban Design. John Wiley & Sons, New York.

Givoni, B. 1998. Climate Considerations in Building and Urban Design. John Wiley & Sons.

Guo, Hongshan, Dorit Aviv, Mauricio Loyola, Eric Teitelbaum, Nicholas Houchois, and Forrest Meggers. "On the Understanding of the Mean Radiant Temperature within Both the Indoor and Outdoor Environment, a Critical Review." Renewable and Sustainable Energy Reviews 117 (2020): 109207. https://doi.org/10.1016/j.rser.2019.06.014.

Hathway, E. A., and S. Sharples. "The Interaction of Rivers and Urban Form in Mitigating the Urban Heat Island Effect: A UK Case Study." Building and Environment 58 (2012): 14-22. https://doi.org/10.1016/j.buildenv.2012.06.013.

Herrmann, Jan, and Andreas Matzarakis. 2011. ‘Mean Radiant Temperature in Idealised Urban Canyons-examples from Freiburg, Germany’. International Journal of Biometeorology 56 (1): 199-203. https://doi.org/10.1007/s00484-010-0394-1.

Holst, Jutta, and Helmut Mayer. 2011. 'Impacts of Street Design Parameters on Human-Biometeorological Variables'. Meteorologische Zeitschrift, October 1, 541-52. https://doi.org/10.1127/0941-2948/2011/0254.

Houghten, F.C., Yagloglou, C.P. 1923. ‘Determining Lines of Equal Comfort’. Journal of the American Society of Heating and Ventilating Engineers 29: 165-176.

Jendritzky, G., and W. Nübler. 1981. 'A Model Analysing the Urban Thermal Environment in Physiologically Significant Terms'. Archives for Meteorology, Geophysics, and Bioclimatology, Series B 29 (4): 313-26. https://doi.org/10.1007/BF02263308.

Johansson, Erik. "Influence of Urban Geometry on Outdoor Thermal Comfort in a Hot Dry Climate: A Study in Fez, Morocco." Building and Environment 41(10) (2006): 1326-38. https://doi.org/10.1016/j.buildenv.2005.05.022.

Kastner, Patrick, and Timur Dogan. 2021. 'Eddy3D: A Toolkit for Decoupled Outdoor Thermal Comfort Simulations in Urban Areas'. Building and Environment 212 (December): 108639. https://doi.org/10.1016/j.buildenv.2021.108639.

Krautheim, Mareike, Ralf Pasel, Sven Pfeiffer, and Joachim Schultz-Granberg. 2014. City and Wind. Climate as an Architectural Instrument. DOM publishers.

Liu, Fan, Hua Qian, Xiaohong Zheng, Lun Zhang, and Wenqing Liang. 2017. 'Numerical Study on the Urban Ventilation in Regulating Microclimate and Pollutant Dispersion in Urban Street Canyon: A Case Study of Nanjing New Region, China'. Atmosphere 8 (9): 164. https://doi.org/10.3390/atmos8090164.

Maiullari, D, B Gherri, C Finizza, M Maretto, and E Naboni. 2021. 'Climate Change and Indoor Temperature Variation in Venetian Buildings: The Role of Density and Urban Form'. Journal of Physics: Conference Series 2042 (1): 012060. https://doi.org/10.1088/1742-6596/2042/1/012060.

Martinelli, L., Lin, T.-P., Matzarakis, A. "Assessment of the Influence of Daily Shadings Pattern on Human Thermal Comfort and Attendance in Rome during Summer Period." Building and Environment 92 (2015): 30-38. https://doi.org/10.1016/j.buildenv.2015.04.013.

Mayer, Helmut, Jutta Holst, Paul Dostal, Florian Imbery, and Dirk Schindler. 2008. 'Human Thermal Comfort in Summer within an Urban Street Canyon in Central Europe'. Meteorologische Zeitschrift 17 (3): 241-50. https://doi.org/10.1127/0941-2948/2008/0285.

Nasrollahi, Nazanin, Yasaman Namazi, and Mohammad Taleghani. "The Effect of Urban Shading and Canyon Geometry on Outdoor Thermal Comfort in Hot Climates: A Case Study of Ahvaz, Iran." Sustainable Cities and Society 65 (2021): 102638. https://doi.org/10.1016/j.scs.2020.102638.

Nikolopoulou, Marialena, and Spyros Lykoudis. "Use of Outdoor Spaces and Microclimate in a Mediterranean Urban Area." Building and Environment 42(10) (2007): 3691-3707. https://doi.org/10.1016/j.buildenv.2006.09.008.

Oke, T.R. 1979. Review of Urban Climatology, 1973-1976. World Meteorological Organization, Technical Note No. 169 (WMO-No. 539), Geneva.

Oke, T.R. 1987. Boundary Layer Climates (2nd ed.). Routledge, London.

Oke, T. R. 1988. 'Street Design and Urban Canopy Layer Climate'. Energy and Buildings 11 (1-3): 103-13. https://doi.org/10.1016/0378-7788 (88)90026-6.

Oke, T.R., G. Mills, A. Christen, and J.A. Voogt. 2017. Urban Climates. Cambridge: Cambridge University Press. https://doi.org/10.1017/9781139016476.

Olgyay, V. 1963. Design with Climate: Bioclimatic Approach to Architectural Regionalism. Princeton, NJ: Princeton University Press.

Ono, Takeshi, Shuzo Murakami, Ryozo Ooka, and Toshiaki Omori. "Numerical and Experimental Study on Convective Heat Transfer of the Human Body in the Outdoor Environment." Journal of Wind Engineering and Industrial Aerodynamics, 4th International Symposium on Computational Wind Engineering (CWE2006) 96(10-11) (2008): 1719-32. https://doi.org/10.1016/j.jweia.2008.02.007.

Parsons, Ken. 2002. Human Thermal Environments: The Effects of Hot, Moderate, and Cold Environments on Human Health, Comfort and Performance, Second Edition. CRC Press.

Parsons, Ken. 2014. Human Thermal Environments: The Effects of Hot, Moderate, and Cold Environments on Human Health, Comfort, and Performance, Third Edition. 3rd edn. CRC Press. https://doi.org/10.1201/b16750.

Pickup, J. 2000., de Dear, R. "An Outdoor Thermal Comfort Index (OUT_SET*) - Part I - The Model and Its Assumptions." In de Dear, R., Kalma, J., Oke, T., Auliciems, A. (Eds.), Biometeorology and Urban Climatology at the Turn of the Millennium, 279-283. World Meteorological Organization.

Santamouris, M., Asimakopoulos, D. (Eds.). 1996. Passive Cooling of Buildings. James & James (Science Publishers), London.

Santamouris, Mattheos, and Dionysia Kolokotsa. 2013. 'Passive Cooling Dissipation Techniques for Buildings and Other Structures: The State of the Art'. Energy and Buildings 57 (February): 74-94. https://doi.org/10.1016/j.enbuild.2012.11.002.

Schmid, H. P., H. A. Cleugh, C. S. B. Grimmond, and T. R. Oke. 1991. 'Spatial Variability of Energy Fluxes in Suburban Terrain'. Boundary-Layer Meteorology 54 (3): 249-276. https://doi.org/10.1007/BF00183956.

Schöneberger, P., Sinsel, T., Ouyang, W., Tan, Z., Bruse, M., and Simon, H. 2025. "Enhancing urban microclimate simulations: Validating ENVI-met's accuracy in modeling multi-directional radiative fluxes and mean radiant temperature in subtropical Hong Kong." Building and Environment 284 (1 October): 113475. https://doi.org/10.1016/j.buildenv.2025.113475.

Sherwood, S.C., Huber, M. 2010. 'An adaptability limit to climate change due to heat stress'. Proceedings of the National Academy of Sciences 107 (21): 9552-9555. https://doi.org/10.1073/pnas.0913352107.

Siple, P.A., Passel, C.F. 1945. 'Measurements of Dry Atmospheric Cooling in Subfreezing Temperatures'. Proceedings of the American Philosophical Society 89 (1): 177-199.

Tansey, Etain, and Christopher Johnson. "Recent Advances in Thermoregulation." Advances in Physiology Education 39 (2015): 139-48. https://doi.org/10.1152/advan.00126.2014.

Tribuiani, Chiara, Luca Tarabelli, Serena Summa, and Costanzo Di Perna. 2020. 'Thermal Performance of a Massive Wall in the Mediterranean Climate: Experimental and Analytical Research'. Applied Sciences 10 (13): 4611. https://doi.org/10.3390/app10134611.

Vardoulakis, Sotiris, Bernard E. A Fisher, Koulis Pericleous, and Norbert Gonzalez-Flesca. 2003. 'Modelling Air Quality in Street Canyons: A Review'. Atmospheric Environment 37 (2): 155-82. https://doi.org/10.1016/S1352-2310 (02)00857-9.

9.5.2 Surface properties, materials and thermal mass

Asaeda, Takashi, and Vu Thanh Ca. 2000. 'Characteristics of Permeable Pavement during Hot Summer Weather and Impact on the Thermal Environment'. Building and Environment 35 (4): 363-75. https://doi.org/10.1016/S0360-1323 (99)00020-7.

Balaras, C.A. 1996. 'The role of thermal mass on the cooling load of buildings. An overview of computational methods'. Energy and Buildings 24 (1): 1-10. https://doi.org/10.1016/0378-7788 (95)00956-6.

Block, Alexander, Klaus Keuler, and Eberhard Schaller. 2004. ‘Impacts of Anthropogenic Heat on Regional Climate Patterns: IMPACTS OF ANTHROPOGENIC HEAT’. Geophysical Research Letters 31 (12): n/a-n/a. https://doi.org/10.1029/2004GL019852.

Chen, Bing, Li Dong, Guangyu Shi, Li-Juan Li, and Liang-Fu Chen. 2014. ‘Anthropogenic Heat Release: Estimation of Global Distribution and Possible Climate Effect’. Journal of the Meteorological Society of Japan. Ser. II 92A, no 0: 157-65. https://doi.org/10.2151/jmsj.2014-A10.

Doulos, L, M Santamouris, and I Livada. "Passive Cooling of Outdoor Urban Spaces. The Role of Materials." Solar Energy 77(2) (2004): 231-49. https://doi.org/10.1016/j.solener.2004.04.005.

Hendel, Martin, and Laurent Royon. "The Effect of Pavement-Watering on Subsurface Pavement Temperatures." Urban Climate 14 (2015): 650-54. https://doi.org/10.1016/j.uclim.2015.10.006.

Iamarino, Mario, Sean Beevers, and C. S. B. Grimmond. 2012. ‘High-Resolution (Space, Time) Anthropogenic Heat Emissions: London 1970-2025’. International Journal of Climatology 32 (11): 1754-67. https://doi.org/10.1002/joc.2390.

López-Cabeza, V.P., Galán-Marín, C., Rivera-Gómez, C., Roa-Fernández, J. "Albedo influence on the microclimate and thermal comfort of courtyards under Mediterranean hot summer climate conditions." Sustainable Cities and Society 81 (2022): 103872. https://doi.org/10.1016/j.scs.2022.103872.

Roberts, Sarah M., T. R. Oke, C. S. B. Grimmond, and J. A. Voogt. 2006. ‘Comparison of Four Methods to Estimate Urban Heat Storage’. Journal of Applied Meteorology and Climatology 45 (12): 1766-1781. https://doi.org/10.1175/JAM2432.1.

Sailor, David J., and Hongli Fan. 2002. ‘Modeling the Diurnal Variability of Effective Albedo for Cities’. Atmospheric Environment 36 (4): 713-25. https://doi.org/10.1016/S1352-2310(01)00452-6.

Sailor, David J., and Lu Lu. "A Top-down Methodology for Developing Diurnal and Seasonal Anthropogenic Heating Profiles for Urban Areas." Atmospheric Environment 38(17) (2004): 2737-48. https://doi.org/10.1016/j.atmosenv.2004.01.034.

Sailor, David J., Matei Georgescu, Jeffrey M. Milne, and Melissa A. Hart. "Development of a National Anthropogenic Heating Database with an Extrapolation for International Cities." Atmospheric Environment 118 (2015): 7-18. https://doi.org/10.1016/j.atmosenv.2015.07.016.

Tsoka, Stella, Katerina Tsikaloudaki, and Theodoros Theodosiou. 2018. 'Analyzing the ENVI-Met Microclimate Model's Performance and Assessing Cool Materials and Urban Vegetation Applications-A Review'. Sustainable Cities and Society 43 (August). https://doi.org/10.1016/j.scs.2018.08.009.

9.5.3 Vegetation, water and coupled microclimatic processes

Alexandri, Eleftheria, and Phil Jones. "Temperature Decreases in an Urban Canyon due to Green Walls and Green Roofs in Diverse Climates." Building and Environment, Part Special:

Building Performance Simulation 43(4) (2008): 480-93. https://doi.org/10.1016/j.buildenv.2006.10.055.

Berardi, Umberto. "The Outdoor Microclimate Benefits and Energy Saving Resulting from Green Roofs Retrofits." Energy and Buildings 121 (2016): 217-29. https://doi.org/10.1016/j.enbuild.2016.03.021.

Cao, Xin, Akio Onishi, Jin Chen, and Hidefumi Imura. "Quantifying the Cool Island Intensity of Urban Parks Using ASTER and IKONOS Data." Landscape and Urban Planning 96(4) (2010): 224-31. https://doi.org/10.1016/j.landurbplan.2010.03.008.

Chang, Chi-Ru, and Ming-Huang Li. "Effects of Urban Parks on the Local Urban Thermal Environment." Urban Forestry & Urban Greening 13(4) (2014): 672-81. https://doi.org/10.1016/j.ufug.2014.08.001.

Diz-Mellado, E., Nikolopoulou, M., López-Cabeza, V.P., Rivera-Gómez, C., Galán-Marín, C. "Extending the adaptive thermal comfort models for courtyards." Building and Environment 203 (2021): 108094. https://doi.org/10.1016/j.buildenv.2021.108094.

Diz-Mellado, Eduardo, Marialena Nikolopoulou, Victoria Patricia López-Cabeza, Carlos Rivera-Gómez, and Carmen Galán-Marín. 2023. 'Cross-Evaluation of Thermal Comfort in Semi-Outdoor Spaces According to Geometry in Southern Spain'. Urban Climate 49 (May): 101491. https://doi.org/10.1016/j.uclim.2023.101491.

Diz-Mellado, Eduardo, Victoria Patricia López-Cabeza, Carlos Rivera-Gómez, and Carmen Galán-Marín. 2023. 'Seasonal Analysis of Thermal Comfort in Mediterranean Social Courtyards: A Comparative Study'. Journal of Building Engineering 78 (November): 107756. https://doi.org/10.1016/j.jobe.2023.107756.

Djedjig, Rabah, Emmanuel Bozonnet, and Rafik Belarbi. 2015. 'Experimental Study of the Urban Microclimate Mitigation Potential of Green Roofs and Green Walls in Street Canyons'. International Journal of Low-Carbon Technologies 10 (1): 34-44. https://doi.org/10.1093/ijlct/ctt019.

Djedjig, Rabah, Emmanuel Bozonnet, and Rafik Belarbi. "Modeling Green Wall Interactions with Street Canyons for Building Energy Simulation in Urban Context." Urban Climate 16 (2016): 75-85. https://doi.org/10.1016/j.uclim.2015.12.003.

Feyisa, Gudina Legese, Klaus Dons, and Henrik Meilby. "Efficiency of Parks in Mitigating Urban Heat Island Effect: An Example from Addis Ababa." Landscape and Urban Planning 123 (2014): 87-95. https://doi.org/10.1016/j.landurbplan.2013.12.008.

Hathway, E. A., and S. Sharples. "The Interaction of Rivers and Urban Form in Mitigating the Urban Heat Island Effect: A UK Case Study." Building and Environment 58 (2012): 14-22. https://doi.org/10.1016/j.buildenv.2012.06.013.

Hendel, Martin, and Laurent Royon. "The Effect of Pavement-Watering on Subsurface Pavement Temperatures." Urban Climate 14 (2015): 650-54. https://doi.org/10.1016/j.uclim.2015.10.006.

López-Cabeza, V.P., Galán-Marín, C., Rivera-Gómez, C., Roa-Fernández, J. "Albedo influence on the microclimate and thermal comfort of courtyards under Mediterranean hot summer

climate conditions." Sustainable Cities and Society 81 (2022): 103872. https://doi.org/10.1016/j.scs.2022.103872.

Manteghi, Golnoosh, Hasanuddin Bin Limit, and Dilshan Remaz. 2015. 'Water Bodies an Urban Microclimate: A Review'. Modern Applied Science 9, no. 6. https://doi.org/10.5539/mas.v9n6p1.

Mazzali, Ugo, Fabio Peron, Piercarlo Romagnoni, Riccardo M. Pulselli, and Simone Bastianoni. "Experimental Investigation on the Energy Performance of Living Walls in a Temperate Climate." Building and Environment 64 (2013): 57-66. https://doi.org/10.1016/j.buildenv.2013.03.005.

Murakawa, Saburo, Takeshi Sekine, Ken-ichi Narita, and Daisaku Nishina. 1991. 'Study of the Effects of a River on the Thermal Environment in an Urban Area'. Energy and Buildings 16 (3-4): 993-1001. https://doi.org/10.1016/0378-7788 (91)90094-J.

Nishimura, Nobuya, Tomohiro Nomura, Hiroyuki Iyota, and Shinya Kimoto. 1998. 'NOVEL WATER FACILITIES FOR CREATION OF COMFORTABLE URBAN MICROMETEOROLOGY'. Solar Energy 64 (4-6): 197-207. https://doi.org/10.1016/S0038-092X(98)00116-9.

Oke, T. R. 1988. 'Street Design and Urban Canopy Layer Climate'. Energy and Buildings 11 (1-3): 103-13. https://doi.org/10.1016/0378-7788 (88)90026-6.

Saaroni, Hadas, and Baruch Ziv. 2003. 'The Impact of a Small Lake on Heat Stress in a Mediterranean Urban Park: The Case of Tel Aviv, Israel'. International Journal of Biometeorology 47 (3): 156-65. https://doi.org/10.1007/s00484-003-0161-7.

Semaan, Mary, and Annie Pearce. "Assessment of the Gains and Benefits of Green Roofs in Different Climates." Procedia Engineering, ICSDEC 2016 - Integrating Data Science, Construction and Sustainability 145 (2016): 333-39. https://doi.org/10.1016/j.proeng.2016.04.083.

Tominaga, Yoshihide, Yuichi Sato, and Satoru Sadohara. "CFD Simulations of the Effect of Evaporative Cooling from Water Bodies in a Micro-Scale Urban Environment: Validation and Application Studies." Sustainable Cities and Society 19 (2015): 259-70. https://doi.org/10.1016/j.scs.2015.03.011.

Tsoka, Stella, Katerina Tsikaloudaki, and Theodoros Theodosiou. 2018. 'Analyzing the ENVI-Met Microclimate Model's Performance and Assessing Cool Materials and Urban Vegetation Applications-A Review'. Sustainable Cities and Society 43 (August). https://doi.org/10.1016/j.scs.2018.08.009.

Victorero, Felipe, Sergio Vera, Waldo Bustamante, Felipe Tori, Carlos Bonilla, Jorge Gironás, and Victoria Rojas. "Experimental Study of the Thermal Performance of Living Walls Under Semiarid Climatic Conditions." Energy Procedia 78 (2015): 3416-21. https://doi.org/10.1016/j.egypro.2015.12.160.

Xue, Fei, Xiaofeng Li, Jie Ma, and Zhiqin Zhang. 2015. 'Modeling the Influence of Fountain on Urban Microclimate'. Building Simulation 8 (3): 285-95. https://doi.org/10.1007/s12273-014-0210-7.

Yang, Jiachuan, and Zhi-Hua Wang. "Optimizing Urban Irrigation Schemes for the Trade-off between Energy and Water Consumption." Energy and Buildings 107 (2015): 335-44. https://doi.org/10.1016/j.enbuild.2015.08.045.

9.5.4 Indoor and semi-outdoor environments under free-running conditions

Allard, F. (Ed.). 1998. Natural Ventilation in Buildings: A Design Handbook. James & James.

Avantaggiato, M., Ladisa, G., Lapenna, L., Capozzoli, A. "Unlocking thermal comfort in transitional spaces: A field study in three Italian shopping centres." Building and Environment 188 (2021): 107428. https://doi.org/10.1016/j.buildenv.2020.107428.

Awbi, H. 2003. B. Ventilation of Buildings (2nd ed.). Routledge.

Awbi, H.B. 2003. Ventilation of Buildings (2nd ed.). Taylor & Francis, London.

Balaras, C.A. 1996. 'The role of thermal mass on the cooling load of buildings. An overview of computational methods'. Energy and Buildings 24 (1): 1-10. https://doi.org/10.1016/0378-7788 (95)00956-6.

Berardi, Umberto. "The Outdoor Microclimate Benefits and Energy Saving Resulting from Green Roofs Retrofits." Energy and Buildings 121 (2016): 217-29. https://doi.org/10.1016/j.enbuild.2016.03.021.

Deuble, M.P., de Dear, R.J. "Mixed-mode buildings: A double standard in occupants' comfort expectations." Building and Environment 54 (2012): 53-60. https://doi.org/10.1016/j.buildenv.2012.01.021.

Diz-Mellado, E., Nikolopoulou, M., López-Cabeza, V.P., Rivera-Gómez, C., Galán-Marín, C. "Extending the adaptive thermal comfort models for courtyards." Building and Environment 203 (2021): 108094. https://doi.org/10.1016/j.buildenv.2021.108094.

Diz-Mellado, E., Tablada, A., Gaitan, C., Soriano, C. "Thermal comfort thresholds for enclosed transitional spaces: in-between courtyards of the Mediterranean area." Urban Climate 47 (2023): 101369. https://doi.org/10.1016/j.uclim.2023.101369.

Diz-Mellado, Eduardo, Marialena Nikolopoulou, Victoria Patricia López-Cabeza, Carlos Rivera-Gómez, and Carmen Galán-Marín. 2023. 'Cross-Evaluation of Thermal Comfort in Semi-Outdoor Spaces According to Geometry in Southern Spain'. Urban Climate 49 (May): 101491. https://doi.org/10.1016/j.uclim.2023.101491.

Diz-Mellado, Eduardo, Victoria Patricia López-Cabeza, Carlos Rivera-Gómez, and Carmen Galán-Marín. 2023. 'Seasonal Analysis of Thermal Comfort in Mediterranean Social Courtyards: A Comparative Study'. Journal of Building Engineering 78 (November): 107756. https://doi.org/10.1016/j.jobe.2023.107756.

Erell, E. 2011., Pearlmutter, D., Williamson, T. Urban Microclimate: Designing the Spaces Between Buildings. Earthscan. ISBN 978-1-84407-467-9.

Erell, Evyatar, David Pearlmutter, and Terence Williamson. 2012. Urban Microclimate: Designing the Spaces Between Buildings. Routledge.

Etheridge, D. 1996., Sandberg, M. Building Ventilation: Theory and Measurement. John Wiley & Sons.

Etheridge, D., Sandberg, M. 1996. Building Ventilation: Theory and Measurement. John Wiley & Sons, Chichester.

Faggianelli, G.A., Brun, A., Wurtz, E., Muselli, M. "Natural cross ventilation in buildings on Mediterranean coastal zones." Energy and Buildings 77 (2014): 206-218. https://doi.org/10.1016/j.enbuild.2014.03.042.

Guo, Hongshan, Dorit Aviv, Mauricio Loyola, Eric Teitelbaum, Nicholas Houchois, and Forrest Meggers. "On the Understanding of the Mean Radiant Temperature within Both the Indoor and Outdoor Environment, a Critical Review." Renewable and Sustainable Energy Reviews 117 (2020): 109207. https://doi.org/10.1016/j.rser.2019.06.014.

Hendriks, Eefje, Noorullah Kuchai, Carolina Pereira Marghidan, and Anna Conzatti. 2025. 'Adapting Housing Design Tools for Indoor Thermal Comfort to Changing Climates'. Sustainability 17 (6): 2511. https://doi.org/10.3390/su17062511.

Liu, Fan, Hua Qian, Xiaohong Zheng, Lun Zhang, and Wenqing Liang. 2017. 'Numerical Study on the Urban Ventilation in Regulating Microclimate and Pollutant Dispersion in Urban Street Canyon: A Case Study of Nanjing New Region, China'. Atmosphere 8 (9): 164. https://doi.org/10.3390/atmos8090164.

Lizana, J., Chacartegui, R., Barrios-Padura, A., Valdivieso, J. "Integrating courtyard microclimate in building performance simulation to mitigate extreme urban heat impacts." Sustainable Cities and Society 78 (2022): 103590. https://doi.org/10.1016/j.scs.2021.103590.

López-Cabeza, V.P., Galán-Marín, C., Rivera-Gómez, C., Roa-Fernández, J. "Albedo influence on the microclimate and thermal comfort of courtyards under Mediterranean hot summer climate conditions." Sustainable Cities and Society 81 (2022): 103872. https://doi.org/10.1016/j.scs.2022.103872.

Maiullari, D, B Gherri, C Finizza, M Maretto, and E Naboni. 2021. 'Climate Change and Indoor Temperature Variation in Venetian Buildings: The Role of Density and Urban Form'. Journal of Physics: Conference Series 2042 (1): 012060. https://doi.org/10.1088/1742-6596/2042/1/012060.

Manapragada, Naga Venkata Sai Kumar, and Jonathan Natanian. 2026. 'A Machine Learning-Based Metamodeling Framework for Fast Urban Microclimate Predictions: A Coastal Mediterranean Case Study'. Energy and Buildings 353 (February): 116891. https://doi.org/10.1016/j.enbuild.2025.116891.

Michael, A., Demosthenous, D., Philokyprou, M. "Natural Ventilation for Cooling in Mediterranean Climate: A Case Study in Vernacular Architecture of Cyprus." Energy and Buildings (2017). https://doi.org/10.1016/j.enbuild.2017.03.040.

Morales, Richard Dean, Amaryllis Audenaert, and Stijn Verbeke. 2025. 'Thermal Comfort and Indoor Overheating Risks of Urban Building Stock - A Review of Modelling Methods and Future Climate Challenges'. Building and Environment 269 (February):112363. https://doi.org/10.1016/j.buildenv.2024.112363.

Murakawa, Saburo, Takeshi Sekine, Ken-ichi Narita, and Daisaku Nishina. 1991. ‘Study of the Effects of a River on the Thermal Environment in an Urban Area’. Energy and Buildings 16 (3-4): 993-1001. https://doi.org/10.1016/0378-7788 (91)90094-J.

Nikolopoulou, M., Steemers, K. 2003. ‘Thermal comfort and psychological adaptation as a guide for designing urban spaces’. Energy and Buildings 35 (1): 95-101. https://doi.org/10.1016/S0378-7788 (02)00084-1.

Oke, T. R. 1988. ‘Street Design and Urban Canopy Layer Climate’. Energy and Buildings 11 (1-3): 103-13. https://doi.org/10.1016/0378-7788 (88)90026-6.

Santamouris, M. 2020. 'Recent Progress on Urban Overheating and Heat Island Research. Integrated Assessment of the Energy, Environmental, Vulnerability and Health Impact. Synergies with the Global Climate Change'. Energy and Buildings 207 (January):109482. https://doi.org/10.1016/j.enbuild.2019.109482.

Yang, Jiachuan, and Zhi-Hua Wang. "Optimizing Urban Irrigation Schemes for the Trade-off between Energy and Water Consumption." Energy and Buildings 107 (2015): 335-44. https://doi.org/10.1016/j.enbuild.2015.08.045.

9.5.5 Indoor–outdoor microclimatic coupling

Guo, Hongshan, Dorit Aviv, Mauricio Loyola, Eric Teitelbaum, Nicholas Houchois, and Forrest Meggers. "On the Understanding of the Mean Radiant Temperature within Both the Indoor and Outdoor Environment, a Critical Review." Renewable and Sustainable Energy Reviews 117 (2020): 109207. https://doi.org/10.1016/j.rser.2019.06.014.

Lizana, J., Chacartegui, R., Barrios-Padura, A., Valdivieso, J. "Integrating courtyard microclimate in building performance simulation to mitigate extreme urban heat impacts." Sustainable Cities and Society 78 (2022): 103590. https://doi.org/10.1016/j.scs.2021.103590.

Maiullari, D, B Gherri, C Finizza, M Maretto, and E Naboni. 2021. ‘Climate Change and Indoor Temperature Variation in Venetian Buildings: The Role of Density and Urban Form’. Journal of Physics: Conference Series 2042 (1): 012060. https://doi.org/10.1088/1742-6596/2042/1/012060.

Pasandi, L., Qian, Z., and Woo, W. L. 2025. "Quantifying urban microclimate feedback on building energy use using a coupled simulation workflow." Building and Environment 285, Part B (1 November): 113657. https://doi.org/10.1016/j.buildenv.2025.113657.

9.6 Microclimatic Modelling, Simulation Tools and Computational Methods

9.6.1 Microclimate and CFD-based modelling approaches

Assimakopoulos, V.D, H.M ApSimon, and N Moussiopoulos. 2003. ‘A Numerical Study of Atmospheric Pollutant Dispersion in Different Two-Dimensional Street Canyon Configurations’. Atmospheric Environment 37 (29): 4037-49. https://doi.org/10.1016/S1352-2310 (03)00533-8.

Chen, G., Xiong, Q., Morris, P. J., Paterson, E. G., Sergeev, A., & Wang, Y. C. 2014. OpenFOAM for computational fluid dynamics. Notices of the American Mathematical Society, 61(4), 354-363. https://doi.org/10.1090/noti1095.

Cui, Zhiqiang, Xiaoming Cai, and Chris J. Baker. 2004. 'Large-Eddy Simulation of Turbulent Flow in a Street Canyon'. Quarterly Journal of the Royal Meteorological Society 130 (599): 1373-94. https://doi.org/10.1256/qj.02.150.

Davarzani, Hossein, Kathleen Smits, Ryan M. Tolene, and Tissa Illangasekare. 2014. 'Study of the Effect of Wind Speed on Evaporation from Soil through Integrated Modeling of the Atmospheric Boundary Layer and Shallow Subsurface'. Water Resources Research 50 (1): 661-80. https://doi.org/10.1002/2013WR013952.

Djedjig, Rabah, Emmanuel Bozonnet, and Rafik Belarbi. "Modeling Green Wall Interactions with Street Canyons for Building Energy Simulation in Urban Context." Urban Climate 16 (2016): 75-85. https://doi.org/10.1016/j.uclim.2015.12.003.

Liu, Fan, Hua Qian, Xiaohong Zheng, Lun Zhang, and Wenqing Liang. 2017. 'Numerical Study on the Urban Ventilation in Regulating Microclimate and Pollutant Dispersion in Urban Street Canyon: A Case Study of Nanjing New Region, China'. Atmosphere 8 (9): 164. https://doi.org/10.3390/atmos8090164.

Loridan, Thomas, and C.s.b. Grimmond. 2012. 'Multi-Site Evaluation of an Urban Land-Surface Model: Intra-Urban Heterogeneity, Seasonality and Parameter Complexity Requirements'. Quarterly Journal of the Royal Meteorological Society 138 (665): 1094-1113. https://doi.org/10.1002/qj.963.

Sailor, David J., and Hongli Fan. 2002. 'Modeling the Diurnal Variability of Effective Albedo for Cities'. Atmospheric Environment 36 (4): 713-25. https://doi.org/10.1016/S1352-2310 (01)00452-6.

Sailor, David J., and Lu Lu. "A Top-down Methodology for Developing Diurnal and Seasonal Anthropogenic Heating Profiles for Urban Areas." Atmospheric Environment 38(17) (2004): 2737-48. https://doi.org/10.1016/j.atmosenv.2004.01.034.

Sailor, David J., Matei Georgescu, Jeffrey M. Milne, and Melissa A. Hart. "Development of a National Anthropogenic Heating Database with an Extrapolation for International Cities." Atmospheric Environment 118 (2015): 7-18. https://doi.org/10.1016/j.atmosenv.2015.07.016.

Tominaga, Yoshihide, Yuichi Sato, and Satoru Sadohara. "CFD Simulations of the Effect of Evaporative Cooling from Water Bodies in a Micro-Scale Urban Environment: Validation and Application Studies." Sustainable Cities and Society 19 (2015): 259-70. https://doi.org/10.1016/j.scs.2015.03.011.

Vardoulakis, Sotiris, Bernard E. A Fisher, Koulis Pericleous, and Norbert Gonzalez-Flesca. 2003. 'Modelling Air Quality in Street Canyons: A Review'. Atmospheric Environment 37 (2): 155-82. https://doi.org/10.1016/S1352-2310 (02)00857-9.

9.6.2 Human-centred simulation frameworks

Bruse, M. 2000. "Assessing Thermal Comfort in Urban Environments Using an Integrated Dynamic Microscale Biometeorological Model System." Proceedings of the AMS Conference (AugDavis_3urban). https://ams.confex.com/ams/AugDavis/techprogram/paper_15005.htm.

Crank, Peter J., Ariane Middel, Melissa Wagner, Dani Hoots, Martin Smith, and Anthony Brazel. 2020. 'Validation of Seasonal Mean Radiant Temperature Simulations in Hot Arid Urban Climates'. Science of The Total Environment 749 (December): 141392. https://doi.org/10.1016/j.scitotenv.2020.141392.

Fiala, D., Havenith, G., Bröde, P., Kampmann, B., Jendritzky, G. 2012. 'UTCI-Fiala Multi-Node Model of Human Heat Transfer and Temperature Regulation'. International Journal of Biometeorology 56 (3): 429-441. https://doi.org/10.1007/s00484-011-0424-7.

Havenith, G., Fiala, D., Błażejczyk, K., Richards, M., Bröde, P., Holmér, I., Rintamäki, H., Benshabat, Y., Jendritzky, G. 2012. 'The UTCI-Clothing Model'. International Journal of Biometeorology 56 (3): 461-470. https://doi.org/10.1007/s00484-011-0451-4.

Havenith, George, and Dusan Fiala. 2016. 'Thermal Indices and Thermophysiological Modeling for Heat Stress'. Comprehensive Physiology 6 (1): 255-302. https://doi.org/10.1002/j.2040-4603.2016.tb00668.x.

Matzarakis, Andreas, Frank Rutz, and Helmut Mayer. 2007. 'Modelling Radiation Fluxes in Simple and Complex Environments-Application of the RayMan Model'. International Journal of Biometeorology 51 (4): 323-34. https://doi.org/10.1007/s00484-006-0061-8.

Pickup, J. 2000., de Dear, R. "An Outdoor Thermal Comfort Index (OUT_SET*) - Part I - The Model and Its Assumptions." In de Dear, R., Kalma, J., Oke, T., Auliciems, A. (Eds.), Biometeorology and Urban Climatology at the Turn of the Millennium, 279-283. World Meteorological Organization.

Psikuta, A., Fiala, D., Laschewski, G., Jendritzky, G., Richards, M., Błażejczyk, K., Mekjavic, I.B., Rintamäki, H., de Dear, R., Havenith, G. 2012. 'Validation of the Fiala Multi-Node Thermophysiological Model for UTCI Application'. International Journal of Biometeorology 56 (3): 443-460. https://doi.org/10.1007/s00484-011-0450-5.

9.6.3 Toolchains for multi-scalar thermal analysis

Crawley, Drury B., Linda K. Lawrie, Frederick C. Winkelmann, W. F. Buhl, Y. Joe Huang, Curtis O. Pedersen, Richard K. Strand, et al. 2001. 'EnergyPlus: Creating a New-Generation Building Energy Simulation Program'. Energy and Buildings, Special Issue: BUILDING SIMULATION'99, 33 (4): 319-31. https://doi.org/10.1016/S0378-7788(00)00114-6.

ENVI-met GmbH. 2023. ENVI-met, version 5. Essen, Germany: ENVI-met GmbH. https://envi-met.com/.

Ibrahim, Yasser, Tristan Kershaw, and Paul Shepherd. 2020. A Methodology For Modelling Microclimates: A Ladybug-Tools and ENVI-Met Verification Study.

Kastner, Patrick, and Timur Dogan. 2021. 'Eddy3D: A Toolkit for Decoupled Outdoor Thermal Comfort Simulations in Urban Areas'. Building and Environment 212 (December): 108639. https://doi.org/10.1016/j.buildenv.2021.108639.

Ladybug Tools. 2023. Honeybee, version 1.8.0. Ladybug Tools. https://www.ladybug.tools/honeybee.html.

Manapragada, Naga Venkata Sai Kumar, and Jonathan Natanian. 2026. 'A Machine Learning-Based Metamodeling Framework for Fast Urban Microclimate Predictions: A Coastal Mediterranean Case Study'. Energy and Buildings 353 (February): 116891. https://doi.org/10.1016/j.enbuild.2025.116891.

Meteotest AG. 2020. Meteonorm, version 8. Bern, Switzerland: Meteotest AG. https://meteonorm.com/.

Robert McNeel & Associates. 2023. Grasshopper 3D, version 1.0. Seattle, WA: Robert McNeel & Associates. https://www.grasshopper3d.com/.

Robert McNeel & Associates. 2023. Rhinoceros 3D, version 8. Seattle, WA: Robert McNeel & Associates. https://www.rhino3d.com/.

Schöneberger, P., Sinsel, T., Ouyang, W., Tan, Z., Bruse, M., and Simon, H. 2025. "Enhancing urban microclimate simulations: Validating ENVI-met's accuracy in modeling multi-directional radiative fluxes and mean radiant temperature in subtropical Hong Kong." Building and Environment 284 (1 October): 113475. https://doi.org/10.1016/j.buildenv.2025.113475.

Tsoka, Stella, Katerina Tsikaloudaki, and Theodoros Theodosiou. 2018. 'Analyzing the ENVI-Met Microclimate Model's Performance and Assessing Cool Materials and Urban Vegetation Applications-A Review'. Sustainable Cities and Society 43 (August). https://doi.org/10.1016/j.scs.2018.08.009.

Zhao, Zeming, Hangxin Li, and Shengwei Wang. 2024. 'Machine Learning-Based Surrogate Models for Fast Impact Assessment of a New Building on Urban Local Microclimate at Design Stage'. Building and Environment 266 (December): 112142. https://doi.org/10.1016/j.buildenv.2024.112142.

9.6.4 Modelling assumptions, uncertainties and scale effects

Alexandri, Eleftheria, and Phil Jones. "Temperature Decreases in an Urban Canyon due to Green Walls and Green Roofs in Diverse Climates." Building and Environment, Part Special: Building Performance Simulation 43(4) (2008): 480-93. https://doi.org/10.1016/j.buildenv.2006.10.055.

Crank, Peter J., Ariane Middel, Melissa Wagner, Dani Hoots, Martin Smith, and Anthony Brazel. 2020. 'Validation of Seasonal Mean Radiant Temperature Simulations in Hot Arid Urban Climates'. Science of The Total Environment 749 (December): 141392. https://doi.org/10.1016/j.scitotenv.2020.141392.

Desogus, G., Di Benedetto, S., Ricciu, R. "The use of adaptive thermal comfort models to evaluate the summer performance of a Mediterranean earth building." Energy and Buildings 104 (2015): 350-359. https://doi.org/10.1016/j.enbuild.2015.07.020.

Eyring, Veronika, Sandrine Bony, Gerald A. Meehl, Catherine A. Senior, Bjorn Stevens, Ronald J. Stouffer, and Karl E. Taylor. 2016. 'Overview of the Coupled Model Intercomparison Project Phase 6 (CMIP6) Experimental Design and Organization'. Geoscientific Model Development 9 (5): 1937-58. https://doi.org/10.5194/gmd-9-1937-2016.

Ibrahim, Yasser, Tristan Kershaw, and Paul Shepherd. 2020. A Methodology For Modelling Microclimates: A Ladybug-Tools and ENVI-Met Verification Study.

Jentsch, Mark F., Patrick A. B. James, Leonidas Bourikas, and AbuBakr S. Bahaj. 2013. 'Transforming Existing Weather Data for Worldwide Locations to Enable Energy and Building Performance Simulation under Future Climates'. Renewable Energy 55 (July): 514-524. https://doi.org/10.1016/j.renene.2012.12.049.

Ji, Yuchen, Jusheng Song, and Pengyuan Shen. "A Review of Studies and Modelling of Solar Radiation on Human Thermal Comfort in Outdoor Environment." Building and Environment 214 (2022): 108891. https://doi.org/10.1016/j.buildenv.2022.108891.

Lizana, J., Chacartegui, R., Barrios-Padura, A., Valdivieso, J. "Integrating courtyard microclimate in building performance simulation to mitigate extreme urban heat impacts." Sustainable Cities and Society 78 (2022): 103590. https://doi.org/10.1016/j.scs.2021.103590.

Loridan, Thomas, and C.s.b. Grimmond. 2012. 'Multi-Site Evaluation of an Urban Land-Surface Model: Intra-Urban Heterogeneity, Seasonality and Parameter Complexity Requirements'. Quarterly Journal of the Royal Meteorological Society 138 (665): 1094-1113. https://doi.org/10.1002/qj.963.

Morales, Richard Dean, Amaryllis Audenaert, and Stijn Verbeke. 2025. 'Thermal Comfort and Indoor Overheating Risks of Urban Building Stock - A Review of Modelling Methods and Future Climate Challenges'. Building and Environment 269 (February):112363. https://doi.org/10.1016/j.buildenv.2024.112363.

Psikuta, A., Fiala, D., Laschewski, G., Jendritzky, G., Richards, M., Błażejczyk, K., Mekjavic, I.B., Rintamäki, H., de Dear, R., Havenith, G. 2012. ‘Validation of the Fiala Multi-Node Thermophysiological Model for UTCI Application’. International Journal of Biometeorology 56 (3): 443-460. https://doi.org/10.1007/s00484-011-0450-5.

Schöneberger, P., Sinsel, T., Ouyang, W., Tan, Z., Bruse, M., and Simon, H. 2025. "Enhancing urban microclimate simulations: Validating ENVI-met's accuracy in modeling multi-directional radiative fluxes and mean radiant temperature in subtropical Hong Kong." Building and Environment 284 (1 October): 113475. https://doi.org/10.1016/j.buildenv.2025.113475.

Tominaga, Yoshihide, Yuichi Sato, and Satoru Sadohara. "CFD Simulations of the Effect of Evaporative Cooling from Water Bodies in a Micro-Scale Urban Environment: Validation and Application Studies." Sustainable Cities and Society 19 (2015): 259-70. https://doi.org/10.1016/j.scs.2015.03.011.

Tsoka, Stella, Katerina Tsikaloudaki, and Theodoros Theodosiou. 2018. 'Analyzing the ENVI-Met Microclimate Model's Performance and Assessing Cool Materials and Urban Vegetation Applications-A Review'. Sustainable Cities and Society 43 (August). https://doi.org/10.1016/j.scs.2018.08.009.

Vardoulakis, Sotiris, Bernard E. A Fisher, Koulis Pericleous, and Norbert Gonzalez-Flesca. 2003. ‘Modelling Air Quality in Street Canyons: A Review’. Atmospheric Environment 37 (2): 155-82. https://doi.org/10.1016/S1352-2310 (02)00857-9.

Zou, J., H. Lu, C. Shu, L. Ji, A. Gaur, and L.L. Wang. 2023. 'Multiscale Numerical Assessment of Urban Overheating under Climate Projections: A Review'. Urban Climate 49. https://doi.org/10.1016/j.uclim.2023.101551.

9.7 Thermal Resilience, Comparative Assessment and Design

9.7.1 Thermal resilience as a comparative construct

Hong, Tianzhen, Jeetika Malik, Amanda Krelling, William O'Brien, Kaiyu Sun, Roberto Lamberts, and Max Wei. 2023. 'Ten Questions Concerning Thermal Resilience of Buildings and Occupants for Climate Adaptation'. Building and Environment 244 (October):110806. https://doi.org/10.1016/j.buildenv.2023.110806.

Khoja, Ahmed, Andrea Moro, and Natalie Essig. 2022. 'iQRe: An Integrated Cross Scale Urban Resilience Assessment Framework'. IOP Conference Series: Earth and Environmental Science 1122 (1): 012015. https://doi.org/10.1088/1755-1315/1122/1/012015.

Manapragada, Naga Venkata Sai Kumar, and Jonathan Natanian. 2026. 'A Machine Learning-Based Metamodeling Framework for Fast Urban Microclimate Predictions: A Coastal Mediterranean Case Study'. Energy and Buildings 353 (February): 116891. https://doi.org/10.1016/j.enbuild.2025.116891.

Orsetti, Eleonora, Nicola Tollin, Martin Lehmann, Vanessa Agudelo Valderrama, and Jordi Morató. 2022. 'Building Resilient Cities: Climate Change and Health Interlinkages in the Planning of Public Spaces'. International Journal of Environmental Research and Public Health 19 (3): 1355. https://doi.org/10.3390/ijerph19031355.

9.7.2 Baseline–future scenario comparison approaches

Belcher, SE, JN Hacker, and DS Powell. 2005. 'Constructing Design Weather Data for Future Climates'. Building Services Engineering Research & Technology 26 (1): 49-61. https://doi.org/10.1191/0143624405bt112oa.

Eyring, Veronika, Sandrine Bony, Gerald A. Meehl, Catherine A. Senior, Bjorn Stevens, Ronald J. Stouffer, and Karl E. Taylor. 2016. 'Overview of the Coupled Model Intercomparison Project Phase 6 (CMIP6) Experimental Design and Organization'. Geoscientific Model Development 9 (5): 1937-58. https://doi.org/10.5194/gmd-9-1937-2016.

Gasparrini, Antonio, Yuming Guo, Francesco Sera, Ana Maria Vicedo-Cabrera, Veronika Huber, Shilu Tong, Micheline de Sousa Zanotti Stagliorio Coelho, et al. 2017. 'Projections of Temperature-Related Excess Mortality under Climate Change Scenarios'. The Lancet. Planetary Health 1 (9): e360-67. https://doi.org/10.1016/S2542-5196(17)30156-0.

Jentsch, Mark F., Patrick A. B. James, Leonidas Bourikas, and AbuBakr S. Bahaj. 2013. 'Transforming Existing Weather Data for Worldwide Locations to Enable Energy and Building Performance Simulation under Future Climates'. Renewable Energy 55 (July): 514-524. https://doi.org/10.1016/j.renene.2012.12.049.

Meinshausen, M., Nicholls, Z. R. J., Lewis, J., Gidden, M. J., Vogel, E., Freund, M., Beyerle, U., Gessner, C., Nauels, A., Bauer, N., Canadell, J. G., Daniel, J. S., John, A., Krummel, P. B., Luderer, G., Meinshausen, N., Montzka, S. A., Rayner, P. J., Reimann, S., Smith, S. J., van den Berg, M., Velders, G. J. M., Vollmer, M. K., and Wang, R. H. J. 2020. 'The shared socio-economic pathway (SSP) greenhouse gas concentrations and their extensions to 2500'. Geosci. Model Dev. 13: 3571-3605. https://doi.org/10.5194/gmd-13-3571-2020.

Morales, Richard Dean, Amaryllis Audenaert, and Stijn Verbeke. 2025. 'Thermal Comfort and Indoor Overheating Risks of Urban Building Stock - A Review of Modelling Methods and Future Climate Challenges'. Building and Environment 269 (February):112363. https://doi.org/10.1016/j.buildenv.2024.112363.

Rodrigues, Eugénio, Marco S. Fernandes, and David Carvalho. 2023. 'Future Weather Generator for Building Performance Research: An Open-Source Morphing Tool and an Application'. Building and Environment 233 (April): 110104. https://doi.org/10.1016/j.buildenv.2023.110104.

Zou, J., H. Lu, C. Shu, L. Ji, A. Gaur, and L.L. Wang. 2023. 'Multiscale Numerical Assessment of Urban Overheating under Climate Projections: A Review'. Urban Climate 49. https://doi.org/10.1016/j.uclim.2023.101551.

9.7.3 Multi-scalar assessment of thermal resilience

Cooley, S., D. Schoeman, L. Bopp, P. Boyd, S. Donner, D.Y. Ghebrehiwet, S.-I. Ito, W. Kiessling, P. Martinetto, E. Ojea, M.-F. Racault, B. Rost, and M. Skern-Mauritzen. 2022. Ocean and Coastal Ecosystems and their Services Supplementary Material. In:Climate Change 2022: Impacts, Adaptation, and Vulnerability. Contribution of Working Group II to the Sixth Assessment Report of the Intergovernmental Panel on Climate Change [H.-O. Pörtner, D.C. Roberts, M. Tignor, E.S. Poloczanska, K. Mintenbeck, A. Alegría, M. Craig, S. Langsdorf, S. Löschke, V. Möller, A. Okem, B. Rama (eds.)]. Available from https://www.ipcc.ch/report/ar6/wg2/.

Douville, H., K. Raghavan, J. Renwick, R.P. Allan, P.A. Arias, M. Barlow, R. Cerezo-Mota, A. Cherchi, T.Y. Gan, J. Gergis, D. Jiang, A. Khan, W. Pokam Mba, D. Rosenfeld, J. Tierney, and O. Zolina. 2021. Water Cycle Changes. In Climate Change 2021: The Physical Science Basis. Contribution of Working Group I to the Sixth Assessment Report of the Intergovernmental Panel on Climate Change [Masson-Delmotte, V., P. Zhai, A. Pirani, S.L. Connors, C. Péan, S. Berger, N. Caud, Y. Chen, L. Goldfarb, M.I. Gomis, M. Huang, K. Leitzell, E. Lonnoy, J.B.R. Matthews, T.K. Maycock, T. Waterfield, O. Yelekçi, R. Yu, and B. Zhou (eds.)]. Cambridge University Press, Cambridge, United Kingdom and New York, NY, USA, pp. 1055-1210, https://doi.org/10.1017/9781009157896.010.

Höppe, P. 1999. 'The Physiological Equivalent Temperature - a Universal Index for the Biometeorological Assessment of the Thermal Environment'. International Journal of Biometeorology 43 (2): 71-75. https://doi.org/10.1007/s004840050118.

IPCC. 2021. Index. In: Climate Change 2021: The Physical Science Basis. Contribution of Working Group I to the Sixth Assessment Report of the Intergovernmental Panel on Climate Change [Masson-Delmotte, V., P. Zhai, A. Pirani, S.L. Connors, C. Péan, S. Berger, N. Caud, Y. Chen, L. Goldfarb, M.I. Gomis, M. Huang, K. Leitzell, E. Lonnoy, J.B.R. Matthews, T.K. Maycock, T. Waterfield, O. Yelekçi, R. Yu, and B. Zhou (eds.)]. Cambridge University Press, Cambridge, United Kingdom and New York, NY, USA, pp. 2339 -2391.

IPCC. 2022. Climate Change 2022: Impacts, Adaptation and Vulnerability. Contribution of Working Group II to the Sixth Assessment Report of the Intergovernmental Panel on Climate Change [H.-O. Pörtner, D.C. Roberts, M. Tignor, E.S. Poloczanska, K. Mintenbeck, A. Alegría, M. Craig, S. Langsdorf, S. Löschke, V. Möller, A. Okem, B. Rama (eds.)]. Cambridge University Press. Cambridge University Press, Cambridge, UK and New York, NY, USA, 3056 pp., doi:10.1017/9781009325844.

IPCC. 2023. Climate Change 2023: Synthesis Report. Contribution of Working Groups I, II and III to the Sixth Assessment Report of the Intergovernmental Panel on Climate Change [Core Writing Team, H. Lee and J. Romero (eds.)]. IPCC, Geneva, Switzerland, pp. 35-115, doi: 10.59327/IPCC/AR6-9789291691647.

IPCC. 2023. Climate Change 2023: Synthesis Report. Contribution of Working Groups I, II and III to the Sixth Assessment Report of the Intergovernmental Panel on Climate Change. IPCC, Geneva.

Italian Ministry of Economic Development. 2019. Integrated National Energy and Climate Plan 2030 (PNIEC). Rome: Ministry of Economic Development.

Khoja, Ahmed, Andrea Moro, and Natalie Essig. 2022. 'iQRe: An Integrated Cross Scale Urban Resilience Assessment Framework'. IOP Conference Series: Earth and Environmental Science 1122 (1): 012015. https://doi.org/10.1088/1755-1315/1122/1/012015.

Knez, I., Thorsson, S., Eliasson, I., Lindberg, F. 2009. ‘Psychological Mechanisms in Outdoor Place and Weather Assessment: Towards a Conceptual Model’. International Journal of Biometeorology 53 (1): 101-11. https://doi.org/10.1007/s00484-008-0194-z.

Martinelli, L., Lin, T.-P., Matzarakis, A. "Assessment of the Influence of Daily Shadings Pattern on Human Thermal Comfort and Attendance in Rome during Summer Period." Building and Environment 92 (2015): 30-38. https://doi.org/10.1016/j.buildenv.2015.04.013.

Mauree, D., E. Naboni, S. Coccolo, A.T.D. Perera, V.M. Nik, and J.-L. Scartezzini. 2019. 'A Review of Assessment Methods for the Urban Environment and Its Energy Sustainability to Guarantee Climate Adaptation of Future Cities'. Renewable and Sustainable Energy Reviews 112:733-46. https://doi.org/10.1016/j.rser.2019.06.005.

Santamouris, M. 2020. 'Recent Progress on Urban Overheating and Heat Island Research. Integrated Assessment of the Energy, Environmental, Vulnerability and Health Impact. Synergies with the Global Climate Change'. Energy and Buildings 207 (January):109482. https://doi.org/10.1016/j.enbuild.2019.109482.

Semaan, Mary, and Annie Pearce. "Assessment of the Gains and Benefits of Green Roofs in Different Climates." Procedia Engineering, ICSDEC 2016 - Integrating Data Science, Construction and Sustainability 145 (2016): 333-39. https://doi.org/10.1016/j.proeng.2016.04.083.

Zhao, Zeming, Hangxin Li, and Shengwei Wang. 2024. 'Machine Learning-Based Surrogate Models for Fast Impact Assessment of a New Building on Urban Local Microclimate at Design Stage'. Building and Environment 266 (December): 112142. https://doi.org/10.1016/j.buildenv.2024.112142.

Zou, J., H. Lu, C. Shu, L. Ji, A. Gaur, and L.L. Wang. 2023. 'Multiscale Numerical Assessment of Urban Overheating under Climate Projections: A Review'. Urban Climate 49. https://doi.org/10.1016/j.uclim.2023.101551.

9.7.4 Design-oriented interpretation of thermal-comfort resilience

Alpino, Matteo, Luca Citino, Guido de Blasio, and Federica Zeni. 2022. 'Gli Effetti Del Cambiamento Climatico Sull'economia Italiana (The Effects of Climate Change on the Italian Economy)'. SSRN Scholarly Paper. Rochester, NY: Social Science Research Network. https://doi.org/10.2139/ssrn.4463030.

Belcher, SE, JN Hacker, and DS Powell. 2005. 'Constructing Design Weather Data for Future Climates'. Building Services Engineering Research & Technology 26 (1): 49-61. https://doi.org/10.1191/0143624405bt112oa.

Eyring, Veronika, Sandrine Bony, Gerald A. Meehl, Catherine A. Senior, Bjorn Stevens, Ronald J. Stouffer, and Karl E. Taylor. 2016. 'Overview of the Coupled Model Intercomparison Project Phase 6 (CMIP6) Experimental Design and Organization'. Geoscientific Model Development 9 (5): 1937-58. https://doi.org/10.5194/gmd-9-1937-2016.

Hendriks, Eefje, Noorullah Kuchai, Carolina Pereira Marghidan, and Anna Conzatti. 2025. 'Adapting Housing Design Tools for Indoor Thermal Comfort to Changing Climates'. Sustainability 17 (6): 2511. https://doi.org/10.3390/su17062511.

Marcus Vitruvius Pollo, De Architectura. Liber I, caput 6. In 'Mirror.Csclub.Uwaterloo.ca/Gutenberg/5/1/8/1/51812/51812-0.Txt'. n.d. Accessed 21 May 2025. https://mirror.csclub.uwaterloo.ca/gutenberg/5/1/8/1/51812/51812-0.txt.

Municipality of Milan. 'Piano Aria e Clima'. n.d. Comune di Milano. Accessed 27 May 2025. https://www.comune.milano.it/aree-tematiche/ambiente/aria-e-clima/piano-aria-clima.

Naboni, E, Havinga L. 2019. Regenerative Design in Digital Practice. A Handbook for the Built Environment. Bolzano, Italy, Eurac Research. ISBN 978-3-9504607-2-8.

Nikolopoulou, M., Steemers, K. 2003. ‘Thermal comfort and psychological adaptation as a guide for designing urban spaces’. Energy and Buildings 35 (1): 95-101. https://doi.org/10.1016/S0378-7788 (02)00084-1.

Spano, Donatella, Valentina Mereu, Valentina Bacciu, Marras Serena, Antonio Trabucco, Marianna Adinolfi, Barbato Giuliana, et al. 2020. Analisi Del Rischio. I Cambiamenti Climatici in Italia. https://doi.org/10.25424/CMCC/ANALISI_DEL_RISCHIO.

Zhao, Zeming, Hangxin Li, and Shengwei Wang. 2024. 'Machine Learning-Based Surrogate Models for Fast Impact Assessment of a New Building on Urban Local Microclimate at Design Stage'. Building and Environment 266 (December): 112142. https://doi.org/10.1016/j.buildenv.2024.112142.

10 List of figures

Figure 1. Conceptual framework for thermal-comfort resilience assessment. The diagram illustrates the logical chain linking microclimatic variables to the assessment of thermal resilience through UTCI calculation, comfort evaluation, scenario comparison, and local UTCI variation (ΔUTCI). Thermal resilience is interpreted as the sensitivity of thermal comfort to climate change and is assessed consistently across urban, building, and component scales.

Figure 2. Projections of the average global surface temperature change relative to the period 1850-1900 (°C).

Figure 3. Predicted global warming for three temperature increase scenarios. Source: IPCC

Figure 4. Delta air temperature between the current scenario and 2050 under a high-end emission pathway. in four capitals located in different climate zones. The difference in the nature of the warming can be seen, concentrated in heat waves in colder climates and more uniform in warmer climates. Graphs produced by the author of this thesis based on weather data generated using Meteonorm 8.0. Copyright: Marcello Turrini, Emanuele Naboni, 2023

Figure 5. Scheme showing urban energy balance. From Erell et al., 2012.

Figure 6. The diagram illustrates the Inputs–Functions–Outputs structure of the proposed methodology. Current and future EPW weather files, together with a three-dimensional digital model of the built environment and a defined assessment domain at human exposure level, constitute the inputs of the workflow. These inputs are processed through a sequence of steps including weather scenario preparation, microclimate simulation, UTCI calculation for current and future conditions, and the computation of local UTCI variations (ΔUTCI). Post-processing operations generate spatial and statistical representations of the results. The outputs support a comparative interpretation of thermal resilience across different configurations and spatial scales.

Figure 7. Hourly Heat Maps on air temperature. Sassuolo 2022, and Δ. There will be hours with temperatures increase higher than 8°C, in summer, bringing to a maximum of about 46°C, which is not happening in the current period. Chart made with Grasshopper and ladybug by the author. Copyright: Marcello Turrini, Emanuele Naboni, 2023

Figure 8. Sassuolo district and 5 selected configurations. UP_1-historical urban fabric. UP_2-modern urban fabric. UP_3-industrial area. UP_4-natural area. UP_5-agricultural area. Copyright: Marcello Turrini, Emanuele Naboni, Barbara Gherri 2022

Figure 9. On the left: Configuration UP_1-Historical urban fabric. On the right: Configuration UP_2-Modern urban fabric Source: Google Maps

Figure 10. On the left: Configuration UP_3-Industrial area. On the right: Configuration UP_4-Natural area. Source: Google Maps

Figure 11. Configuration UP_5 - Agricultural area. Source: Google Maps

Figure 12. Building 3D models with Rhinoceros. Additional information was added to the GIS models, including tree positions (as point markers) and a material-based distinction between pavements and exterior building walls. Source: GIS database of Emilia Romagna Region, elaborated with Rhinoceros 3D. Copyright: Marcello Turrini, Emanuele Naboni, Barbara Gherri 2022

Figure 13. UP-1. Historical urban fabric. 3D model via Rhinoceros 3D. Copyright: Marcello Turrini, Emanuele Naboni, Barbara Gherri 2022

Figure 14. UP-2. Modern urban fabric. 3D model via Rhinoceros 3D. Copyright: Marcello Turrini, Emanuele Naboni, Barbara Gherri 2022

Figure 15. UP-3. Industrial area. 3D model via Rhinoceros 3D. Copyright: Marcello Turrini, Emanuele Naboni, Barbara Gherri 2022

Figure 16. UP-4. Natural area. 3D model via Rhinoceros 3D. Copyright: Marcello Turrini, Emanuele Naboni, Barbara Gherri 2022

Figure 17. UP-5. Agricultural area. 3D model via Rhinoceros 3D. Copyright: Marcello Turrini, Emanuele Naboni, Barbara Gherri 2022

Figure 18. Grasshopper and Morpho components for workspace and location settings. Copyright: Marcello Turrini, Emanuele Naboni, Barbara Gherri 2022

Figure 19. Morpho and Grasshopper components for grid domain setup. Copyright: Marcello Turrini, Emanuele Naboni, Barbara Gherri 2022

Figure 20. Components for transforming Rhinoceros objects into ENVI-met building objects. Copyright: Marcello Turrini, Emanuele Naboni, Barbara Gherri 2022

Figure 21. Components for transforming Rhinoceros objects into ENVI-met surface objects. Copyright: Marcello Turrini, Emanuele Naboni, Barbara Gherri 2022

Figure 22. ENVI-met panel for tree configuration. The geometry is fully customizable, along with the foliage albedo data.

Figure 23. Comparison between Dry Bulb Temperature and Global Horizontal Radiation in 2022 and 2050 during the hottest week of the year. On August 17, radiation does not show significant differences in cloud cover.

Figure 24. Sorting output files of ENVI-met with Morpho. Copyright: Marcello Turrini, Emanuele Naboni, Barbara Gherri 2022

Figure 25. UTCI calculation for 2022 and 2050 with morpho, Ladybug and native Grasshopper components. Copyright: Marcello Turrini, Emanuele Naboni, Barbara Gherri 2022

Figure 26. UP_1 - Historical Urban Fabric. UTCI on 17 August at 4:00 pm. 2022 on the left, 2050 on the right. Copyright: Marcello Turrini, Emanuele Naboni, Barbara Gherri 2022

Figure 27. Variation in UTCI between 2022 and 2050 in the Configuration UP_1 – Historical urban fabric. The area within the dashed rectangle is the area actually used for numerical evaluation, as it is free from bias resulting from the edge effect of the CFD. Copyright: Marcello Turrini, Emanuele Naboni, Barbara Gherri 2022

Figure 28. Distribution of UTCI variation in the UP_1 configuration between 2022 and 2050, referring to August 17 at 4:00 p.m. The red curve represents the relative frequency of UTCI variations, showing a peak around 3.3°C and an average of 3.7 °C, lower than the other configurations in gray. Copyright: Marcello Turrini, Emanuele Naboni, Barbara Gherri 2022

Figure 29. UP_2 - Modern Urban Fabric. UTCI on 17 August at 4:00 pm. 2022 on the left, 2050 on the right. Copyright: Marcello Turrini, Emanuele Naboni, Barbara Gherri 2022

Figure 30. Variation in UTCI between 2022 and 2050 in the Configuration UP_2 – Modern urban fabric. The area within the dashed rectangle is the area actually used for numerical

evaluation, as it is free from bias resulting from the edge effect of the CFD. Copyright: Marcello Turrini, Emanuele Naboni, Barbara Gherri 2022

Figure 31. Distribution of UTCI variation for the configuration UP_2 - Modern urban fabric. The curve shows dispersed thermal behavior, with a mean value of around 4.3°C and no dominant peak, indicating uneven climate resilience. Copyright: Marcello Turrini, Emanuele Naboni, Barbara Gherri 2022

Figure 32. UP_3 – Industrial area. UTCI on 17 August at 4:00 pm. 2022 on the left, 2050 on the right. Copyright: Marcello Turrini, Emanuele Naboni, Barbara Gherri 2022

Figure 33. Variation in UTCI between 2022 and 2050 in the Configuration UP_3 – Industrial area. The area within the dashed rectangle is the area actually used for numerical evaluation, as it is free from bias resulting from the edge effect of the CFD. Copyright: Marcello Turrini, Emanuele Naboni, Barbara Gherri 2022

Figure 34. Distribution of UTCI variation for the UP_3 configuration. The curve shows a marked concentration between 4.9°C and 5.0°C, with a high mean value and low variability, indicative of low, diffuse, and uniform climate resilience. Copyright: Marcello Turrini, Emanuele Naboni, Barbara Gherri 2022

Figure 35. UP_4 – Natural area. UTCI on 17 August at 4:00 pm. 2022 on the left, 2050 on the right. Copyright: Marcello Turrini, Emanuele Naboni, Barbara Gherri 2022

Figure 36. Variation in UTCI between 2022 and 2050 in the Configuration UP_4 – Natural area. The area within the dashed rectangle is the area actually used for numerical evaluation, as it is free from bias resulting from the edge effect of the CFD. Copyright: Marcello Turrini, Emanuele Naboni, Barbara Gherri 2022

Figure 37. Distribution of UTCI variation for the configuration UP_4 - Natural area. The curve shows an irregular and multimodal profile, with an average of around 4.4°C, indicating a heterogeneous thermal response linked to internal variability in the soil, vegetation, and proximity to water. Copyright: Marcello Turrini, Emanuele Naboni, Barbara Gherri 2022

Figure 38. UP_5– Agricultural area. UTCI on 17 August at 4:00 pm. 2022 on the left, 2050 on the right. Copyright: Marcello Turrini, Emanuele Naboni, Barbara Gherri 2022

Figure 39. Variation in UTCI between 2022 and 2050 in the Configuration UP_5 – Agricultural area. The area within the dashed rectangle is the area actually used for numerical evaluation, as it is free from bias resulting from the edge effect of the CFD. Copyright: Marcello Turrini, Emanuele Naboni, Barbara Gherri 2022

Figure 40. Distribution of UTCI variation for the configuration UP_5 - Agricultural area. The curve shows a very marked peak between 4.7°C and 4.8°C, with a mean value of 4.8°C and a limited range between 4.1 and 5.8°C, indicating high thermal homogeneity and low climate resilience. Copyright: Marcello Turrini, Emanuele Naboni, Barbara Gherri 2022

Figure 41. Summary comparison between the five morphological configurations analyzed (from left: historical urban fabric, modern urban fabric, industrial area, natural area, agricultural area), with visualization of the 3D models, the absolute UTCI values simulated for August 17 at 4:00 p.m. in the two scenarios (2022 and 2050), and the relative UTCI variation (delta). The figure highlights how the thermal response to climate change is strongly influenced by urban morphology: compact and shaded (historic) areas show limited increases, while more exposed and unmitigated (industrial, agricultural) areas show a marked and homogeneous increase in perceived heat stress. Copyright: Marcello Turrini, Emanuele Naboni, Barbara Gherri 2022

Figure 42. Statistical distribution of UTCI variation between 2022 and 2050 for the five morphological configurations analyzed. The curves represent the relative frequency of UTCI variation within each configuration, while the dotted lines indicate the average value for each case. The graph clearly shows the greater thermal resilience of the historic fabric, with a low average and concentrated distribution, compared to the marked vulnerability of the agricultural and industrial configurations, characterized by high peaks, low internal variability, and an average above 4.7°C. Copyright: Marcello Turrini, Emanuele Naboni, Barbara Gherri 2022

Figure 43. UTCI in the surrounding of the convent of San Sepolcro in Parma. Overheating problems related to climate change are evident, when the UTCI on august 5th 2080 at 3pm is higher than 50°C

Figure 44. Hourly dry bulb temperature in Parma for the year 2022 (top) and projected temperature change for 2080 relative to 2022 (bottom), highlighting critical summer

overheating and anticipated future intensification. Copyright: Marcello Turrini, Emanuele Naboni, 2023

Figure 45. Hourly wind speed for a representative day of each month in Parma for 2022 (top) and 2080 (bottom). Each horizontal segment covers 24 hours, from 00:00 (left) to 24:00 (right), and represents the typical daily wind profile for that month. The red line shows the average wind speed, while the blue area indicates the daily range. In 2080, summer wind speeds will increase significantly during the hottest hours, potentially intensifying thermal discomfort due to increased convective heat. Copyright: Marcello Turrini, Emanuele Naboni, Barbara Gherri 2022

Figure 46. The cloister. Three porticoed galleries are on the sides facing north, east and west. A green pavement is in the entire area of the open space. A well is in the middle. Only some small edges on the northern part are the elevated vegetation. Copyright: Marcello Turrini, Emanuele Naboni, Barbara Gherri 2022

Figure 47. Configuration SS_1 - Base case. Green permeable pavement, open to the sky, three porticoed sides. Rendering on the left by Armin Pirngruber. Source of the image on the right: https://internoverde.it/chiostro-delle-maestre-luigine/

Figure 48. Configuration SS_2 - Shading. Representation of the shading element on the cloister. Direct radiation, inclined with respect to the vertical, is blocked by the vertical elements, while radiative exchange with the sky and vertical ventilation is guaranteed. Renderings by Armin Pirngruber. Copyright: Marcello Turrini, Emanuele Naboni, Barbara Gherri, 2022

Figure 49. Configuration SS_3 - Humidity. Dense canopies of vegetation and water provide humidity to the cloister. Renderings by Armin Pirngruber. Copyright: Marcello Turrini, Emanuele Naboni, Barbara Gherri, 2022

Figure 50. Configuration SS_4 - Ventilation. The opening on the ground floor of the cloister connects the internal space to the outside, guaranteeing wind penetration. Renderings by Armin Pirngruber. Copyright: Marcello Turrini, Emanuele Naboni, Barbara Gherri, 2022

Figure 51. The four proposed configurations: SS_1 - Base case, SS_2 - Shading, SS_3 - Humidity, SS_4 - Ventilation. View from north. Copyright: Marcello Turrini, Emanuele Naboni, Barbara Gherri, 2022

Figure 52. Detailed 3D model of the cloister (left) and simplified version for the simulations (right). Copyright: Marcello Turrini, Emanuele Naboni, Barbara Gherri, 2022

Figure 53. Grasshopper and Morpho components for workspace and location settings at the building scale. Copyright: Marcello Turrini, Emanuele Naboni, Barbara Gherri, 2022

Figure 54. Dry bulb temperature in Parma on august 5th 2022 and 2080. Maximum temperature is 39 °C in 2022 and 46.9 in 2080, both at 3:00 pm. Copyright: Marcello Turrini, Emanuele Naboni, Barbara Gherri, 2022

Figure 55. FOX file data for August 5th, 2022 – 2080: in 2080, temperatures exceed 45°C, specific humidity is lower, and diffuse radiation and longwave radiation are more intense than in 2022. Copyright: Marcello Turrini, Emanuele Naboni, Barbara Gherri, 2022

Figure 56. SS_1 – Base case. UTCI on 5 August at 3:00 pm. 2022 on the left, 2080 on the right. Copyright: Marcello Turrini, Emanuele Naboni, Barbara Gherri, 2022

Figure 57. Variation in UTCI between 2022 and 2080 in the Configuration SS_1 – Base case. Maximum value (M) and minimum value (m) are shown. Copyright: Marcello Turrini, Emanuele Naboni, Barbara Gherri, 2022

Figure 58. Distribution of UTCI variation for the configuration SS_1 – Base case. The curve shows a narrow distribution, with a peak around 7.4°C and a high frequency concentrated between 7.4°C and 7.5°C, indicating homogeneous thermal behavior and the lack of resilient microzones. Graph made by the author. Copyright: Marcello Turrini, Emanuele Naboni, Barbara Gherri, 2022

Figure 59. Absolute UTCI values for the configuration SS_2 – Shading. A uniform behavior can be observed in the entire surface of the cloister. Copyright: Marcello Turrini, Emanuele Naboni, Barbara Gherri, 2022

Figure 60. Variation in UTCI between 2022 and 2080 in the Configuration SS_2 – Shading. Maximum value (M) and minimum value (m) are shown. Copyright: Marcello Turrini, Emanuele Naboni, Barbara Gherri, 2022

Figure 61. Distribution of UTCI variation for the SS_2 configuration - Shading. The curve shows a clear peak around 7.2°C, with the highest values between 7.1 °C and 7.2 °C. Graph made by the author. Copyright: Marcello Turrini, Emanuele Naboni, Barbara Gherri, 2022

Figure 62. Absolute UTCI values for the configuration SS_3 – Humidity. A uniform behavior can be observed in the entire surface of the cloister. Copyright: Marcello Turrini, Emanuele Naboni, Barbara Gherri, 2022

Figure 63. Variation in UTCI between 2022 and 2080 in the Configuration SS_3 – Humidity. Maximum value (M) and minimum value (m) are shown. Copyright: Marcello Turrini, Emanuele Naboni, Barbara Gherri, 2022

Figure 64. Distribution of UTCI variation for the configuration SS_3 - Humidity. The narrow curve, with a peak around 7.3°C, indicates a homogeneous and widespread thermal response without thermally privileged areas. Graph made by the author. Copyright: Marcello Turrini, Emanuele Naboni, Barbara Gherri, 2022

Figure 65. Absolute UTCI values for the configuration SS_4 – Ventilation. An asymmetrical behavior can be observed in the entire surface of the cloister, due to asymmetrical surface temperature of the pavement combined with wind flow. Copyright: Marcello Turrini, Emanuele Naboni, Barbara Gherri, 2022

Figure 66. Variation in UTCI between 2022 and 2080 in the Configuration SS_4 – Ventilation. Maximum value (M) and minimum value (m) are shown. The asymmetric behavior is more evident here. Copyright: Marcello Turrini, Emanuele Naboni, Barbara Gherri, 2022

Figure 67. Distribution of UTCI variation for the configuration SS_4 – Ventilation. Wide distribution, with a long tail to the right and values up to 10°C. Graph made by the author. Copyright: Marcello Turrini, Emanuele Naboni, Barbara Gherri, 2022

Figure 68. Summary comparison between the four morphological configurations analyzed (from left: SS_1-base case, SS_2-shading, SS_3-humidity, SS_4-ventilation), with visualization of the top views, the absolute UTCI values simulated for August 5 at 3:00 p.m. in the two

scenarios (2022 and 2080), and the relative UTCI variation (delta). Copyright: Marcello Turrini, Emanuele Naboni, Barbara Gherri 2022

Figure 69. Statistical distribution of UTCI variations for the configurations. Graph by the author. Copyright: Marcello Turrini, Emanuele Naboni, Barbara Gherri, 2022

Figure 70. The building as a bridge station over the tracks. Source: ITALFERR

Figure 71. Plan of the station. A huge void over the tracks is in the central part, while two conditioned boxes for commercial use are on the left and the right side of the void. Source: ITALFERR

Figure 72. Dry bulb temperature in Xirbi. On top in the current scenario, below the delta between 2050 and current scenario. Graph by the author via Grasshopper and Ladybug Tools. Copyright: Marcello Turrini, Emanuele Naboni, 2023

Figure 73. Dry bulb temperature analysis in the hottest week. Peaks are on August 18 and 19. Graph by the author. Copyright: Marcello Turrini, Emanuele Naboni,, 2022

Figure 74. Cloud cover in the hottest week of Xirbi. August 18 is free of clouds both in the current and 2050 scenario. Graph by the author. Copyright: Marcello Turrini, Emanuele Naboni, 2022

Figure 75. Wind velocity and direction in summer. The prevailing direction is from north. Copyright: Marcello Turrini, Emanuele Naboni, 2022

Figure 76. Variation of the two glass facades in the 5 configurations. The red part represents the opening. Copyright: Marcello Turrini, Emanuele Naboni, 2022

Figure 77 Wind simulation for configuration XI_1—The closure of the two facades keeps internal natural ventilation levels very low. Copyright: Marcello Turrini, Emanuele Naboni, 2022

Figure 78. UTCI for configuration XI_1. 2022 on the left, 2050 on the right. Copyright: Marcello Turrini, Emanuele Naboni, 2022

Figure 79. UTCI variation for the configuration XI_1. Copyright: Marcello Turrini, Emanuele Naboni, 2022

Figure 80. Statistical distribution of the UTCI variation for configuration XI_1. Copyright: Marcello Turrini, Emanuele Naboni, 2022

Figure 81. Wind flow for configuration XI_2. Copyright: Marcello Turrini, Emanuele Naboni, 2022

Figure 82. UTCI for configuration XI_2. 2022 on the left, 2050 on the right. Copyright: Marcello Turrini, Emanuele Naboni, 2022

Figure 83UTCI variation for the configuration XI_2. Copyright: Marcello Turrini, Emanuele Naboni, 2022

Figure 84. Statistical distribution of the UTCI variation for configuration XI_2. Copyright: Marcello Turrini, Emanuele Naboni, 2022

Figure 85. Wind flow for configuration XI_3. Copyright: Marcello Turrini, Emanuele Naboni, 2022

Figure 86. UTCI for configuration XI_3. 2022 on the left, 2050 on the right. Copyright: Marcello Turrini, Emanuele Naboni, 2022

Figure 87. UTCI variation for the configuration XI_3. Copyright: Marcello Turrini, Emanuele Naboni, 2022

Figure 88. Statistical distribution of the UTCI variation for configuration XI_3. Copyright: Marcello Turrini, Emanuele Naboni, 2022

Figure 89. Wind flow for configuration XI_4. Copyright: Marcello Turrini, Emanuele Naboni, 2022

Figure 90. UTCI for configuration XI_4. 2022 on the left, 2050 on the right. Copyright: Marcello Turrini, Emanuele Naboni, 2022

Figure 91. UTCI variation for the configuration XI_4. Copyright: Marcello Turrini, Emanuele Naboni, 2022

Figure 92. Statistical distribution of the UTCI variation for configuration XI_4. Copyright: Marcello Turrini, Emanuele Naboni, 2022

Figure 93. Wind flow for configuration XI_5. Copyright: Marcello Turrini, Emanuele Naboni, 2022

Figure 94. UTCI for configuration XI_5. 2022 on the left, 2050 on the right. Copyright: Marcello Turrini, Emanuele Naboni, 2022

Figure 95UTCI variation for the configuration XI_5. Copyright: Marcello Turrini, Emanuele Naboni, 2022

Figure 96. Statistical distribution of the UTCI variation for configuration XI_5. Copyright: Marcello Turrini, Emanuele Naboni, 2022

Figure 97. Comparison of the configurations. Copyright: Marcello Turrini, Emanuele Naboni, 2022

Figure 98. Statistical distribution of UTCI variations in all the configurations. Copyright: Marcello Turrini, Emanuele Naboni, 2022

11 Acknowledgements

I would first like to thank my family and the people closest to me, whose constant support accompanied me throughout my PhD journey.

I would also like to warmly thank Professor Barbara Gherri and Professor Emanuele Naboni, who taught me how to conduct research and consistently provided guidance, encouragement, and constructive feedback.

In addition, I wish to thank the PhD coordinator, Professor Andrea Spagnoli, the former coordinator Professor Sandro Longo, and the entire Faculty Board of the Faculty of Engineering and Architecture at the University of Parma, for their role in shaping and supporting my doctoral path.

I am also grateful to Professor Stefano Schiavon of the University of California, Berkeley, for welcoming me into one of the most historically and internationally recognized research environments, as well as to all the research partners I met worldwide during my doctoral studies.

OpenAI ChatGPT (model o3 and 5.2) was used during the preparation of this thesis as a support tool for drafting, translation, and linguistic refinement. All outputs were reviewed and integrated by the author, who retains full academic responsibility.